

The Gödel Universe

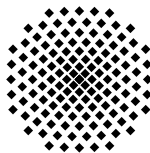
Physical Aspects and Egocentric Visualizations

Von der Fakultät für Mathematik und Physik der Universität Stuttgart
zur Erlangung der Würde eines Doktors
der Naturwissenschaften (Dr. rer. nat.) genehmigte Abhandlung

Vorgelegt von
Frank Grave
aus Ludwigsburg

Hauptberichter: Prof. Dr. Günter Wunner
Mitberichter: Prof. Dr. Daniel Weiskopf

Tag der mündlichen Prüfung: 21. Mai 2010



1. Institut für Theoretische Physik der Universität Stuttgart

2010

The brain is a computing machine connected with a spirit.

— Kurt Gödel

Contents

Abstract	ix
Kurzbeschreibung	xi
Conventions and Abbreviations	xiii
1 Introduction	1
2 Mathematical Foundations of Relativity	7
2.1 Manifolds	8
2.1.1 Vectors, Tangent Spaces and Tensors	8
2.1.2 Riemannian and Pseudo-Riemannian Geometry	10
2.1.3 Local Tetrads	10
2.2 Einstein's Field Equations	12
2.2.1 Christoffel Symbols, Riemann Tensor, Ricci Tensor and Ricci Scalar	12
2.2.2 Field Equations and the Cosmological Constant	13
2.3 Motion of Particles	14
2.3.1 Geodesic Equations	14
2.3.2 Parallel and Fermi-Walker Transport	16
2.4 Killing Vector Fields and Isometries	17
3 Visualization of Einstein's Theory from an Egocentric Perspective	19
3.1 Visualization Using Raytracing	20
3.1.1 Classical 3D Raytracing	20
3.1.2 Relativistic 4D Raytracing	22
3.1.3 Advantages and Drawbacks	23
3.2 Interactive Approaches	23
3.2.1 Graphics Processing Units	25
3.2.2 General Purpose Graphic Processing Units – GPGPU	27
3.2.3 Compute Unified Device Architecture – CUDA	28
3.2.4 Advantages and Drawbacks	32
4 The Gödel Universe in a Nutshell	35

4.1	The <i>ΛCDM</i> Model and Cosmological Observations	36
4.2	The Nature of Gödel's Space-Time	36
4.2.1	Line Element	37
4.2.2	Geodesics	39
4.2.3	Local Tetrads	40
4.2.4	Test Particles	41
4.2.5	And Yet It Rotates – Or Not?	42
4.2.6	Light Cone Structure	45
4.2.7	The Symmetries of Gödel's Spacetime	48
4.3	A Brief History of Time Travel	49
4.3.1	Time Travel Universes	49
4.3.2	Causality Violations	52
4.3.3	Remedies to Paradoxes	53
5	Analytical Investigations	57
5.1	Geodesics	58
5.1.1	Geodesics for Special Initial Conditions	59
5.1.2	Geodesics for Arbitrary Initial Conditions	61
5.2	Isometric Transport	68
5.2.1	Isometric Transport of Points	68
5.2.2	Isometric Transport of Vectors	69
5.3	Mapping of Arbitrary Curves	71
5.3.1	Mapping of Geodesics	71
5.3.2	Mapping of the Gödel Horizon	72
5.3.3	Mapping of Worldlines and Generation of CTCs	73
5.4	Living in Gödel's Universe	77
5.4.1	Gödel's Universe and the Cosmological Constant	78
5.4.2	Gödel's Universe and Best-Fit <i>WMAP</i> Data	79
6	The Gödel Engine	81
6.1	Appearance of Objects	82
6.2	Mathematical Preparation	83
6.3	Implementation	89
6.3.1	Object Types and Object-Based Algorithm	89
6.3.2	The Graphical User Interface – Gödel Engine Server	92
6.3.3	Rendering Images – Gödel Engine Client	92
6.3.4	Core Rendering Loop	93
6.4	Technical Discussion	99
6.4.1	Advantages	99
6.4.2	Drawbacks	101

7 Visualization of the Gödel Universe	105
7.1 Light Propagation	107
7.1.1 Light Cones and Wavefronts	107
7.1.2 Frequency Shifts	110
7.1.3 Emission Time	111
7.2 From Flat Spacetime to Gödel's Metric	112
7.2.1 Fixed Grid	112
7.2.2 Fixed Distances	118
7.3 Quasistatic and Illuminated Objects	120
7.3.1 Objects in the (XY) -Plane	120
7.3.2 Objects at Arbitrary Positions	126
7.3.3 Shadows	132
7.4 Relativistically Moving Objects	133
7.4.1 Geodesical Motion Restricted to the Causal Region	136
7.4.2 Visualization of Geodesical Time Travel	142
7.4.3 Objects Moving on Closed Timelike Curves	148
7.4.4 On the Impossibility of Visualizing Causality Violations	157
8 Playground	159
8.1 Our Solar System	159
8.2 Stars from our Galaxy – The Hipparcos Catalog	162
8.3 Star Trek	167
9 Conclusion and Outlook	169
10 Schlussfolgerungen und Ausblick	177
A Details on the Gödel Metric	185
A.1 Cylindrical Coordinates	185
A.2 Scaled Cylindrical Coordinates	187
B Details on the Solution of the Geodesic Equations	191
B.1 Special Initial Conditions	191
B.2 General Initial Conditions	192
C Details on the Solution of the Equations of Isometric Transport	195
C.1 Transformation of Points	195
C.2 Transformation of Vectors	196
List of Figures	201

Index	206
Bibliography	207
Danksagung	215
Vita	219

ABSTRACT

Albert Einstein, often characterized as the “greatest physicist of all time”, has revealed the curved nature of space and time when he founded the general theory of relativity, which was verified on the large scale in numerous experiments over the last century. Kurt Gödel – the famous logician, mathematician and philosopher – is best known for his incompleteness theorem, being one of the most important theorems of mathematical logic. During their time in Princeton, Gödel and Einstein became close friends. Both were outstanding researchers in their respective fields of study and, luckily, the symbiosis yielded fruit. Most notably, Gödel found a general relativistic model with a multitude of intriguing and counter-intuitive properties: **The Gödel universe**.

Kurt Gödel’s universe is one of the most interesting exact solutions of Einstein’s equations. This model represents an alternative universe merely consisting of homogeneous dust which is rotating around every point. In addition to its mathematical beauty and simplicity resulting from the high symmetry of the underlying spacetime, this metric demonstrates an intrinsic property of the general theory of relativity: It describes a theoretically feasible spacetime in which time travel is possible beyond an optical horizon.

This work targets the following question: **Is it possible to conceive a mental image of such a peculiar universe?**

Therefore, we derive the analytical solution of the geodesic equations of Gödel’s universe for both particles and light in a special set of coordinates, which reveals the physical properties of this spacetime in a very transparent way. We also recapitulate the equations of isometric transport for points and derive the solution for Gödel’s universe. The equations of isometric transport for vectors are introduced and solved. We utilize these results to transform different classes of curves along Killing vector fields. In particular, we generate non-trivial closed timelike curves (CTCs) from circular CTCs. All analytical results then serve as a starting point for visualizations of the Gödel universe.

We illustrate optical effects from a first person’s point of view: What does an observer in the Gödel universe actually see? These egocentric visualizations of a general relativistic spacetime illustrate aspects of Einstein’s insights to the expert as well as to the layperson. Using raytracing in four dimensions, we are able to adopt such an egocentric point of view. This well-known approach is characterized by its generic rendering procedure. It can be applied as long as an

analytical expression for a metric is available. Unfortunately, this method is very costly and we are only able to utilize ambient illumination. However, due to the relatively simple structure of the geodesics in Gödel's universe, it is possible to devise a technique which directly calculates the appearance of an object – as long as it is resting or moving quasistatically – without the explicit generation of primary ray segments or tedious intersection calculations. Along with programmable graphics hardware, we achieve a tremendous speedup for the visualization of general relativistic effects. This enables us to interactively explore physical aspects and optical effects of Gödel's universe. We also demonstrate how the analytical solutions allow for a dynamic lighting with local illumination models. Beyond that, a straightforward shadow model can be realized. Our implementation is tailored for Gödel's universe and is at least four to five orders of magnitude faster than previous approaches. However, we must rely on raytracing for the visualization of fast moving objects. Above all mathematical considerations and technical innovations, this work presents egocentric visualizations of time travel within general relativity which has not yet been done.

To facilitate the understanding of the optical appearance of the Gödel universe, a multitude of insightful scenarios is introduced. We increase the complexity factor of the scenes slowly but steadily: From the simplest shapes, such as coordinate grids or spheres, via illuminated and non-primitive objects through to time traveling entities or a fictional solar system where a spaceship is flying into the starry sky.

Here we go on a journey through the Gödel universe!

KURZBESCHREIBUNG

Albert Einstein, oftmals als „der größte Physiker aller Zeiten“ bezeichnet, hat die gekrümmte Beschaffenheit von Raum und Zeit aufgespürt, als er die allgemeine Relativitätstheorie entwickelte. In den letzten hundert Jahren wurde diese Theorie in zahlreichen Experimenten als eine korrekte Beschreibung der Welt für große Längenskalen bestätigt. Auf der anderen Seite ist Kurt Gödel – der bedeutende Logiker, Mathematiker und Philosoph – durch seinen Unvollständigkeitssatz bekannt, welcher einer der wichtigsten Sätze der mathematischen Logik ist. Während ihrer gemeinsamen Zeit in Princeton wurden Gödel und Einstein enge Freunde. Beide waren in ihren jeweiligen Forschungsgebieten herausragende Wissenschaftler und diese Symbiose hat glücklicherweise Früchte getragen. Gödel konnte insbesondere ein allgemeinrelativistisches Modell auffinden, welches sich durch eine Vielzahl an faszinierenden und kontraintuitiven Eigenschaften auszeichnet: **Das Gödel-Universum**.

Das Universum von Kurt Gödel ist eine der interessantesten exakten Lösungen der Gleichungen von Einstein. Dieses Modell beschreibt ein alternatives, aber theoretisch mögliches Universum, welches einzig und allein aus homogenem und um jeden Punkt rotierenden Staub besteht. Neben seiner mathematischen Eleganz und Einfachheit, welche aus der hohen Symmetrie der zugrunde liegenden Raumzeit resultiert, zeigt diese Metrik eine intrinsische Eigenschaft der allgemeinen Relativitätstheorie auf: In diesem Modell offenbart sich die Möglichkeit von Zeitreisen hinter einem optischen Horizont.

Diese Arbeit zielt auf die folgende Frage ab: **Ist es möglich, eine Vorstellung von solch einem ungewöhnlichen Universum zu entwickeln?**

In dieser Arbeit wird die analytische Lösung der Geodätengleichungen für Teilchen und Licht für das Gödel-Universum hergeleitet. Dazu werden spezielle Koordinaten verwendet, welche die physikalischen Eigenschaften dieser Raumzeit sehr klar zum Vorschein bringen. Außerdem werden die Gleichungen des isometrischen Transports von Punkten rekapituliert und deren Lösung für das Gödel-Universum bestimmt. Zudem werden die Gleichungen des isometrischen Transports von Vektoren hergeleitet und gelöst. Diese Ergebnisse werden verwendet, um verschiedene Kategorien von Kurven entlang von Killing-Vektorfeldern zu transportieren. Insbesondere werden dadurch nicht-triviale geschlossene zeitartige Kurven (closed timelike curves oder CTCs) aus kreisförmigen CTCs erzeugt. Alle analytischen Resultate dienen als Ausgangspunkt für Visualisierungen des Gödel'schen Universums.

Um herauszufinden, was ein Beobachter im Gödel-Universum tatsächlich *sieht*, werden die optischen Effekte in der Ich-Perspektive dargestellt. Diese egozentrischen Visualisierungen einer allgemeinrelativistischen Raumzeit verdeutlichen dem Experten (aber auch dem wissenschaftlichen Laien) viele Aspekte der Erkenntnisse Einsteins. Solch eine Sichtweise wird mit Hilfe von vierdimensionalem Raytracing ermöglicht, welches durch seine generische Rendering-Prozedur gekennzeichnet ist. Sie kann immer dann angewendet werden, wenn ein analytischer Ausdruck der Metrik gegeben ist. Leider ist dieser Ansatz sehr teuer und ermöglicht ausschließlich ein ambientes Beleuchtungsmodell. Aufgrund der relativ einfachen Struktur der Geodäten im Gödel-Universum kann jedoch ein spezialisiertes Verfahren entwickelt werden, welches dieses Problem vermeidet. Diese Methode berechnet das Erscheinungsbild eines Objektes direkt, ohne Primärstrahlsegmente zu erzeugen oder langwierige Schnittberechnungen durchzuführen, solange dieser Gegenstand ruhend oder quasistatisch bewegt wird. Unter Verwendung von programmierbarer Grafikhardware wird dadurch eine gewaltige Beschleunigung der Visualisierung allgemeinrelativistischer Effekte erzielt. Dadurch wird es möglich, physikalische Eigenschaften und optische Effekte des Gödel'schen Universums interaktiv zu erforschen. Zusätzlich wird durch die analytischen Lösungen der Weg für eine dynamische Beleuchtung unter Verwendung eines lokalen Beleuchtungsmodells geebnet. Darüber hinaus kann ein sehr einfaches Schattenmodell realisiert werden. Die Implementierung ist für das Gödel-Universum maßgeschneidert und ist dabei mindestens vier bis fünf Größenordnungen schneller als bisherige Ansätze. Allerdings muss für die Visualisierung schnell bewegter Objekte auf klassisches Raytracing zurückgegriffen werden. Jenseits aller mathematischen Erörterungen und technischen Neuerungen stellt diese Arbeit die erste Veröffentlichung dar, welche Zeitreisen im Rahmen der allgemeinen Relativitätstheorie in einer egozentrischen Sichtweise visualisiert.

Um das optische Erscheinungsbild des Gödel-Universums zu erklären, wird eine Vielzahl aufschlussreicher Szenarien untersucht. Dabei wird der Schwierigkeitsgrad der Szenen langsam aber stetig erhöht: Von den einfachsten Formen wie Koordinatengittern oder Kugeln, über beleuchtete und nicht-primitive Objekte, bis hin zu zeitreisenden Gegenständen oder einem fiktiven Sonnensystem, durch welches ein Raumschiff in den Sternenhimmel fliegt.

Auf zu einer Reise durch das Gödel-Universum!

CONVENTIONS AND ABBREVIATIONS

Conventions: Following the conventions for quantities and units [Int] introduced by the International Organization for Standardization (ISO) we use:

\mathbf{x} (vectors, points) \mathbf{T} (tensors) \mathbf{A} (matrices)

Note that a vector in flat, three-dimensional space (or the spatial projection of a vector in a tetrad) is often written as \vec{x} . For the components of vectors, higher order tensors or other indexed quantities we write:

x^μ contravariant component	$g_{\mu\nu}$ covariant metric tensor
x_μ covariant component	$\Gamma_{\mu\nu}^\rho$ Christoffel symbols of 2 nd kind

To distinguish between coordinate and tetrad representations, we use Greek indices for coordinates and Latin indices in brackets for tetrads:

v^μ vector in coordinates	$v^{(i)}$ vector with respect to a local tetrad
$e_{(i)}^\mu$ transformation matrix to local representation	$\theta_{\mu}^{(i)}$ transformation matrix to coordinate representation

We do not distinguish between tensors and their components. Furthermore, the line element ds^2 is often called metric. The metric tensor g is always formulated so that the signature is positive, i. e. $\text{sign}(g) = +2$.

Using the Einstein summation convention, we sum over lower and upper indices of the same name without explicitly writing the summation sign. In general relativity, this convention yields $u^\mu v_\mu \equiv \sum_{\mu=0}^3 u^\mu v_\mu$. A lower index of zero, i. e. \dot{x}_0^μ , is not a covariant index but expresses, unless otherwise denoted, that the property is an initial value. The covariant derivative of, for example, a vector v^μ is denoted as $v^\mu_{;\nu}$, and the partial derivative is expressed as $v^\mu_{,\nu}$. Definitions and occurrences of important terms are written using ***slanted boldface letters***. The Gödel metric itself is introduced in Sec. 4.2, and is typically expressed using a cylindrical coordinate set (T, R, ϕ, Z) in which the line element is of the form

$$ds^2 = r_G^2 (g_{\mu\nu} dx^\mu dx^\nu).$$

All properties derived from this form of the metric scale with the Gödel radius r_G accordingly. In some illustrations, scaled pseudo-Cartesian coordinates, $X = R \cos(\phi)$, $Y = R \sin(\phi)$, are used.

Program code is always written in a typewriter font and appears boxed if not located in continuous text:

```
int a = b + c; //adding two integers
```

Programs themselves – or important libraries – appear in small capital letters: `OpenGL`, `CUDA`, `Gödel Engine`.

When visualizing the Gödel universe from an egocentric perspective, we are confronted with a very large number of visible images of one object. Therefore, we have to distinguish several distinct classes of optical effects for the clarity of the presentation. A physical entity is denoted as an **object** and a visible image is designated as an **object image** or **image**. In Gödel's universe, we are also confronted with the visual effects of time traveling objects. Then, one physical entity might be *existent* more than once: The entity leaving for time travel and the *same* entity returning from the journey. We distinguish both by using the description **instances** of a physical object.

In addition to this work, there are several accompanying movie sequences provided on a storage medium. If an image in this document is taken from a movie clip, we indicate the filename using `AssociatedFilm.avi`.

Abbreviations:

ALU	Arithmetic Logical Unit
API	Application Programming Interface
CNC	Closed Null Curve
CPU	Central Processing Unit
CTC	Closed Timelike Curve
CUDA	Compute Unified Device Architecture
fps	frames per second
GE	renderings created with the <code>Gödel Engine</code>
GPU	Graphics Processing Unit
GLSL	<code>OpenGL</code> Shading Language
GUI	Graphical User Interface
GV	renderings created with the <code>GeoVis</code> framework
iff	if and only if
ly	light year
POI	Point of Interest
PTC	Past-Traveling Curve

INTRODUCTION

"I went to the office just to have the privilege of walking home with Kurt Gödel." — ALBERT EINSTEIN

Motivation: As a good friend of Albert Einstein, Kurt Gödel published an article in 1949 entitled *"A remark about the relationship between relativity theory and idealistic philosophy"* [G690] to pay tribute to Einstein on the occasion of his 70th birthday. One of Gödel's thoughts, which he detailed in this article, was the influence of general relativity on the nature of time. He discussed the possibility of reversed time ordering and, as a consequence, the breakdown of causality. In the same year, Gödel published a mathematical model of a universe in which time travel is possible. In this model, light rays are always restricted to a limited region which, therefore, represents an optical horizon. Exactly this optical horizon divides the spacetime into two parts. In the inner part, time travel is not possible and causality is conserved. When traveling beyond the optical horizon it is possible to travel into the past of a person located in the causal inner region.

Why are we interested in the egocentric visualization of such a peculiar model? On the one hand, we know that our universe is not of Gödel type. In the standard cosmological model (Λ CDM model), our universe is described as a homogeneous and isotropic spacetime with a positive cosmological constant, where the Hubble-expansion leads to a gravitational redshift. The Gödel universe, however, is a homogeneous but non-isotropic world model which is rotating around every point. The cosmological constant is negative and no gravitational redshift arises. The most important difference between these two models is yet even more profound: While the Λ CDM-model is causal, the Gödel universe permits time travel and, therefore, causality violations. On the other hand, it is easily verified that the Gödel spacetime is an exact solution of Einstein's field equations. Moreover, numerous spacetimes allowing time travel have been found, making time travel more than an isolated feature of a single metric and, ultimately, an inherent property of the theory of relativity itself. Time travel is, *in principle*, possible if we only take general relativity into account. On the large scale, the general theory of relativity is still the

standard theory for all quantitative investigations. Egocentric visualizations enable us to visualize the remarkable optical effects of relativity (also resulting from time travel) and the Gödel spacetime can be regarded as the “standard model” of time travel universes.

From a technical perspective, the processing power of computers has increased tremendously over the last decades. To visualize general relativity, standard raytracing methods must be extended because light rays are curved and the velocity of light is not infinite. In prior implementations, the geodesic equations are integrated numerically to determine the curved rays on which light travels. The resulting segments are then used for intersection calculations similar to standard raytracing to find the direction under which a certain object is seen. This procedure is very costly and the resulting images lack illumination beyond ambient lighting because the incident light direction is indeterminable due to the arbitrarily high complexity of the lightlike geodesics. The straightforward implementation of an analytical solution to the geodesic equations in order to generate these segments decreases rendering time drastically, but still does not result in interactive frame rates. In this work, we also want to face those issues and reduce the gap between common visualization standards and relativistic visualizations within the domain of the Gödel universe: Our approach avoids a numerical integration and directly computes the locations where a resting or quasistatic object is visible. We can interactively alter the visualization parameters and discover effects which are hardly possible to find with non-interactive methods. Exploiting the analytical solution, it is also possible to apply a local illumination model.

Our efforts also cater to researchers of other fields of study and even to the scientific layperson. Visualization has proven to be a powerful resource to explain relativity to individuals without profound knowledge of this theory. Most notably, the Major Special Exhibition Albert Einstein 2005/2006 in Bern¹ revealed a tremendous public interest in correct visualizations of special and general relativity. In this exhibition, both static movies as well as interactive exhibits were displayed. While the movie sequences targeted the comprehension of theoretical trains of thoughts, interactive installations enabled a rather intuitive understanding of specific effects due to the haptic interaction and the prompt visual feedback.

Since the Gödel metric is an exact and fairly manageable solution to the field equations, we can investigate the following hypotheses by means of a case study on the Gödel universe:

- 1. Egocentric visualizations enable us to understand time travel intuitively.**
- 2. Interactive approaches facilitate the discovery of unknown optical effects.**
- 3. It is possible to visualize causality violations.**

We will return to these hypotheses when concluding this work in Ch. 9.

¹http://www.bhm.ch/en/ausstellungen_sonder_01a.cfm

Contributions of the author: This thesis is the yield of a DFG-funded project with four participating institutes: The “1. Institut für Theoretische Physik” as well as the “Institute for Visualization and Interactive Systems” of the Universität Stuttgart, the “Institut für Quantenphysik” of the Ulm University and the “Theoretische Astrophysik Tübingen”. Additionally, many papers have been composed and accepted. The following paragraphs provide information on my contributions to these publications.

An introductory paper, “*Wave Fronts in General Relativity Theory*” [GFAMA08], was published at the Eleventh Marcel Grossmann Meeting. I seized on an idea which I had already investigated within the context of my diploma thesis [Gra04]. Non-egocentric, finite light cones and wave front structures are computed using an integrator which was ported from GEOVIS [Mü06] (a 4D raytracing framework for general relativity) to JAVA. Using a graphical user interface, one can choose between several spacetimes and the initial conditions; the program then precalculates the structures. After this step, the visualization parameters, such as the camera position and several types of projections, can be adjusted interactively. Finally, the results are shown in an OpenGL window. I was responsible for the entire implementation of the application (JWFRONT) and major parts of the paper.

The basic optical properties of quasistatic objects in the Gödel universe were revealed in the first publication within this project: “*Visualization of the Gödel Spacetime*” [GMW*07], where we focused on the visualization of quasistatic motion *within* the Gödel horizon. The entire draft and all but one rendering were the results of my simulations. The egocentric visualizations were computed using the GEOVIS framework and the depictions of geodesics (without an exemplary camera) resulted from applications which I built on top GEOVIS.

In the paper “*Visiting the Gödel Universe*” [GB08], I developed an interactive postrendering technique for analytically given spacetimes while my co-author focused on a (non-interactive) local illumination model for the Gödel universe. I extended GEOVIS so that – besides the actual RGB data – a data file is generated, which includes the entire information that is stored in the surface intersections (positions, directions, texture coordinates, ...). This data file is then used, for example, to interactively re-texture the objects of the scene. Also, frequency shifts and time shifts are included and the postrendering computations are implemented as shaders.

Using the most beneficial ideas of my colleagues, we published [GMDW09] the interactive rendering approach “*The Gödel Engine - An interactive approach to visualization in general relativity*”. Using special analytical solutions to the geodesic equations alongside numerically integrated equations of isometric transport, I was able to overcome two major disadvantages of the previous publication. First, the image generation was ameliorated to interactive frame rates, even when a local illumination model had been applied. Second, the tedious generation of the data file was avoided for the Gödel universe. I drafted the paper and devised and implemented the approach. This thesis enhances several ideas from the paper and extends the application, for example, regarding several analytical results which were not available for the original paper.

The most recent paper, “*The Gödel universe: Exact geometrical optics and analytical investigations on motion*” [GBM*09], summarizes the analytical results of our project and includes the solutions to both the geodesic equations and the equations of isometric transport (for points as well as vectors). In close cooperation with all project partners, several interesting aspects were developed and investigated. I conducted the actual derivations as well as analyses and was responsible for drafting the paper.

My recent contributions as co-author include the `GEODESICVIEWER`, the `MOTION4D` library and the *Catalogue of Spacetimes*. The `GEODESICVIEWER` [MG10] focuses on the non-egocentric visualization of geodesics in spacetimes, for which an analytical expression of the metric is known. It provides a graphical user interface, which enables the choice of the metric, integrators and initial conditions for geodesics. The published version was mainly implemented by T. Müller. However, I developed a similar application as preparatory work for the actual publication. This application, `GEOVIEW`, already includes the base functionality of the final `GEODESICVIEWER`, but not its advanced features. Moreover, it was specially adapted to the Gödel universe to verify, for example, the analytical solutions to the geodesic equations. Both versions of the application rely on the `MOTION4D` library [MG09a] and the metrics themselves are documented in the *Catalogue of Spacetimes* [MG09b]. I focused on the Gödel universe in these two publications.

Outline: The subsequent chapters are organized as follows: We review the basic concepts of the general theory of relativity in Ch. 2. Beginning with the mathematical description of four-dimensional pseudo-Riemannian manifolds, we recapitulate the foundation of this theory: Einstein’s field equations express the connection between the mass and energy distribution in a general relativistic model and the curvature of the spacetime. If a test particle is propagating within a general relativistic model, its motion is either governed by the geodesic equations or the Fermi-Walker-transport (if forces beyond gravitation are present). Spacetimes inheriting specific symmetries allow for isometric transformations which are expressed by Killing vector fields. We also focus on the concept of local tetrads, which are utilized in the subsequent sections to formulate observers, objects and initial conditions of motion with respect to a local frame.

Ch. 3 provides details on the set of tools and techniques used to visualize optical effects of the theory of relativity. After a recap of three-dimensional and four-dimensional raytracing, we continue with modern interactive approaches. Therefore, we explain the functionality of graphics processing units, which can also be used for general purpose computations. Several programming languages exist to enable arbitrary code execution on a graphics processing unit. We introduce one of them and give a straightforward example of a simple program to get acquainted to the programming model.

The last introductory chapter, Ch. 4, focuses on the theoretical background of the Gödel universe itself. We refer to numerous publications in order to overview interesting properties of the Gödel model that have been found since its discovery. Additionally, we conduct several short calcula-

tions of, for example, local tetrads, the stress-energy tensor and the light cone structure. These calculations are relatively simple to accomplish and offer a fair complement to the related work as well as a consistent notation throughout this document. We close this chapter with a summary of time travel universes in general relativity and a compilation of theoretical and philosophical aspects regarding time travel and causality violations.

The next chapters deal with the visualization of the Gödel universe. We must formulate a specific arrangement of objects and an observer. After this definition of a scene, we must calculate which photons – emitted by an arbitrary point of any object – arrive in the observer's eye. All photons absorbed at the same time generate the visual impression of the scene at any one time. Consequently, knowledge of the propagation of light is crucial for this egocentric visualization. Therefore, we solve the geodesic equations for light and massive particles in Ch. 5. We discuss timelike motion on geodesics and come to the conclusion that such time travel is possible but not causality violating. Then, the equations of isometric transport for points as well as vectors are solved. These solutions permit the mapping of curves. We generate an interesting class of closed timelike curves using isometric transformations and circular closed timelike curves. The motion on these paths provides the possibility of causality violations.

The solutions found in Ch. 5, combined with the computational power of modern graphics cards, equip us with a powerful set of tools which enable a new approach in the visualization of general relativity. In Ch. 6, we introduce the *GÖDEL ENGINE*, an interactive, point-based method to render scenes formulated within the Gödel universe from an egocentric point of view. The analytical solution of the geodesic equations, alongside the isometric transformations, are used to realize a fast rendering algorithm. To include several optical effects and to generate renderings which appear more realistic, we apply a local illumination model. Even the computation of basic self-shadowing effects is easily realizable. After the details on the core rendering algorithm, we analyze the assets and drawbacks of this new method: We are able to generate physically correct and optically appealing images extraordinarily fast, but we can only implement static or quasistatically moving objects. For the visualization of fast moving objects, such as time traveling objects, we must fall back to a generic raytracing approach and lose the high performance and the local illumination model of the *GÖDEL ENGINE*.

Finally, Ch. 7 discusses the visualization of the Gödel universe. First, the propagation of light is examined from a slightly different point of view when compared to the analytical discussions and theoretical foundations of the previous chapters. Then, a collection of insightful scenes is visualized. We illustrate the optical appearance of grids and large coordinate objects, several resting or quasistatically moving objects which are illuminated, fast motion on geodesics, time travel on geodesics and motion on closed timelike curves. The discussion of each scene is always composed of the same elements: A diagrammatic definition of the scene itself (“What is shown?”), a quantitative analysis of the optical appearance utilizing a specific type of graph (“What can be expected?”) and the egocentric visualizations themselves (“What does the observer actually see?”). Whenever the object is moving close to the speed of light, we also visualize the apparent

surface temperature and the local light emission times on the objects using tone mapping. The local light emission times allow us to identify time traveled objects, which is the main focus of the visualization of the Gödel universe. However, we identify that the visualization of causality violations is as problematic as their theoretical treatment.

The last main chapter of this work is the “playground” section, where three sophisticated scenes are shown: The creation of the inner solar system, the implementation of the Hipparcos catalog into the GÖDEL ENGINE and the opening credits of “Star Trek: The Next Generation” rendered for the Gödel universe.

MATHEMATICAL FOUNDATIONS OF RELATIVITY

“No matter how hard you try to teach your cat general relativity, you’re going to fail.” — BRIAN GREENE

In 1905, Einstein founded the theory of special relativity [Ein05], where the correct transformation between coordinate systems in relative motion at a high relative velocity is described. General relativity, a geometric theory of gravitation, was discovered in 1915 [Ein15] and extends special relativity regarding gravitation. Confirmed by countless experiments, Einstein’s theory is considered a valid description of our universe on the large scale. In the theory of relativity, the three spatial dimensions and time itself cannot be described as separate entities but form a four-dimensional spacetime continuum. These spacetimes are represented by four-dimensional pseudo-Riemannian manifolds which are solutions to Einstein’s field equations.

The theory of relativity has profoundly changed our view of space and time. Lengths, elapsed times or even masses of objects become dependent on the relative speed between an observer and the investigated object. The spacetimes of general relativity are described with curved manifolds. Here, the circumference of a circle or the volume of a sphere becomes dependent on the position on the manifold.

In this chapter, only a very short introduction to the concepts of general relativity will be given. First, the mathematical principles of pseudo-Riemannian manifolds are reviewed. Then, the description of general relativistic spacetimes, the propagation of particles along worldlines and the basic characteristics of Einstein’s field equations are outlined. Very detailed presentations and the following equations can be found, for example, in [Rin06, MTW73, Nak90, Wal84, Gra04, Mü06].

2.1 Manifolds

Let \mathcal{M} be a set. \mathcal{M} is an m -dimensional, differentiable **manifold**, if \mathcal{M} is a topological space with certain properties. There exists a family of pairs $\{(U_i, \varphi_i)\}_{i \in I}$. The family $\{U_i\}_{i \in I}$ consists of open sets and cover \mathcal{M} , i. e. $\bigcup U_i = \mathcal{M}$, whereas the family $\{\varphi_i\}_{i \in I}$ is constituted of homomorphisms mapping $U_i \rightarrow U'_i \subseteq \mathbb{R}^m$. If two sets, U_i and U_j , overlap, then an infinitely often differentiable function $\mathbb{C}^\infty \ni \psi_{ij} = \varphi_i \circ \varphi_j^{-1}$ exists that maps the overlap region. The pairs (U_i, φ_i) are denoted as a **chart** and the family $\{(U_i, \varphi_i)\}_{i \in I}$ is an **atlas**. The manifold is **parameterized** using the family $\{\varphi_i\}_{i \in I}$. Fig. 2.1 illustrates these definitions.

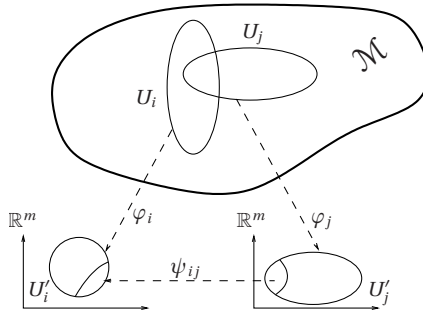


Figure 2.1: A manifold is a set which can be locally identified with a real-valued coordinate system.

2.1.1 Vectors, Tangent Spaces and Tensors

Usually, a vector is interpreted as the directed connection between two points in \mathbb{R}^m . However, this straightforward definition is not possible for arbitrary manifolds \mathcal{M} . We define a **vector** using a directional derivative on the manifold in the following way: A **curve** c is a function $c: \mathbb{R} \supseteq (a, b) \rightarrow \mathcal{M}$ and a function on \mathcal{M} is defined as $f: \mathcal{M} \rightarrow \mathbb{R}$. The tangent vector in $c(0)$ is then obtained using

$$\left. \frac{df(c(\lambda))}{d\lambda} \right|_{\lambda=0} = \left. \frac{d}{d\lambda} (f \circ \varphi^{-1} \circ \varphi \circ c(\lambda)) \right|_{\lambda=0} = \frac{\partial (f \circ \varphi^{-1}(x^\nu))}{\partial x^\mu} \cdot \left. \frac{dx^\mu(c(\lambda))}{d\lambda} \right|_{\lambda=0}.$$

Fig. 2.2 illustrates the idea of defining curves on a manifold.

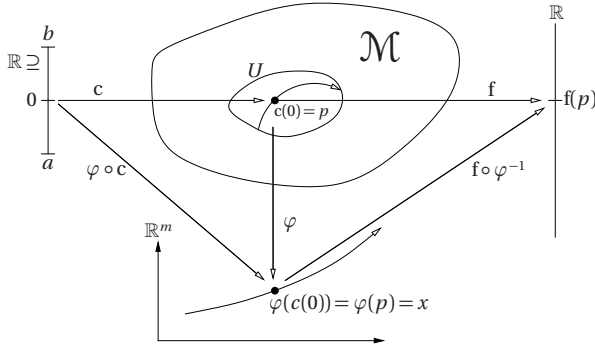


Figure 2.2: Definition of a curve on a manifold using an “indirection” over \mathbb{R}^m .

We set

$$t^\mu := \left. \frac{dx^\mu(c(\lambda))}{d\lambda} \right|_{\lambda=0}$$

and can then write

$$\left. \frac{df(c(\lambda))}{d\lambda} \right|_{\lambda=0} = t^\mu \frac{\partial}{\partial x^\mu} (f \circ \varphi^{-1}(x^v)).$$

The tangential vector \mathbf{t} in $\mathcal{T}_p \mathcal{M} := \mathcal{T}_p \mathcal{M}$ is then given by the differential operator

$$\mathbf{t} := t^\mu \frac{\partial}{\partial x^\mu} \equiv t^\mu \partial_\mu, \tag{2.1}$$

where the components t^μ of the vector \mathbf{t} are given with respect to the vectors $\{\partial_\mu\}$. The set of all tangent vectors for a fixed point $p = c(0)$ span the **tangent vector space** $\mathcal{T}_p \mathcal{M}$, where a possible base is given by the **coordinate base** $\{\partial_\mu\}$. The **cotangent vector space** (or **dual vector space**) $\mathcal{T}_p^* \mathcal{M}$ is defined as the set of all functions $df : \mathcal{T}_p \mathcal{M} \rightarrow \mathbb{R}$. A base of the cotangent vector space is given by the differentials $\{dx^\mu\}$ and a vector $s \in \mathcal{T}_p^* \mathcal{M}$ is written as $s = s_\nu dx^\nu$. Using these two vector spaces, a **scalar product** (inner product) $\langle \cdot, \cdot \rangle : \mathcal{T}_p^* \mathcal{M} \otimes \mathcal{T}_p \mathcal{M} \rightarrow \mathbb{R}$ is defined as

$$\langle \mathbf{s}, \mathbf{t} \rangle := s_\mu t^\mu. \tag{2.2}$$

It can be shown that

$$\langle dx^\mu, \partial_\nu \rangle = \delta_\nu^\mu, \tag{2.3}$$

where δ_ν^μ is the Kronecker-delta. The scalar product also defines the **norm** of a vector \mathbf{u} , i. e.

$$\|\mathbf{u}\|^2 = \langle \mathbf{u}, \mathbf{u} \rangle. \tag{2.4}$$

A **tensor** is defined as a multilinear mapping

$$T : \otimes^q \mathcal{T}_p^* \mathcal{M} \otimes \otimes^p \mathcal{T}_p \mathcal{M} \rightarrow \mathbb{R} \quad (2.5)$$

and can be written as

$$T = T^{\mu_1 \dots \mu_q}_{\nu_1 \dots \nu_p} \partial_{\mu_1} \otimes \dots \otimes \partial_{\mu_q} \otimes dx^{\nu_1} \otimes \dots \otimes dx^{\nu_p}. \quad (2.6)$$

Obviously, vectors are tensors. Lower indices are denoted as **covariant indices** and superscripts are designated as **contravariant indices**. Raising and lowering of indices is achieved using the metric tensor, for example $v_\mu = g_{\mu\nu} v^\nu$ or $u^\mu = g^{\mu\nu} u_\nu$.

2.1.2 Riemannian and Pseudo-Riemannian Geometry

Manifolds on which a symmetric **metric** g is defined enable measurements of distances and angles. The infinitesimal distance between two points on the manifold is given by the **line element**

$$ds^2 := g_{\mu\nu} dx^\mu \otimes dx^\nu \equiv g_{\mu\nu} dx^\mu dx^\nu. \quad (2.7)$$

Since the metric tensor g is symmetric, it can be diagonalized (at least locally), resulting in n positive and m negative values along the diagonal. The **signature** of a metric is $\text{sign}(g) = n - m$. If the metric is positive definite we speak of **Riemannian geometry**.

In relativity, the metric tensor is **Lorentzian**, i. e. it describes a four-dimensional manifold with a signature of $\text{sign}(g) = \pm 2$. Throughout this work, the first coordinate is timelike and the remaining dimensions are spatial. To emphasize this continuum of spatial dimensions and time itself, a point p on these manifolds is also characterized as an **event**. The metric tensor is not positive definite and the manifold is of **pseudo-Riemannian geometry**. Note that the sign of the signature is physically irrelevant. We follow the convention that $\text{sign}(g) = +2$. Since the metric is not positive definite, the squared length of a vector $\langle \mathbf{u}, \mathbf{u} \rangle = \|\mathbf{u}\|^2$ can take any real value. We distinguish between **timelike vectors** ($\|\mathbf{u}\|^2 < 0$), **lightlike vectors** ($\|\mathbf{u}\|^2 = 0$) and **spacelike vectors** ($\|\mathbf{u}\|^2 > 0$). Special relativity is described with the flat Minkowski-spacetime, where the metric is given by the diagonal tensor $g_{\mu\nu} = \text{diag}(-c^2, 1, 1, 1)$, where c is the velocity of light.

2.1.3 Local Tetrads

It can be shown that, due to the symmetry of the metric tensor, a locally flat spacetime exists around every nonsingular point $p \in \mathcal{M}$. In this **local tetrad** or **local Minkowski system** the laws of special relativity apply. In mathematical terms, the local tetrad is identified with an orthonormal base of the tangent space $\mathcal{T}_p \mathcal{M}$. It can be easily constructed using the coordinate base $\{\partial_\mu\}$, as depicted in Fig. 2.3.

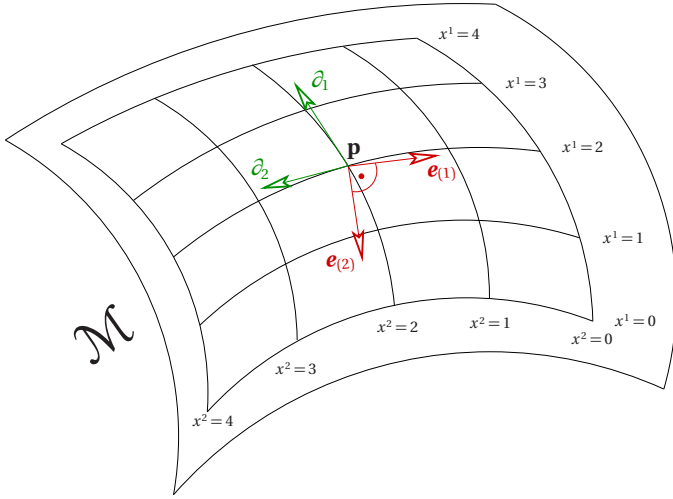


Figure 2.3: A two-dimensional manifold. The partial derivatives $\{\partial_\mu\}$ (green) in a point \mathbf{p} define a base of $\mathcal{T}_\mathbf{p}\mathcal{M}$. Suitable linear combination yields an orthonormal frame $\{\mathbf{e}_{(i)}\}$ (red).

Linearly combining the coordinate base,

$$\mathbf{e}_{(i)} = e_{(i)}^\mu \partial_\mu, \quad (2.8)$$

so that the orthonormality condition

$$\mathbf{g}(\mathbf{e}_{(i)}, \mathbf{e}_{(j)}) = \eta_{(i)(j)} \quad (2.9)$$

is fulfilled, yields an orthonormal frame $\{\mathbf{e}_{(i)}\}$. The transformation matrices $e_{(i)}^\mu$ must be invertible, i. e. $\det(e_{(i)}^\mu) \neq 0$. In order to distinguish between **coordinate indices** and **tetrad indices**, we use Greek letters and Latin letters in brackets, respectively. The **dual tetrad** $\{\boldsymbol{\theta}^{(i)}\}$, a base of $\mathcal{T}_\mathbf{p}^*\mathcal{M}$, is defined via

$$\langle \boldsymbol{\theta}^{(i)}, \mathbf{e}_{(j)} \rangle = \langle \boldsymbol{\theta}^{(i)} dx^\mu, e_{(j)}^\nu \partial_\nu \rangle = \theta_\mu^{(i)} e_{(j)}^\nu \stackrel{!}{=} \delta_\nu^\mu, \quad (2.10)$$

hence $\theta_\mu^{(i)} = (e_{(i)}^\mu)^{-1}$.

Local tetrads are interpreted as the local reference frame of small objects or observers in a spacetime. Consider two objects at the same point \mathbf{p} . They can be in relative motion or rotated with respect to one another. Therefore, a local tetrad in a point \mathbf{p} is unique except for Lorentz

transformations $A_{(i)(j)}$ – which also include spatial rotations. If a local tetrad is adapted to the symmetries of a particular spacetime we denote this tetrad as a **natural local tetrad**. A local vector \mathbf{u} is transformed to the coordinate representation using

$$\mathbf{u} = u^{(i)} \mathbf{e}_{(i)} = u^{(i)} e_{(i)}^\mu \partial_\mu = u^\mu \partial_\mu, \quad (2.11)$$

and the back transformation is achieved analogously.

2.2 Einstein's Field Equations

The field equations, describing the interaction between the spacetime curvature and the distribution of mass and energy, are widely accepted in the scientific world. However, these equations are very complicated and are almost never analytically solvable. Except for highly symmetric spacetimes such as black holes, worm holes or the Gödel universe, one must resort to numerical methods to solve the field equations. But even if an analytical expression for a spacetime can be found, it is seldom possible to analytically study the propagation of light or freely moving particles in such a spacetime. We will now review the constituent parts of the field equations. After that, the interpretation of the field equations themselves is specified.

2.2.1 Christoffel Symbols, Riemann Tensor, Ricci Tensor and Ricci Scalar

The **affine connection** is a function ∇ which transports vectors between two infinitesimally neighboring tangent spaces, $\mathcal{T}_{p_1}\mathcal{M}$ and $\mathcal{T}_{p_2}\mathcal{M}$, and therefore connects two tangent spaces. If we require that this transport preserves the inner product between two vectors, i. e. $\nabla_\sigma g_{\mu\nu} = 0$, the function is given by the **covariant derivative**

$$\nabla_\mu v^\nu := \partial_\nu v^\mu + \Gamma_{\mu\sigma}^\nu v^\sigma =: v^\mu{}_{;\nu} =: \frac{Dv^\sigma}{Dx^\nu}. \quad (2.12)$$

The **Christoffel symbols** of the second kind are given by the metric and its derivatives

$$\Gamma_{\nu\sigma}^\mu = \frac{1}{2} g^{\mu\rho} (g_{\rho\nu,\sigma} + g_{\rho\sigma,\nu} - g_{\nu\sigma,\rho}), \quad (2.13)$$

where we have set $g_{\mu\nu,\sigma} := \partial_\sigma g_{\mu\nu}$. Note that the Christoffel symbols do not form a tensor, as they do not show the correct behavior under coordinate transformations. The **Riemann tensor** is given by

$$R_{\nu\rho\sigma}^\mu := \Gamma_{\nu\sigma,\rho}^\mu - \Gamma_{\rho\sigma,\nu}^\mu + \Gamma_{\rho\iota}^\mu \Gamma_{\nu\sigma}^\iota - \Gamma_{\sigma\iota}^\mu \Gamma_{\nu\rho}^\iota \quad (2.14)$$

and describes the curvature of a spacetime. If the Riemann tensor vanishes, the spacetime is flat, and vice versa. By calculating a specific trace of the Riemann tensor, we obtain the **Ricci tensor**

$$R_{\nu\sigma} := R_{\nu\mu\sigma}^\mu. \quad (2.15)$$

The **Ricci scalar** is obtained by the contraction of the Ricci tensor, namely

$$R := R^\mu{}_\mu = g^{\mu\nu} R_{\mu\nu}. \quad (2.16)$$

2.2.2 Field Equations and the Cosmological Constant

The **Einstein tensor** consists of the Ricci tensor, the Ricci scalar and the metric itself, and reads $G_{\mu\nu} = R_{\mu\nu} - \frac{1}{2} R g_{\mu\nu}$. The most general form of Einstein's field equations is

$$G_{\mu\nu} + \Lambda g_{\mu\nu} = \varkappa T_{\mu\nu}, \quad \varkappa = \frac{8\pi G}{c^4}, \quad (2.17)$$

with the **gravitational constant** G , the **cosmological constant** Λ , the speed of light c and the stress-energy tensor $T_{\mu\nu}$.

The left side of Einstein's field equations contains expressions on the curvature of a spacetime and the right side describes the distribution of mass and energy in this spacetime. The equality of both sides reveals a mutual influence of both entities. Either we have a certain mass distribution in a spacetime and know that the spacetime is curved, or we take a curved spacetime and know that there must be masses (or energy) present which generate the curvature. Solving these equations for an initial mass and energy distribution yields the spacetime curvature and, finally, the metric tensor g . Another way of looking at these equations is to choose a "designer" spacetime with a certain curvature and then calculate the stress-energy tensor T . Using the latter approach, spacetimes such as the Morris-Thorne wormhole [MT88] have been discovered.

Originally, the cosmological constant Λ was not part of the field equations. In 1917, Einstein introduced the cosmological constant into the field equations in order to make a static universe possible. However, the Minkowski spacetime – being the description of a flat spacetime – is no longer the solution to the field equations for nonzero Λ and the absence of any masses ($T_{\mu\nu} = 0$). It is obvious that the constant must be extraordinary small because we would otherwise not obtain a vacuum solution approximating the flat Minkowski spacetime. It can be estimated [Rin06] that

$$|\Lambda| < 10^{-51} \frac{1}{\text{m}^2}. \quad (2.18)$$

After it became clear that we do not live in a static universe, Einstein eliminated Λ from his equations and described it as "the biggest blunder of my life". However, recent investigations of the WMAP data [SVP*03, SBD*07, KDN*09] indicate that we live in a universe with a positive cosmological constant. After the novercal consideration of Λ before these results, scientists tried to find interpretations on the meaning of this constant. This led to the inclusion of Λ on the right side of the field equations and thus Λ can be associated with the vacuum energy density

$$\rho_{\text{vac}} = \rho_\Lambda = \frac{\Lambda}{\varkappa} \leq \rho_{\text{crit}} = \frac{3H_0^2}{8\pi G}, \quad (2.19)$$

where H_0 is the Hubble constant and ρ_{crit} an upper bound [Str04] resulting from astronomical observations. Our universe is, because $\Lambda > 0$, a **de Sitter spacetime**. Furthermore, the positive sign of the cosmological constant yields a distance-proportional repulsive force [Rin06] of $\Lambda c^2 \tau/3$. As a consequence, our universe is not only non-static, but it also expands exponentially. As we will see in Ch. 4, there is a nonzero cosmological constant in the Gödel universe as well. Contrary to our universe, Λ is negative. Therefore, the Gödel universe is an **anti de Sitter spacetime**.

2.3 Motion of Particles

The geodesic equations govern the propagation of photons in geometrical optics as well as massive particles moving solely under the influence of gravitation. Spacelike geodesics are not the focus of this work and will not be discussed. Along the geodesical path of a particle, the local tetrad is parallel transported.

Generally, massive particles travel on timelike worldlines. If the particle is accelerated by interior forces, these lines are non-geodesical and the local tetrad is then Fermi-Walker transported. We also discuss how to utilize the symmetries of a spacetime via isometrical transformations along Killing vector fields.

2.3.1 Geodesic Equations

In geometrical terms, a geodesic is a curve connecting two points, **A** and **B**, the straightest possible way. This is equivalent to the requirement of a locally extremal length of the curve, $L_{AB} = \int_A^B ds$. Variation with respect to x^μ leads to the **geodesic equations**

$$\frac{d^2 x^\mu}{d\lambda^2} + \Gamma_{\rho\sigma}^\mu \frac{dx^\rho}{d\lambda} \frac{dx^\sigma}{d\lambda} = 0, \quad (2.20)$$

a set of four ordinary second order differential equations, parameterized with an **affine parameter** λ . For timelike motion, this parameter can be identified with the **proper time** τ of a particle. For lightlike motion, λ has no physical meaning. We abbreviate $(dx^\mu)/(d\lambda)$ with \dot{x}^μ .

The geodesic equations are solved using an initial value problem. Since these equations are of second order, we must specify an initial position $\mathbf{x}|_{\lambda=0} = \mathbf{x}_0$ as well as an initial direction $\dot{\mathbf{x}}|_{\lambda=0} = \dot{\mathbf{x}}_0$. Additionally, the initial direction must have the correct norm,

$$\|\dot{\mathbf{x}}_0\|^2 = \kappa c^2, \quad (2.21)$$

where we have $\kappa = 0$ for lightlike geodesics and $\kappa = -1$ for timelike motion.

We can also formulate the initial direction with respect to a local tetrad as shown in Fig. 2.4. The temporal component of the initial direction, $\dot{x}_0^{(0)}$, is then calculated using the constraint equation (2.21), which reads, with respect to the local tetrad, $\eta_{(i)(j)}\dot{x}_0^{(i)}\dot{x}_0^{(j)} = \kappa c^2$. Since any vector $\mathbf{u} = u^{(a)}e_{(a)}$ expressed in a local system is treated like any vector in special relativity, the sign of $\dot{x}_0^{(0)}$ determines whether the geodesic is evolving into the future (+) or into the past (-).

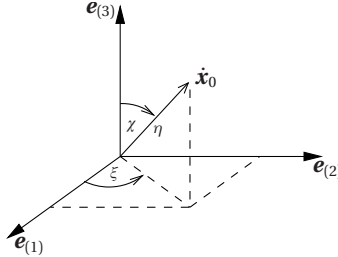


Figure 2.4: Formulating the initial direction of a geodesic with respect to a local tetrad, cf. [MG09b].

If the spacetime has certain symmetries, the **Lagrangian formalism** can be used to derive analytical solutions to the geodesic equations. For the mathematical details, we refer the reader to [MTW73]. The Lagrangian itself is given by the constraint equation (2.21) and can be written as

$$\mathcal{L}(\mathbf{x}, \dot{\mathbf{x}}) = g_{\mu\nu} \dot{x}^\mu \dot{x}^\nu \stackrel{!}{=} \kappa c^2. \quad (2.22)$$

Using the Euler-Lagrange equations, one finds **constants of motion**

$$k_i := \frac{d\mathcal{L}}{dt^i}, \quad (2.23)$$

if $\partial\mathcal{L}/\partial x^i = 0$. These constants of motion, alongside the Lagrangian itself, can be used to formulate an equivalent set of first order differential equations, which are generally easier to solve than the corresponding second order equations. Even if the geodesic equations may not be solved completely analytically, this approach can facilitate the retrieval of special solutions.

However, the geodesic equations can only be solved for highly symmetric spacetimes. Generally, one must resort to numerical methods to obtain solutions. Usually this is done by transforming the equations to a set of eight first order equations using $\mathbf{y} = (y^\mu, y^{\mu+4}) = (\mathbf{x}, \dot{\mathbf{x}})$. Then, the result is of the form $\dot{\mathbf{y}} = \mathbf{f}(\mathbf{y})$ and can be numerically integrated using, for example, a fourth order Runge-Kutta integrator [PTVF07] from the **Numerical Recipes** library or the methods provided by the **Gnu Scientific Library (GSL)** [GNU]. Müller and Grave [MG09b] provide a powerful library for the numerical integration of the geodesic equations.

2.3.2 Parallel and Fermi-Walker Transport

An alternative but equivalent definition of geodesics is to require that the tangent vector $\mathbf{u} = \dot{\mathbf{x}}$ is transported locally parallel along the curve. It can be shown that this **parallel transport** is realized by the affine connection ∇ , see eq. (2.12). Any vector \mathbf{X} is parallel transported along a geodesic $\mathbf{x}(\lambda)$ using

$$\mathbb{P}_{\mathbf{u}} X^\mu = \frac{dX^\mu}{d\lambda} + \Gamma_{\rho\sigma}^\mu u^\rho X^\sigma = 0. \quad (2.24)$$

If we parallel transport a vector along a closed curve, the transported vector will, in general, not match the initial one. The discrepancy between the two vectors is governed by the Riemann tensor $R^\mu{}_{\nu\rho\sigma}$ and, hence, by the curvature of the spacetime. Note that the geodesic equations are reproduced after setting $\mathbf{X} = \mathbf{u}$.

If a massive particle is accelerated with an additional interior force resulting from, for example, a rocket propulsion, the motion is non-geodesical. In general, massive particles propagate on timelike worldlines, $x^\mu(\tau)$, if nonzero interior forces are present. For a four-acceleration

$$a^\mu = \frac{du^\mu}{d\tau} + \Gamma_{\nu\sigma}^\mu u^\nu u^\sigma, \quad (2.25)$$

the **Fermi-Walker transport** of a vector \mathbf{X} is given by the **Fermi-Walker derivative** $\mathbb{F}_{\mathbf{u}}$, videlicet

$$\mathbb{F}_{\mathbf{u}} X^\mu = \frac{dX^\mu}{d\lambda} + \Gamma_{\rho\sigma}^\mu u^\rho X^\sigma + \frac{g_{\rho\sigma}}{c^2} (u^\rho a^\mu - a^\rho u^\mu) X^\sigma = 0. \quad (2.26)$$

Using the Fermi-Walker transport, we can investigate how a comoving tetrad is evolving. We construct the initial tetrad so that $\mathbf{e}_{(0)}(\tau = 0) = \mathbf{u}_0$. The acceleration with respect to the local comoving frame then reads $a^\mu = a^{(i)} e_{(i)}^\mu$. We arrive at the first order differential equations system

$$\frac{dx^\mu}{d\tau} = e_{(0)}^\mu, \quad (2.27a)$$

$$\frac{de_{(i)}^\mu}{d\tau} = \frac{1}{c^2} \left(\eta_{(i)(j)} a^{(j)} e_{(0)}^\mu - \eta_{(0)(i)} a^{(j)} e_{(j)}^\mu \right) - \Gamma_{\nu\sigma}^\mu e_{(0)}^\nu e_{(i)}^\sigma. \quad (2.27b)$$

The integration of these 20 equations results in the worldline as well as the Fermi-Walker transported tetrad for any given $a^{(i)} = a^{(i)}(\tau)$. If we set $a^{(i)} = 0$, i. e. the interior forces to zero, the motion is geodesical and the upper equations describe the parallel transport of a local tetrad along a timelike geodesic. The parallel transport, formulated non-locally, directly results from the geodesic equations (2.20): Any vector \mathbf{Y}^μ is parallel transported along a geodesic using

$$\frac{dY^\mu}{d\tau} + Y^\nu u^\sigma \Gamma_{\nu\sigma}^\mu = 0, \quad (2.28)$$

where u^σ is the particle's current velocity along the geodesic.

2.4 Killing Vector Fields and Isometries

Symmetries of a problem allow for transforming a given coordinate set to another more convenient set of coordinates in which the properties of the underlying model become clearer. Consider the analysis of the characteristics of two particles rotating around each other under the influence of classical Newtonian gravity: A reasonable choice is a rotating polar coordinate system with its origin located at the center of the mass. This concept can be used in general relativity through *isometries*. An *isometric transformation* is an infinitesimal coordinate transformation

$$x'^{\mu} = x^{\mu} + \varepsilon \xi^{\mu}(x^{\nu}), \quad \varepsilon \ll 1, \quad (2.29)$$

and is represented by a **Killing vector field** ξ^{μ} , cf. [MTW73,Rin06]. It determines the directions in which the infinitesimal transformation must be executed in order to retain the metric and thus the physics of the spacetime described. A Killing vector itself is a solution to the **Killing equation**

$$\xi_{\mu;\nu} + \xi_{\nu;\mu} = 0. \quad (2.30)$$

When we restrict ourselves to a one-parameter family of transformations with $x'^{\mu} = x^{\mu}(\eta + \varepsilon)$ and $x^{\mu} = x^{\mu}(\eta)$, the previous relation is equivalent to the following system of first order differential equations, the **equations of isometric transport for points**

$$\frac{dx^{\mu}(\eta, \lambda)}{d\eta} = \xi^{\mu}(x^{\nu}(\eta, \lambda)). \quad (2.31)$$

The variable η measures the finite isometric transformation along the Killing vector field, whereas λ represents the parameterization of an arbitrary worldline itself. Alongside the initial condition x_0^{μ} , eqns. (2.31) uniquely determine the orbits of the corresponding Killing vector field [Ste90]. The solutions to these equations are lines of **finite isometric displacements**.

In order to transform, for example, initial directions and local tetrads, we must isometrically transport a vector. These **equations of isometric transport for vectors** are found directly after differentiating eq. (2.31) with respect to λ and read

$$\frac{du^{\mu}}{d\eta} = \frac{d\xi^{\mu}}{dx^{\nu}} u^{\nu}. \quad (2.32)$$

VISUALIZATION OF EINSTEIN'S THEORY FROM AN EGOCENTRIC PERSPECTIVE

"Nimble thought can jump both sea and land." — WILLIAM SHAKESPEARE

Einstein's theory is, albeit its mathematical beauty, very hard to understand intuitively because it does not play a crucial role in daily life. We either need extremely high relative velocities or very large masses. One can try to form mental images of relativistic effects, but it is difficult to generate these ideas just by pondering over the equations. One of the first essays on the optical effects of relativity is due to Gamow [Gam39]. He stated that a fast traveling person would appear length-contracted. However, this is not correct because there is a fundamental difference between *measuring* the length contraction and *seeing* the optical effect. Measuring is conducted simultaneously at the moving object, whereas seeing is simultaneously in the eye of an observer. It can be shown that the optical perception of the length contraction counteracts with the time light takes to travel. As a result, the fast traveling object would appear rotated; cf. [Ter59] and [Bor05]. In the visualization of Einstein's theory of relativity from an egocentric perspective, we investigate the propagation of light and the visual appearance of objects in a given spacetime. This enables us to develop an intuitive approach to understanding optical effects in relativity.

In recent years, the computational power of modern computers has increased to a level which made egocentric visualizations of the theory of relativity possible. Numerous exhibitions of special and general relativistic images, movies and interactive applications have shown that a general audience can access the general principles of relativity faster and on a more intuitive level compared to the classical "pencil and paper" approach. In a mathematically challenging field such as relativity, computer supported egocentric visualization can help to create a "nimble" imagination.

3.1 Visualization Using Raytracing

In this section, the basic concepts of egocentric visualization are discussed. First, the concept of classical 3D raytracing is reviewed. After the discussion of the benefits and problems of relativistic raytracing, the basic idea of interactive visualization is explained. We will see that interactive visualizations are usually implemented on graphics cards and are tailor-made for a specific spacetime.

3.1.1 Classical 3D Raytracing

How do we see? Ancient Greeks, such as Euclid [Euc45], assumed that visual perception is the result of rays *leaving* one’s eye. These rays then scan objects which thereby become visible. For sure, we know by now that our visual perception works in the opposite direction. Light sources, such as the sun, emit light. This light is reflected from surfaces, becomes refracted or traverses transparent objects. A very small fraction of this light is subsequently absorbed in our eyes, and our brain reconstructs an image of the scenery. A numerical implementation of this mechanism in such a way is not efficient. Therefore, the procedure is reversed and follows – in a way – Euclid’s idea of visual perception.

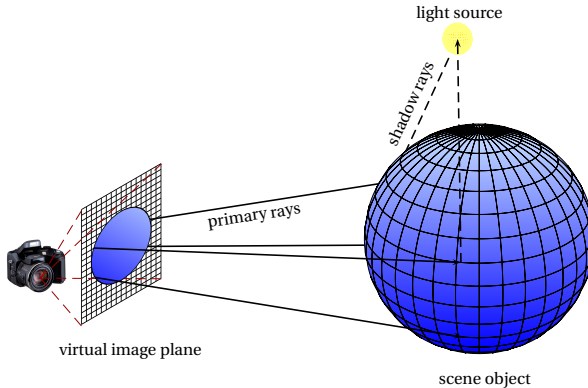


Figure 3.1: Classical three-dimensional raytracing.

In classical **3D raytracing**, as depicted in Fig. 3.1, a **primary ray** is cast from the camera through a virtual image plane – representing the pixels of the final image – into the scenery, and intersections between the ray and objects are calculated. Shadow rays are generated at these intersection points, which connect them to light sources (or other objects) to apply local illumination mod-

els. We do not consider ideal reflections or transmissions along **secondary rays** and thus this introduction outlines the raytracing procedure as described by Whitted [Whi80]. All light contributions are then accumulated to determine the final color of a surface point hit by a primary ray. Note that light rays are straight lines and the finite speed of light is not taken into account because the space is assumed to be Euclidean.

Numerous local illumination models exist, and for details, we refer to [FVDFH95]. As a brief introduction, the **Phong illumination model** is reviewed. This very simple local illumination model for a point light source, introduced in 1975 [Pho75], is an mostly empirical model. However, due to the simplicity of the model, the straightforward implementation as well as the realistic appearance of the renderings, this model is still popular. The total illumination of a point is calculated by the sum of three lighting components, namely the **ambient**, the **diffuse** and the **specular** contribution, i. e.

$$I_{\text{total}} = I_{\text{ambient}} + I_{\text{diffuse}} + I_{\text{specular}}. \quad (3.1)$$

The ambient light component is a global contribution which does not consider any local properties such as the incident light direction. This light component is calculated by multiplying the intensity of the ambient light, I_0 , with an heuristic material component k_{ambient} , i. e.

$$I_{\text{ambient}} = I_0 k_{\text{ambient}}. \quad (3.2)$$

Thus, objects rendered using solely ambient light appear flat. The diffuse fraction of the total intensity results from the Lambert's cosine law and is calculated with

$$I_{\text{diffuse}} = I_{\text{incident}} k_{\text{diffuse}} \langle \vec{l}, \vec{n} \rangle, \quad (3.3)$$

where I_{incident} is the intensity of the incident light, k_{diffuse} is another material parameter, \vec{l} is the normalized direction under which the incident light ray hits the point and \vec{n} is the surface normal of unit length. Thus, this light component finally depends on the arrangement of the object and the point light source, and the rendered image appears more plastic: Depending on the cosine in the upper equation, some regions of the object appear brighter than others. The last contribution to the overall illumination, the specular component, is responsible for sharp highlights on the object and is computed using

$$I_{\text{specular}} = I_{\text{incident}} k_{\text{specular}} \langle \vec{r}, \vec{v} \rangle^n. \quad (3.4)$$

Besides the third material parameter, k_{specular} , we find the n^{th} power of the cosine between the normalized reflected ray direction and the viewing direction, under which the point is visible. If the reflected light ray direction is very similar to the viewing direction, then the point appears bright. The exponent n describes how small and focused the resulting highlight on the object is. For $n = 1$, we obtain a distribution comparable to the diffuse component and for high n , the specular light component results in a very small and bright spot. Usual implementations of this algorithm offer the possibility to set the material coefficients for each object separately, sometimes even for each color channel.

3.1.2 Relativistic 4D Raytracing

4D raytracing is an extension to 3D raytracing. In four dimensions, the speed of light is limited to $c \approx 3 \times 10^8$ m/s or $c = 1$ in geometrical units. If the Lorentz transformation and the hereby resulting physical effects are implemented, one is able to visualize effects of special relativity (cf. [KZ, Wei01, SSM07]) within the Minkowski metric of flat spacetime. Weiskopf [Wei01, WA99] extended Gröne’s work [Gro96] (**RAYViS**) to enable the implementation of metrics and integration of geodesics. This challenging task of obtaining correct visualizations of characteristics in general relativity will be explained below.

Objects in a general relativistic scene can be implemented in several different ways. Properties such as the center or the surface of a **coordinate object** are described in pseudo-Cartesian coordinates. Very large objects are defined as coordinate objects. This kind of object definition does not take the curvature of the spacetime into account, so we are restricted to relatively flat regions of the spacetime when using these objects. This is used to define, for example, a background texture to the surroundings of a black hole. When objects in a highly curved area of the spacetime are needed, we can use objects formulated with respect to a local tetrad, where the laws of special relativity apply. The usage of such **local objects** was not possible until the **GeoViS** framework [Mü06] became available. Using this local definition, it is possible to visualize the correct appearance of fast moving small objects regarding, for example, the speed of light. We also specify the camera with reference to a local tetrad. All local objects must be small because the local tetrad is a linear approximation of the metric and, therefore, large objects would lead to false results.

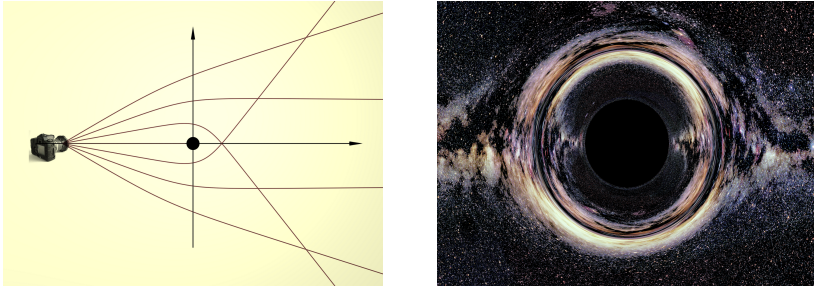


Figure 3.2: Four-dimensional raytracing used to visualize the Milky Way background behind a black hole, revealing an Einstein ring.

Finally, we can also formulate **objects using light flashes**. Here, the object is defined by the two-dimensional wavefront evolving from a light flash. A practical implementation of this kind of object can be realized using a large number of small mirrors which must be arranged so that

a light flash emitted at its center is refocused a time $\Delta\tau$ later. The duration of this time period determines the size of the object.

After defining a certain arrangement of objects and a camera, we can integrate the geodesic equations for the primary light rays as described in Sec. 2.3.1. The initial position is given by the camera location. A lightlike initial direction is defined for every pixel of the camera, depending on the type of camera (e.g. pinhole camera, panorama camera, 4π camera, etc.). The paths of moving objects must be integrated as well, for instance after providing a timelike initial direction for geodesical motion.

The numerical integration yields a curved ray as shown in Fig. 3.2. Usually, the rays are represented by about 1000 four-dimensional linear segments. Then, each segment must be tested for intersections with all objects in the scene. If the object is moving, the corresponding timelike curve contains the information about the object reaching a certain point at a certain time. An intersection is found when a light ray intersects the object regarding *both* space and time.

3.1.3 Advantages and Drawbacks

It is possible to implement a multitude of physical effects for a variety of spacetimes using the generic 4D raytracing approach. We can, in principle, implement every analytically given spacetime into the G_{EO}V_{IS} framework in a relatively straightforward manner. We must simply specify the metric, the Christoffel symbols and a test if the geodesic is propagating in a valid region of the spacetime. Furthermore, because the underlying physics are independent of the spacetime, we can, for example, visualize the redshift of freely moving particles for many metrics.

However, there are two main problems in general relativistic raytracing: First, the numerical integration of geodesics on today's standard CPUs usually takes about ten milliseconds per ray. The calculation of intersections between this ray and a single object requires another millisecond. The amount of time that is necessary for calculating a large image of a complex scenery easily exceeds an entire day, even if a cluster is used. Second, if no analytical solution is available, we cannot implement lighting computations beyond ambient illumination. The inherent problem is that it is basically impossible to connect two spacetime points with curved rays using an initial value problem. Simply speaking, we do not know the direction in which an arbitrarily bent shadow ray must start in order to reach the light source. For interactive visualizations, we either need extraordinary powerful clusters or another idea.

3.2 Interactive Approaches

In recent years, several relativistic scenarios were implemented in interactive simulations utilizing modern graphics hardware. Such as the work of Savage et al. [SSM07], many implementations are restricted to special relativistic scenarios where light paths resemble straight lines.

Beyond that, Müller [Mü08] realized interactive visualizations of general relativistic wormholes using an analytical solution, with limitations such as ambient lighting. Another work explains how an observer near a black hole perceives the stars of the Hipparcos catalog. Müller and Weiskopf [MW10] provided an interactive and GPU-based approach, which additionally considers the Fraunhofer diffraction due to the finite aperture of the observer’s camera. The visualization of the Hipparcos catalog, Sec. 8.2, is based on their implementation. In our previous work [GB08], we introduced a generic approach to visualize various spacetimes by means of a slow preprocessing step and an interactive postprocessing method to alter certain parameters of a scene. It is, however, not possible to move objects unless another preprocessing step is done. Also, the concept of a non-interactive local illumination model exploiting the symmetries of spacetime – in our case, the Gödel universe – has been introduced. In [GMDW09], we discuss how to overcome the slow preprocessing step. Our implementation is tailored for Gödel’s universe and will be discussed in Sec. 6, which presents the revised and highly improved GÖDEL ENGINE.

All visualizations of general relativity – interactive, semi-interactive or non-interactive – were previously restricted to the visualization of primitive objects such as spheres or cubes. This limitation is overcome using the GÖDEL ENGINE. The basic concept of interactive visualizations of general relativity is to *connect points* in a spacetime. If we are able to connect points, we can directly calculate where an object is seen. This idea is illustrated in Fig. 3.3, where, as an outlook to the following chapters, a lightlike geodesic in Gödel’s universe is shown.

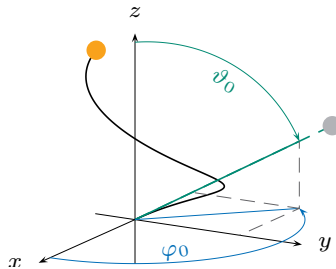


Figure 3.3: The origin of the Gödel universe is connected to an arbitrary point (yellow). From the initial conditions of the geodesic, we directly obtain the horizontal and vertical viewing angles (φ_0, ϑ_0) under which this point can be seen (gray).

The specific procedure to connect points in the Gödel universe is detailed in Ch. 6. If we are able to connect points in a spacetime, we can obtain the initial conditions for the corresponding geodesics. Based on these values, we can derive the initial direction and therefore the direction under which an object is visible. Such an approach is not only much faster but also results in

more realistic images because local illumination models beyond ambient lighting become possible. The technique is fundamentally different to the raytracing concept, where we integrate lightlike geodesics without being able to anticipate if an object is intersected or not.

We can either use look-up tables for image-based approaches or utilize analytical solutions of the geodesic equations for object-space methods. After a short introduction to graphics processing units and their role in scientific computing, both methods will be detailed.

3.2.1 Graphics Processing Units

The purpose of graphics hardware (or graphics processing units, **GPUs**) is to accelerate the overall graphical performance of modern computers. Driven by the needs of the computer industry and the demand for more and more realistic three-dimensional computer games, the performance of these chips has increased tremendously over the last two decades. Supporting sophisticated shading and lighting effects, modern graphics cards can simulate complex scenarios in nearly photo-realistic quality at interactive rates. Advanced programming libraries, for example **OPENGL** or Microsoft's **DIRECTX**, enable access to hardware-accelerated visualizations. Detailed information on programming GPUs using **OPENGL** can be found in standard computer graphics literature [SWND05, Ros05, WL04].

GPUs compared to CPUs

Comparing [NVI] the peak performance of current graphics cards and Central Processing Units (**CPUs**), we find a significant discrepancy. Currently, GPUs are able to execute about 10^{12} floating point operations per second (1 tera-FLOPS) and have a memory bandwidth of about 200 GB/s. Corresponding values for CPUs are roughly one magnitude smaller. The reason for this discrepancy is explained with the different tasks which these processors must fulfill. While a CPU must accomplish a variety of tasks rather flexibly, a GPU is a highly specialized structure. It must execute similar commands very frequently because every pixel on the screen results from the same three-dimensional scenery. This suggests a highly parallel architecture, which is compared to a CPU in Fig. 3.4. In this figure, we see a quad-core CPU in contrast to the general structure of a GPU. A core is denoted as an Arithmetic Logic Unit (**ALU**), which is handled by a **control unit**. A local **cache** is a small memory area where often used data can be stored and quickly accessed by the ALUs. The global memory (Dynamic Random Access Memory: **DRAM**) is much larger than the cache, but slower to access. Thus, the structure of a GPU is quite different except for a comparable global memory.

Current GPUs consist of a few hundred ALUs. Additionally, the design trends to multi-chip architectures, which further increase speed. As stated in Moore's law, computing power doubles approximately every 18 months and, therefore, is growing exponentially: Every generation of

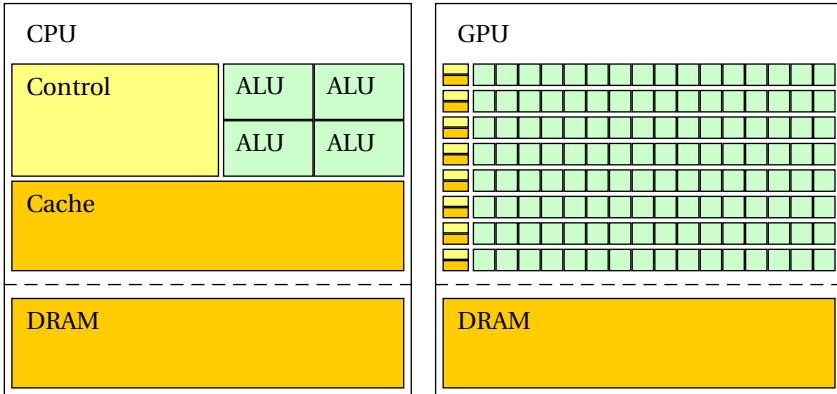


Figure 3.4: Comparison of CPU and GPU, cf. [NVI].

graphics hardware is approximately twice as fast as the predecessor. Moreover, the architecture itself evolves and new capabilities are introduced. In the last few years, double precision GPUs became available. Before that, only single precision floating point operations had been possible. While single precision is sufficient for classical rendering, such as in computer games, double precision can be necessary for accurate numerical simulations.

Rendering pipeline

Rendering is the calculation of an image of a virtual three-dimensional scene. On GPUs, this process is divided into several steps. The procedure to obtain an image from a scene is called the **rendering pipeline**. A simplified diagram of the pipeline is shown in Fig. 3.5. Detailed explanations can be found in [SWND05, Ros05, WL04].

In a nutshell, the **scene description** is a collection of points (**vertices**) and instructions on how these vertices are arranged in general as triangles or meshes. Also, information on colors and textures is provided. The vertices, now stored on the GPU, become available to the first kind of GPU program, which is denoted as a **vertex shader**. In this step, they are processed and arranged as primitives. Shader programs are denoted as **kernels** and the programming language is called **shading language (GLSL for OpenGL)**. The shader code is very close to the C language. Within the vertex shader, the geometry of the scene can be modified in a variety of ways. For example, we can map a regular grid on a spherical grid (or any other type). The scene is then **rasterized** to the screen resolution, where every object is divided into pixel-sized **fragments**. Each fragment

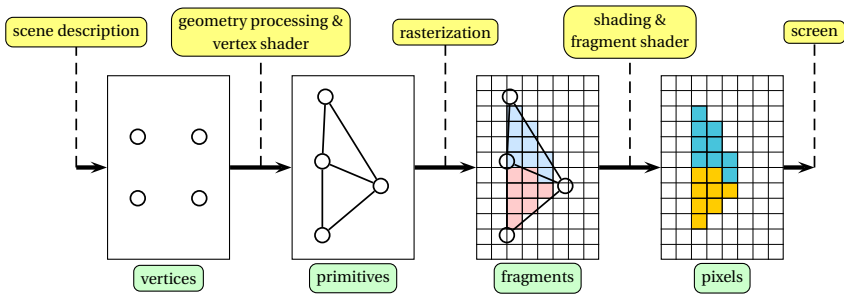


Figure 3.5: Rendering pipeline.

may still include information on the distance to the camera (as value in the **depth buffer**). Every visible property, for example the color, is now constant on a particular fragment. After rasterization, all shading calculations (like lighting or transparency effects) are executed. In this step, the fragments become accessible by the second type of GPU program, the **fragment shader**. This kernel can modify the final color of a fragment in any way. For example, sophisticated lighting models can be applied or the fragment can simply be discarded if desired. After this final step, the resulting contents stored in the **frame buffer** are finally drawn on the screen.

3.2.2 General Purpose Graphic Processing Units – GPGPU

GPUs available since 2006 are freely programmable, thus we can execute user-written shaders and are not restricted to the instructions of the `OPENGL` or `DIRECTX` library. Due to its intrinsic structure, the graphics processing unit is highly suitable for **data-parallel processing** and a **high arithmetic intensity**. In other words, programs are suitable for porting to the GPU, if the same computation is done on a large number of data elements and only a few memory accesses are needed for a large number of instructions. The usual “trick” is to code a parallel program as a shader and to upload the initial data of a simulation encoded in vertex arrays or textures. For example, a vertex array can contain the initial data of a physical grid, where the nodes are connected with springs. Each node now possesses information on initial positions and velocities. The vertex shader can then integrate the equations of motion for each node and transform the initial data so that the new grid resembles the simulation after a certain integration time. Simulations based on the vertex approach are called **object-space algorithms**, whereas calculations using the fragment shader are **image-based approaches**.

Object-space algorithms

In the field of egocentric visualizations in general relativity, object-space algorithms are feasible if at least certain analytical solutions of the geodesic equations are available that are not too complicated to treat. Then, points in the spacetime can be connected. Usually, the first point is a vertex of an object and the second point is the observer. By connecting these points, the initial values for the interconnecting geodesic and, in the end, the viewing direction (under which the vertex is visible) are found (see Fig. 3.3). The GÖDEL ENGINE, Sec. 6, uses an object-space algorithm.

For example, Müller and Weiskopf [MW10] interactively visualized the Hipparcos catalog for an observer falling either freely or quasistatically into a black hole by using a combination of the analytical solution as well as lookup-tables.

Image-based approaches

If the complete analytical solution to the geodesic equations is not available or the analytical expressions are too complicated to handle, one can resort to image-based approaches. Here, lookup-tables for specific situations can be generated. For instance, Müller [Mü08] provided an image-based approach by interactively visualizing a Morris-Thorne wormhole.

Another more general approach is introduced in our previous work [GB08], where an arbitrary scene is rendered using the GEOVIS framework. In the first step, the desired images are pre-calculated using a custom file format. Two files per image are generated, one containing the RGB data of the calculated image for the currently used scene, the other file holding detailed information about each intersection of each ray with the scene. This data is used to generate several lookup-tables for the current image, which includes a pixel mask to stencil empty pixels, frequency-shift as well as time-shift data and details regarding the intersection of the curved ray with an object. In the postrendering process, the lookup-tables are then used as textures in the corresponding fragment shader. With these shaders and the user input concerning the parameters of the desired effect, it is possible to interactively visualize the precalculated data in various ways. However, if the scene is changed with respect to the position of the visualized objects, the slow precalculation step must be executed again. Therefore, this approach is semi-interactive. This procedure is related to *deferred shading*, which was introduced by Deering et al. [DWS*88]. There, a large framebuffer is used to store surface properties of each pixel before calculating the final pixel color.

3.2.3 Compute Unified Device Architecture – CUDA

It was rather tedious to write GPGPU code in the beginning because one had to directly implement functions in Assembler. In 2007, ATI introduced its Stream Software Development Kit

(**STREAM SDK**). NVIDIA followed in 2008 with its also proprietary Compute Unified Device Architecture (**CUDA**). Both approaches use a language similar to C. The upcoming **OPENCL** library (Open Computing Language) will provide a free application programming interface (**API**) for heterogeneous programming on CPUs, GPUs and other processors. The **GÖDEL ENGINE**, Sec. 6, was written using CUDA. We will now outline the CUDA programming model and then close this section with a simple example.

Programming scheme

As mentioned in Sec. 3.2.1, GPU programs are denoted as kernels. For example, if a scientific problem can be formulated with a parallel approach on a grid, the simulation must be executed on each node. Usually, this is achieved with identical kernels for each node. One simulation step is achieved after executing the kernel for each *thread* of execution for each node.

The CUDA programming model defines the simulation grid simply as a *grid*, which is partitioned into several *blocks* of threads. A shared memory area for each thread block exists, so threads of one block can communicate with one another. However, thread blocks must be independent from each other because no information between threads of different blocks can be interchanged. Fig. 3.6 illustrates this structure.

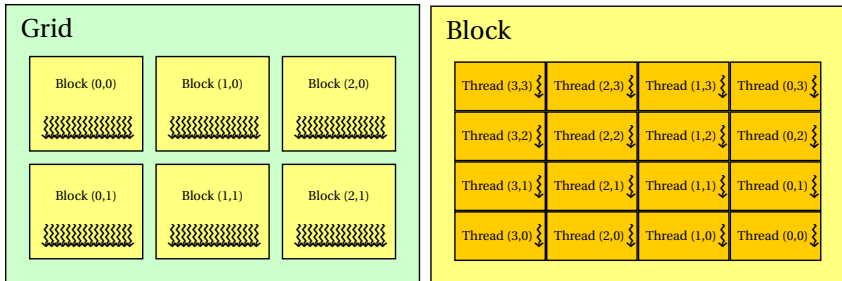


Figure 3.6: Arrangement of threads in blocks on a grid, cf. [NVI].

The program flow of a CUDA application usually consists of C or C++ code executed on the CPU and CUDA code run on the GPU. A variety of functions exist that provide access to the GPU so that data can be uploaded to the GPU or read back. Also, functions to start a kernel on the GPU are provided. Fig. 3.7 illustrates this procedure. Note that the CPU is denoted as the *host*, whereas the GPU is the *device*.

Serial C code is executed on the CPU, initializes the GPU and, if necessary, data is uploaded to it. Then, a kernel is called. The GPU itself decides in which order all blocks on the grid will

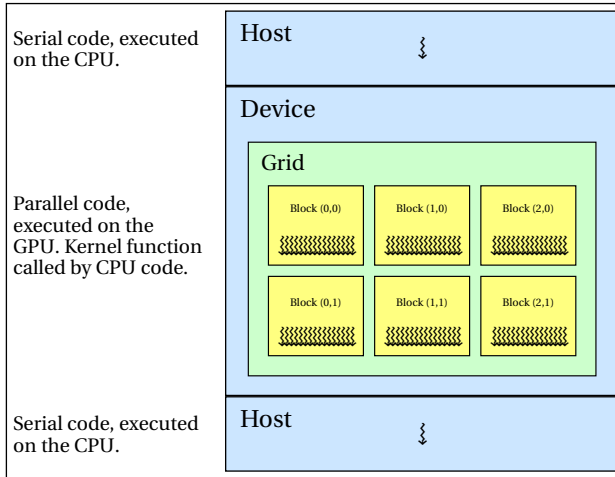


Figure 3.7: Symbolic program flow of a CUDA application [NVI].

be executed. After all threads have finished, the result of the simulation can be read back to the CPU or directly rendered to the screen because the data is already available on the GPU.

Example

As a simple example, we will transpose a matrix using both a straightforward method on the CPU, in contrast to a CUDA implementation on the GPU, and then compare the results. The CPU method is simply given by the following fragment:

```
for( unsigned int y = 0; y < size_y; ++y)
  for( unsigned int x = 0; x < size_x; ++x)
  {
    outMatrix[(x * size_y) + y]
      = inMatrix[(y * size_x) + x];
  }
```

Using CUDA, we must first set up the device. GPU memory is allocated, the initial matrix is copied from the CPU to the GPU and then the kernel is called:

```

//allocate device memory
float* d_idata; float* d_odata;
cudaMalloc( (void*)&d_idata, mem_size );
cudaMalloc( (void*)&d_odata, mem_size );

//copy host memory to device
cudaMemcpy( d_idata, h_idata, mem_size,
            cudaMemcpyHostToDevice );

// define grid and block sizes
dim3 grid ( size_x/BLOCK_DIM, size_y/BLOCK_DIM, 1);
dim3 block( BLOCK_DIM, BLOCK_DIM, 1 );

// run the kernel
transpose_naive<<<grid,block>>> ( d_odata, d_idata,
                                size_x, size_y);

```

After the kernel has finished, the results can be read back similarly. The kernel code is given by the following lines of code:

```

__global__ void transpose_naive( float *odata,
                                float* idata, int width, int height )
{
    unsigned int xIndex = blockDim.x*blockIdx.x
                      + threadIdx.x;
    unsigned int yIndex = blockDim.y*blockIdx.y
                      + threadIdx.y;
    if (xIndex < width && yIndex < height)
    {
        unsigned int index_in = xIndex+width*yIndex;
        unsigned int index_out = yIndex+height*xIndex;
        odata[index_out] = idata[index_in];
    }
}

```

We must decode the index of the “node” on the grid – here a matrix entry – using the variables `blockDim`, `blockId` and `threadId`. Then, the transposition of matrix elements is equivalent to the CPU approach. The corresponding program, executed on a standard desktop PC with a mid-end GPU (Athlon 64 X2 4600+, 2GB RAM, GeForce 8800 GTS), reveals a significant speedup:

```
> transpose
Transposing a 256 by 4096 matrix of floats...
transpose average time (CPU only):      79.463 ms
---
Initialization time (GPU):             33.076 ms
Naive transpose average time (GPU):     9.383 ms
Optimized transpose average time (GPU): 0.558 ms
```

Note that the initialization time is the time needed for initializing the CUDA device and for copying the initial data to the GPU. This is, by far, the largest amount of time the simulation on the GPU needs. Thus, we obtain the best results if we can formulate a problem so that the communication between the CPU and GPU is minimized. This is a fundamental design approach in the GÖDEL ENGINE, which will be detailed in Sec. 6. Moreover, if the transposition kernel itself is optimized to conform to the structure of the GPU, the calculation time can be decreased further. We refer to [NVI, Ngu07] for further details and insightful examples.

3.2.4 Advantages and Drawbacks

The most important benefit of interactive approaches using modern graphics hardware is the speedup of the image calculation. Moving from rendering times of hours or even days to several frames per second enables a user feedback to the application, which is then almost responding in real time. For scientific visualizations, no tedious preparations have to be undertaken because we can interactively adjust the parameters of the scene and obtain the visual changes almost immediately. Furthermore, a layperson can interact with an application instead of watching a prerendered movie. Image quality can be increased as well because local illumination models become possible. In Sec. 7, we will show that the Gödel universe reveals several optical effects very clearly when using an interactive approach. These effects might not have been found without an interactive approach.

However, interactive techniques are restricted to specific spacetimes. It is, in principle, possible to unite all spacetimes of which analytical solutions to the geodesic equations are known under a single rendering engine. However, due to the mostly very complicated solutions, those metrics cannot be treated in the same manner. To resolve this problem, the different root-finding procedures for the viewing directions of a vertex must be specified for each analytical solution and thus be encapsulated. The rendering procedure should therefore be completely separated from the calculation of the viewing directions. This approach results in many special cases which can hardly be united within a single framework. For instance, the GÖDEL ENGINE renders visible images of objects in special pairs and stitches them under certain circumstances, cf. Sec. 6.3.4. Therefore, the implementation of the rendering loop is adjusted to the specific requirements of the analytical solution and cannot be encapsulated. Above all, most spacetimes are too complex and analytical solutions to the geodesic equations are not known.

If an interactive visualization is possible, the CUDA implementation is more beneficial compared to a shader approach because it is very easy to obtain – even intermediate – simulation results directly by copying them from the GPU to the CPU. We then have the data available as `float`-arrays or a comparable structure. A shader approach yielded textures which had to be rendered into a separate buffer and then decoded on the CPU. This is possible but cumbersome. Furthermore, CUDA implementations tend to be faster than comparable shader approaches, presumably due to specific driver optimizations.

THE GÖDEL UNIVERSE IN A NUTSHELL

“If we could travel into the past, it’s mind-boggling what would be possible. For one thing, history would become an experimental science, which it certainly isn’t today. The possible insights into our own past and nature and origins would be dazzling. For another, we would be facing the deep paradoxes of interfering with the scheme of causality that has led to our own time and ourselves. I have no idea whether it’s possible, but it’s certainly worth exploring.” — CARL SAGAN

Kurt Gödel’s universe is one of the most interesting exact solutions to Einstein’s equations. Despite its mathematical simplicity, due to the high symmetry of the underlying spacetime, it demonstrates the possibilities lying within the theory of general relativity. Gödel’s model of an alternative universe – only consisting of homogeneous dust, rotating around every point – describes a theoretically feasible spacetime in which time travel is possible beyond an optical horizon, which itself is not an impenetrable physical barrier for massive particles.

In this section, we review the related work on the Gödel universe and discuss the interpretations on time travel as well. Additionally, several computations are presented in order to round out the introduction to the Gödel universe. These calculations are either new results or they reproduce the results of others in the set of coordinates we chose for this work. Most of these findings are easily verified using computer algebra programs such as MAPLE [map], in combination with the GRTENSOR II-package [grt].

We start with a brief summary of the current cosmological standard model, then introduce the basic properties of the Gödel universe and conclude with a review of the most important time travel universes in general relativity alongside the theoretical treatment of causality violations.

4.1 The Λ CDM Model and Cosmological Observations

The standard model of cosmology, the Lambda Cold Dark Matter model or Λ CDM model, is based on the Friedmann-Lemaître-Robertson-Walker metric. Since the focus of this work is the egocentric visualization of the Gödel model, we refer the reader to standard literature such as [Rin06] for a more detailed presentation. Another insightful synopsis can be found in Eisele's work [Eis07].

Spergel et al. [SBD*07,SVP*03] fitted the three year WMAP data to the Λ CDM model and found that the relative energy density of the baryonic matter is only four percent and the cold dark matter represents one fifth of the total energy in our universe. The largest fraction by far is the dark energy: 76 percent of our universe consists of this type of energy. Unfortunately, the nature of the dark energy is difficult to interpret. It can be treated as a vacuum energy density or be associated with the cosmological constant. The energy density is positive and reveals a negative pressure [Car01], which yields a repulsive force. Thus, our universe is expanding at an accelerating rate. Independent investigations of type-Ia supernovae [Kee03] coincide with Spergel's results.

Another specific field of research is the investigation whether or not our universe is globally rotating and how large this rotational rate may be. Barrow et al. [BJS85] analyzed the temperature distribution of the cosmic microwave background for several models with slight anisotropies. These results serve the calculation of cosmic vorticities, i. e. the global rotation of each investigated model. On the basis of this work, Jaffe et al. [JBE*05] and Bridges et al. [BMLH07, BMC*08] investigated how specific globally rotating cosmological models can be harmonized to the first-year and three-year WMAP data. They found a best-fit approximation for a small, but non-vanishing, rotation rate.

We use the bound for the cosmological constant as well as the findings from Jaffe et al. and Bridges et al. for an analysis of sensible rotational rates of the Gödel universe; see. Sec. 5.4.

4.2 The Nature of Gödel's Space-Time

Kurt Gödel was fascinated by general relativity. He soon discovered that this theory does not necessitate a global time order and therefore allows time travel. Gödel tried to find a solution to Einstein's field equations with this property [Gö90] and succeeded in discovering a world model later named after him.

The cosmological solution of Einstein's field equations, published in 1949 [Gö49], represents a basic model of a rotating universe with negative cosmological constant Λ . In Fig. 4.1, the first page of the publication, along with a picture of Einstein and Gödel, is displayed. The spacetime curvature originates from a homogeneous matter distribution which rotates around every point

with a constant rotation rate. The stress-energy tensor consists of an ideal fluid whose pressure and mass density are connected to the cosmological constant and the rotation scalar of Gödel's universe [KWSD04]. Due to the homogeneity, the spacetime is not asymptotically flat.

REVIEWS OF MODERN PHYSICS

VOLUME 21, NUMBER 3

JULY, 1949

An Example of a New Type of Cosmological Solutions of Einstein's Field Equations of Gravitation

KURT GÖDEL

Institute for Advanced Study, Princeton, New Jersey

1. THE MAIN PROPERTIES OF THE NEW SOLUTION

ALL cosmological solutions with non-vanishing density of matter known at present¹ have the common property that, in a certain sense, they contain an "absolute" time coordinate,² owing to the fact that there exists a one-parametric system of three-spaces everywhere orthogonal on the world lines of matter. It is easily seen that the non-existence of such a system of three-spaces is equivalent with a rotation of matter relative to the compass of inertia. In this paper I am proposing a solution (with a cosmological term $\neq 0$) which exhibits such a rotation.

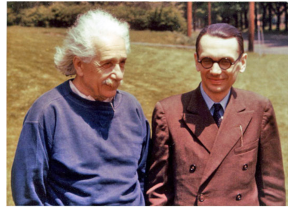


Figure 4.1: Gödel's original publication alongside a picture of him and Einstein.

A particularly puzzling feature of Gödel's universe is the existence of **closed timelike curves (CTCs)**. Gödel himself was the first who pointed out their existence within the framework of general relativity, although the van Stockum dust cylinder model from 1937 already inherited CTCs [Sto37]. Over the last decades, these metrics stimulated many discussions on the philosophical consequences of time travel and causality violations within the theory of relativity. In particular, Hawking established the so-called chronology protection conjecture, which states that the laws of nature prevent time travel on all but sub-microscopic scales [Haw92].

A summary of the most important time travel universes is provided in Sec. 4.3.1, the paradox issues resulting from time travel are reviewed in Sec. 4.3.2 and possible remedies preventing the formation of causality violations are synopsized in Sec. 4.3.3.

4.2.1 Line Element

Using Gödel's original formulation of the spacetime [Gö49] and $\text{sign}(g_{\mu\nu}) = +2$, the line element reads

$$ds^2 = a^2 \left(-dx_0^2 + dx_1^2 - \frac{e^{2x_1}}{2} dx_2^2 + dx_3^2 - 2e^{x_1} dx_0 dx_2 \right), \quad (4.1)$$

where a is a positive parameter. The line element of Gödel's universe in cylindrical coordinates [KWS04], with the velocity of light c and the **Gödel radius** $r_G = 2a$, reads

$$ds^2 = -c^2 dt^2 + \frac{dr^2}{1 + (r/r_G)^2} + r^2 [1 - (r/r_G)^2] d\phi^2 + dz^2 - \frac{2\sqrt{2}r^2 c}{r_G} dt d\phi. \quad (4.2)$$

Due to the homogeneity of Gödel's universe, there is no gravitational redshift, only Doppler shift arises due to relative motion. The mass distribution generating the curvature of Gödel's universe consists of dust which is rigidly rotating around every point. The angular velocity of this rotation is inversely proportional to the Gödel parameter $a = r_G/2$. The Gödel radius r_G can be identified [KWS04] with the **rotation scalar**

$$\Omega_G = \frac{\sqrt{2}c}{r_G}, \quad (4.3)$$

making it inversely proportional to the angular velocity of the rotating matter.

This set of coordinates is very intuitive compared to other formulations such as [Gö49, Pfa81]. In the limit $r_G \rightarrow \infty$, this spacetime yields the nonrotating, flat spacetime of special relativity in cylindrical coordinates. Therefore, a specific situation, e.g. a certain arrangement of objects, can be designed in flat spacetime before introducing rotation to this model. Another formulation for the metric is found after we apply the simple transformation

$$T = \frac{t}{r_G}, \quad R = \frac{r}{r_G}, \quad \varphi = \phi, \quad Z = \frac{z}{r_G}. \quad (4.4)$$

In these coordinates, the metric is scaling with r_G and reads

$$ds^2 = r_G^2 \left(-c^2 dT^2 + \frac{dR^2}{1 + R^2} + R^2(1 - R^2)d\varphi^2 + dZ^2 - 2\sqrt{2}cR^2 dT d\varphi \right). \quad (4.5)$$

Obviously, $R = 1$ marks the Gödel radius. We will use this line element to describe Gödel's universe (unless otherwise denoted). Since the unit of ds^2 is m^2 , time T is measured in s/m , while all other coordinates are dimensionless. In several illustrations, pseudo-Cartesian coordinates ($X = R \cos(\varphi)$, $Y = R \sin(\varphi)$) are used.

In general relativity, it is difficult to find a suitable interpretation of a given set of coordinates because they do not bear any physical meaning. For instance, Schwarzschild coordinates of the black hole metric can be interpreted as the coordinates of a distant observer because the metric is asymptotically flat and the line element is converging to the Minkowski line element. We follow this idea and construe the given coordinate set of the line element (4.2) as the coordinates of an observer located at the origin of this coordinate system: For $r/r_G \ll 1$, the line element converges to the Minkowski metric in cylindrical coordinates. Note that due to the homogeneity of the Gödel spacetime, this train of thought is possible for any observer and a proper coordinate system.

4.2.2 Geodesics

Numerous publications exist concerning the solutions to the geodesic equations of Gödel's universe. They were first solved in 1956 by Kundt [Kun56], who utilized the symmetries of the space-time represented by the Killing vector fields and the thereby resulting constants of motion. Chandrasekhar and Wright [CW61] derived the solutions independently five years later. They found that there are no geodesical closed timelike curves in the Gödel universe and noted that this fact seems to be contrary to Gödel's statement that the "circular orbits" allow one "to travel into the past, or otherwise influence the past". Nine years later, Stein [Ste70] pointed out that the "circular orbits" of Gödel's model are by no means geodesics and that Chandrasekhar's and Wright's conclusion was incorrect; see also [OS03]. Other detailed studies of the geodesics in Gödel's universe followed by Pfar [Pfa81] and Novello et al. [NST83]. The latter provided a detailed discussion on geodesical motion using the effective potential as well as the analytical solution. They already assumed that any geodesic can be generated from geodesics starting at the origin by a suitable isometric transformation.

Kajari et al. [KWSD04] found a very convenient set of coordinates in which Gödel's universe reveals its properties more apparent. Also, the symmetries of Gödel's universe were provided alongside a special solution to the geodesic equations. In contrast to our solution, Kajari et al. restrict the solution to the $\{t, r, \varphi\}$ -subspace and therefore neglect the z -coordinate of Gödel's universe.

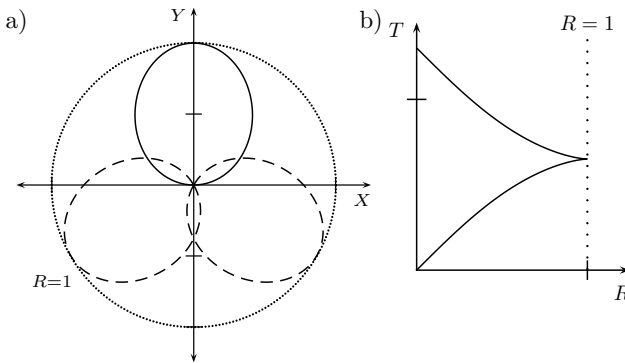


Figure 4.2: Lightlike geodesics in the (XY) -subspace depicted using pseudo-Cartesian coordinates (cf. Fig. 2 in [KWSD04]) in Fig. 4.2a. Photons emitted at the origin propagate counterclockwise into the future, reach a maximum radial distance of $R = r/r_G = 1$ and then return to the origin. Fig. 4.2b) shows $R(T)$ and reveals that the coordinate time monotonically increases for lightlike geodesics which start at the origin.

Fig. 4.2 depicts several lightlike geodesics starting at the origin. Photons reach the Gödel radius and their orbits are closed in the (XY) -subspace¹. Thus $R = 1$ constitutes an optical horizon beyond which an observer located at the origin cannot see because photons starting with $R_0 > 1$ do not reach the origin. Due to the homogeneity of the spacetime, any observer resting with respect to the worldlines of the matter distribution is surrounded by an equivalent optical horizon. The **Gödel horizon** itself is not an impenetrable barrier or “point of no return” such as the Schwarzschild horizon; it only acts as a mirror for geodesics starting at the origin (and becomes thereby defined). A photon emitted beyond the horizon of any observer can cross it, but will never reach him. We provide more details on the respective horizons of distinct observers in Sec. 5.3.2. The geodesic equations themselves are solved in Sec. 5.1 for arbitrary initial conditions.

4.2.3 Local Tetrads

If an observer is traveling on a stationary circular orbit with a four-velocity $\mathbf{u} = c\Gamma(\partial_T + \zeta\partial_\phi)$, we find the local tetrad (cf. [BJ00, MG09b] and Sec. 2.1.3)

$$\mathbf{e}_{(T)} = \frac{\Gamma}{r_G} (\partial_T + \zeta\partial_\phi), \quad \mathbf{e}_{(R)} = \frac{1}{r_G} \sqrt{1 + R^2} \partial_R, \quad (4.6a)$$

$$\mathbf{e}_{(\phi)} = \frac{\Delta\Gamma}{r_G} (A\partial_T + B\partial_\phi), \quad \mathbf{e}_{(Z)} = \frac{1}{r_G} \partial_Z, \quad (4.6b)$$

where

$$A = R^2 [-\sqrt{2}c + (1 - R^2)\zeta], \quad B = c^2 + \sqrt{2}R^2 c\zeta, \quad (4.7a)$$

$$\Gamma = \frac{1}{\sqrt{c^2 + 2\sqrt{2}R^2 c\zeta - R^2(1 - R^2)\zeta^2}}, \quad \Delta = \frac{1}{Rc\sqrt{1 + R^2}}. \quad (4.7b)$$

A static observer is identified with $\zeta = 0$. The corresponding tetrad then simplifies to

$$\mathbf{e}_{(T)} = \frac{1}{r_G c} \partial_T, \quad \mathbf{e}_{(R)} = \frac{1}{r_G} \sqrt{1 + R^2} \partial_R, \quad (4.8a)$$

$$\mathbf{e}_{(\phi)} = \frac{1}{r_G R \sqrt{1 + R^2}} \left(-\frac{\sqrt{2}R^2}{c} \partial_T + \partial_\phi \right), \quad \mathbf{e}_{(Z)} = \frac{1}{r_G} \partial_Z. \quad (4.8b)$$

In Sec. 5, the static tetrad is used because an observer resting in this tetrad will only propagate through time with regard to the line elements (4.2) or (4.5). The transformation rules between local and coordinate formulation are provided in App. A.

These tetrads, however, are not well-defined for $R = 0$. Since the angular coordinate is undefined at $R = 0$, we cannot formulate initial directions in the ∂_ϕ -direction. Nevertheless, we can

¹In this work, we denote the projection onto a plane as a subspace.

exploit the rotational symmetry of this spacetime. A geodesic can start with $u_0^\phi = 0$ and then be rotated around the Z -axis afterwards in order to generate geodesics that start at the origin and propagate in an arbitrary initial direction. Another possibility is to transform the tetrads as well as the line element to Cartesian coordinates in order to avoid the coordinate singularity in $R = 0$. Unfortunately, Gödel's universe loses its mathematical elegance when considering a set of coordinates which is not adjusted to the symmetries of the spacetime.

4.2.4 Test Particles

Now, we detail how massive particles propagate when they are placed at any point in spacetime. Let a test particle initially rest at an arbitrary event $x_p^\mu = (T, R, \phi, Z)$ with an initial 4-velocity $u_p^\mu = (1, 0, 0, 0)$. We inspect the geodesic equations (2.20) and insert $\Gamma_{00}^\mu = 0$, cf. App. A. The result is

$$\dot{u}_p^\mu = 0. \quad (4.9)$$

Thus, an observer with zero initial velocity will not move away from its original position *with respect to the chosen set of coordinates* – it will only evolve into the future.

However, the particle will spin because its restframe rotates when compared to the initial restframe given by eqns. (4.8). We can show that by parallel transporting the initial restframe using eq. (2.28). Since $\dot{u}_p^\mu = 0$, we have $\dot{u}_p(\lambda) = \dot{u}_p$. Thus, we can directly write

$$\frac{de_{(a)}^\mu}{d\tau} = -e_{(a)}^\nu u_p^\sigma \Gamma_{\nu\sigma}^\mu. \quad (4.10)$$

After inserting the Christoffel symbols, eqns. (A.13), we find the nonzero components

$$\frac{de_{(1)}^\mu}{d\tau} = \Omega_G e_{(2)}^\mu, \quad (4.11)$$

$$\frac{de_{(2)}^\mu}{d\tau} = -\Omega_G e_{(1)}^\mu \quad (4.12)$$

where Ω_G is the rotation scalar, eq. 4.3. Obviously, the solution is

$$e_{(1)}^\mu(\tau) = \cos(\Omega_G \tau) e_{(1)}^\mu + \sin(\Omega_G \tau) e_{(2)}^\mu, \quad (4.13)$$

$$e_{(2)}^\mu(\tau) = -\sin(\Omega_G \tau) e_{(1)}^\mu + \cos(\Omega_G \tau) e_{(2)}^\mu. \quad (4.14)$$

Consequently, a resting local observer corotates with the matter of Gödel's universe. However, this result can be easily misinterpreted. We will detail this problem in the following section.

4.2.5 And Yet It Rotates – Or Not?

There is basic problem when trying to intuitively understand the mass distribution in Gödel's universe because matter rotates *everywhere* in the same manner. Consider the following situation of two observers located at some distance to each other. Both state that matter rotates counterclockwise around them, cf. [Gö49] where the angular velocity of the matter is positive. In Fig. 4.3, we see that an inconsistency arises: Does matter move “upwards” or “downwards” in between?

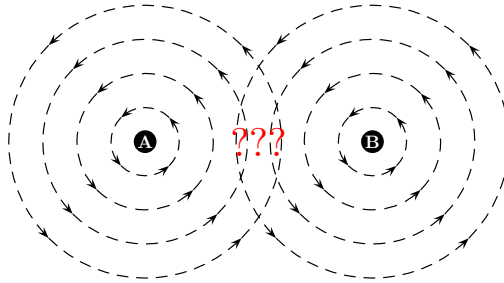


Figure 4.3: Homogeneity and rotating matter.

The physical interpretation of the dynamics in Gödel's universe, i. e. the analysis of “what rotates with respect to whom”, is a very serious question and there are many potential answers. Gott [Got02] states that “*You could equally well view Gödel's universe as static and non-rotating, as long as self-confessed 'nondizzy observers' would be spinning like whirling dervishes with respect to the universe as a whole*”. Gödel himself [Gö95] already had a similar interpretation: “*Of course, it is also possible and even more suggestive to think of this world as a rigid body at rest and of the compass of inertia as rotating everywhere relative to this body.*” albeit stating in the original publication [Gö49] that “*matter everywhere rotates relative to the compass of inertia with ... [a constant] ... angular velocity*”. Consequently, it is very difficult to determine what rotates with respect to whom.

Similarly, Rindler [Rin09] asserts that “*though Gödel's Universe is rigid and infinite, the Foucault pendulum planes everywhere in it rotate in unison, a clear affront to adherents of Mach's Principle*”. The precise formulation of a Foucault pendulum is a tedious endeavor. Usually, they are interpreted as infinitesimally small [NMAA08] or treated equivalently as gyroscopes [DSS02]. Another possibility is the consideration of free test particles, as stated in [DSS02]. The locality of these considerations in combination with the non-vanishing rotational scalar, alongside the homogeneity of the spacetime, constitutes the problem of finding a meaningful interpretation of the mass distribution.

In the last section, we reviewed the simple calculation of the parallel transport of a restframe and found that it rotates with a constant angular velocity given by the rotational scalar of the Gödel universe. Now, we investigate a different point of view, which hopefully stimulates future work. Consider the stress-energy tensor $T_{\mu\nu}$, which consists of the following entities [MTW73]:

entry	interpretation
T^{00}	energy density
T^{j0}	momentum density
T^{0k}	energy flux
T^{jk}	stress

A vacuum energy density can be associated to the cosmological constant [Car01] via $T_{\text{vac}}^{\mu\nu} = -\rho_{\text{vac}} g^{\mu\nu}$, where $\rho_{\text{vac}} = -p_{\text{vac}} = \Lambda c^2 / \kappa$ and $\kappa = 8\pi G / c^4$. $T_{\text{mat}}^{\mu\nu}$ as well as $T_{\text{vac}}^{\mu\nu}$ are calculated with respect to the given set of coordinates $\{T, R, \phi, Z\}$ as well as using the local formulation (4.8). In the coordinate dependent formation, we find

$T_{\text{mat}}^{\mu\nu}$ – global formulation

$$T_{\text{mat}}^{\mu\nu} = \begin{pmatrix} \frac{4}{\kappa c^2 r_G^4} & 0 & 0 & 0 \\ 0 & 0 & 0 & 0 \\ 0 & 0 & 0 & 0 \\ 0 & 0 & 0 & 0 \end{pmatrix} = \begin{pmatrix} \rho_{\text{mat}} & 0 & 0 & 0 \\ 0 & 0 & 0 & 0 \\ 0 & 0 & 0 & 0 \\ 0 & 0 & 0 & 0 \end{pmatrix} \quad (4.15)$$

and

$T_{\text{vac}}^{\mu\nu}$ – global formulation

$$T_{\text{vac}}^{\mu\nu} = \begin{pmatrix} -\frac{2}{r_G^4 \kappa c^2} \frac{1-R^2}{1+R^2} & 0 & -\frac{2\sqrt{2}}{r_G^4 \kappa c} \frac{1}{1+R^2} & 0 \\ 0 & 2 \frac{1+R^2}{r_G^4 \kappa} & 0 & 0 \\ -\frac{2\sqrt{2}}{r_G^4 \kappa c} \frac{1}{1+R^2} & 0 & \frac{2}{r_G^4 \kappa} \frac{1}{R^2(1+R^2)} & 0 \\ 0 & 0 & 0 & \frac{2}{r_G^4 \kappa} \end{pmatrix}. \quad (4.16)$$

Obviously, $T_{\text{mat}}^{\mu\nu}$ represents a perfectly homogeneous and static matter distribution where no rotation at all is visible. In contrast to that, the vacuum energy density $T_{\text{vac}}^{\mu\nu}$ possesses a non-zero “rotating” energy flux term. Thus, using this coordinate dependent representation, the matter distribution is static, but the vacuum energy “rotates” around every point. Comprehending that the latter energy form moves in any way is difficult because the origin of the vacuum energy itself is hard to find. In our universe, where the cosmological constant is positive, the vacuum

energy density is also positive, which results in negative pressure (see above). The cosmological constant in Gödel's universe is negative, thus the “rotating” vacuum energy density must also be negative. In the local formulation, using eqns. (4.8), we find both contributions to the stress-energy tensor to be diagonal:

$T_{\text{mat}}^{(a)(b)}$ – local formulation

$$T_{\text{mat}}^{(a)(b)} = \begin{pmatrix} \frac{4}{\kappa r_G^2} & 0 & 0 & 0 \\ 0 & 0 & 0 & 0 \\ 0 & 0 & 0 & 0 \\ 0 & 0 & 0 & 0 \end{pmatrix} = \begin{pmatrix} \rho_{\text{mat}} c^2 & 0 & 0 & 0 \\ 0 & 0 & 0 & 0 \\ 0 & 0 & 0 & 0 \\ 0 & 0 & 0 & 0 \end{pmatrix}, \quad (4.17)$$

and

$T_{\text{vac}}^{(a)(b)}$ – local formulation

$$T_{\text{vac}}^{(a)(b)} = \begin{pmatrix} -\frac{2}{r_G^2 \kappa} & 0 & 0 & 0 \\ 0 & \frac{2}{r_G^2 \kappa} & 0 & 0 \\ 0 & 0 & \frac{2}{r_G^2 \kappa} & 0 \\ 0 & 0 & 0 & \frac{2}{r_G^2 \kappa} \end{pmatrix} = \begin{pmatrix} \rho_{\text{vac}} c^2 & 0 & 0 & 0 \\ 0 & p_{\text{vac}} & 0 & 0 \\ 0 & 0 & p_{\text{vac}} & 0 \\ 0 & 0 & 0 & p_{\text{vac}} \end{pmatrix}. \quad (4.18)$$

Thus, from a local perspective, no rotation at all is visible. We must try to find an answer to the question whether the vacuum energy density “rotates” or not. As an alternative, the following interpretation seems to be the most sensible: The local tetrad itself must be rotating, which is also confirmed by the discussion in Sec. 4.2.4. All infinitesimally small observers will rotate with respect to the matter, which is static and given by eq. (4.15). Two observers in close proximity will both see the other rotate around him but both will not rotate *around* each other because they rest in the static dust distribution. Now, regard an observer of non-zero size. Then, every point (or pointlike elementary particle of which he consists) will rotate exactly as the infinitesimal observers before. The extended observer, however, will not rotate *as a whole* because every particle rests with respect to the dust distribution. Each atom only has an additional “spin”. If the interpretation above is correct, then any local tetrad in Gödel's universe is only valid at its center. Even investigations of very small objects would lead to errors that are larger than the imprecisions resulting from the linear approximation (which defines the tetrad). The conclusion of this section is that infinitesimally small objects do rotate and extended objects *probably* not. Consequently, some results found in several articles [NMAA08, DSS02] must be called into question because infinitesimally small Foucault pendulums or gyroscopes are investigated. If our interpretation is correct, then the compass of inertia as defined by a *macroscopic* Foucault pendulum would be aligned (*not* rotating) with the static matter distribution.

The assumptions made in this section are not to be taken as mathematical proof and thus we adopt the “classical” interpretation of the Gödel universe: Throughout this work, we follow the interpretation given in the original publication [Gö49] and, therefore, emphasize the local perspective in Gödel’s universe as a clearly defined problem. Accordingly, almost all objects are formulated with respect to the local tetrad. Of course, we must extend the object’s size so that it can be seen: We *visualize* extended objects but *interpret* them as pointlike.

It remains unclear whether a fast traveling and extended object rotates corresponding to the appropriate equations of transport or if we must, in a sense, subtract the “rest rotation”. A possible direction towards finding an answer is the *spin-curvature coupling* (see [MTW73] on p. 1120f.), which describes the coupling of the spin of a *macroscopically rotating* body to the tidal gravitational forces of the curved spacetime. In our case, one must investigate the coupling of a *microscopical rotation* to the gravitation.

4.2.6 Light Cone Structure

To illustrate the causal structure of the Gödel universe we rely on an analysis of light cones. This is a standard approach often used. For the Gödel universe, explicitly we refer to [KWSD04, NMAA08]. The latter publication [NMAA08] focuses on exactly these geometrical interpretations of light cones. They construct the Gödel universe by investigating a “naive spiral world” and add the features of Gödel’s universe bit by bit in order to create a comprehensive, geometrical interpretation of the spacetime.

Contrasting flat spacetime and Gödel’s universe

The finiteness of the speed of light and the impossibility to travel faster than c define the causal structure of special relativity, which is depicted in Fig. 4.4a. In this picture, we identify two spatial coordinates X and Y , and the temporal coordinate T , where the latter is multiplied with the velocity of light c . Now, let a light flash be emitted at the origin of the coordinate system. In this representation, light propagates into the future as a cone (red) because the Z -coordinate is suppressed. If the time direction is reversed, we investigate on which paths light can arrive at the origin. Thereby, we obtain the (blue) past light cone. The realizable worldlines which pass through the origin are limited to the regions inside the two cones, such as the red curve in this figure: One cannot travel faster than the speed of light and, therefore, not outside the light cones.

Of course, we can initiate a light flash at any event in the Minkowski spacetime. All light cones are of the same shape when using Cartesian coordinates. In Fig. 4.4b, several light cones in the (XY) -plane are drawn. We denote the collection of these cones as the *local light cone structure* of a spacetime. In special relativity, the light cone structure is not only a local property, as the spacetime and the local tetrad at the origin coincide: The local tetrad of an observer is valid

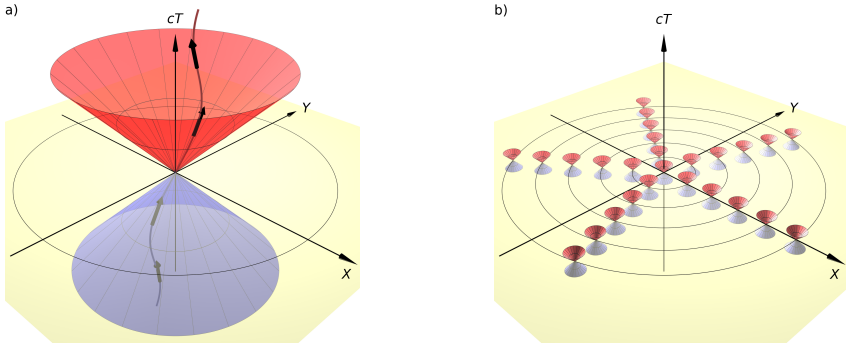


Figure 4.4: Light cone structure in special relativity. Fig. 4.4a shows how past and future light cones restrict the possible motion on a worldline and Fig. 4.4b illustrates the homogeneity of the Minkowski metric.

not only in a limited region because the linear approximation to the metric is the metric itself. Consequently, the light cones can be drawn arbitrarily large. In curved spacetimes, contrarily, the light cone structure is an exclusively local property.

Time travel in Gödel's universe

In Gödel's universe, the local light cone structure is very different compared to flat spacetime; see Fig 4.5a. In this figure, we see the influence of the nonzero rotational scalar Ω_G , eq. (4.3), on the local light cone structure (known as **frame dragging** [MTW73]). At the origin, the light cone is vertically oriented, exactly as in special relativity. Furthermore, coordinate time and proper time coincide for an observer at the origin. This circumstance verifies the discussion at the end of Sec. 4.2.1 where we interpreted the coordinates as the “natural” description for an observer located at the origin. Remember that the Gödel universe is homogeneous and, therefore, any observer can declare his position as the origin of a coordinate system. From any point of view, Fig. 4.5a is reproduced.

Due to the frame dragging, the light cones widen and tilt the further they are away from the origin. The Z -direction is, at any point, always within the light cones because otherwise, particles initially at rest could not retain their position as calculated in Sec. 4.2.4. The tilting effect of the cones is not particularly noteworthy because many metrics inherit this effect. However, in contrast to the causally normal spacetimes in relativity, the light cones beyond the Gödel radius r_G decline so that the plane of constant coordinate time is intersected.

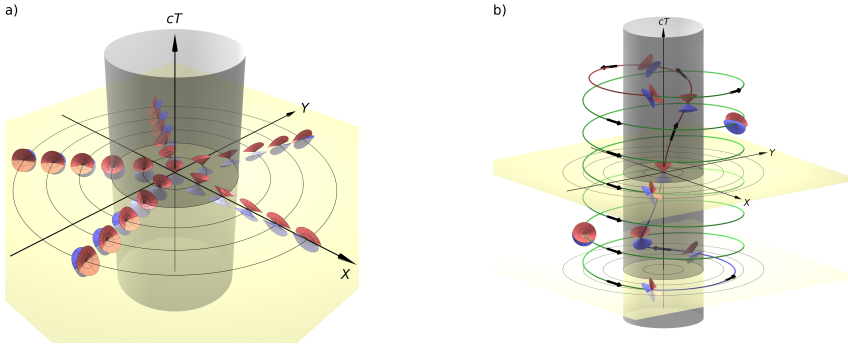


Figure 4.5: Light cones and time travel in the Gödel universe. Fig. 4.5a shows the light cones for various positions. The planes of constant coordinate time are intersected for light cones beyond the Gödel horizon (which is depicted as the gray cylinder). A non-trivial CTC is shown in Fig. 4.5b and illustrates Gödel's original idea to prove that CTCs exist through every point in this spacetime.

This is exactly the crux where causality breaks down in the Gödel universe. If the local future light cone intersects the $T = \text{const.}$ -plane, then a traveler located there cannot only travel into his own local future (as he is forced to due to the laws of special relativity), but he can also travel into the past of an observer who is located at the origin. When traveling at a velocity large enough – but always slower than c – a voyager can travel on a circular path around the origin and beyond the horizon. If the local velocity is very high, the traveler will propagate into the past of the observer on a ***past traveling curve*** or ***PTC***. For a given distance to the origin, exactly one velocity exists so that the voyager travels on a temporally closed circle. This kind of curve is designated as a ***closed timelike curve*** or ***CTC***. The smaller the radius of the CTC, the higher the required local velocity becomes. In the limiting case $v \rightarrow c$, this radius is given by $R = 1$ and the curve is no longer timelike, but lightlike. This ***closed lightlike curve*** or ***CNC*** (closed null curve) is not a geodesic, but can be, in principle, created by a suitable arrangement of mirrors along the horizon.

Fig. 4.5b shows a possible CTC. One can interpret the curve as the flight path of a spaceship. It leaves the origin (red segment), travels on a PTC (green) and returns to the origin *at the moment of departure (with respect to an observer resting there)* along the blue part of the flight path. Note that the traveler on the spaceship will have aged after such a journey because he *always* propagates into his own local future. Consequently, the voyager returning after his time travel is older than the departing version of himself.

Gödel's universe is one of the simplest solutions of Einstein's field equations that allows for CTCs. As pointed out by Gödel [Gö49], geometrically very simple CTCs, corresponding to the circular orbits discussed above, exist. These orbits were also discussed by Raychaudhuri et al. [RT80] and Pfarr [Pfa81], who categorized them into CTCs, PTCs and CNCs. Rosa and Letelier [RL07] found that CTCs are stable under tiny changes of the stress-energy tensor.

In Sec. 5.3.3, we revisit the ideas presented in this section and analyze them on a more detailed level. Using a circular CTC and the analytical solutions to the equations of isometric transport, we will construct a CTC which passes through the origin. This non-trivial class of CTCs is investigated from a visualization standpoint in Sec. 7.4.3.

4.2.7 The Symmetries of Gödel's Spacetime

Gödel's metric facilitates analytical investigations because it is highly symmetric and possesses five independent Killing vector fields. Gödel himself already took advantage of four isometry groups to show that his cosmological solution is spacetime homogeneous [Gö49]. A more detailed examination of the Killing fields was later performed by Navez [Nav70]. He showed that Gödel's universe is endowed with five independent Killing vector fields and he examined the structure of the corresponding Lie algebra. The Killing equations for Gödel-type spacetimes were also discussed by Raychaudhuri et al. [RT80]. They derived the necessary conditions for Gödel-type metrics to inherit at least four independent Killing vector fields – constituting the minimum requirement to satisfy the homogeneity of the spacetime. Based upon this work, and independent of Naves' work [Nav70], Rebouças et al. [RT83] showed that these conditions lead to five independent Killing vector fields.

Based upon the notation of Kajari's work [KWS04], the five independent solutions of the Killing equations (2.30) for the scaled cylindrical coordinate set $\{T, R, \phi, Z\}$ read

$$\xi_0^\mu = \delta_0^\mu, \quad \xi_2^\mu = \delta_2^\mu, \quad \xi_3^\mu = \delta_3^\mu, \quad (4.19a)$$

$$\xi_1^\mu = \frac{1}{q(R)} \begin{pmatrix} \frac{R}{\sqrt{2}c} \cos \varphi \\ \frac{1}{2}(1+R^2) \sin \varphi \\ \frac{1}{2R}(1+2R^2) \cos \varphi \\ 0 \end{pmatrix}, \quad (4.19b)$$

$$\xi_4^\mu = \frac{1}{q(R)} \begin{pmatrix} \frac{R}{\sqrt{2}c} \sin \varphi \\ -\frac{1}{2}(1+R^2) \cos \varphi \\ \frac{1}{2R}(1+2R^2) \sin \varphi \\ 0 \end{pmatrix}, \quad (4.19c)$$

where

$$q(R) = \sqrt{1+R^2}. \quad (4.20)$$

The first three Killing vectors (eq. (4.19a)) are trivial, correspond to the constants of motion (5.3) and represent infinitesimal transformations in T , ϕ and Z , respectively. Eqns. (4.19b) and (4.19c) reveal that a radial transformation generally affects time and the angular coordinate as well. Note that lower indices in Killing vectors serve to distinguish different vector fields. These five Killing vectors, together with the equations of isometric transport for points, eq. (2.31), and vectors, eq. (2.32), offer the possibility to transform a scenario formulated in Gödel's universe (which is discussed in Sec. 6.2). These transport equations are solved in Sec. 5.2; the solutions are used in Sec. 5.3 and in the GÖDEL ENGINE (see Ch. 6). The actual scene definition for the visualization of time travel on a CTC (Sec. 7.4.3) also uses the analytical results.

4.3 A Brief History of Time Travel

The Gödel universe is the first model within the domain of general relativity which permits time travel and CTCs. After Gödel's discovery, a multitude of other metrics addressing time travel was introduced. In addition to that, there are many publications which cover the implications of causality violations on a logical level. This section summarizes the most important time travel universes. We then close this chapter with an outline on the implications, problems and proposed remedies to the issues which result from time travel and causality violations. For more detailed presentations, we refer to standard literature such as [Haw01, Got02] or to Thorne's paper [Tho92].

4.3.1 Time Travel Universes

Since Gödel's discovery, a large number of other spacetimes were discovered which permit time travel. A complete recital is beyond the scope of this work, thus we use the list provided by Visser [GSR03] as a basis and detail key aspects of the models. For several models, egocentric visualizations were created. Zatloukal [Zat05] has provided egocentric renderings for the Kerr spacetime and wormhole spacetimes were visualized by Müller [Mü08] as well as Fechtig [Fec03]. The images presented in these works are restricted to causally normal phenomena.

Van Stockum dust cylinder

Gödel himself was the first who pointed out the existence of time travel within the framework of general relativity, although the van Stockum dust cylinder model of 1937 already possesses CTCs [Sto37, Tip73]. Moreover, the interior metric (an infinitely long and rotating dust cylinder) was already found by Lanczos [Ste98, Lan24] in 1924. The solution is very similar to the Gödel spacetime because it describes a rotating dust distribution and the geodesics are confined to a maximum radial extent [Ste98]. It can be shown that the spacetime can be divided into a causal

region and a part where time travel is, in principle, possible. However, the most important difference is that the rotating cylinder solution is not homogeneous: The dust cylinder is infinitely long but has a finite radius. Thus, the spacetime is only rotationally symmetric around a single axis. Note that the Van Stockum dust cylinder is sometimes denoted as a Tipler cylinder. Furthermore, spinning cosmic strings are very similar to the dust solution (but have a different asymptotic behavior [LC02]).

Kerr-type black holes

The metric of a rotating black hole was found by Kerr [Ker63]. In general, rotating black holes are described with three parameters: A mass m , an angular momentum per unit mass a and a charge e . There are three important geometrical surfaces: The inner and outer horizon, $r_{\pm} = m \pm (m^2 - a^2 - e^2)^{1/2}$, and the ergosphere r_e , which is defined by $r_e^2 + a^2 + (2mr_e - e^2)a^2 \sin^2(\theta) / (r_e^2 + a^2 \cos^2(\theta)) = 0$.

Carter [Car68] has shown that different types of CTCs exist depending on the properties of the metric. In the extremal case, $a^2 + e^2 > m^2$, the two horizons disappear and the “naked” ring singularity remains. It is then possible to start *“from any point in the outer regions of the space, to travel to the interior, move backwards in time ... as far as desired, ... and then return to the original position”*. Time travel is even possible in the non-extremal case, $a^2 + e^2 \leq m^2$, where the two horizons exist. While the outer parts of the spacetime are well-behaved, the inner region $r < r_-$ is acausal. Then, after *“(irreversibly) crossing it on a timelike path, [one] can enter a region where causality is violated just as in the previous case”*. Since it is very certain that a large number of rotating black holes exists, these spacetimes represent the most probable candidates for time machines which – if Carters interpretations are correct – already exist. However, extremal black holes are often considered unphysical and even if $a^2 + e^2 \leq m^2$, the *“spacetime near and inside the chronology horizon $[r_-]$ will be altered by an instability due to the infalling, blue-shifted perturbations; and this alteration will (hopefully) prevent CTCs from arising”* [Tho92].

Gott time machines

The Gott time machine [Got91, Cut92] is another exact solution of Einstein's field equations and thus is principally realizable within the theory of relativity. The spacetime consists of two infinitely long and parallel strings which move past each other [Tho92]. Roughly speaking, if the relative velocity is high enough, a (single) chronology horizon is formed around the two moving strings. Inside the horizon, the spacetime is causal but the exterior allows for the creation of CTCs. Due to several reasons, for instance the infinite length, and thus infinite mass of the strings, even the theoretical feasibility of this spacetime is highly questionable.

Wormhole metrics

A wormhole metric [MT88, Vis96] is usually characterized as an asymptotically flat spacetime, where two specific and very distant points in space are additionally connected by a shortcut – the throats of a wormhole. In this region, the spacetime is highly curved. In fact, the research on wormholes was more or less initiated by the science-fiction novel “Contact”, written by Carl Sagan. The author assigned Kip Thorne to investigate [Tho95] if such “shortcuts” through space and time are physically feasible. Put simply, the two throats may not only connect two distant locations but also two points in time. Thus, a voyage through a wormhole could also be a travel back in time and the formation of CTCs seems possible. Frolov and Novikov [FN90] state that *“the interaction of a wormhole with the surrounding matter and with the external gravitational field almost inevitably transforms it into a time machine”*. Unfortunately, most wormhole metrics require massive amounts of exotic matter, i. e. matter with negative masses (repelled by gravitational forces) and are therefore not considered realizable on a practical level.

Alcubierre warp drive

The Alcubierre warp drive [Alc94] is definitely inspired by the Star Trek series. It is formulated within the domain of general relativity and offers a possibility to travel faster than the speed of light. Therefore, the spacetime behind a spaceship is expanded and contracted in front of it. The region in between (where the spaceship rests) and outside of this extremely curved part is relatively flat. There, the spaceship rests locally. However, from a distant point of view, outside the “warp-bubble”, the observer is moving along with the bubble – at an arbitrarily high speed. Note that time travel is not possible with this warp drive (as suggested in many other publications). Alcubierre himself states at the end of the paper that *“the metric ... contains no closed causal [i. e. timelike] curves, it is probably not very difficult to construct a spacetime that does contain such curves using a similar idea to the one presented here”*.

Other Gödel-type metrics

The Gödel universe was modified and extended in many ways. Besides Gödel universes in more than four dimensions (such as Kerr-Newman-Gödel black holes in the minimal supergravity theory in five dimensions [Her03, PW09]), there are many Gödel-like spacetimes. Several publications exist on slightly generalized Gödel-type metrics where an additional degree of freedom is introduced, for example [RT83, Hua99]. For a specific choice of the accessory parameter, the original Gödel metric is reproduced. Furthermore, Carneiro [Car00] discussed how the currently observed large scale structure of Friedmann type could have evolved from a “*primordial*” Gödel universe.

Summary

As indicated by this section (and detailed in a vast number of publications discussing whether CTCs are realizable), there are a multitude of spacetimes which permit CTCs. However, the technical realization seems impossible because there are just as many reasons or mechanisms – exotic matter, vast energy requirements and back coupling of the spacetime when constructing a CTC – that prevent or at least severely complicate the actual construction of a time machine. The lively discussion is in full swing and the matter is far from being brought to a conclusion. We only conclude that time travel is *an intrinsic feature of general relativity* regardless of the theoretical or technical feasibility.

4.3.2 Causality Violations

The mere idea of traveling through time is a popular topic in literature as well as in motion pictures. The first novel addressing time travel was H. G. Wells’ “The Time Machine” [Wel92], originally published in 1895, where the protagonist can travel through the epochs of Earth’s history using a self-built device. This work, however, focuses on the social ranks of a distant future and indirectly correlates them to the class distinctions prevalent in the 19th century. Another interesting example is Isaac Asimov’s work, “The End of Eternity” [Asi75], where we find a society built completely on the concept of time travel. The “Eternals”, a group of guardians existing “outside time”, initiate reality changes using time travel in order to create the world in a desired way. This novel approaches time travel paradoxes as well, elevating itself to a more scientific level.

Moreover, there are quite a few Star Trek episodes approaching this topic. In the episode “Déjà vu”, we see the Enterprise trapped in a “time loop”. The crew must go through the same events over and over again. From a physical point of view, their problem is very closely related to **closed timelike curves** or CTCs because the entire spaceship returns to the same point in space *and* time again and again. However, there is an important difference to the physical concept of CTCs: Not the spaceship alone is returning to the same event over and over again, also the crew’s memories are erased. They only experience déjà vu which finally help them to resolve the situation and “break the loop”. However, when traveling on a closed timelike curve, the traveler’s watch (i. e. his proper time) will behave similar to special relativity. A voyager moving on a CTC would not forget anything due to the motion and he would age normally. To enunciate this effect: The traveler can travel on a CTC into the past of some outside observer but not into his *own* past.

The basic dilemma of time travel is the possibility of causality violations. It is commonly illustrated using the grandfather paradox, which was first verbalized in 1943 by René Barjavel [Bar]. A person travels into his past and kills his grandfather before the latter met his wife. Then, the reason for the traveler’s existence is wiped out and the traveler cannot exist because he would never have been born. However, if the traveler is not conceived, then the grandfather would not have been killed. Therefore, the grandfather could have children which, ultimately, resulted in

the traveler's birth. The traveler could, consequently, travel into the past and kill his grandfather. This easily verbalized experiment ultimately results in a paradox situation and we cannot conclude the result. The grandfather paradox even limits the possible definitions of a scene in the Gödel universe, which will be covered in Sec. 7.4.4.

4.3.3 Remedies to Paradoxes

Several theoretical remedies exist concerning the paradox situation mentioned above. Following the targeted popularity of this section, we will illustrate the ideas with well-known series or movies.

Histories – Many of them

In “Back to the Future II”, Doc Brown explains to Marty McFly how traveling into the past can lead to another “timeline”. Throughout the movies, both go to great lengths in order to restore the original timeline – with minor modifications that are pleasant for them. The concept of alternative timelines can be found in two, well-known concepts: The idea of parallel universes, which is mainly restricted to science fiction, as well as the many-world interpretation of quantum mechanics.

If we consider *loop quantum gravity* [Rov08], an ansatz to unite general relativity and quantum mechanics, we find that spacetime turbulences exist on the Planck-scale, which Wheeler denoted as quantum foam [WFR00]. In an inflationary phase of the history of our universe, this quantum foam could have been extremely expanded, which would have generated distinct and causally non-connected universes. Nevertheless, this interpretation is highly speculative. This effect cannot – not even in principle – be confirmed or falsified because the resulting universes are causally separated and there are no means of exchanging information. We only state that this interpretation of quantum foam is the closest approximation to the popular scientific concept of parallel universes.

The *many-world interpretation* was conceived by Everett [Eve57] and the figurative designation was devised by DeWitt [DG73]. The basic idea is that the wave function does not collapse when a measurement is conducted. Thus, every time a measurement – or generally speaking, an arbitrary decision is made – the wave function is not projected onto a single possible outcome. On the contrary, each possible result is realized and an infinite number of universes is generated: If someone decides to walk in a specific direction, there will be a reality where he walks to the left, another where he moves straight along, one in which he heads to the right, or simply turns around and a distinct reality for any other direction in between. Everything that can happen will take place (or has already occurred). All resulting realities represent individual timelines which cannot interact with each other.

However, there is a notable difference between the parallel universes concept and the many-worlds theory, although causality is not violated in both cases: In the first case, the time traveler “jumps” between already existing universes. Thus, returning to the grandfather paradox, he would not kill *his own* grandfather but an ancestor of the other universe. Hence, a paradox situation does not arise because just the *traveler of the other universe* will not be born. In the many-world interpretation, however, the travel back in time is a quantum-mechanical experiment. At the moment of time travel, an infinite number of universes would be created. Following the interpretation of DeWitt and Everett, every outcome is realized and thereby, each traveler arrived in a distinct universe. Since the original traveler leaves, his universe causality is conserved.

After having discussed the implications of an infinite number of timelines, we apply Ockham's razor² and focus on a single universe with a unique history.

History is self-consistent

Hiro, a character in the science fiction series “Heroes”, can travel through time simply by concentrating on the desired destination. He tries to change the past in an obviously causality violating way. Consider the episode “Cautionary Tales” where he tries to undo the assassination of his father. If he succeeded, the paradox would arise because the reason for his travel through time would be erased. However, he repeatedly fails to achieve his goal and accepts that he cannot save his father. This storyline illustrates the **Novikov self-consistency principle** [FMN*90] which states that “*if CTC's are permitted, then the semiclassical laws of physics . . . should be augmented by a principle of self-consistency, which states that a local solution to the equations of physics can occur in the real Universe only if it can be extended to be part of a global solution, one which is well defined throughout the (nonsingular regions of) classical spacetime*”. This principle does not forbid time travel in general, but makes a statement on the realizability of specific journeys. Causality violating time travel is forbidden because it cannot be described in a globally consistent way. However, the principle does generally not forbid time travel. Novikov supposes in [Nov92] that the construction of time machines is possible. In this work, several classes of self-consistent time travels on CTCs are discussed, where self-interaction is explicitly allowed. The underlying spacetime is a wormhole where the two throats represent, for instance, two holes on a billiard table. Moreover, an infinite number of self-consistent solutions exist concerning this scenario, cf. Echeverria et al. [EKT91]. To illustrate self-consistency, we refer to a modified version of the grandfather paradox. Consider the traveler not attempting to kill his grandfather, but introducing him to his grandmother instead. Thus, the traveler would ultimately be the reason for his own birth. We are not able to determine the cause and the effect because the origin of the traveler cannot be identified. This results in an **ontological paradox** (and also a **predestination paradox**); see [MVM09] for an introduction to these concepts. These types of paradoxes are not

² “Entities must not be multiplied beyond necessity.”

forbidden by the Novikov principle because they are self-consistent. However, the Novikov principle and the allowed paradoxes restrict the free will: If Hiro, the character mentioned above, had succeeded in saving his father, he would have already known his triumph. He would not have witnessed the homicide of his father, but instead would have seen his future self capturing the potential assassin. However, we know that this has not happened. Thus, the future Hiro cannot decide to move back in time. Such a decision cannot be made in accordance with the Novikov principle. Consequently, this principle limits the free will. Note that this restriction is not an issue when considering parallel universes or the many-worlds interpretation.

History cannot be altered

A repeated theme in Star Trek Voyager is the spaceship “Relativity”, which is able to travel through time. Its mission is to prevent paradoxes in the history of the universe. Contrary to the “Déjà vu” episode, this spaceship “exists outside of space and time”. To put a physical meaning to this rather unscientific description, we detect that this interpretation is closely related to the local comoving frame of a traveler: The Relativity’s proper time (and therefore the crew’s memory, age and experiences) remain unaffected by the travel. The focus of this episode is, however, on something different. In this science fiction universe, some sort of agency exists that counteracts the effects of paradoxes and renders time travel effects impossible. To find a scientific analogy to this plot, we consider Hawking’s work. The **chronology protection conjecture** [Haw92] is based on the investigations of the formation of CTCs. He finds that “*it seems that the back reaction [of the increasingly large expectation value of the stress-energy tensor] would prevent closed timelike curves from appearing*” and thus “*it seems that there is a chronology protection agency which prevents the appearance of closed timelike curves and so makes the universe safe for historians*” and that the laws of nature prevent time travel on all but sub-microscopic scales. As a closing remark, he concludes that “*there is also strong experimental evidence in favor of the conjecture from the fact that we have not been invaded by hordes of tourists from the future*”. However, in recent years, Hawking changed his mind a bit. On Kip Thorne’s 60th birthday in the year 2000, Hawking gifted him a calculation. He estimated (as Thorne recites [GSR03], p. 103) that the quantum mechanic probability for a time machine to work is extraordinary small but not zero: 10^{-60} . Moreover, in his popular scientific book “The Universe in a Nutshell” [Haw01] he takes up a still skeptical but somewhat milder position. Note that he specifies the probability for a successful time travel as $10^{-10^{60}}$, which is considerably smaller than the value mentioned above, but still not zero. A successful time travel is clearly a hardly accomplishable endeavor. However, we are interested in the *theoretical* feasibility and thus we conclude that time travel *seems* very improbable, but not completely impossible. We cannot answer the question whether or not time travel is realizable when solely focusing on general relativity because this theory is not a complete theory of everything. Visser [GSR03] assumes that “*... if chronology protection is the answer, we will have to wander deep in the guts of quantum gravity to know for certain*”.

ANALYTICAL INVESTIGATIONS

“All which is beautiful and noble is the result of reason and calculation.” — CHARLES PIERRE BAUDELAIRE

In this chapter, we discuss the solutions to the geodesic equations as well as the equations of isometric transport of points and vectors. These results then serve as a foundation for fast visualizations of the Gödel universe, as discussed in Ch. 6. After addressing the special case of geodesics starting at the origin, we introduce the general solution and explain under which circumstances time travel on geodesics is possible. In Sec. 5.2, we derive analytical expressions on finite isometric transformations along Killing vector fields for points as well as directions. All results are then used in Sec. 5.3 to isometrically transform initial conditions for geodesics in order to map, for example, the special solution of the geodesic equations onto the general solution. Finally, we carry out a detailed analysis of circular CTCs and use finite isometric transformations to generate a class of non-circular CTCs. In the appendices B and C, we describe several details regarding the solutions to the geodesic equations as well as the equations of isometric transport for easier reproduction of our results by the reader. The last section in the appendix provides interesting estimates of our results using astronomical data.

The analytical investigation of motion and symmetries in Gödel’s universe were presented in our previous publication [GBM*09] and are reviewed and reformulated in this section. In contrast to this publication, we use a different set of coordinates in this work. In [GBM*09], we used the notation of Kajari [KWS04], where the coordinate time directly corresponds to the proper time of any observer who is resting with respect to the mass distribution. However, in this work we chose to use the scaled coordinates provided by eqns. (4.4). In this set of coordinates, the line element is scaled by the factor r_G^2 , cf. eq. (4.5), and therefore, all results scale with the Gödel radius r_G (or a power of it). Please note that the properties of this work slightly differ from [GBM*09] due to the scaling with the Gödel radius r_G , although the same notation is used. The essential physical features remain unchanged but appear more clearly.

5.1 Geodesics

The geodesic equations (2.20) are solved using the Lagrangian formalism. The Lagrangian \mathcal{L} reads

$$\mathcal{L} = r_G^2 \left(-c^2 \dot{T}^2 + \frac{\dot{R}^2}{1+R^2} + R^2(1-R^2)\dot{\phi}^2 + \dot{z}^2 - 2\sqrt{2}cR^2 \dot{T}\dot{\phi} \right). \quad (5.1)$$

Additionally, the constraint $\mathcal{L} = g_{\mu\nu} u^\mu u^\nu = \kappa c^2$, cf. eq. (2.21), must be fulfilled. We focus on timelike motion ($\kappa = -1$) and lightlike geodesics ($\kappa = 0$). Since the Lagrangian is independent of T , ϕ and Z , we find three constants of motion $k_i \propto \partial \mathcal{L} / \partial \dot{x}^i$, where

$$k_0 = -c \dot{T} - \sqrt{2}R^2 \dot{\phi}, \quad (5.2a)$$

$$k_2 = R^2 (1 - R^2) \dot{\phi} - \sqrt{2}R^2 c \dot{T}, \quad (5.2b)$$

$$k_3 = \dot{Z}. \quad (5.2c)$$

The quantities k_0 , k_2 and k_3 represent the conservation of energy, angular momentum and the Z -component of momentum, respectively. We can express the constants of motion, eqns. (5.2), in relation to the static local tetrad, eqns. (4.8). The result for both lightlike and timelike geodesics is

$$k_0 = -\frac{1}{r_G} u_0^{(0)}, \quad (5.3a)$$

$$k_2 = \frac{1}{r_G} \left(R_0 \sqrt{1 + R_0^2} u_0^{(2)} - \sqrt{2} R_0^2 u_0^{(0)} \right), \quad (5.3b)$$

$$k_3 = \frac{1}{r_G} u_0^{(3)}. \quad (5.3c)$$

The parameter $R_0 = R(0)$ is the initial radial coordinate of the geodesic. Since any vector $\mathbf{u} = u^{(a)} \mathbf{e}_{(a)}$ expressed in a local system is treated like any vector in special relativity, the sign of $u_0^{(0)}$ determines whether the geodesic is evolving into the future (+) or into the past (-). As a result, k_0 is associated with the time direction. Expressing the constants of motion using the stationary tetrad, eqns. (4.6), yields no further insights, even if the extremal angular velocities of the observer are used.

Eqns. (5.2) can be solved for \dot{T} , $\dot{\phi}$ and \dot{Z} . Substituting the result of this calculation in eq. (5.1), the Lagrangian becomes solely dependent on R and \dot{R} . Using the constraint $\mathcal{L}(R, \dot{R}) = \kappa c^2$, we can solve this equation for \dot{R} . The result of this calculation is a set of differential equations of motion equivalent to the general formulation of the geodesic equations, eq. (2.20). We find the

equations of motion for both photons and massive particles in the form

$$c\dot{T} = -k_0 \frac{1-R^2}{1+R^2} - \frac{\sqrt{2}k_2}{1+R^2}, \quad (5.4a)$$

$$\dot{R}^2 = (\bar{\kappa}c^2 - k_3^2)(1+R^2) - \frac{k_2^2}{R^2} + 2\sqrt{2}k_0k_2 + k_0^2(1-R^2), \quad (5.4b)$$

$$\dot{\phi} = \frac{k_2 - \sqrt{2}R^2k_0}{R^2(1+R^2)}, \quad (5.4c)$$

$$\dot{Z} = k_3, \quad (5.4d)$$

where $\bar{\kappa} = \kappa/\tau_G^2$. Contrary to the general formulation, eqns.(4.4), this set of equations is only of first order in λ and, by far, easier to solve.

5.1.1 Geodesics for Special Initial Conditions

In this section we will present the solution of the geodesic equations for special initial conditions. We consider arbitrary timelike and lightlike geodesics starting at the origin of the coordinate system. Solely lightlike geodesics had been considered by Kajari et al. [KWSD04]. Although the general solution to the geodesic equations is introduced in the next section, the special solution is necessary to overcome the coordinate singularity in $R = 0$. In principle, we could obtain the special solution from the general solution by applying the limit $R_0 \rightarrow 0$ for the initial radial coordinate R_0 . Unfortunately, this limit is complicated to calculate.

The constants of motion, eqns. (5.3), can be simplified for geodesics starting at the origin. In particular, k_2 vanishes, and the equations of motion are simplified considerably. We arrive at

$$c\dot{T} = -k_0 \frac{1-R^2}{1+R^2}, \quad (5.5a)$$

$$\dot{R}^2 = K_p - K_m R^2, \quad (5.5b)$$

$$\dot{\phi} = \frac{-\sqrt{2}k_0}{1+R^2}, \quad (5.5c)$$

$$\dot{Z} = k_3, \quad (5.5d)$$

using the abbreviations

$$K_p = \bar{\kappa}c^2 + k_0^2 - k_3^2, \quad (5.6a)$$

$$K_m = -\bar{\kappa}c^2 + k_0^2 + k_3^2. \quad (5.6b)$$

Solving these equations is straightforward and outlined in App. B. The solution reads

$$T(\lambda) = \frac{k_0}{c} \lambda + \frac{\sqrt{2}}{c} [\phi_1(\lambda) + p_{1/2}(\lambda)] + T_0, \quad (5.7a)$$

$$R(\lambda) = \sqrt{\frac{K_p}{K_m}} \left| \sin(\sqrt{K_m} \lambda) \right|, \quad (5.7b)$$

$$\phi(\lambda) = \phi_1(\lambda) + p_{1/2}(\lambda) - p_0(\lambda) + \phi_0, \quad (5.7c)$$

$$Z(\lambda) = k_3 \lambda, \quad (5.7d)$$

with

$$p_q(\lambda) = \pi \sigma_0 \left\lfloor \frac{\sqrt{K_m}}{\pi} \lambda + q \right\rfloor, \quad (5.8a)$$

$$\phi_1(\lambda) = \arctan \left(\frac{k_0 \sqrt{2}}{\sqrt{K_m}} \tan(-\sqrt{K_m} \lambda) \right), \quad (5.8b)$$

where we used the abbreviation for the initial temporal direction σ_0 ; see eq. (5.10a). The expression $\lfloor y \rfloor$ is the mathematical floor function, which ensures the continuous differentiability of the solution, except for $R = 0$. As stated in Sec. 4.2.3, we cannot directly generate geodesics starting in ∂_ϕ -direction due to the coordinate singularity of the cylindrical coordinate system. This coordinate singularity is avoided by interpreting the integration constant ϕ_0 as the local starting direction in the (XY) -plane. For $\phi_0 = 0$, the geodesic starts in positive X -direction if the particle propagates into the future, i.e. $k_0 < 0$. On the other hand, $\phi_0 = \pi/2$ is a geodesic starting in negative Y -direction for $k_0 > 0$. Note that the special solution of the geodesic equations, eqns. (5.7), generalize the results of the work of Kajari et al. [KWSD04]. Setting $k_3 = 0$ and $\bar{\kappa} = 0$ reproduces their results regarding lightlike motion in the (XY) -subspace.

Fig. 5.1 illustrates several geodesics with non-zero initial velocity in the Z -direction. Those geodesics do not reach the Gödel horizon. However, the optical Gödel horizon is of cylindrical shape because geodesics with $u^{(3)} = \epsilon$ with $\epsilon \ll 1$ (almost planar geodesics) come arbitrarily close to the horizon for sufficiently small ϵ . These geodesics still reach any Z -value after an appropriate number of cycles. Timelike geodesics also do not reach the horizon when starting from the origin, even in the planar case. Both effects are caused by the radial solution, eq. (5.5b), where the prefactor becomes $\sqrt{K_p/K_m} < 1$ in both cases. Fig. 5.1b shows that geodesics starting at the origin do not violate causality – as measured by the observer \mathbf{O} – because $dT/d\lambda \geq 0$.

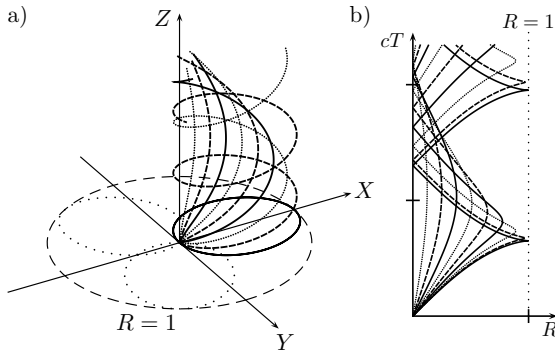


Figure 5.1: Lightlike geodesics starting at the origin. For better orientation, the Gödel horizon and three planar geodesics (compare Fig. 4.2) are provided in Fig. 5.1a. The non-planar geodesics are solid, dashed or densely dotted curves. The angle to the Z -axis between neighboring geodesics differs by 10° . Fig. 5.1b: Coordinate time as a function of radial coordinate. Non-planar geodesics do not reach the Gödel radius. Timelike geodesics are of similar shape but reach smaller maximal radial distances from the origin.

5.1.2 Geodesics for Arbitrary Initial Conditions

We will now discuss the general solution to the geodesic equations for timelike and lightlike motion. For this task, the full geodesic equations (5.4) for arbitrary initial conditions, eqns. (5.3), must be solved. Using the general solution, we will then discuss whether or not causality can be violated when traveling on geodesics.

An outline of the derivation of the general solution is provided in App. B.2. We use the abbreviations

$$B_1 = K_p + 2\sqrt{2}k_0k_2, \quad (5.9a)$$

$$B_2 = \sqrt{K_p^2/4 + K_p k_2(\sqrt{2}k_0 + k_2)}, \quad (5.9b)$$

$$C_1 = \frac{1}{2\sqrt{K_m}} \arcsin \left(\frac{K_p + 2\sqrt{2}k_0k_2 - 2R_0^2 K_m}{\sqrt{K_p^2 + 4K_p k_2(\sqrt{2}k_0 + k_2)}} \right), \quad (5.9c)$$

where the constants K_p and K_m are identical to those defined in eqns. (5.6). To distinguish between radially outgoing or incoming initial conditions as well as the initial temporal direction

of a geodesic, we use the signum functions

$$\sigma_0 = \text{sgn} \left(u_0^{(0)} \right), \quad (5.10a)$$

$$\sigma_1 = \text{sgn} \left(u_1^{(0)} \right). \quad (5.10b)$$

The integration constant of the radial equation (5.4b), namely C_1 , is determined via $R(0) = R_0$. Furthermore, we introduce the auxiliary functions

$$v(\lambda) = \sqrt{K_m}(-\sigma_1 \lambda + C_1), \quad (5.11a)$$

$$\phi_2(\lambda) = \arctan \left\{ \frac{\sigma_1}{2\sqrt{K_m}(k_2 + \sqrt{2}k_0)} \left[(2K_m + B_1) \tan(v(\lambda)) - \sqrt{B_1^2 - 4K_m k_2^2} \right] \right\}, \quad (5.11b)$$

$$\phi_3(\lambda) = \arctan \left\{ \frac{\sigma_1}{2\sqrt{K_m}k_2} \left[B_1 \tan(v(\lambda)) - \sqrt{B_1^2 - 4K_m k_2^2} \right] \right\}, \quad (5.11c)$$

$$\tilde{p}(\lambda) = \pi \sigma_1 \sigma_0 \left[\frac{\sqrt{K_m}}{\pi} (\sigma_1 \lambda - C_1) + \frac{1}{2} \right], \quad (5.11d)$$

where the latter function $\tilde{p}(\lambda)$ ensures the continuous differentiability of the solution and is analogous to eq. (5.8a) of the special solution. Finally, the analytical solutions for both arbitrary time-like and lightlike geodesics are found in the form

$$T(\lambda) = \frac{k_0}{c} \lambda + \frac{\sqrt{2}}{c} [\varphi_2(\lambda) + \tilde{p}(\lambda)] + C_3, \quad (5.12a)$$

$$R(\lambda) = \sqrt{\frac{B_1/2 - B_2 \sin(2v(\lambda))}{K_m}}, \quad (5.12b)$$

$$\phi(\lambda) = \phi_2(\lambda) - \phi_3(\lambda) + C_2, \quad (5.12c)$$

$$Z(\lambda) = k_3 \lambda + Z_0. \quad (5.12d)$$

The integration constants C_2 and C_3 can be specified by $\phi(0) = \phi_0$ and $T(0) = T_0$. If the geodesic is only directed along the local $\mathbf{e}_{(3)}$ -axis, i.e. $u_0^{(1)} = u_0^{(2)} \equiv 0$, we obtain straight lines parallel to the Z -axis, where $T(\lambda) = k_0 \lambda / c + T_0$.

In Fig. 5.2, several planar lightlike geodesics are shown. Fig. 5.2a shows the projection onto the (XY) -subspace and Figs. 5.2b-d display the correlation between radial coordinate R and coordinate time T . Most photons in Fig. 5.2 partially travel back in time. This travel through time is in most cases restricted to regions beyond the Gödel horizon and therefore not measurable by \mathbf{O} . Fig. 5.2b, in which several geodesics starting at $R_0 = 1/2$ are plotted, reveals an exception. The magnified square shows that the corresponding photon reenters the Gödel horizon before crossing it.

To investigate how far a traveler T can travel into the past of an observer \mathbf{O} , we use the general solution to the geodesic equations (5.12). We consider an arbitrary initial position and any

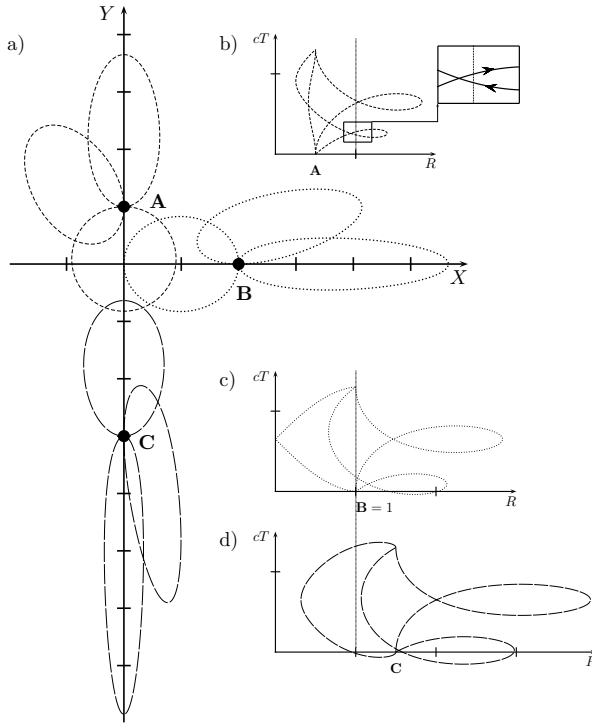


Figure 5.2: Planar lightlike geodesics resulting from the general analytical solution to the geodesic equations. In Fig. 5.2a, nine geodesics at different initial positions are shown. Position **A** is at $R_0 = 1/2$, position **B** shows geodesics starting on the horizon $R_0 = 1$, and in **C** we have $R_0 = 3/2$. In each starting point, geodesics propagate in the $+\mathbf{e}_{(1)}$ - or $\pm\mathbf{e}_{(2)}$ -direction, respectively. Non-planar geodesics show a behavior similar to the special solution, Fig. 5.1, i.e. they are smaller in radial extent. Figs. 5.2b-d show the radial coordinate of the geodesics as a relation between T and R .

initial direction within the local $\{\mathbf{e}_{(1)}, \mathbf{e}_{(2)}\}$ -subspace. It can be shown that $u_0^{(3)}$ must be zero in order to maximize time travel¹. Solving the radial solution with respect to the curve parameter,

¹Time travel can only be realized if the geodesic is partially propagating beyond the horizon. To maximize the part of the geodesic lying beyond the horizon, we must set $u_0^{(3)}$ to zero. Otherwise, the effective velocity in the (XY) -subspace is reduced and the geodesic becomes smaller in radial extent.

eq. (5.12b), results in an infinite number of solutions due to the periodicity of $R(\lambda)$. We choose the first two solutions λ_1 (where the photon or the massive particle arrives at the horizon) and λ_2 (where it reappears from beyond the horizon). Inserting λ_1 and λ_2 into the time solution, eq. (5.12a), yields a difference in coordinate time

$$\Delta T = T(\lambda_2) - T(\lambda_1). \quad (5.13)$$

Again, coordinate time and proper time of an observer \mathbf{O} are identical – except for the scaling factor r_G , cf. eq. (4.8). Fig. 5.3 shows the result of these considerations. In Fig. 5.3a, the minimal time difference Δt , eq. (5.13), is plotted for a given initial radial coordinate R_0 . We find these values by numerically searching the angle ξ_0 for fixed R_0 , where ΔT becomes minimal. The local angle between the starting direction and the $\mathbf{e}_{(1)}$ -axis is denoted as ξ_0 . The correlation between ξ_0 and R_0 is shown in Fig. 5.3b. Radii ρ_1, \dots, ρ_5 denote certain initial positions for the lightlike case, which we will now discuss. We set $\rho_1 = 1/4$, $\rho_2 = 1/2$, $\rho_3 = 1$, $\rho_4 \approx 1.4$ and $\rho_5 \approx 1.7$. Obviously, time travel is only possible for $R_0 \lesssim \rho_5$.

Fig. 5.3a reveals that a maximum time travel exists (i. e. minimal ΔT with $\Delta T < 0$) for a given initial velocity. In the time travel region ($0 \leq R_0 \leq \rho_5$ in the lightlike case), ΔT appears constant for a large region of initial radii ($\rho_1 \leq R_0 \leq \rho_4$). Unfortunately, equation (5.13) is too complicated to treat it analytically, despite its simple structure. Analytical investigations are restricted to special cases, and for a detailed analysis in general we must resort to numerical investigations. We find that ΔT is constant up to at least within 10^{-10} in the region $\rho_1 \leq R_0 \leq \rho_4$. The global minimum can be estimated with $\Delta T(R_0 = \rho_2, \xi_0)$ because $(d\Delta T(r_0 = \rho_2, \xi_0))/(d\xi_0) \equiv 0$ (exactly) for $\xi_0 = 0$. The global minimum $\Delta T_{\min}^c = \Delta T(r_0 = \rho_2, \xi_0)$ then reads

$$\begin{aligned} \Delta T_{\min}^c &= \frac{1}{2c} \left[\pi(\sqrt{2}-1) - 2\sqrt{2} \arctan\left(\frac{\sqrt{7}}{5}\right) \right] \\ &\approx -\frac{1}{c} \times 3.7645439 \times 10^{-2}. \end{aligned} \quad (5.14)$$

For timelike geodesical motion, the plateau region becomes smaller, but it is still constant up to at least within 10^{-10} . The maximum time travel on timelike geodesics, $\Delta T_{\min}(v) < \Delta T_{\min}^c$, converges to ΔT_{\min}^c for $v \rightarrow c$. A traveler \mathbf{T} needs a velocity of at least $v = v_{\min} \gtrsim 0.980172c$ (with respect to the local frame (4.8)) to travel through time. If v is smaller, $\Delta T_{\min}(v)$ is defined, but is positive. In this case, the massive particle might travel through time, but only beyond the horizon and thus is not visible to \mathbf{O} .

Fig. 5.3b shows the correlation between a certain initial radial coordinate R_0 and the local angle ξ_0 under which the geodesic must start for maximum time travel. In the region $\rho_1 \leq R_0 \leq \rho_4$, two initial directions ξ_0 exist under which the time difference ΔT_{\min}^c is found. Apart from this region, ξ_0 is unique for a given R_0 and either takes the value $\pi/2$ or $-\pi/2$. For radii $R_0 > \rho_4$, the initial direction is parallel to the $\mathbf{e}_{(2)}$ -axis of the local rest frame (eqns. (4.8)). Hence, the geodesic starts locally parallel to the motion of matter. For $R < \rho_1$, it starts in the opposite direction.

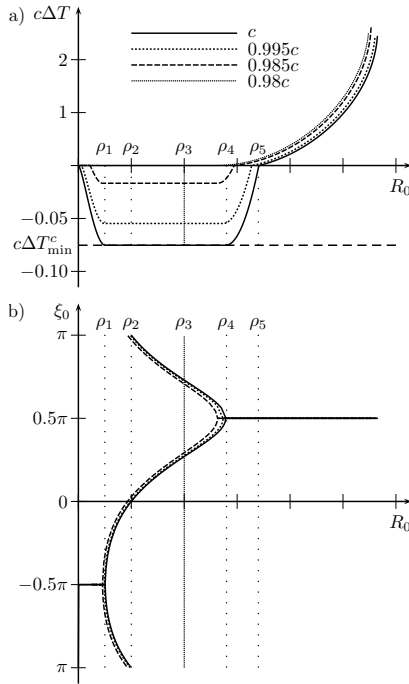


Figure 5.3: Time travel on geodesics. Fig. 5.3a shows how far a traveler T (photon or massive particle) can travel into the past for a given initial radial coordinate R_0 (maximum time travel ΔT_{\min} for fixed R_0). Fig. 5.3b explains under which direction the traveling particle must start, where ξ_0 denotes the angle to the local $\mathbf{e}_{(1)}$ -axis in the $\{\mathbf{e}_{(1)}, \mathbf{e}_{(2)}\}$ -subspace. Starting in another direction can also result in time travel, but results in $\Delta T > \Delta T_{\min}$. Note that the time axis in Fig. 5.3a is magnified by a factor of 20 for $\Delta T < 0$.

To investigate if causality is violated, we detail the results of [NST83]. The situation now discussed is illustrated in Fig. 5.4 and Fig. 5.5 from two different perspectives. In Fig. 5.4, we see a radially outgoing lightlike geodesic starting at $R_0 = 1/2$. For this geodesic, we achieve the maximum time travel, cf. eq. (5.14). Now, consider a traveler T moving extremely close to the speed of light. Then, the voyager's path is almost identical to the lightlike geodesic shown in Fig. 5.4. An observer O will see a traveler T only on those segments of the geodesic that are within the

observer's horizon. Fig. 5.2b reveals that, from O 's perspective, T reenters from beyond the horizon (B) before leaving it (A). Due to the finite speed of light, the observer will not see the traveler at the moment he reenters or leaves the horizon but a certain light travel time later. Since the Gödel horizon is of circular shape, the time span that the light takes to travel from the horizon to the origin is independent of the exact position on the horizon (as long as we restrict ourselves to the (XY) -plane). Therefore, this time span is identical for the traveler reentering the horizon as well as leaving it. We can, as a consequence, neglect the light travel time in our current considerations. Consequently, O will see T travel through time on a geodesical path and this effect is not a mere consequence of the finiteness of the speed of light.

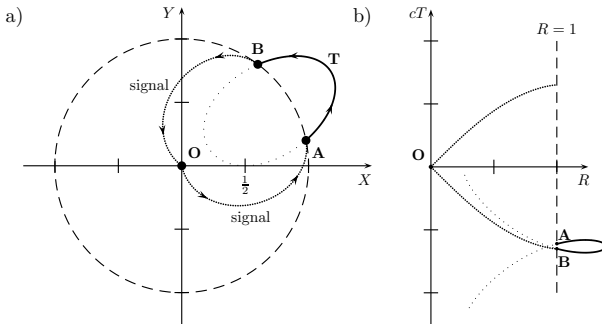


Figure 5.4: Testing if causality can be violated on geodesics. A traveler T moves partially beyond the horizon of an observer O (Fig. 5.4a). He leaves the horizon passing A and reenters it passing B . The observer B sends a light pulse to O , informing him of the arrival of T . Then, O signals A this information. If this information arrived *before* T passes the horizon, B could stop the traveler, resulting in a paradox. Fig. 5.4b reveals that no causality violation arises because the information arrives in the future light cone of the event “ T passes A ”. Note that we use a lightlike geodesic for the path of T as the limiting case $v \rightarrow c$.

After discovering that time travel on geodesics is possible, we now discuss whether or not causality is violated. The relevant geodesic segment of T beyond the horizon of the geodesic is not a CTC because the particle crosses the horizon at different angular coordinates and the path is therefore not closed. Although the cause and the effect – T must leave the horizon before reentering it – appear reversed, we do not have a causality violation in the classical meaning. A violation of causality would only arise if the effect (information about the reentered traveler) could be transported to the local past light cone of the cause (event of the traveler leaving the horizon). In other words: O must provide the information about the time travel (from his point

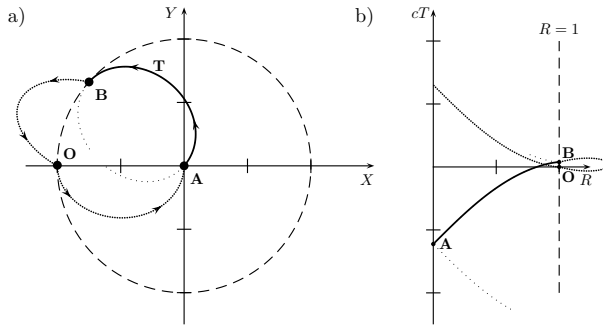


Figure 5.5: Isometrically transporting A to the spatial origin yields the situation from the point of view of observer A (Fig. 5.5a). Both O and B are located on the horizon of A . The traveler's motion is restricted to the interior of *this* horizon and no time travel arises. From this perspective, the signal from B to O travels back in time with respect to A (Fig. 5.5b).

of view) to A *before* T crosses the horizon in the “first” place. Therefore, B must signal O the arrival of the traveler and O then must send this information to A . Finally, A must receive this signal *before* the traveler passes his position. Only then can he decide to stop the traveler and we would end in a paradox situation, where causality is violated.

Although a lightlike geodesic is depicted, we can still use this image as the limiting case $v \rightarrow c$. It can be easily estimated, using $\lambda = \pi/(2\sqrt{K_m})$ in eq. (5.7a), that a signal from the origin to the horizon would need a time span (measured by O) of

$$\Delta T = \frac{\pi}{c} \left(\frac{\sqrt{2}-1}{2} \right) \approx \frac{1}{c} \times 1.30129. \tag{5.15}$$

Signaling back and forth doubles this time span. It is by far longer than the absolute value of the maximum time travel, eq. (5.14). The signal of the reentering traveler therefore reaches A in the future light cone in the event of T crossing the horizon, cf. Fig. 5.4b. Therefore, causality is conserved although the traveler travels partially back in time.

From the perspectives of A and B , the traveler behaves causally normal because their positions are both located on the same geodesic and, therefore, this geodesic is restricted entirely to the respective horizon of each observer. In Fig. 5.5, the experiment is shown with reference to A . An isometric transport of B to the origin would result in an equivalent characterization of the situation. Note that we already utilized solutions of the equations of isometric transport for points, cf. Sec. 5.2.1, in order to generate Fig. 5.5. Both observers will consequently see the traveler at all

times and the traveler will never move back in time. However, one of the signals from or to \mathbf{O} will now partially travel back in time with respect to the observer now resting at the origin. Therefore, for each of the three observers, exactly one segment of the three geodesics – the traveler’s path or one of the geodesics transporting signals – describes travel back through time. Since we regard the limit $v \rightarrow c$ for the traveler’s velocity, each travel through time (for the respective observer) is equal to the maximum time travel on geodesics, eq. (5.14).

In any case, the traveler T will not travel through time regarding his *own* rest frame. His proper time τ evolves unaffected from the considerations and measurements done by \mathbf{O} . Due to the homogeneity of the spacetime, the traveler T always rests at the center of “his” Gödel horizon.

5.2 Isometric Transport

In this section, we derive analytical expressions for finite isometric transformations for all five Killing vector fields of Gödel’s universe.

5.2.1 Isometric Transport of Points

As detailed in Sec. 2.4, we must solve eq. (2.31) in order to calculate the integral lines of isometric displacement. For the trivial Killing vector fields, eqns. (4.19a), we directly obtain straight lines along T , ϕ and Z in cylindrical coordinates. The solution to eqns. (4.19b) and (4.19c) is more difficult to derive. We discuss the derivation of the solution in App. C.

The complete solution to the equations of isometric transport (2.31) for the Killing vector field ξ_1^μ (eq. (4.19b)) and ξ_4^μ (eq. (4.19c)) reads

$$T_1(\eta) = \sigma \frac{\sqrt{2}}{c} \arctan \left(\frac{D_2 e^\eta + \frac{1}{4}}{\sqrt{D_1 D_2 - \frac{1}{16}}} \right) + D_3, \quad (5.16a)$$

$$R_1(\eta) = \sqrt{D_1 e^{-\eta} + D_2 e^\eta - \frac{1}{2}}, \quad (5.16b)$$

$$\phi_1(\eta) = \sigma \arcsin \left(\frac{-D_1 e^{-\eta} + D_2 e^\eta}{R_1(\eta) \sqrt{R_1^2(\eta) + 1}} \right) + \frac{1 - \sigma}{2} \pi, \quad (5.16c)$$

$$Z_1(\eta) = D_4, \quad (5.16d)$$

and

$$T_4(\eta) = T_1(\eta), \quad R_4(\eta) = R_1(\eta), \quad Z_4(\eta) = Z_1(\eta), \quad (5.17a)$$

$$\phi_4(\eta) = \phi_1(\eta) + \pi/2. \quad (5.17b)$$

The lower indices in the solution denote the connection to the Killing vectors ξ_1^μ and ξ_4^μ , respectively. The parameter σ distinguishes whether the starting angle ϕ_0 is within the right or the left half plane and reads

$$\sigma = \begin{cases} +1, & \text{if } \phi_0 \in \text{right half plane,} \\ -1, & \text{if } \phi_0 \in \text{left half plane.} \end{cases} \quad (5.18)$$

If the starting angle ϕ_0 is $\pm\pi/2$, i. e. the starting point is on the Y -axis, both $T_i(\eta)$ and $\phi_i(\eta)$ become constant. The integration constants arrive at

$$D_1 = \frac{1}{2} \left(R_0^2 + \frac{1}{2} - R_0 \sqrt{R_0^2 + 1} \sin \phi_0 \right), \quad (5.19a)$$

$$D_2 = \frac{1}{2} \left(R_0^2 + \frac{1}{2} + R_0 \sqrt{R_0^2 + 1} \sin \phi_0 \right), \quad (5.19b)$$

$$D_3 = T_0 - \sigma \frac{\sqrt{2}}{c} \arctan \left(\frac{D_2 + \frac{1}{4}}{\sqrt{D_1 D_2 - \frac{1}{16}}} \right), \quad (5.19c)$$

$$D_4 = Z_0, \quad (5.19d)$$

where R_0 and ϕ_0 are the initial radial coordinate and initial angle, respectively. In Fig. 5.6 and Fig. 5.7, the lines of finite isometric displacements are shown for the Killing vector field ξ_1^μ of the Gödel metric.

5.2.2 Isometric Transport of Vectors

So far we only know how to apply finite isometric transformation to points in Gödel's universe. To transport vectors isometrically, we must solve eq. (2.32). The solution to this equation is an isometrically transported arbitrary vector u^μ along the lines of finite isometric displacements. For the trivial Killing vector fields (4.19a), we have $du^\mu/d\eta \equiv 0$. Hence, vectors remain unchanged when they are transported along these three fields. However, the analysis of a transport along the non-trivial vector fields, eqns. (4.19b) and (4.19c), is more interesting. The differential equations for the Killing vector field (4.19b), using eq. (4.20), read

$$\frac{du^T}{d\eta} = \frac{\cos \phi}{\sqrt{2cq^3(R)}} u^R - \frac{R \sin \phi}{\sqrt{2cq(R)}} u^\phi, \quad (5.20a)$$

$$\frac{du^R}{d\eta} = \frac{R \sin \phi}{2q(R)} u^R + \frac{1}{2} q(r) \cos \phi u^\phi, \quad (5.20b)$$

$$\frac{du^\phi}{d\eta} = -\frac{\cos \phi}{2R^2 q^3(R)} u^R - \frac{\left(\frac{1}{2} + R^2\right) \sin \phi}{Rq(R)} u^\phi, \quad (5.20c)$$

$$\frac{du^Z}{d\eta} = 0. \quad (5.20d)$$

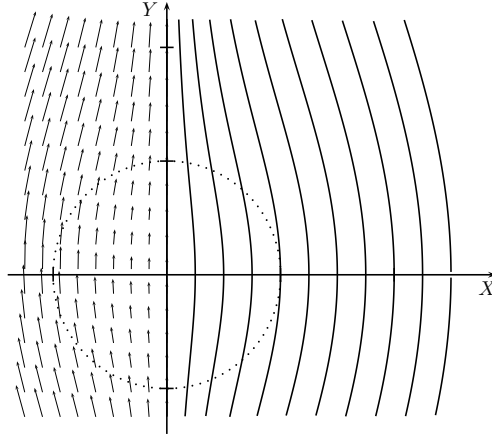


Figure 5.6: Projection of Killing vector field ξ_1^μ onto the (XY) -plane ($T = \text{const.}$ and $Z = \text{const.}$ in Cartesian coordinates). The left half-plane shows the vector field itself, and the right half-plane illustrates the integral curves of finite isometric displacements along ξ_1^μ . The Gödel horizon appears as the dotted circle.

As detailed in App. C.2, the solution with respect to the local tetrad (eqns. (4.8)) is

$$u^{(0)}(\eta) = u_0^{(0)}, \quad (5.21a)$$

$$u^{(1)}(\eta) = \cos(F(\eta))u_0^{(1)} - \sin(F(\eta))u_0^{(2)}, \quad (5.21b)$$

$$u^{(2)}(\eta) = \sin(F(\eta))u_0^{(1)} + \cos(F(\eta))u_0^{(2)}, \quad (5.21c)$$

$$u^{(3)}(\eta) = u_0^{(3)}, \quad (5.21d)$$

where, using eq. (5.18), we have

$$F(\eta) = \sigma [\arctan(L_+(\eta)) - \arctan(L_-(\eta)) + D_5], \quad (5.22a)$$

$$D_5 = \arctan(L_-(0)) - \arctan(L_+(0)), \quad (5.22b)$$

$$L_\pm(\eta) = \frac{D_2 e^\eta \pm \frac{1}{4}}{\sqrt{D_1 D_2 - \frac{1}{16}}}. \quad (5.22c)$$

An arbitrary vector is rotated around $e_{(3)}$ by an angle of $F(\eta)$ with respect to the local rest frame at the destination point $x_1^\mu(\eta)$, if isometrically transformed along the Killing vector field ξ_1^μ . The solution for the vector field ξ_4^μ is now trivial. As this transformation only yields an angular offset

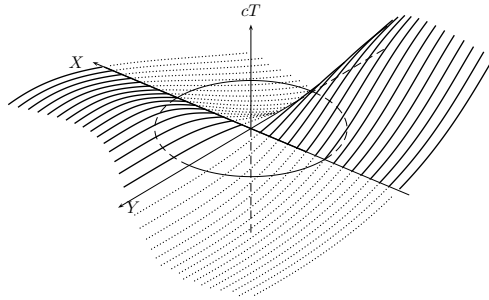


Figure 5.7: Isometrically transporting points on the X -axis along the Killing vector field ξ_1^μ , showing the lines of finite isometric transport. Solid lines indicate transport to positive T -values; dotted lines illustrate negative time values. The Gödel radius appears as the partly dashed circle.

of $\Delta\phi = \pi/2$, eq. (5.17b), the solution to the equations of isometric transport of vectors (2.32) is identical to the solution for the vector field ξ_1^μ , eq. (5.21). With these results, we are able to map the special solution of the geodesic equations, Sec. 5.1.1, onto the general solution as presented in Sec. 5.1.2 by means of isometrically transforming initial conditions. Note that $F(\eta) = 0$ if $\phi_0 = \pm\pi/2$ and, therefore, vectors are not rotated when they are transported along the Y -axis.

5.3 Mapping of Arbitrary Curves

In this section, we will use finite isometric transformations to map several classes of curves. In this way, the general solution to the geodesic equations will be reproduced, the Gödel horizon for different observers will be calculated, and a non-circular class of CTCs will be generated.

5.3.1 Mapping of Geodesics

With the results of the previous section, we are able to generate the solutions to the geodesic equations, eqns. (5.12), using geodesics starting at the origin² and finite isometric transformations.

Consider an arbitrary initial position x_0^μ and any lightlike or timelike local initial direction $u_0^{(a)}$. First, we rotate these initial conditions around the z -axis using the Killing vector field ξ_2^μ until

²More precisely, we only need geodesics with $\phi_0 = Z_0 = T_0 = 0$ and arbitrary k_3 in eqns. (5.7) to generate any geodesic. Due to the obvious symmetries of Gödel's universe, manifested in the trivial Killing vectors ξ_0, ξ_2 and ξ_3 (eqns. (4.19a)), all geodesics starting at the origin can be created using this subset.

$\phi = \pi/2$. This step is necessary because only then the initial position can be isometrically translated to the origin using ξ_1^μ (compare Fig. 5.6). After this rotation by $\Delta\phi = \pi/2 - x_0^\phi$, we use the solution to the equations of isometric transport for ξ_1^μ , eqns. (5.16), to reach $R = 0$. Solving eq. (5.16b) for η provides

$$\eta_1 = -\ln\left(2R_0^2 + 1 + 2R_0\sqrt{R_0^2 + 1}\right). \quad (5.23)$$

Finally, we translate the resulting point to $Z = 0$ using the Killing vector ξ_3^μ . The isometrically transformed initial direction is then found by inserting η_1 into eqns. (5.21). In this way, the local initial direction is rotated by an angle $\alpha = F(\eta_1)$, eq. (5.22a).

The initial conditions, $\tilde{x}_0^\mu = (x_0^T, 0, \pi/2, 0)$ and the rotated local direction $u^{(a)}(\eta_1) = \tilde{u}_0^{(a)}$, are then inserted into the special solution of the geodesic equations, eqns. (5.7). The resulting geodesic is then isometrically transformed back using the above transformations inverted and in reverse order. Inserting these results in the appropriate equations, finite isometric transformations for points and vectors as well as the special solution to the geodesic equations reproduces the general solution of Sec. 5.1.2.

Obviously, general solutions of the geodesic equations can be mapped onto other general solutions as well. Therefore, we consider arbitrary initial conditions as described above and a desired initial position x_1^μ . The component x_0^μ is rotated around the Z -axis until $\varphi = \pi/2$ is reached, isometrically translated along ξ_1^μ to map onto the desired radial coordinate $R = x_1^R$, then rotated to the destination angular coordinate $\phi = x_1^\phi$ and finally isometrically translated in time and the Z -coordinate to arrive at x_1^μ . Again, the initial direction is only rotated due to the Killing vector field ξ_1^μ by an angle $F(\tilde{\eta}_1)$, where

$$\tilde{\eta}_1 = \ln\left(\frac{2R_1^2 + 1 + 2R_1\sqrt{R_1^2 + 1}}{2R_0^2 + 1 + 2R_0\sqrt{R_0^2 + 1}}\right). \quad (5.24)$$

Numerical implementations of this procedure and the general solution to the geodesic equations are identical.

5.3.2 Mapping of the Gödel Horizon

Since Gödel's universe is homogeneous, every observer O, A or B can legitimately declare his position as the origin of a coordinate system, where the line element takes the form of eq. (4.5). These origins yield equivalent formulations of the Gödel horizon. Fig. 5.2 indicates how these horizons are shaped.

The Gödel horizon around any point is the convex hull of all lightlike geodesics starting there. Furthermore, the horizon itself is a closed null curve (CNC) because $ds^2 = 0$ along the Gödel radius. We could use the general solution to the geodesic equations to calculate the exact shape. However, the usage of finite isometric transformations is by far more elegant.

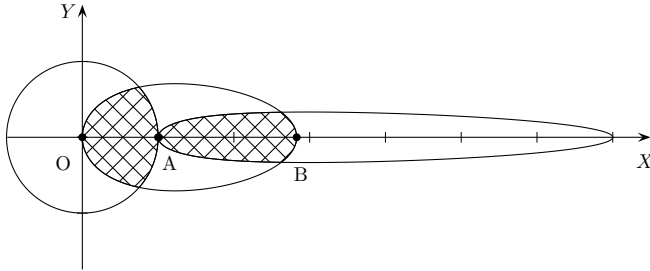


Figure 5.8: Three horizons of three different observers O , A and B . Crosshatched regions mark common causality regions. Note that O and B do not share a common region.

Due to the homogeneity of the spacetime, each observer states that “his” horizon is circular within the (XY) -plane. Fig. 5.8 shows three different horizons. Each horizon is depicted referring to the coordinate system of O . A results from an isometric transport of O along ζ_4^μ with $\eta = \eta_1$, eq. (5.23), and using $R_0 = 1$. Observer B is subject to a similar transformation, where $\eta = 2\eta_1$.

We find that O and A share a common causality region marked by the left crosshatched area. A traveler T moving arbitrarily in this region will not travel through time from both observers’ perspectives. A and B share a similar region, but the horizons O and B are merely tangential to each other. Therefore, motion restricted to the horizon around O is not visible for B . Furthermore, only A is jointly visible to O as well as B . Note that each horizon is circular for the corresponding observer and only appears deformed due to the distortion caused by the chosen set of coordinates.

5.3.3 Mapping of Worldlines and Generation of CTCs

In this section we will discuss how worldlines are isometrically transformed. This will be used to generate interesting closed timelike curves (CTCs) from a circular set of worldlines, where $T(\lambda)$ is constant.

Circular CTCs

In Sec. 4.2.6, we reviewed that the light cones beyond the Gödel horizon intersect the plane of constant coordinate time. A voyager must propagate into his own local future, but he can travel into the past of an observer located at the origin of the coordinate system (compare Fig. 4.5b,

where a complex flight curve is shown). The simplest forms of CTCs are circles with constant coordinate time

$$x^T = \text{const}, x^R = R_{\text{ctc}} = \text{const}, x^\phi = \omega\tau, x^Z = 0 \rightarrow u^T = u^R = u^Z = 0, \quad (5.25)$$

where $R_{\text{ctc}} \geq 1$. We generate CTCs when we set u^T to zero because $x^T = \text{const}$. To find the corresponding direction in the local frame of reference, eqns. (4.8), we transform a local vector to the coordinate representation using eqns. (A.23):

$$u^T = \frac{1}{r_G c} \left(u^{(0)} - \frac{\sqrt{2}R}{\sqrt{1+R^2}} u^{(2)} \right), \quad (5.26a)$$

$$u^R = \frac{1}{r_G} \sqrt{1+R^2} u^{(1)}, \quad (5.26b)$$

$$u^\phi = \frac{1}{r_G R} \frac{1}{\sqrt{1+R^2}} u^{(2)}, \quad (5.26c)$$

$$u^Z = \frac{1}{r_G} u^{(3)}. \quad (5.26d)$$

The circular CTCs are then constructed after using $u^T = u^R = u^Z = 0$ in the equations above. This results in a local timelike four-velocity $u^{(a)} = (\gamma c, 0, \gamma v_\phi, 0)$, where the spatial velocity is given by

$$v_\phi = c \sqrt{\frac{1}{2} [(1/R_{\text{ctc}})^2 + 1]} \leq c, \quad (5.27)$$

and the non-zero component of the four-velocity u^μ is

$$u^\phi = \omega = \frac{c}{r_G R_{\text{ctc}}} \frac{1}{\sqrt{R_{\text{ctc}}^2 - 1}}. \quad (5.28)$$

The coordinate radius R_{ctc} is given by eq. (5.27) and reads

$$R_{\text{ctc}} = \sqrt{\frac{1}{2(v_\phi/c)^2 - 1}}. \quad (5.29)$$

The minimal radius for a circular closed timelike curve is given by $R_{\text{ctc}} = 1$ in scaled coordinates and is obtained in the lightlike limit $v_\phi \rightarrow c$. For a lower local velocity, the radius R_{ctc} increases, and in the limit $R_{\text{ctc}} \rightarrow \infty$, a local velocity of $v_\phi = c/\sqrt{2}$ is necessary to create a closed timelike curve. Inserting the four-velocity into the Lagrangian, eq. (5.1), proves that this four-velocity is indeed a timelike vector. The four-acceleration is calculated using eq. (2.25), and the only non-zero component turns out to be

$$a^R = \omega^2 R_{\text{ctc}} \{ [R_{\text{ctc}}^2 + 1][2R_{\text{ctc}}^2 - 1] \}, \quad (5.30)$$

which is positive $\forall R_{\text{ctc}} > 1$. As a consequence, the traveler must accelerate radially outwards³ to sustain the circular motion on the CTC. Note that only one angular velocity ω exists for each radius $R_{\text{ctc}} > 1$ to form a CTC. Other values of ω generate possible but non-closed worldlines. These worldlines are not causality violating and are comparable to the helix segment of the CTC in Fig. 4.5b. Using the equations above, we calculate the Fermi-Walker transport of an arbitrary vector X^μ , eq. (2.27), and obtain the coupled system of linear differential equations

$$\dot{X}^T(\tau) = -X^R(\lambda) \frac{\sqrt{2}R_{\text{ctc}}^2}{r_G \sqrt{R_{\text{ctc}}^2 - 1}(R_{\text{ctc}}^2 + 1)}, \quad (5.31a)$$

$$\dot{X}^R(\tau) = X^T(\lambda) \frac{\sqrt{2}c^2 R_{\text{ctc}}^2 (R_{\text{ctc}}^2 + 1)}{r_G (R_{\text{ctc}}^2 - 1)^{3/2}}, \quad (5.31b)$$

$$\dot{X}^\phi(\tau) = X^R(\lambda) \frac{2cR_{\text{ctc}}^2}{r_G (R_{\text{ctc}}^2 - 1)^{3/2} (R_{\text{ctc}}^2 + 1)}, \quad (5.31c)$$

$$\dot{X}^Z(\tau) = 0. \quad (5.31d)$$

With the abbreviations

$$B_3 = -\frac{\sqrt{R_{\text{ctc}}^2 - 1}}{c(R_{\text{ctc}}^2 + 1)}, \quad (5.32a)$$

$$B_4 = \frac{\sqrt{2}}{(R_{\text{ctc}}^2 + 1)\sqrt{R_{\text{ctc}}^2 - 1}}, \quad (5.32b)$$

the integration arrives at

$$X^t(\tau) = B_3 [E_2 \cos(v\tau) - E_1 \sin(v\tau)], \quad (5.33a)$$

$$X^r(\tau) = E_2 \sin(v\tau) + E_1 \cos(v\tau), \quad (5.33b)$$

$$X^\varphi(\tau) = B_4 [E_2 \cos(v\tau) - E_1 \sin(v\tau)] + E_3, \quad (5.33c)$$

$$X^z(\tau) = E_3 \lambda, \quad (5.33d)$$

where

$$v = \frac{\sqrt{2}cR_{\text{ctc}}^2}{r_G(1 - R_{\text{ctc}}^2)}. \quad (5.34)$$

Before we determine the integration constants E_i , we formulate this solution with regard to a local comoving frame. First, eqns. (5.33) are expressed using the local rest frame, eqns. (4.8), denoted as $X^{(a)}$. To transform this intermediate result into a local comoving frame, we must only apply a Lorentz boost. Obviously, the traveler T is moving in the $e_{(2)}$ -direction of the rest frame. Hence, to transform the Fermi-Walker transported vector into the comoving frame of the

³with respect to the chosen cylindrical coordinates

traveler T , we apply a Lorentz boost to $X^{(a)}(\tau)$ in the same direction with $\beta = v_\phi/c$ (compare eq. (5.27)). To express the fact that the comoving frame results from a Lorentz transformation $\Lambda_{(a)(b)}$ of the local rest frame, we designate the resulting vector as $X^{(a\lambda)}$. Then, the local initial conditions $X^{(a\lambda)}(0) = X_0^{(a\lambda)}$ fix the integration constants. The result of this calculation is

$$X^{(0\lambda)}(\tau) = X_0^{(0\lambda)}, \quad (5.35a)$$

$$X^{(1\lambda)}(\tau) = X_0^{(1\lambda)} \cos(v\tau) + X_0^{(2\lambda)} \sin(v\tau), \quad (5.35b)$$

$$X^{(2\lambda)}(\tau) = -X_0^{(1\lambda)} \sin(v\tau) + X_0^{(2\lambda)} \cos(v\tau), \quad (5.35c)$$

$$X^{(3\lambda)}(\tau) = X_0^{(3\lambda)}. \quad (5.35d)$$

Now, we consider the special case $X_0^{(a\lambda)} = (0, 1, 0, 0)$ and calculate the rotation angle α after one orbit. After one period, i. e. $\omega\tau_o = 2\pi$, we find that

$$\tau_o = \frac{2\pi r_G R_{\text{ctc}}}{c} \sqrt{R_{\text{ctc}}^2 - 1}, \quad (5.36a)$$

$$\alpha = v\tau_o = -\frac{2\sqrt{2}\pi R_{\text{ctc}}^3}{\sqrt{R_{\text{ctc}}^2 - 1}}, \quad (5.36b)$$

where we have used ω from eq. (5.28). In the limit $R_{\text{ctc}} \rightarrow 1$, we find a closed null curve (CNC), where the spatial components describe the Gödel horizon. The local velocity of the corresponding photon, eq. (5.27), is c (as expected) and the proper time τ_o , eq. (5.36a), converges to zero. However, a photon must be forced on a circular orbit because this curve does not represent a geodesic. This could be achieved, for example, using an appropriate arrangement of mirrors.

Mapping of CTCs

The circular CTCs can now be mapped onto CTCs which pass through the origin. We transport a circular CTC along the Killing vector field ξ_4^μ , eq. (4.19c). Using an approach similar to the mapping of geodesics, Sec. 5.3.1, we calculate the isometric transformation of the point $x^\mu = (T_0, R_{\text{ctc}}, \pi, 0)$ to the origin, arriving at the same curve parameter η_1 , eq. (5.23), which is now used in the solution to the equations of transport for ξ_4^μ , eqns. (5.17). The same transformation is applied to each point of the worldline. The resulting behavior can be anticipated when analyzing Fig. 5.6 and Fig. 5.7. The distance of lines of finite isometric transport, Fig. 5.6, decreases for larger distances to the origin. Thus, we expect that the transformed circle must appear deformed, resulting in a smaller radius of curvature for those parts of the worldline now distant from the origin. Fig. 5.7 reveals that the coordinate time values of one semi-cycle will be pushed to negative values while the other semi-cycle will experience a shift to positive values. This expected qualitative behavior is verified by the results shown in Figs. 5.9 and 5.10.

Apparently, the results of the previous section, which have been formulated regarding a local frame, are still valid.

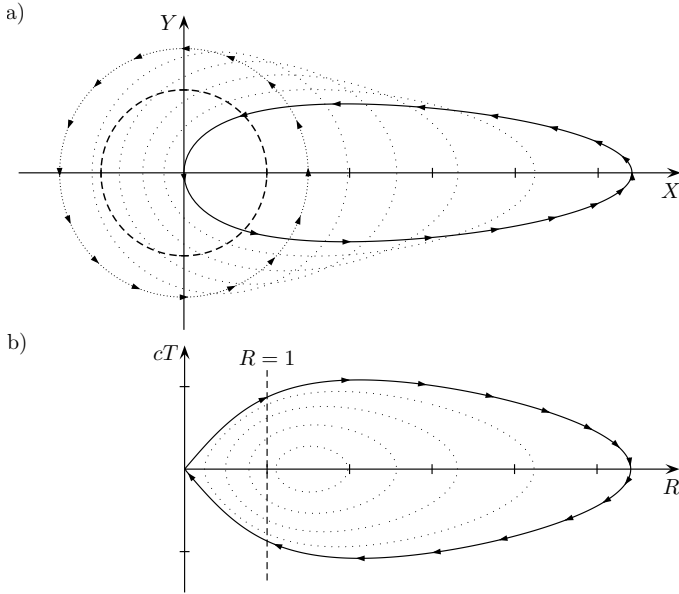


Figure 5.9: Isometrically transporting a circular CTC of radius $R_{\text{ctc}} = 3/2$ (densely dotted circle) along the Killing vector field ξ_4^μ in positive X -direction. In Fig. 5.9a, sparsely dotted curves represent the isometric transport and each of these dotted curves is a CTC itself. The arrowheads indicate the traveler's flight direction. The resulting CTC (solid curve) represents a traveler starting at the origin, moving beyond the Gödel horizon – indicated as a dashed circle in Fig. 5.9a or a dashed line in Fig. 5.9b – and returning to the origin at the coordinate time of departure. Fig. 5.9b: Observer time as a function of the radial coordinate of the CTC. Note that coordinate time coincides with the proper time of a resting observer \mathcal{O} (scaled by a factor of τ_G). Therefore, the traveler \mathcal{T} is moving back in time with respect to \mathcal{O} . Also note that $dT/d\tau > 0$ as long as $R < 1$.

5.4 Living in Gödel's Universe – Estimates on the Size of Physical Properties

Out of curiosity, we provide estimates of characteristics of the Gödel universe taking the following into account: a) estimates for the cosmological constant and b) best-fit approximations from the *WMAP* data.

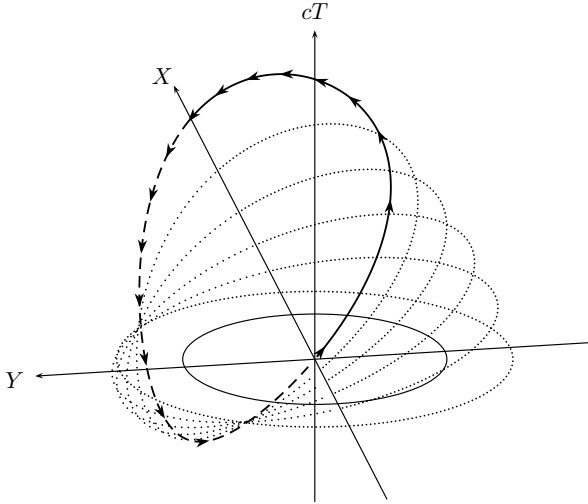


Figure 5.10: Three-dimensional presentation of Fig. 5.9a. Isometrically transporting a circular CTC does not only result in a different spatial appearance but affects the time coordinate as well. Dashed or sparsely dotted curve segments are below the (XY) -plane; solid or densely dotted curve parts have $T \geq 0$. The Gödel horizon is indicated by a solid circle.

5.4.1 Gödel's Universe and the Cosmological Constant

The cosmological constant Λ is limited to

$$|\Lambda| < 10^{-51} \frac{1}{\text{m}^2} \quad (5.37)$$

due to cosmological observations [Rin06]. In Gödel's universe, the cosmological constant is related to the Ricci scalar R , cf. [Gö49], and reads

$$\Lambda = \frac{R}{2} = -\frac{2}{r_G^2}. \quad (5.38)$$

Note that Gödel [Gö49] used the field equations in the form $G_{\mu\nu} = \sigma T_{\mu\nu} + \Lambda g_{\mu\nu}$, whereas we use $G_{\mu\nu} + \Lambda g_{\mu\nu} = \sigma T_{\mu\nu}$. This convention results in a different sign for the cosmological constant. Eq. (5.38) determines the minimal Gödel radius, which is

$$r_G \approx 4.47 \times 10^{25} \text{m} \approx 0.35 r_{\text{univ}}, \quad (5.39)$$

where we set $r_{\text{univ}} = 13.7 \times 10^9$ ly. The maximum time travel on lightlike geodesics, eq. (5.14), is

$$\Delta T_{\text{min}}^c \approx -1.78 \times 10^8 \text{ a.} \quad (5.40)$$

For circular CTCs with a radius $R_{\text{ctc}} = 2$ (in scaled coordinates) and eq. (5.36a), we obtain a proper time

$$\tau_o \approx 1.02 \times 10^{11} \text{ a} \quad (5.41)$$

for the round trip, where the local tetrad is rotated by an angle of

$$\alpha \approx -6.532 \times 360^\circ \quad (5.42)$$

due to the Fermi-Walker transport, eq. (5.36b). The local velocity, eq. (5.27), is

$$v_\phi \approx 0.79 c. \quad (5.43)$$

5.4.2 Gödel's Universe and Best-Fit WMAP Data

Barrow et al. [BJS85] derived upper limits for the rotation of the universe. Following the notation of that paper, Jaffe et al. [JBE*05] and Bridges et al. [BMLH07, BMC*08] investigated how Bianchi VII_h models can be fitted to the first-year and three-year WMAP data. They found that the best-fit approximation is achieved when using a very small rotation rate ω of the universe of roughly

$$\omega \approx 5 \times 10^{-10} H_0, \quad (5.44)$$

where H_0 is the Hubble constant. We take $H_0 \approx 75$ (km/s)/(Mpc) and identify ω with the rotation scalar Ω_G (compare eq. (4.3)). Solving for the Gödel radius results in

$$r_G \approx 2.69 \times 10^9 r_{\text{univ}}. \quad (5.45)$$

The values corresponding to the results of the last section read

$$\Delta T_{\text{min}}^c \approx 1.3877 \times 10^{18} \text{ a,} \quad (5.46a)$$

$$\tau_o \approx 8.03 \times 10^{20} \text{ a,} \quad (5.46b)$$

while v_ϕ and α remain unchanged.

THE GÖDEL ENGINE

“Even the best planning is not so omniscient as to get it right the first time.” — FREDERICK PHILLIPS BROOKS, JR.

In Sec. 3.2.4, we discussed the advantages and drawbacks of interactive visualization techniques using modern graphics hardware. Unfortunately, all interactive methods for an egocentric visualization in general relativity handle only special cases: An approach is usually restricted to a single spacetime and specific arrangements of objects in a scene. Another technique is to interactively postprocess an arbitrary general relativistic scene using a prerendered dataset [GB08].

In this chapter, we describe our interactive visualization approach, the “GÖDEL ENGINE”. We introduced this rendering engine for the Gödel universe in our previous work; see [GMDW09]. However, our program was rewritten from scratch. We only reused core code fragments and adapted them to the scaled coordinate system, eqns. (4.4) and (4.5). The reason behind this effort is that not all analytical expressions – such as the expressions on the isometric transport for points and vectors (Sec. 5.2) – had been available at the time of publication of the paper. New results would have been tedious or impossible to incorporate into the old version. The following sections detail the processing of our analytical solutions as well as their implementation.

The primary objective of our approach is to visualize optical effects of quasistatic objects in the Gödel spacetime in the most flexible way. First, we implemented a variety of different objects such as spheres or rectangles. To overcome the limitation to primitives, we also made *geometry images* [GGH02] available. This image format stores arbitrary geometrical shapes as RGB data in an image file. In this way, we are able to visualize complex objects within the Gödel spacetime. We also focus on the performance of our approach. Due to the potential of modern graphics hardware, see Sec. 3.2.2 and Sec. 3.2.3, we are able to execute most of the computations on the GPU and, by this means, minimize the comparably slow data communication between CPU and GPU. This object-based technique, cf. Sec. 3.2.2, is the first published work enabling arbitrary observer and object positions as well as the inclusion of an interactive local illumination model.

6.1 Appearance of Objects

Before discussing the implementation details of the GÖDEL ENGINE, we detail the basic optical appearance of objects in the Gödel universe. This discussion is necessary at this point because the GÖDEL ENGINE is adapted to several prerequisites resulting from the properties of geometrical optics in the Gödel spacetime.

We also provide important definitions to distinguish the multitude of visual representations of a single object. Therefore, we consider an arbitrary observer who is resting with respect to the rotating matter. Due to the homogeneity of the Gödel universe, such an observer can interpret his location in the spacetime as the origin of a coordinate system and the line element takes the form of Gödel's metric; see Sec. 4.2.1.

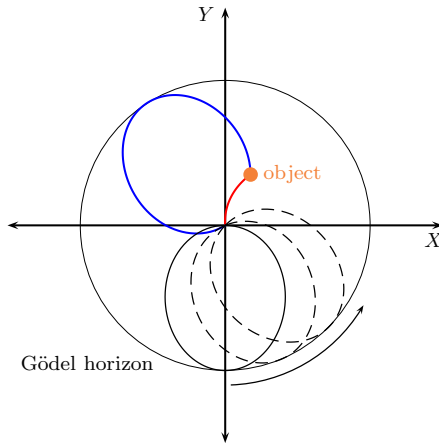


Figure 6.1: Geodesics in the (XY) -plane. The example null geodesics and the rotational symmetry of the spacetime illustrate the existence of an optical horizon. An object (orange) can be seen twice.

In Fig. 6.1, the paths of light rays starting at the origin are depicted as in Fig. 5.1. Again, the Gödel radius at $R = r/r_G = 1$ marks the maximum radial distance that an object can reach before it disappears from the point of view of the observer, who is located at the origin. Consequently, the Gödel horizon is an optical horizon. Objects beyond the Gödel horizon are simply not visible from the origin of this coordinate system. If an entity is located within the Gödel horizon it will be visible at least twice, as illustrated in Fig. 6.1, because two possible paths exist for light to travel from an object to the observer located at the origin.

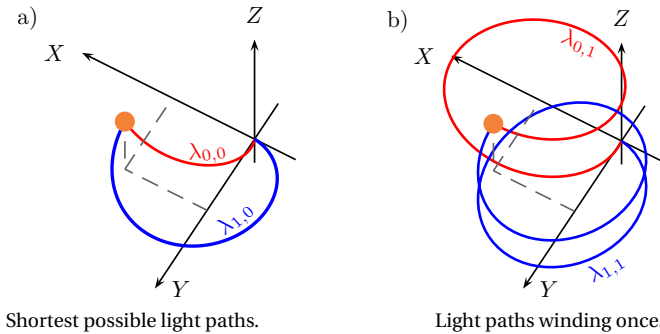


Figure 6.2: Light paths from a small sphere (orange) to an observer located at the origin. An infinite number of possible light paths exists with any number of windings. The indices (i, n) of a curve parameter λ serve to distinguish the different geodesics. Fig. 6.2a) shows the two curves without a full winding, whereas Fig. 6.2b) depicts the interconnecting light rays with one winding along the helix-shaped geodesics. In Sec. 6.3.1, these curve pairs are used to define image pairs. The number of full windings defines the order of the image.

By pushing the entity to a position with $Z \neq 0$ within the horizon, it will be visible infinitely often (Fig. 6.2): An infinite number of – potentially very narrow – helix-like paths exists and each of these curves connect the object to the observer. Fig. 6.3 shows an example rendering of a small sphere located above the (XY) -plane and within the Gödel horizon. We denote a physical entity within the Gödel universe as an **object** and the multitude of its visible appearances as **object images** or **images**. In Fig. 6.2, we see that there are always two images of the same order. The first index in $\lambda_{i,n}$ denotes whether the geodesic is on the outbound part of the geodesic ($i = 0$) or on the incoming part, which has already reached the horizon ($i = 1$) within this cycle. The **order** n of an image is the number of full windings the **interconnecting geodesic** possesses. We distinguish the images of the order n with the terms **even** for $i = 0$ and **odd** for $i = 1$. If an object is **illuminated** by a point light source, the corresponding images from the light source’s “point of view” are denoted as **light images**.

6.2 Mathematical Preparation

This section describes how the analytical results of the previous chapter are used to calculate the optical appearance of an arbitrary object. First, we calculate where and how often a single point is seen in Gödel’s universe. Therefore, we consider an observer resting at the origin and use the



Figure 6.3: Optical appearance of an infinitely often visible sphere (only a finite number of object images are shown) located within the Gödel horizon ($Z > 0$).

analytical solution for special initial conditions of the geodesic equations, Sec. 5.1.1. The calculation of the *interconnecting null geodesics* between this observer and the point results in the viewing directions under which this point can be seen. Visualizations for an arbitrary observer position can be, in principle, obtained using the general solution of the geodesic equations, cf. Sec. 5.1.2. However, we use an isometric transport, Sec. 5.2, of the entire scene to change the observer's position to the origin. Also, a local illumination model is realized using isometric transport by transferring the point light source to the origin accordingly.

For a fast visualization technique, the question to be solved is as follows: What are the sets of initial conditions such that resulting geodesics interconnect a given point to the observer's position? In Fig. 6.4, such a geodesic, connecting observer and an object, is shown. For now, the observer is located at the origin.

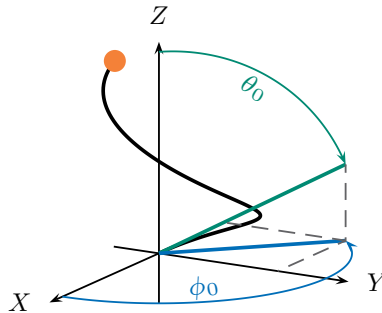


Figure 6.4: The starting direction of the geodesic is formulated using the local angular coordinates θ_0 and ϕ_0 , as measured in the tetrad of the observer.

First, we consider an observer resting at the origin of the coordinate system before handling arbitrary camera positions. To find all geodesics which connect the origin to an arbitrary static point with the spatial coordinates $\mathbf{x}_p = (R_p, \phi_p, Z_p)$, the equations

$$x^\mu(\lambda) = x_p^\mu, \quad \mu = 1, 2, 3, \quad (6.1)$$

must be solved, where the left-hand side corresponds to the analytical solution (eq. (5.7)) and the right-hand side is the point \mathbf{x}_p . The radial equation ($\mu = 1$) reads

$$\left| \sin \left(\sqrt{K_m} \lambda \right) \right| = R_p \sqrt{\frac{K_m}{K_p}} \quad (6.2)$$

and – using eqns. (5.6) for lightlike geodesics as well as eqns. (5.3) – yields the solutions

$$\lambda_n = \frac{1}{\sqrt{c^2 + (u_0^{(3)})^2}} \left[+h_a(u_0^{(3)}) + n\pi \right], \quad (6.3a)$$

$$\lambda_n = \frac{1}{\sqrt{c^2 + (u_0^{(3)})^2}} \left[-h_a(u_0^{(3)}) + (n+1)\pi \right], \quad (6.3b)$$

where

$$h_a(u_0^{(3)}) = \arcsin \left(R_p \sqrt{\frac{c^2 + (u_0^{(3)})^2}{c^2 - (u_0^{(3)})^2}} \right). \quad (6.4)$$

The index n denotes the number of full cycles that the geodesic has run through since starting from the origin. The unknown parameter $u_0^{(3)}$ is determined by eq. (5.7d), in which eqns. (6.3) are inserted. This computation results to

$$\frac{(u_0^{(3)})}{\sqrt{c^2 + (u_0^{(3)})^2}} \left[+h_a(u_0^{(3)}) + n\pi \right] =: Z_0(u_0^{(3)}, n) \stackrel{!}{=} Z_p, \quad (6.5a)$$

$$\frac{(u_0^{(3)})}{\sqrt{c^2 + (u_0^{(3)})^2}} \left[-h_a(u_0^{(3)}) + (n+1)\pi \right] =: Z_1(u_0^{(3)}, n) \stackrel{!}{=} Z_p. \quad (6.5b)$$

Fig. 6.5 shows an exemplary plot of the equations between Z_p and $u_0^{(3)}$ for fixed R_p and n . For each fixed n , eq. (6.5a) either has one solution or no solution because the left side of the equation is monotonically increasing but bounded. Eq. (6.5b) reveals no monotonic behavior and can have one, two or no solutions. Nevertheless, both equations define a combined relation represented by a closed curve. For a point spatially located at (R_p, ϕ_p, Z_p) , this relation then has

two solutions or none. Hence, the point is either visible twice or it is not visible at all (for fixed n). The cases $Z_p = \pm \hat{Z}_p$ mark two exceptions. Here, the relation has a single root of second order. Since $n \in \mathbb{Z}$, an infinite number of similar relations exist. Therefore, eqns. (6.5) can have an infinite number of solutions, which are arranged in solution pairs.

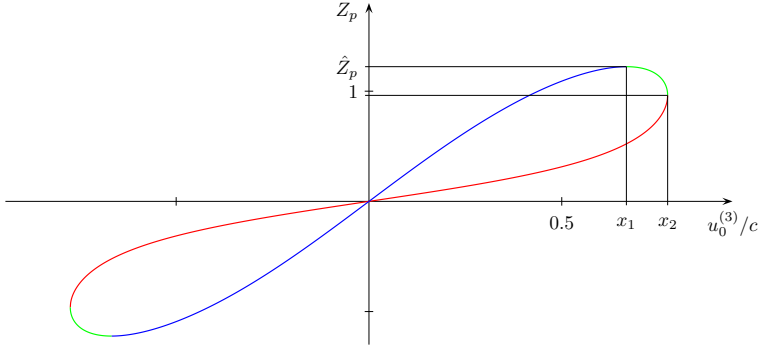


Figure 6.5: Exemplary plot of the left sides of eqns. (6.5), where we set $R_p = 0.5$ and $n = 0$. Depending upon these two parameters, this relation changes, but its basic properties remain conserved. The red curve corresponds to eq. (6.5a), whereas the blue curve visualizes eq. (6.5b). The green segment depicts eq. (6.5b) but is assigned to the red curve. By that means, each branch has one solution at most for a fixed Z -coordinate of the point x_p^μ . The relation is symmetric to the origin.

Unfortunately, eqns. (6.5) cannot be solved analytically. Thus, these two equations must be handled numerically using, for example, a Regula-Falsi method. Algorithms – such as the Newton method, which requires the derivatives of the equations above – are not applicable because the iteration easily leaves the compact support of the arcsin function. Consequently, the result of the computation is undefined. We tested several Regula-Falsi variants; the specific “Illinois” version converges reliably and fast. The numerical effort is negligible compared to the numerical integration of geodesics. To simplify the numerical calculation of the solutions, we rearrange the relation (6.5) as shown in Fig. 6.5. The green curve segment is assigned to the red curve. In other words, we relate the possible second solution of eq. (6.5b) to the other branch. As a consequence, each branch now has one solution or none. We can estimate whether or not a solution exists, before starting the numerical algorithm. Thus, we can be sure to find all (unique) solutions of each branch once the algorithm has commenced and we do not run the risk of missing a solution. The numerical difficulties arising from $u_3^{(0)} = x_1$ and $u_3^{(0)} = x_2$, cf. Fig. 6.5, are discussed in Sec. 6.3.4 on p. 96 as well as in Sec. 6.4.

We distinguish each solution of each branch with a separate index. For example, the curve parameter, cf. eqns. 6.3, is now denoted as $\lambda_{i,n}$ (see also Fig. 6.2). Solutions of the red branch are identified with $i = 0$, whereas $i = 1$ corresponds to the blue curve. Note that we use lightlike geodesics propagating into the past, i. e. $\sigma_0 = -1$ in eq. (5.10a).

Having derived the solutions to eqns. (6.5) – a set of parameters $\{u_0^{(3)}\}$ – we know the vertical angles $\{\theta_{i,n}\}$ under which the object is visible using $\theta_0 = \arccos(u_0^{(3)})$; see (Fig. 6.4). The horizontal viewing angles $\{\phi_{i,n}\}$ can be calculated using eq. (5.7c) and $\lambda = 0$. Thereby, we find a set of initial conditions for geodesics connecting a point and the origin. Now, we can calculate the directions under which all images of this point can be seen. A correct occlusion of the several images of an object is achieved by considering the relative lengths of the corresponding geodesics, which are given by $\lambda_{i,n}$. The spatial direction and final (visual) position of each image – formulated regarding the local static tetrad, eqns. (4.8) – is then given by

$$\vec{v}_{i,n} = \begin{pmatrix} \sin(\theta_{i,n})\cos(\phi_{i,n}) \\ \sin(\theta_{i,n})\sin(\phi_{i,n}) \\ \cos(\theta_{i,n}) \end{pmatrix}, \quad \vec{x}_{i,n} = \lambda_{i,n}\vec{v}_{i,n}. \quad (6.6)$$

To be precise, this direction must be scaled with r_G , cf. eqns. (A.23), but we are only interested in the direction itself, not its correct norm. Also, the position $\vec{x}_{i,n}$ of the point does not represent a physical distance; it solely enables a depth sorting of objects because the perceived distance of the point is monotonically increasing with the curve parameter λ . Consider, for example, two points along one null geodesic: The point corresponding to the larger curve parameter will be occluded by the point with the smaller curve parameter.

In addition to an observer at the origin, we can also place a point light source there in order to illuminate the object. The use of a local illumination model is then possible because we can compute if and how the origin is connected to an arbitrary point. The only difference is the time direction in which the geodesics are traced. To calculate the position of an object, geodesics are traced back into the past. The illumination of an object requires geodesics propagating into the future, i. e. $\sigma_0 = +1$.

Using the derivation presented in this section, we can avoid an expensive numerical integration of geodesics and tedious intersection calculations. Note that it is still not possible to generate visualizations for arbitrary positions of an observer or point lights. Although the analytical solution to arbitrary initial conditions exists, it can be shown that this solution is too complex for an interactive visualization. In order to generate visualizations for arbitrary observer positions, we must formulate the scene so that the observer is located at the origin. Only then can we use the procedure detailed above. In computer graphics, a typical approach is to apply an affine transformation in three dimensions in order to change the observer's position as required. Unfortunately, we cannot adopt this idea directly if we wish to translate, scale and rotate a scene. In curved spacetimes, such an affine transformation does not conserve the underlying physical properties of the scene.

However, we can use the concept of finite isometric displacements to transform the entire scene because an isometric displacement does not change the metric tensor and, therefore, also not the investigated physical properties. Consider, for example, an observer located on the Gödel horizon¹ and a pointlike object at an arbitrary position. This situation is depicted in Fig. 6.6a, where the observer is shown as a yellow circle and the object as a gray circle.

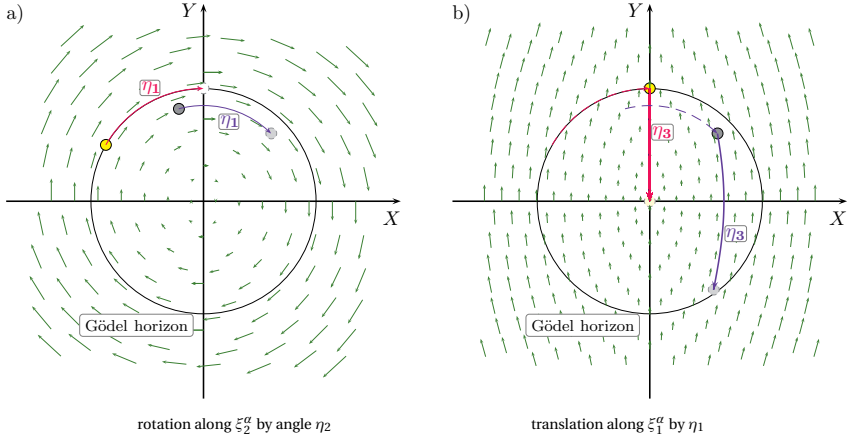


Figure 6.6: Concatenation of isometric transformations. The yellow object denotes an observer or a light source, the gray object resembles an arbitrary visualized object. If the yellow object is located at $Z \neq 0$, it will be shifted along the trivial Killing vector field ξ_3 (eq. (4.19a)) as well. The gray object is isometrically displaced using the same parameters η_i . This results in a physically equivalent formulation of the scene, where we clearly see that the gray object is visible from the yellow object's point of view because the first resides within the horizon of the latter.

We can answer the question whether the observer can see the object by isometrically pushing the observer's position to the origin and applying the same transformation to the object. First, the observer is rotated by an angle of $\Delta\varphi = \eta_2$ around the Z -axis using the isometry ξ_2 , eq. (4.19a), until he is located on the Y -axis. Then, the observer is isometrically displaced to the origin along the non-trivial Killing vector field ξ_1 , eq. (4.19b); see Fig. 6.6b. Note that both the position of an observer as well as his viewing direction are transformed and that this procedure is therefore comparable to the mapping of geodesics discussed in Sec. 5.3. Hence, the observer is transformed using a curve parameter η_1 , eq. (5.23), for the finite transformations given by

¹ Clearly, an observer is always located in the middle of *his* horizon. Here, we investigate the case that the observer is located on a horizon defined by the line element (4.5).

eqns. (5.16) and (5.21). Both transformations are applied to the pointlike object and we find that, cf. Fig. 6.6b, the object is located within the Gödel horizon of the observer and thus visible from his point of view. If the observer is not located at $Z = 0$, additional transformations along the appropriate Killing vector fields must be executed. This is trivial and identical to the complete procedure described in Sec. 5.3.

Now, we are able to generate visualizations for arbitrary observer positions using the special solution to the geodesic equations in conjunction with finite isometric transformations. Furthermore, arbitrary point light source positions can be used. Before we render the scene from an observer's point of view, we isometrically change the scene so that the *light source* is located at the origin. Being able to connect the origin and arbitrary spacetime points, it is directly possible to calculate whether or not a certain point is illuminated.

In contrast to our previous work [GMDW09], we have implemented the analytical solutions of the equations of isometric transport. This enables us to create interactive visualizations of different types of object formulation as discussed in the next section, where we also discuss the technical details of point light sources.

6.3 Implementation

The GÖDEL ENGINE is composed of a server application and a client rendering program; see Fig. 6.7. We use the Qt toolkit², a user interface framework including a set of cross-platform C++ libraries. It is available under the LGPL license. This library is a construction set for the development of graphical user interfaces (*GUIs*), where simple elements such as text input fields, selection boxes, file browsers as well as commonly used program elements, for example network sockets or OPENGL functions, are available. These classes are easily subclassed and straightforward to implement.

In the following, we will discuss each program component, starting with the basic data structure of visualizable objects. Then, the graphical user interface and the client renderer are discussed. Also, the communication between server and client is briefly outlined. We close this section with the rendering loop – the core of the GÖDEL ENGINE.

6.3.1 Object Types and Object-Based Algorithm

As a compromise between the memory usage and the performance of the application, we initialize a number of *reference data objects* on the GPU. The base class `ObjectData` provides the basic functionality for all reference objects. The reference data for different geometrical shapes is derived via sub-classing. These different object types such as spheres (`ObjectDataSphere`) and

²<http://qt.nokia.com/products>

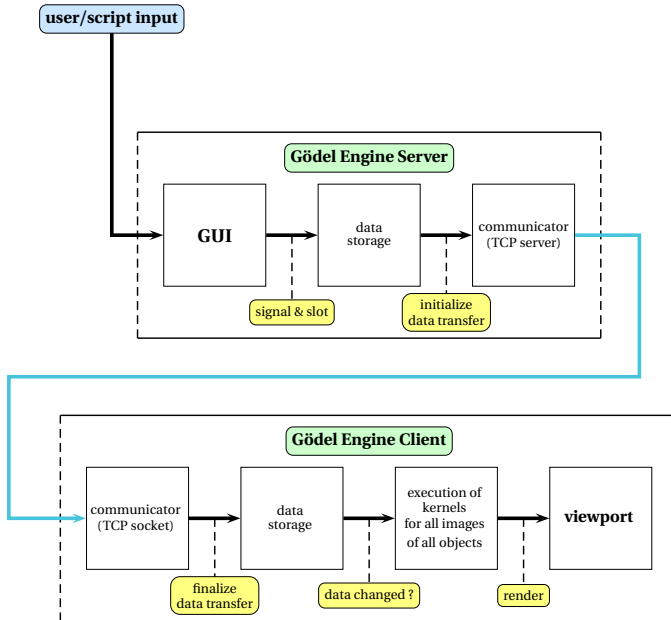


Figure 6.7: Internal structure of the GÖDEL ENGINE. The server receives input data through user interaction or script files. The data is then stored and synchronized with the client application which is responsible for the rendering.

rectangles (`ObjectDataPlane`) are then initialized when starting the program. To visualize non-primitive geometries, we use **geometry images** [GGH02], an efficient way to store mesh data in images. In brief, geometry images store vertex and normal information of a mesh in a plain image. The red, green and blue channels of the image correspond to the x , y and z -component of a vertex (or a normal), respectively. We load such an image and then generate the triangle mesh by traversing the image pixels. Fig. 6.8 shows an exemplary rendering of the “Stanford Bunny” in three-dimensional space using vertex and normal geometry images.

These reference objects now contain, inter alia, information on the vertices of the triangle mesh, normals for illumination and texture coordinates for texture-mapping. This data is then uploaded to the GPU and stored in **vertex buffer objects**. This is beneficial because we do not have to upload the geometry data from the CPU to the GPU every time the scene is changed. The reference data, for instance the unit sphere, remains unchanged throughout the runtime of the

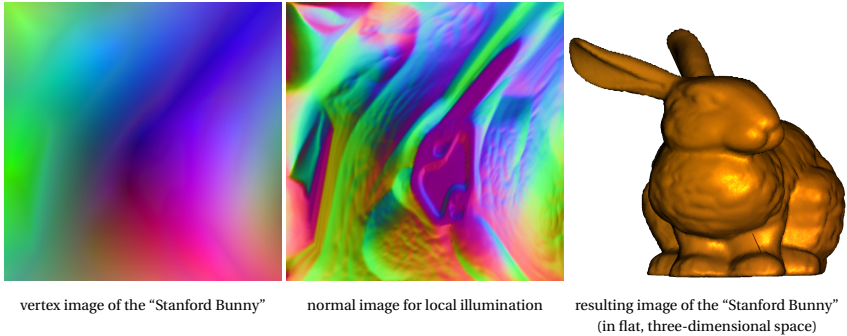


Figure 6.8: Illustration of geometry images. The first subimage stores the vertex data, where each pixel contains the color-coded information of the (XYZ) -coordinates of a single point of the mesh. The second subimage contains information about the normals in each vertex required to enable a local illumination model. The right subimage shows the resulting rendering in flat space. The geometry images have been obtained from <http://research.microsoft.com/en-us/um/people/hoppe/proj/gim/>.

application. Instead, we generate *display data objects* at the startup of the application. These objects will contain the final vertex positions $\vec{x}_{i,n}$ and intermediate data created during a rendering pass. All data objects are then made accessible to the CUDA kernels which calculate the appearance of all images of every object, as described in Sec. 6.2.

We implemented this structure, where we used the OPENGL interoperability of the CUDA framework: A vertex buffer object can be “mapped” to CUDA with a specific command. This vertex buffer object is then available to the CUDA kernels as `float` array and can be modified directly within a kernel. After the kernel is finished, the results of the CUDA computations are mapped back to OPENGL and can then be drawn to the screen; see Sec. 3.2.1 and esp. Sec. 3.2.2 for details. Every time the scene parameters change, the display data objects must be recalculated.

A scene is now defined as a collection of `Object` instances. Such an instance stores the object’s type, position, size, the relative precision of the triangle mesh and several other visualization parameters but *not* the actual mesh data. The object instance only accesses the reference data objects depending on the actual object type. This collection is stored as a vector in the `ObjectHandle` class. This singleton class also stores all reference and display data objects. There are two display data objects for each data type, such as the vertices of an object as seen from the observer. This is due to the fact that one physical object can have an infinite number of images and these images must be conveniently arranged into image pairs.

6.3.2 The Graphical User Interface – Gödel Engine Server

The GÖDEL ENGINE SERVER is used to alter the global scene parameters such as the color of the ambient light source, the number of objects within the scene as well as their visualization parameters, such as position, size and texture. A screenshot of the application is shown in Fig. 6.9.

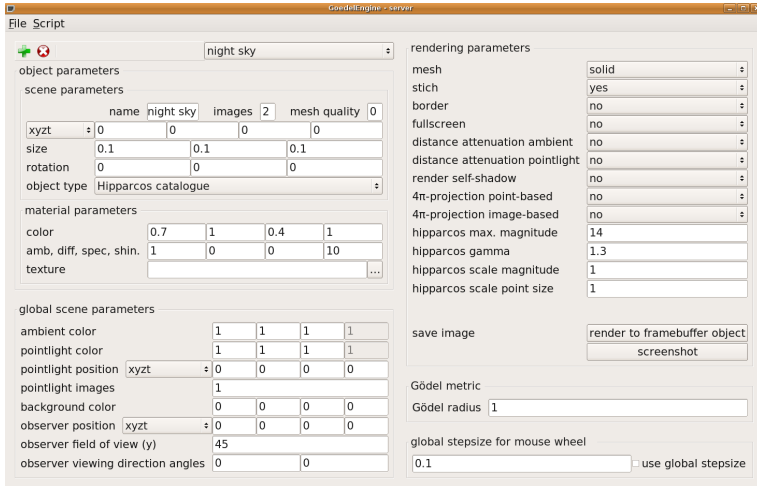


Figure 6.9: Screenshot of the GÖDEL ENGINE server application. Changing a scene parameter invokes a `signal` which then calls the associated `slot` function that handles the data update, as indicated in Fig. 6.7.

Every time a scene parameter is changed, the corresponding GUI element triggers a *signal* which then calls a specific function (*slot*). This slot then handles the update of the internal data. A new value of a text input field, for example, is passed to the `ObjectHandle` to update the position of the selected object. The `ObjectHandle` then stores the new data and passes it to the actual rendering engine, the GÖDEL ENGINE CLIENT, using the `Communicator`. This singleton works as a `TcpServer` when used within the GÖDEL ENGINE SERVER, cf. Fig. 6.7.

6.3.3 Rendering Images – Gödel Engine Client

The actual rendering is executed by the GÖDEL ENGINE CLIENT, also a separate program containing a plain `OPENGL` window and the `CUDA` kernels necessary for image generation. In the client, the `Communicator` class is operating as a `TcpSocket`, listening to the GÖDEL ENGINE

SERVER. Each time a parameter changes, the socket receives a message-type token and the actual data. Depending on the type of the token, the arriving data is interpreted. By this means, the `ObjectHandle` of the server and all clients are synchronized at all times. Having prepared the internal data for visualization, we will discuss the core rendering loop of the GÖDEL ENGINE CLIENT in the following section.

6.3.4 Core Rendering Loop

Each change of a parameter – such as the displacement of an object or an adjustment of the point light source – triggers a signal which invokes the `paintGL` routine of the OPENGL window. In this section, we discuss the execution of each kernel and the actual rendering to the screen (see Fig. 6.7). Note that the actual implementation does not calculate all object images before rendering them to the viewport. For memory efficiency, we loop over all image pairs of all objects. Thus, the procedure below must be executed often before the scene is completely drawn. The intermediate results are rendered to the back buffer of the OPENGL window. After all computations are completed, the back and front buffers are swapped. Thereby, only the complete result is drawn at once on the screen and not image pair by image pair.

Preparation of the scene parameters

At the beginning of the rendering pass, the OPENGL framebuffer and the depth buffer are cleared and await new drawing instructions. Then, the isometric displacement coefficients η_i are calculated as described in Sec. 6.2 and as shown in Fig. 6.6 for both the observer and the point light source position. If the observer and the point light source are not located at the same position, we arrive at two different sets of isometric displacement coefficients. Now, we loop over all objects of the scene. A shader program is activated and some data, such as the texture ID of the object and the color of the point light source, is uploaded to the GPU. The isometric displacement coefficients are used to calculate the object's center point and rotation. To calculate the visual distortion of the object, the observer is isometrically transformed to the origin and the object accordingly; see Fig. 6.6. For the local illumination model using the point light source, we change the objects' position (eqns. (5.16)) and rotation (eqns. (5.22)) analogously. Since all objects are formulated with regard to a local reference frame, we only compute the transported local tetrads on the CPU.

Initialization of the rendering on the GPU

First, the reference data objects are read out and stored in display data objects. The vertices are rotated, scaled and translated to conform to the desired scene description. Also, the transformation from the local tetrad to a coordinate representation (eqns. (A.21)) is applied. Now, all

vertices are calculated with respect to a coordinate system in which the observer (or the point light source) is located at the origin.

Calculation of the visual position of each vertex

After the initialization step, the display data objects for the vertices are passed to the CUDA kernel which calculates the visual appearance of the object's image as seen by the observer (cf. Sec. 6.2). This kernel basically solves eqns. (6.5) for every vertex of the scene. The initial values for the Regula-Falsi-iteration are as follows: For a given spatial vertex position, we find the solution of the red branch ($|Z_p| \leq |Z_0(x_2, n)|$) after setting $u_{\min}^{(3)} = 0$ and $u_{\max}^{(3)} = x_2$ (cf. Fig. 6.5). The value of x_2 is easily obtained by setting the argument of the arcsin function, eq. (6.4), to unity and solving for $u_0^{(3)}$. Then, we iterate eq. (6.5a) until the solution is found. If we have $|Z_1(x_2, n)| < |Z_p| \leq |Z_1(x_1, n)|$, we use x_1 and x_2 as starting values for the iteration of eq. (6.5b). The parameter x_1 marks the root of $(dZ_1)/(du_0^{(3)})$ and cannot be found analytically. Therefore, we must precompute $x_1 = x_1(R_p, n)$. This calculation results in a two-dimensional lookup-table $(R_p, n) \rightarrow x_1$, where $R_p \in [0, 1]$ and $n \in \mathbb{N}$. A resolution of 4096 in $R_p \in [0, 1]$, with an additional linear interpolation, is sufficient. Of course, we must restrict the simulation to a finite value n_{\max} of the order n . The maximum order n_{\max} has been set to 1024. After this calculation, we have found the even image of a vertex for a given order n . The odd image of a vertex is found analogously after setting $u_{\min}^{(3)} = 0$ and $u_{\max}^{(3)} = x_1$ for an iteration of eq. (6.5b).

Depending on the desired accuracy of the triangle mesh, this calculation converges in typically less than ten iterations. Note that the geodesics which interconnect an observer \mathbf{O} and the vertices evolve into the past of \mathbf{O} , such as in standard four-dimensional raytracing, because the observer *collects* all incoming photons with his camera.

If an object is visible to the observer, the numerical iteration has a valid solution and the visual position $\vec{x}_{i,n}$ is calculated. The solution of the iteration is represented by a set of initial conditions for the interconnecting geodesic. These values are now stored in a temporary display data object because they are also needed for illumination calculations in a later step.

Calculation of illumination values and self-shadowing effects

After having calculated the basic geometrical appearance of an object image, we calculate the illumination coefficients per vertex. Therefore, the "appearance" of the object's image is calculated "as seen by" the point light source. We can use the same kernel as above, however with a small but important difference. Now, we are not interested in the optical appearance as if an observer is located at the position of the point light. Instead, we *illuminate* the object with the light source. Therefore, the interconnecting geodesics propagate into the future. We consider all possible paths connecting the light source and the object up to a specific order.

At this point, we have the visual appearance of every vertex of the current object image with respect to the observer and, in a way, the light source. We also stored the initial conditions for the interconnecting geodesics between the observer and the vertices. This data can then be used to illuminate the object.

The point light kernel uses the initial conditions of the geodesics calculated before. Using the special solutions for lightlike geodesics, eqns. (5.7), two directions with respect to the local frame of reference of the object are calculated. First, the direction under which the ray originating from the light source intersects the surface point is calculated (\vec{l}). Using the surface normal \vec{n} in this point, we calculate the reflected ray direction \vec{r} . Second, the direction under which the primary ray hits the object is computed. Using the surface unit normal \vec{n} , the normalized spatial projections of the primary ray direction \vec{v} , the incident light direction \vec{l} and the reflected light ray \vec{r} , we can apply the Phong illumination model as described in Sec. 3.1.1.1.

However, we introduce a minor modification so that objects, which are illuminated solely with an ambient light component, appear more plastic. Therefore, we consider an angular dependency for this component by calculating the cosine between \vec{n} and \vec{v} during the ambient light kernel execution. Thereby, central regions of object images are relatively bright and the visually peripheral areas are faded to black. This procedure is closely related to a headlight *in flat space*.

Note that in flat, three-dimensional space the viewing direction under which the vertex is seen, \vec{v}_1 , is identical to the direction under which the primary ray hits the point (\vec{v}_2) as long as no light refraction is considered. In general relativity, those two directions will be arbitrarily different due to the curved interconnecting geodesics. Obviously, we must use the $\vec{v} = \vec{v}_2$ in order to apply the Phong model.

To enable a heuristic distance attenuation of these illumination calculations, we multiply the ambient illumination coefficient with $(1 + \lambda_a)^{-k}$, where λ_a is the curve parameter of the primary ray at the surface intersection point. We set $\lambda_a = 0$ at the observer position. Therefore, the ambient light component gets only marginally reduced, if the object is very close to the observer. The parameter k denotes the magnitude of the distance attenuation; linear and quadratic attenuation can be used. Similarly, the diffuse and specular lighting component is multiplied with a factor $(1 + \lambda_a + \lambda_b)^{-k}$, where λ_b is the curve parameter of the geodesic between the light source and the vertex. Thus, we interpret the affine curve parameter of a geodesic as a measure for the length of a curve segment. The illumination values themselves are stored per vertex – comparable to *texture space lighting*, cf. [BL03].

We restrict the simulation to self-shadowing effects of a single object image. If the scalar product between the reflected light ray and the normal of a surface point B is negative, the light ray intersects the object from the inside. Therefore, it must have already intersected the object – which must have a closed surface for such considerations – at another point A and can therefore be neglected in point B . An approach such as *shadow volumes* [Cro77] to visualize the shadowing effects of a single object or even different entities is, in principle, possible but very

challenging: In flat, three-dimensional space the shadow volumes are easily determinable, but in Gödel's universe these geometrical structures must be computed using the general solution to the geodesic equations and thus represent spatial slices of a very complicated shape. **Shadow mapping** [Wil78] seems more promising but it has not been tested yet.

In contrast to that, a shadow computation using standard four-dimensional raytracing is easily devisable. The light source illuminates the scene and the lighting values are stored similar to standard texture space lighting [BL03]. Since the light ray is constructed incrementally and intersection tests with the scenery are commenced at the position of the point light source, a light ray can be directly discarded after the first intersection with an object. Thereby the shadowing calculation is automatically completed.

Stitching

The first numerical difficulty we encounter during the solution of eqns. (6.5) arises if the vertical viewing direction of a vertex is around $\Theta = \arccos(x_1)$, cf. Fig. 6.5. The implementation very reliably finds both images of a vertex for a given n , even if $|Z_p| \lesssim |\hat{Z}_p|$ (see Fig. 6.5). However, if, for example, two vertices in the object's triangle mesh are within this limit, the next vertex might already be violating this condition and thus be invisible to the observer (for this order n) and must be tagged as invalid. Since we use a object-based method, not only the latter vertex is invisible. We also lose the entire triangle defined by these three vertices. Consequently, the triangle mesh will contain regions of valid vertices which might be permeated with (several) invalid areas – depending on the position of the object with respect to the observer. Valid and invalid domains are thereby separated by **borderlines** which are defined by the edges of the last valid vertices. In brief, such a vertex is found if it is valid and an adjacent vertex is invalid. This circumstance is, unfortunately, inevitable using an object-space algorithm. Hence, a remedy must be applied.

We use a stitching algorithm which computes the borderlines in an image pair of a triangle mesh. If a vertex is visible, for example, in the even image of the n^{th} order, then it must also be visible in the odd image of the same order because the relation illustrated in Fig. 6.5 has either two solutions or none (for fixed n). Thus, if a vertex is part of the borderline in the even image, it must also be part of the odd image. Consequently, we have a one-to-one correlation between each vertex in the even image and in the odd image. To generate a continuous surface, we simply calculate the mean value of all corresponding vertices of the even and the odd image (of the same order) along this line. Locating these two vertices is easily accomplished because both have the same array index in the meshes for the even and the odd image. The underlying reason for this behavior is that x_1 represents a root of second order for $|Z_p| = |\hat{Z}_p|$, as shown in Fig. 6.5. As a consequence, vertices close to this border are closely neighboring in our data structure. The information lost after this linear interpolation in order to close the meshes is negligible. We call the stitching algorithm, as illustrated in Fig. 6.10, in the core rendering loop, where the illumination values are additionally interpolated at the borderline.

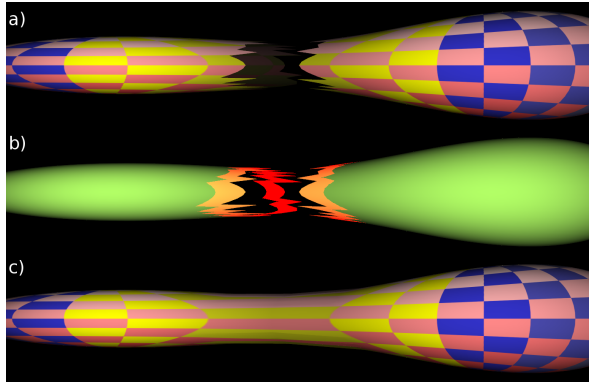


Figure 6.10: Stitching of an image pair to a continuous surface. Fig. 6.10a shows discontinuities in the visualization of a very coarse mesh. Fig. 6.10b illustrates the last valid vertices, i. e. the borderline, calculated for the even and odd image (red). The corresponding vertices of each image are merged using the mean value of both. Finally, the image can be drawn as a continuous surface (Fig. 6.10c).

Rendering to the viewport

At this point, the visual appearance of an image pair is calculated and can finally be rendered to the screen. Therefore, all data objects containing the display data are mapped back to the OPENGL context. Then, the vertex buffer objects can be rendered to the viewport, for example, the screen. For large, high-quality images, the rendering target can also be a **framebuffer object**, which is an off-screen rendering target that may have a much higher resolution than the screen.

Since all data is stored on the GPU, we can directly draw all arrays using `glDrawArrays`. At the beginning of the core rendering loop, a shader program was activated. This program now processes all vertex buffer objects alongside the additional data necessary for visualization. Textures, additional object color, global colors for ambient and point light sources are therefore computed per fragment by means of linearly interpolating the calculated data between the vertices. Of course, the vertex transformation itself is non-linear and thus we introduce an error due to the linear interpolation. To analyze this error qualitatively, we consider four different cases of object positions:

1. *Objects close to the observer:*

Objects close to the observer appear relatively undistorted. Thus, even a coarse triangle mesh produces a negligible error due to the linear interpolation.

2. *Objects close to the horizon, no stitching:*

If an object is at a larger distance to the observer but the stitching kernel is not required because all vertices are valid, we observe the following: The object images appear very distorted and the linear implementation might not be sufficient. In most cases, the images are rather small and it is fairly unproblematic to use very fine triangle meshes so that the edge length of the triangle is smaller than one pixel. Thus, the error can be eliminated but the rendering performance is decreased unnecessarily because we use very small triangles in the entire mesh – which is not required in general.

3. *Object images that need to be stitched:*

As shown in Fig. 6.10, the stitching algorithm joins vertices that are at a considerable distance to one another. Thus, edge lengths are heavily increased. Even the finest mesh that we implemented could not prevent imprecisions because no sub-pixel lengths of the triangles' edges can be attained. The correct qualitative appearance – large variations in vertex positions but not in texture coordinates – is reproduced but we might show a slightly incorrect region of the texture.

4. *Object images that surround the observer:*

As shown in, for example, Fig. 7.29 on p. 139, images of a sphere can visually surround the observer. In this case, nearly all triangle edges of an object become drastically extended and even the finest mesh (as implemented in the current version of the GÖDEL ENGINE) introduces a large error. This visual property mostly arises if objects are moving close to the speed of light, where we must use G_{EO}V_IS to generate the renderings. The issue does not pose a dominant problem for quasistatic objects rendered with the GÖDEL ENGINE because there are only a few sets of scene parameters which result in such renderings.

We could use **tessellation** (which is supported by the most recent graphics hardware) in order to overcome the last three problems. For this, a separate rendering pass must be introduced, where the size of a triangle is analyzed in object space *after* the visual position of each vertex is computed. If a triangle is enlarged beyond a critical value, it must be subdivided into smaller triangles. Then, the visual position must be calculated for the newly introduced vertices. This procedure must be iterated until no further subdivision is required. Note that tessellation is not yet implemented.

All fragments are drawn to the viewport and the next image pair is calculated, until all images of all objects are drawn to the viewport. Since the depth buffer of the OPENGL context is enabled, the rendering order of the objects and their images is irrelevant and the object occlusion is correct.

To be precise, this is only correct as long as no transparent objects are used. Unfortunately, the GPU discards fragments that lie behind already rendered fragments to increase performance. Thus, all vertices would have to be sorted from back to front. Since we render a huge amount of vertices, such a manual depth sorting would tremendously diminish the rendering speed.

Moreover, we do not have all vertices of the entire scene available all the time, as we render image pairs and discard the intermediate data after the vertices are rendered to the viewport. However, *depth peeling* offers a straightforward remedy but has not been implemented because we do not focus on transparent objects.

6.4 Technical Discussion

The GÖDEL ENGINE reveals a drastically improved rendering performance when compared to classical raytracing. Additionally, the applicability of a local illumination model facilitates the generation of images which appear more realistic and appealing than renderings that are generated using solely ambient lighting. However, technical problems must be addressed as well.

6.4.1 Advantages

Of course, the object-based rendering procedure of the GÖDEL ENGINE cannot be directly compared to raytracing in terms of rendering performance because these two methods are profoundly different. The GÖDEL ENGINE does not improve an existing approach but rather presents an alternative to raytracing for the Gödel universe. Thus, we cannot legitimately compare the specialized GÖDEL ENGINE and the generic raytracing algorithm in general. However, we do focus on the Gödel spacetime and, therefore, we can relate both techniques.

The direct comparison between a standard raytracing approach and our implementation reveals a drastic difference in performance. A reference scene containing one object has been rendered using both methods on a standard, dual-core desktop PC (AMD 64X2 4600+) with a resolution of 1024x512 pixels. We did not use supersampling in the raytracing approach, to which we compare [Mü06]; thus we rendered the images from the GÖDEL ENGINE with no antialiasing or other image quality improving methods. The local illumination model was deactivated because no CPU implementation was available. Additionally, we only used a single core. Note that raytracing scales very well on clusters.

n	CPU A	CPU B	GE V1	speedup $\times 10^5$	GE V2	speedup $\times 10^5$
0	41 s	605 s	4.1 ms	0.1 to 1.5	11.7 ms	0.035 to 0.51
1	79 s	1105 s	7.8 ms	0.1 to 1.4	17.2 ms	0.046 to 0.64
2	113 s	1639 s	11.2 ms	0.1 to 1.5	22.8 ms	0.050 to 0.72

In the table above, the first column denotes the maximum image order of a reference sphere we visualized. CPU A is a raytracing approach which implements the analytical solution. CPU B is also a raytracing approach but uses a 4th order Runge-Kutta integration for the geodesic equations. We chose the integration parameters to match the image quality of our interactive approach. The GPU rendering time (GE V1 and V2) was measured on a GeForce 8800 GTS. Although

a GPU implementation of a numerical integrator is possible, no better performance compared to the analytical approach is to be expected. The columns labeled GE V1 and GE V2 refer to the two different versions of the GÖDEL ENGINE. The former column presents the results of the first version as published in [GMDW09] and the latter provides the corresponding values of the GÖDEL ENGINE as used for this work. Note that our new version of the GÖDEL ENGINE realizes the point-based visualization of additional scenarios such as the Hipparcos catalog, the implementation of the complete analytical solution to the equations of isometric transport for points (eqns. (5.16)) as well as vectors (eqns. (5.21)) and also implements an improved user interface. Due to the results of the first version, we did not focus on pure performance and thus the new implementation is roughly three times slower. Ultimately, this circumstance does not pose a problem because the current release still offers an average performance gain of four to five orders of magnitude.

Our approach enables us to visualize models such as a local illumination effects. We consider the correct angular dependency between reflected shadow ray and the direction under which the primary ray intersects the object, both measured in the respective local frame of reference. With 16xMSAA and more complex objects and scenarios, the rendering time increases to non-interactive rates but still remains under a second for a reasonable size of the scene: Fig. 6.11 shows an exemplary rendering of several objects, including the Stanford Bunny implemented as geometry image. The scene consists of nearly two million triangles and the stitching kernel must be executed for the Earth sphere. Additionally, light images of the zeroth order are considered. This image requires less than a second – using the first version of the GÖDEL ENGINE – to render on the hardware specified above.

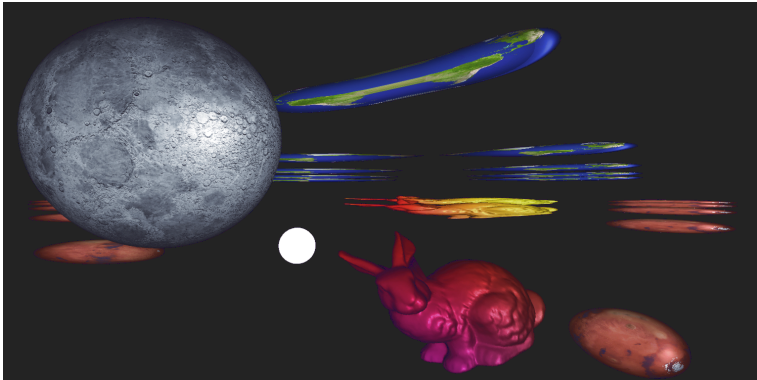


Figure 6.11: High quality image of multiple appearing object images and a point light source (white) rendered in 730 ms.

While a primitive object, such as a sphere, is rendered using a raytracing approach very fast, a complex triangulated mesh, such as the Stanford Bunny, is extremely tedious to compute using the current implementation of the GEOVIS framework because no accelerating data structures such as octrees are implemented yet. Thus, each individual triangle takes *about* as long as the entire sphere. It can be estimated that such an image needs approximately one year to render using raytracing – without a local illumination model. The speedup factor in such a case is approximately 10^7 . However, the values presented in this section are to be considered as a rough estimate and only serve as proof that a considerable performance leap is achieved *for scenarios that are typical in the field of general relativistic, egocentric visualizations*.

An optimized implementation of raytracing is $\mathcal{O}(n)$ in screen resolution and $\mathcal{O}(\log n)$ with respect to the complexity of the geometry, i. e. the number of primitives. Object-space algorithms are (for disadvantageous sceneries) $\mathcal{O}(n)$ regarding the screen resolution and $\mathcal{O}(n)$ considering the complexity.

Due to the considerably improved rendering performance, we are able to find several optical effects which might not have been found using a non-interactive approach. These new insights are presented in Sec. 7.3, where the visualizations of illuminated and quasistatically moving objects are discussed. The prompt feedback of the application upon parameter adjustments allows us to “experience” the Gödel universe on a more intuitive level and thus understand its visual effects more directly. Accordingly, laypersons or scientists of other research areas can easily get “acquainted” with the Gödel universe. Nevertheless, there are two key problems, which are discussed in the following section.

6.4.2 Drawbacks

The GÖDEL ENGINE must cope with two kinds of complications. First, the numerical root-finding, which leads to the calculation of the viewing directions, is problematic for certain parameters and, second, the approach itself is limited to quasistatically moving objects.

Numerical issues

As stated in Sec. 6.2, numerical difficulties arise for certain scene parameters. The first problem, indicated by the abscissa $u_3^{(0)} = x_1$ in Fig. 6.5, was eliminated by implementing the stitching algorithm, cf. Sec. 6.3.4. However, the second challenge, $u_3^{(0)} = x_2$, is harder to solve. Recall that we use a numerical Regula-Falsi solver to find the solutions for eqns. (6.5). If the tangent to the relation is vertical, as indicated in Fig. 6.5 for $u_3^{(0)} = x_2$, such numerical solvers have difficulties to extract a precise solution if only single precision is utilized. In addition to that, the region of the relation where the tangent is almost vertical can be comparably large for disadvantageous scene parameters. This is shown in Fig. 7.19a, where a vertex is fairly close to the observer.

The numerical problems can be seen in the rendering under certain circumstances. The visualization of extended objects (internally represented as triangle meshes) is relatively robust because a slightly imprecise viewing direction of a single vertex does not stand out in a large mesh. However, in Ch. 8.2, we visualize the optical appearance of the stars in the Hipparcos catalog using a point-based approach. For this scenario, we do not use triangle meshes for the visualization but rather isolated point sprites, one for each star. If the exact solution for the vertical viewing direction is around the value x_2 , the corresponding star shows a shivering motion when a scene parameter (such as the Gödel radius or the position of the observer) is altered in small steps. Moreover, the iteration becomes unstable and does not necessarily converge, which results in an intermittent disappearance of the star for specific scene parameters. To ameliorate these effects, we can utilize the double-precision support of recent graphics hardware. Then, the scene parameters of the Hipparcos visualizations can cover a larger range of values, where the renderings do not show the shortcomings described above. We only calculate those routines in double precision which are directly associated to the Regula-Falsi procedure. Thus, the rendering performance does not drastically decrease. For example, on a GeForce 280 GTX, the rendering speed drops to 50% after switching from single to double precision.

Limitation to quasistatically moving objects

In the previous sections, we discussed how resting objects are correctly visualized. Naturally, we can move objects on arbitrary curves quasistatically, as long as their local velocity is small compared to the speed of light. For fast moving objects, we must consider the optical effects resulting from the finiteness of the speed of light. As stated at the beginning of Ch. 3, seeing is simultaneously in the eye of an observer. This circumstance is comparable to an airplane traveling close to the speed of sound. The location of the airplane will not coincide with the direction under which we can hear it.

Unfortunately, we are only able to visualize static and quasistatic objects with the GÖDEL ENGINE. Although it is, in principle, possible to visualize fast moving objects, the rendering performance would decrease drastically to a point where the underlying, object-based algorithm is slower than the classical raytracing method. The reason behind this restriction is explained in the following:

The GÖDEL ENGINE searches for the initial conditions of lightlike geodesics which connect an arbitrary but static point with the observer. Consider a small object traveling on an arbitrary worldline close to the speed of light. For every event on the (discretized) worldline, we can calculate under which directions the object is visible. Since the calculation method presented in Sec. 6.2 yields the initial conditions for the interconnecting lightlike geodesics, we can easily calculate the light travel time from the surface point to the observer, cf. eq. (5.7a). By that means, we would know in which image of a film sequence the surface point could be seen. We could open

the involved image files, write the image pixels and move on to the next point of the object's worldline. Using this approach, each file of the image sequence would have to be opened, modified and closed a multitude of times. This problem is intensified in Gödel's universe because we can see a single point arbitrarily often. Each of this point's images is seen along a different geodesic with a different light travel time. Thus, for the visualization of one point of the worldline we would have to operate on a large number of different files. This approach is not desirable because it would be very slow and the hard disk would operate practically the entire time. Nevertheless, this approach can be modified to perform a quantitative analysis of the egocentric visualizations. This procedure is detailed in Sec. 7.4.

To decrease the number of file operations we can, again, iterate over the discretized worldline, but keep the image of the sequence fixed. For every point on the worldline, we calculate where and when the object is seen. If the time of visibility τ_{vis} is close to the current observer time τ_{obs} , the object can be seen in this picture of the sequence. As a consequence, an additional (heuristic) test must be employed which decides if the object can be seen or not, i. e. $|\tau_{\text{vis}} - \tau_{\text{obs}}| \stackrel{!}{<} \Delta\tau_{\text{heur}}$. In addition to this criteria, we must choose the stepsize for the discretization of the worldline. Although the file operations are minimized, we trade this benefit in a massive redundancy in the calculation because the worldline must be evaluated as described above in every single image. Intersecting the worldline with the past light cone of the observer using this method therefore results in the calculation of a very large number of heuristic tests. Only those parts of an object are drawn to the final image of the sequence, which fulfill the heuristic criteria. This approach has been tested (with an hierarchical implementation of the heuristics' calculation) and resulted in two major problems: The stepsize of the discretization and the heuristic parameter must be carefully chosen by the user. If both entities are too large, we obtain false images, which tend to be too large as well. Very small values yield correct silhouettes, but many pixels are missing because the heuristic test is too restrictive. These tests have been implemented without considering that the local tetrad of the moving object is Lorentz transformed, with respect to the local static tetrad of a resting object. Using this transformation, special relativistic effects, such as the length contraction of the moving object, can be enabled. Unfortunately, this contraction would complicate the numerical difficulties even more. Although it is in general possible to use this approach, it can be estimated that the rendering performance is inferior to those results generated by classical raytracing.

Another approach is to interpret the retrieval of the light travel times for a fast object as a root finding problem similar to the computation of the vertical viewing directions; see eqns. (6.5). A close inspection of this idea results in the conclusion that both problems are coupled: The light travel time critically depends on the position of a vertex. Thus, both roots must be found simultaneously by solving a two-dimensional problem. This is aggravated by the fact that we, again, have to face the compact support of the underlying functions and, consequently, the numerical algorithm must not use derivatives. Two-dimensional bisection procedures seem promising,

but only at least at first sight: We neither can estimate the approximate value of the root nor the number of solutions for an arbitrarily moving and potentially time traveling object. Thus, we would be forced to reduce the procedure to very special and limited sets of worldlines – making the targeted universality of the rendering procedure obsolete. Ultimately, the sharp distinction between the GÖDEL ENGINE (used for quasistatic objects) and the GEOVIS framework (for objects that travel at velocities close to the speed of light) is a sensible choice.

VISUALIZATION OF THE GÖDEL UNIVERSE

“Visualization is daydreaming with a purpose.” — ROBERT (BO) BENNET

Secs. 6.2 and 6.1 provided a first insight into the optical appearance of objects in Gödel’s universe. However, this discussion was limited to the specific prerequisites and implementation details of the GÖDEL ENGINE. This chapter discusses the egocentric visualization on a qualitative as well as quantitative basis in order to provide a deeper understanding of the Gödel universe: Why does a certain object moving in a specific direction appear like it does?

To achieve this goal, we split the scene parameters and visualization types into different classes. First, the propagation of light is reviewed and also broadened by consulting extended light cone structures and spatial wave fronts. Note that these illustrations are not created using an egocentric perspective. The lion’s share of this chapter, however, is dedicated to egocentric visualizations. To accept the challenge of creating comprehensible illustrations of objects in Gödel’s world model, the first renderings presented will use a very restricted set of scene parameters.

The first scenario visualized is a cylindrical coordinate grid. We animate the optical characteristics of a regular as well as equidistant cylindrical coordinate grid. This enables us to intuitively comprehend the dynamics introduced to the Gödel universe when changing the rotation scalar, eq. (4.3). The second class of scenes consists of static and quasistatic objects. Closely related to the simple cases detailed in Sec. 6.1, especially Figs. 6.1 and 6.2, we consult objects in the equatorial plane of the observer and then, objects at arbitrary positions. Using the GÖDEL ENGINE, these objects are quasistatically moved and illuminated. Before investigating the visualization of time travel, we must understand the optical appearance of an object moving close to the speed of light. Therefore, we utilize the GEOVIS framework. We consider several timelike geodesics on which a locally formulated sphere propagates. This object starts at the observer’s position and its motion, consequently, is restricted to the causal region of the observer. After the analysis of these results, the visualization of geodesical time travel (as analytically described in Sec. 5.1.2) is

presented. Up to this point, we restrict the visualization parameters so that only two images of the sphere are visible. Abandoning this constraint yields a higher number of visible images of an object and the complexity of the visualization thus increases.

In back of the studies on static, quasistatic, moving and partially time traveling objects, we approach the visualization of time travel on a CTC. Both perspectives, the observer's and the traveler's, are discussed in detail. We find that, in the light of the restricted possibilities regarding the actual scene definition, the optical appearance of the journey on a CTC is surprisingly accessible to interpretations.

We close this work with three complex classes of scenes, which are documented in the “*playground*” chapter. First, we offer a formulation of our inner solar system for the Gödel universe. Second, the Hipparcos catalog is adapted and implemented into the GÖDEL ENGINE so that the user can interactively fly through the stars of the catalog. And finally, we visualize the opening credits of the “Star Trek – The Next Generation” series as it would be seen in the Gödel universe.

Most of the visualizations introduced in this section are images of movie sequences. The caption of the image denotes the filename of the video on the accompanying storage medium. Images rendered with the GÖDEL ENGINE will be labeled using “(GE)” in the image caption, whereas “(GV)” is used for renderings obtained by the GEOVIS framework. Within this chapter, we also present two useful and convenient tools used to generate images. These tools are worthy of mentioning, but do not require separate chapters within the focus of this work.

As discussed in Sec. 4.2.4, any locally formulated object or observer resting at an arbitrary point rotates with a constant angular velocity given by the rotation scalar Ω_G , eq. (4.3), around the local $\mathbf{e}_{(3)}$ -axis due to the parallel transported local tetrad. We neglect this effect for the observer to simplify the interpretations of the optical effects. Since most egocentric visualizations are presented in a panorama- or 4π -projection, the full 2π information of all horizontal viewing directions is available¹. Thus, the rotation of a spatially resting observer can easily be incorporated into the existent visualizations: Usually, the central region of an image depicts the scenery as seen along the positive X -direction. If the observer is rotated by an angle of π and his point of interest is located along the negative X -axis instead of the positive direction, the right half of any egocentric image can simply be removed and attached at the left border of the other half-image. The center of the newly formed image then represents the observer's current line of sight: The negative X -direction. This directly allows for the correct visualization of the rotated observer.

¹The visualizations of grids presented in Sec. 7.2, where we solely focus on geometrical aspect, are generated using a standard pinhole camera with a relatively small field of view.

7.1 Light Propagation

This section provides an alternative view on the lightlike geodesics in the Gödel spacetime. We do not investigate single geodesics but whole bundles, rendered as finite light cone structures and spatial wavefronts. An interactive tool, `GOEDELWAVEFRONT`, allows a playful approach to the propagation of light. Also, frequency shifts, due to the gravitational field caused by relative motion, are briefly reviewed, and an approach to visualize time travel is explained.

7.1.1 Light Cones and Wavefronts

In Sec. 4.2.6, we reviewed the light cone structure of Gödel's universe. These illustrations, coordinate-dependent and non-egocentric, represent the limitations to the possible flight directions of a traveler moving in a plane of constant Z . If the traveler is located beyond the horizon of an observer, the traveler's light cone intersects the $T = \text{const.}$ plane and thus he can journey into the past of the observer. However, these images only reveal the initial light cone and, therefore, only the initial directions in which a traveler can move. In this section, we examine how these light cones evolve. The resulting **finite light cones** determine the paths on which a traveler can move *on geodesics*. Note that an *accelerated* voyager can leave these illustrative structures as long as he travels within his *local* light cone. In addition to the finite light cones, we display **spatial wavefronts** in Gödel's spacetime.

In our previous publication [GFAMA08], we presented a tool, `JWFRONT`, to visualize such wavefronts and light cone structures. This tool offers a graphical user interface, where we can specify an initial event of a light flash and several visualization parameters. The program then calculates a bundle of lightlike geodesics starting at the initial point. After the precalculation step in which the geodesics are calculated, a wavefront is defined as the spatial surface generated by the bundle for a fixed coordinate time $t = t_i$. A finite light cone is determined similarly. In the latter case, we use the time coordinate instead of the third spatial coordinate. The visualization is drawn using Cartesian coordinates and `OPENGL`, where the camera position and field of view can be altered by the user. The diffuse and specular illumination bears no physical interpretation; it facilitates the geometrical interpretation of the structures shown.

`JWFRONT` has been completely rewritten in C++ and optimized for the Gödel universe. To generate the finite light cone structures as well as the spatial wavefronts, we use the analytical solution to the geodesics equations (5.12) instead of a numerical integration. Therefore, the numerical preparation of the visualized structure is completed much faster and the overall performance of the application, `GOEDELWAVEFRONT`, is much higher compared to `JWFRONT`.

Additionally, we use a different parameterization for the spatial wavefront. In `JWFRONT`, light cones and wavefronts are defined by evaluating the bundle of null geodesics for a *fixed coordinate time*. However, no global time order in Gödel's universe exists and, consequently, the

coordinate time should not be used for the definition of the wavefront surface. We choose the curve parameter λ of the lightlike geodesics for the parameterization of the wavefront. This is not only to be regarded as a remedy to the time order problem in Gödel's universe. When using the coordinate time, we focus on a global perspective on the wavefront. This point of view is highly dependent on the choice of coordinates and the interpretation of the coordinate time. The curve parameter λ represents the intrinsic or "natural" parameterization of any wavefront in general relativity because the usage of λ – which is closely related to the proper time τ , being the curve parameter of a timelike geodesic – offers a more local perspective. While it is not possible to associate λ to a proper time on a lightlike geodesic directly, we can still interpret the curve parameter as the relative length of any lightlike geodesic segment. Therefore, we define the wavefront by the spatial extent of the underlying lightlike geodesics and not with respect to the time coordinate of the spacetime.

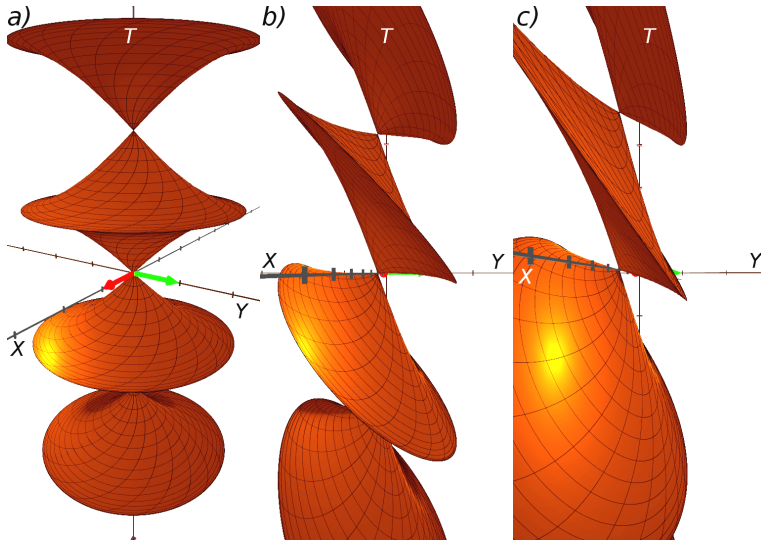


Figure 7.1: Finite light cones in Gödel's universe ([ExtendedLightCone.avi](#)). From left to right, the light cones initial point is located at a radial coordinate of $R = 0; 1; \frac{3}{2}$. The black lines on the structures represent contour lines or selected lightlike geodesics defining the cones along their respective curved paths.

Fig. 7.1 shows three finite light cones in Gödel's universe. The first light cone is calculated at the origin and the second cone is starting at the horizon. The visualization in Fig. 7.1c is generated

for an initial point beyond the horizon ($R = 3/2$). We clearly see that, from left to right, the light cones tilt. Consider the future light cone (above the (XY) -plane) in Fig. 7.1b, where the cone tangents the plane $T = 0$ and, contrary to Fig. 4.5a on p. 47, partially evolves below this plane. Therefore, a traveler moving on timelike geodesics can also travel back in time a little – with respect to the observer at the origin. This additional information is only obtainable using the finite light cone and is not contained in Fig. 4.5a.

The surfaces introduced in Fig. 7.1 reveal in a very transparent way that the geodesics refocus: An observer resting at the origin and emitting a light flash will see a periodical blinking, resulting from the returning photons. Of course, we assume that the observer will *not* absorb all returning photons at the first refocusing event. In that case, he would see the refocusing of the light only once.

The intensity of the returning light flash will decrease over time because only light restricted to the equatorial plane of the observer returns to the same spatial position. This can be understood by investigating Fig. 7.2, where the spatial wavefront of a light flash starting at the origin is depicted. Light emitted with a non-zero component in the $e_{(3)}$ -direction periodically returns to $R = 0$, but not to $Z = 0$. Consequently, this large fraction of the light will not return to the observer's position.

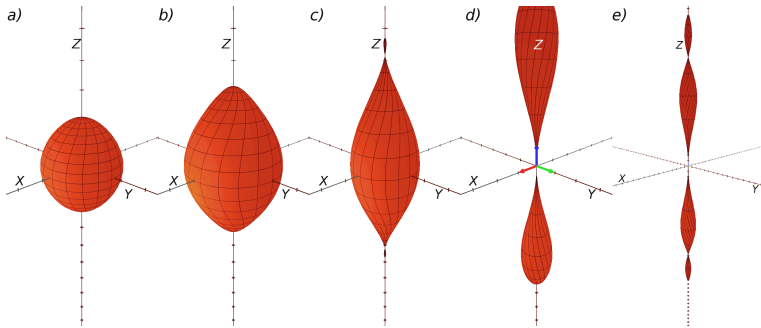


Figure 7.2: Spatial projection of a wavefront in the Gödel universe (`WavefrontOrigin.avi`).

Starting from the left, a light flash propagates into the future. The curve parameter is $\lambda \in \{1; \frac{1}{2}\pi; \frac{3}{4}\pi; \pi; 4\pi\}$. For small values of the curve parameter, for example $\lambda \lesssim 1$ in this sequence, the wavefront is of spherical shape.

The spatial wavefront displays pinch-offs along the Z -axis, defining several caustics. We can, already, hazard the guess that objects “above” or “below” an observer appear intensely magnified: The light emitted by a small object will be refocused at the origin, but spans a nonzero solid angle, thus visually enlarging the object.

The image sequence 7.2 can also be interpreted regarding the object formulation in Gödel's universe. A large object shaped such as the wavefront in Fig. 7.2e can, under certain circumstances, visually define a sphere for an observer located at the origin: If this geometry emits a light pulse so that all light travels to the observer as indicated by the wavefront when read from *right to left*, the observer will perceive² such an object as a sphere.

7.1.2 Frequency Shifts

A **frequency shift** arises if electromagnetic radiation emitted from an object is shifted to lower frequencies (**red shift**) or to higher frequencies (**blue shift**) of the electromagnetic spectrum. In classical physics as well as special relativity, frequency shifting occurs when the light source and the observer move with a nonzero relative velocity. This is the so-called (relativistic) **Doppler effect**. In general relativity, there is an additional **gravitational frequency shift** effect. Simply speaking, when a photon moves away from a strong gravitational source it loses energy. Therefore, its wavelength is shifted towards the lower-energetic, red end of the spectrum. Vice versa, a photon is blue shifted when moving towards a gravitational source. Due to the homogeneity of Gödel's universe, there is no gravitational red shift; only Doppler shift, due to relative motion, arises.

Mathematically speaking, the photon is parallel transported from the emission event to the observer along a lightlike geodesic and the frequency ν and the total frequency shift z are then connected via

$$z_{\text{total}} = \frac{\nu_{\text{observer}}}{\nu_{\text{emission}}} = \frac{\langle \mathbf{k}_{\text{observer}}, \mathbf{e}_{(0),\text{observer}} \rangle}{\langle \mathbf{k}_{\text{emission}}, \mathbf{e}_{(0),\text{emission}} \rangle}. \quad (7.1)$$

The vector \mathbf{k} denotes the lightlike wave vector of the photon, which is parallel transported along the interconnecting lightlike geodesic from the point of emission to the observer. Then, the total frequency shift is calculated by evaluating the scalar products of the wave vector and the timelike base vector, $\mathbf{e}_{(0)}$, of the respective local tetrad. This definition differs from the convention used in standard literature, where $z := 1 - \frac{\nu_{\text{observer}}}{\nu_{\text{emission}}}$ is often used. In our case, light is red shifted for $z_{\text{total}} \in (0; 1)$, and the frequency is blue shifted for $z_{\text{total}} > 1$.

The temperature of an object is associated to a spectrum. This spectrum is then shifted according to the equation above. After transforming the shifted spectrum to **chromaticity coordinates** XYZ by folding the spectrum with the **CIE color matching functions**, the RGB values for this temperature can be calculated in a given color system. If we normalize the colors with respect to the intensity (the CIE Y color component), we obtain the mapping between the apparent temperature and the perceived color as shown in Fig. 7.3. Throughout this work, a temperature of 6000 Kelvin is used for any object. The color associated to this temperature is light blue.

²To be precise, one must consider the direction of time: The wavefront shown in Fig. 7.2 propagates into the future and winds counterclockwise around the X -axis. In raytracing, we consider a wavefront which is winding clockwise into the past. The geometrical shapes of both are identical, merely the geodesical (black) lines reveal the difference in the winding behavior.

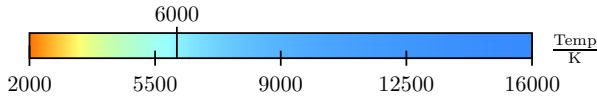


Figure 7.3: Mapping the temperature of a black body to a color. In all images depicting the frequency shift of an object, we assume a surface temperature of 6000 Kelvin. Note that resulting temperatures beyond this range value are clamped to 2000K or 16000K, respectively.

If we assume black body radiation, the emitted spectrum is of Planck type. Shifting such a distribution is easy because a shifted Planck spectrum is again of this type. Thus, a one-dimensional lookup texture, as shown in Fig. 7.3, associates a temperature to its apparent color and could be used to obtain the shifted colors. Here, the general and extensible approach of [Wal] is adapted, although black body radiation is used. For details on CIE color coordinates and the transformation of spectra to a color system that is usable for monitors or beamers, we refer to [Wal] as well.

7.1.3 Emission Time

If we look at the stars in our universe, we know that we are looking into the past. The visual appearance of the Large Magellanic Cloud *here and now* results from light emitted over 150,000 years ago; the appearance of the Andromeda Galaxy *here and now* consists of light which was emitted approximately 2,500,000 years ago. If we ask which visual impression an observer has, we need all photons that the observer receives *at the same time*. In general, these photons will not be emitted *at the same time*.

The propagation of light is complex in Gödel's universe because any object can appear an infinite number of times. For increasing order of the image, the associated light travel time increases as well. Hence, higher order images reveal images from a distant past. Fortunately, it is possible to extract this kind of information from the intermediate data generated during the raytracing algorithm: We compute the local tetrad of an object's discrete worldline, which is closest to a light ray segment. If this segment then intersects the object, we extract the time component of the tetrad and store this information into the associated image pixel of the observer's camera. Unlike our approach presented in [GB08], we do not display the coordinate time but the proper time of emission as measured with respect to the local frame of the object. This enables us to sort the images of an object by their relative age. We assume a color distribution which maps "older" travelers to a deep blue color, whereas "younger" voyagers appear in a bright red tone, cf. Fig. 7.4. In each visualization that is following this approach, we provide the exact age definition for the red and the blue color in proper time measured in units of r_G/c . In between, we apply a linear

color gradient from red to green to blue. Note that the clocks of the observer and all objects are synchronized so that $\tau_{\text{object}} = 0$ for $\tau_{\text{observer}} = 0$.



Figure 7.4: Mapping of a local emission time (age) of an object to a color. Between the minimum and maximum value, a linear interpolation from red to green to blue is applied. The mapping parameters are adjusted so that all visible objects are correlated to a color within this table.

This method for image generation is most beneficial for Gödel's spacetime because it yields the possibility to visualize time travel as well. If a specific object reappears from beyond the Gödel horizon before it disappears *and* this object is older than the disappearing one, then the associated traveler has indeed traveled through time. We will make extensive use of this idea.

7.2 From Flat Spacetime to Gödel's Metric

In this section, we discuss the influence of a varying Gödel radius r_G on the optical appearance of a cylindrical grid, extending the discussion of our previous publication [GMW*07]. Two different definitions of a cylindrical grid are analyzed. First, we formulate a fixed cylindrical coordinate grid in unscaled cylindrical coordinates (eq. 4.2). Second, an alternative and non-equivalent formulation using lightlike geodesics is explained and interpreted. Since we only focus on the distortion effects, geometrical units are used. Throughout and only in this section, we use **unscaled cylindrical coordinates**, in other words the line element (4.2). Consequently, the coordinates are represented using **lower case letters**, i. e. $\{t, x, y, z\}$. In this set of coordinates, the metric converges to the Minkowski line element for $r_G \rightarrow \infty$ and, therefore, the influence of a varying Gödel radius becomes clearer.

7.2.1 Fixed Grid

The straightforward approach to define a grid in Gödel's universe is to utilize the set of coordinates itself. Consequently, this definition of a grid is coordinate dependent. We define a polar grid with radial axes and rings of constant r . In addition to the fixed coordinate grid, we utilize a large sphere in several visualizations, which is not expressed with respect to a local flat frame of reference. In most cases, these coordinate objects do not yield any physical meaning.

In Figs. 7.5a-d, we see several egocentric visualizations, accompanied with explanatory images, cf. Figs. 7.5e-h. The Gödel radius is decreasing from left to right, and we calculate the optical appearance of the grid for an observer located above the (xy) -plane. The viewing direction of the

observer is the negative z -direction. Hence, the center of the grid is shown. The top left image is calculated using a very large Gödel radius and the egocentric visualization shows an almost undistorted grid because the lightlike geodesics resemble almost straight lines. This circumstance is rooted in the behavior of the line element (4.2): The metric converges to the Minkowski spacetime in cylindrical coordinates in the limit $r_G \rightarrow \infty$. For a decreasing Gödel radius, the curvature of the Gödel universe and its rotation scalar increase. In this case, the geodesics appear more curved. The explanatory images in the bottom row of Fig. 7.5 depict the interconnecting geodesics of the four corner pixels of the egocentric visualizations above.

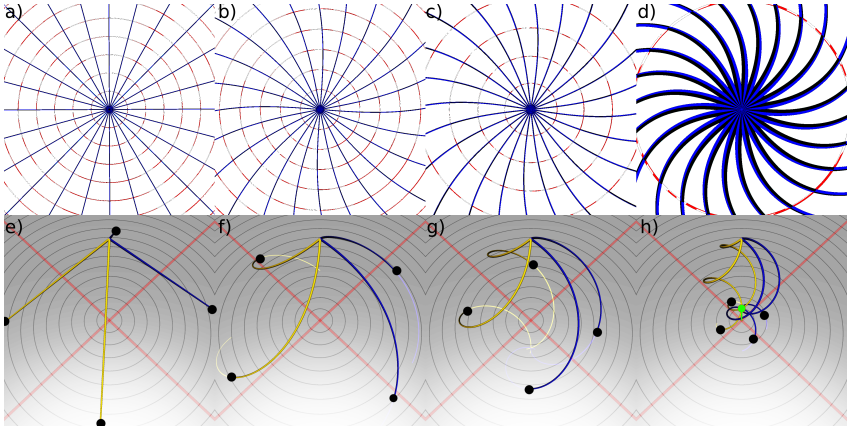


Figure 7.5: An equidistant polar grid as seen from an observer at $z = 10$ who is looking “down” ([RegularGridFromAbove.avi](#)). The top row shows the egocentric visualization of an equidistant polar grid (GV). The radii of the concentric rings are whole-numbered and the radial axes are separated by an angle of 15° . The bottom row shows several exemplary lightlike geodesics between the observer (located at $z = 10$), which serve as a qualitative explanation for the visual appearance shown in the top row. Black dots mark the intersection between the visual ray and (xy) -plane. The green dot in Fig. 7.5h shows the point where all four geodesics intersect – slightly above the plane. Due to the resulting magnification, the grid in Fig. 7.5d appears more massive. The Gödel radius is varied from left to right ($r_G \in \{4000, 20, 10, 4\}$).

If we closely inspect the top row and the explanatory images below, we might suspect a disagreement in the qualitative behavior: While the primary rays depicted in the bottom row wind *clockwise*, the polar grid shown in the top row reveals a *counterclockwise* rotation. This is, in fact, not a conflict; all images are correct. Consider a specific image pixel, for example a corner

pixel. The associated primary ray intersects the grid at a certain angular coordinate φ_0 . If the Gödel radius decreases, the ray winds *clockwise* and hits the grid at a smaller angle $\varphi_1 < \varphi_0$. This primary ray is still mapped to the same pixel we considered. Now, a smaller angular coordinate φ_1 is associated with this pixel and the image therefore appears rotated *counterclockwise*³.

The third and, in particular, the last column reveal another feature of this metric: The grid appears enlarged. Magnification of an object occurs if geodesics corresponding to a relatively large region of the observer's field of view originate from a very small area of this object. In the last column, this effect becomes very extensive. If we take a closer look at Fig. 7.5h, we see that the geodesics intersect slightly above the (xy) -plane. If the coordinate grid had been placed there, it had appeared infinitely magnified from the observer's point of view. In fact, the displayed grid also appears point inverted because the intersection point is located slightly above the (xy) -plane.

Additionally, the surface brightness should appear reduced (like in special relativistic aberration). The total luminosity of one fixed area of the grid remains unchanged but is seen in a larger field of view. Note that no intensity effects are incorporated into these visualizations. Thus, the images do not change in luminosity.

The next image sequence, shown in Fig. 7.6, displays the observer's visual impression, if he is located at $z = 1$ and his line of vision is the positive x -direction. We cannot place him directly at the origin because the coordinate grid would then be seen from the inside – covering the entire image. Additionally, we utilize a large and non-locally formulated Earth sphere with a radius of $r_E = 5$. The Gödel radii amount to similar values as used before: $r_G \in \{4000, 10, 4.8, 4\}$. For this reason, the coordinate sphere lies partially beyond the Gödel horizon in Figs. 7.5c-d.

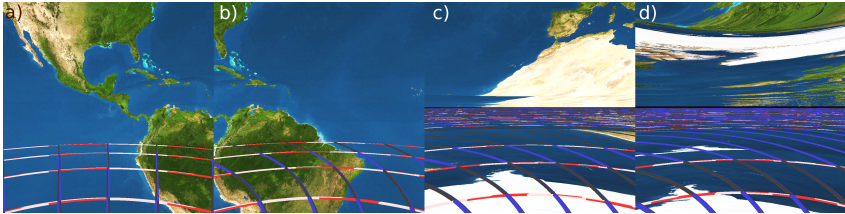


Figure 7.6: An equidistant polar grid and a coordinate sphere with the radius $r = 5$ (GV). The observer rests slightly above the (xy) -plane ($z = 1$) and the viewing direction is the positive x -direction. The Gödel radius decreases from left to right, i. e. $r_G \in \{4000, 10, 4.8, 4\}$ (`RegularGridFromWithin.avi`).

³This idea can be compared to the following simple situation: Consider the two functions $f(x - a)$ and $f(x)$, where $a > 0$. Although the function $f(x - a)$ is shifted by $-a$, we obtain this function after translating $f(x)$ by a to the *right* and not to the *left*.

Such a large sphere can, in principle, be constructed in Gödel's universe. As shown in Sec. 4.2.4, any point initially resting at a certain position remains there over time. We interpret this coordinate sphere as a dust cloud. However, we do not focus on the physical interpretation of the sphere; we are only interested in the geometrical aspects of primary rays.

As presumed, the first picture in Fig. 7.6 shows the scene as in flat spacetime. Then, after decreasing the Gödel radius to $r_G = 10$, the scene appears to be rotated to the left. The reason behind this effect is identical to the counterclockwise rotation of the grid shown (as previously illustrated in Fig. 7.5). A clockwise rotation of the visual rays is manifested in an initial bending to the *right* in this case. Therefore, the visible parts of the scene appear as if they have moved to the *left* when compared to the undistorted image of a nearly flat spacetime.

However, after decreasing the Gödel radius *below* the radius of the Earth sphere, our observer gets some unexpected impressions of this scenery. If we closely inspect the image sequence shown in Fig. 7.6, we note that parts of the Earth sphere become invisible in Figs. 7.5c-d. This is simply due to the fact that the equatorial region of the large Earth sphere now lies beyond the Gödel horizon. Those parts are, consequently, not visible to an observer located at $r = 0$. As soon as the radius of the Earth sphere r_E is smaller than the Gödel radius r_G , we have

$$\cos(\alpha) = \frac{r_G}{r_E}, \quad (7.2)$$

as shown in Fig. 7.7. The region of the Earth sphere, where the latitude is between $\pm|\alpha|$, is beyond the visual range of the observer.

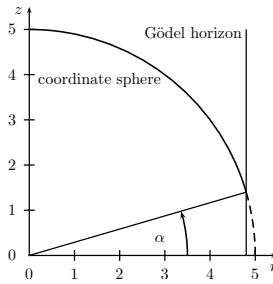


Figure 7.7: Illustrating the visually missing parts of the Earth sphere. The invisible region of the sphere beyond the horizon is indicated by the dashed segment.

Although an increasingly large region of the Earth sphere cannot be seen for a decreasing Gödel radius, our observer does not perceive a large black region as one might expect. Instead, only a thin, horizontal black line appears in images 7.6c and 7.6d. To be precise, only an infinitesimally thin line – corresponding to the observer's horizontal plane – will be black on the pictures

taken. This effect can be understood if Fig. 7.8 is closely inspected. In this image, we see a non-egocentric rendering of the coordinate sphere and a bundle of geodesics. If the component of the initial direction along the local z -axis, $u_0^{(3)}$, is not zero, the sphere is intersected after a potentially very high number of windings n . Of course, n determines the order of the visual images showing a specific region of the sphere. Only those geodesics residing exclusively in the (xy) -plane of the observer do not reach the sphere. These equatorial geodesics define the infinitesimally thin line mentioned above. We could, in principle, visualize this effect if we trace the primary rays sufficiently long into the past of the observer, yielding arbitrarily high order images of the Earth sphere.

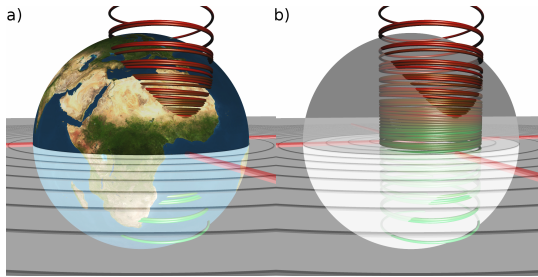


Figure 7.8: A coordinate sphere ($r_E = 5$) and a polar grid in the Gödel universe $r_G = 4.8$. Only some parts of the Earth will be visible to the observer. In this image, several illustrative geodesics are drawn and represent a vertical field of view of not more than 6° . Regardless of a very small but nonzero component of the initial direction in the $\mathbf{e}_{(3)}$ -direction, these primary rays do intersect the sphere after a certain number of windings. Thus, these visual rays correspond to higher order images of the sphere.

For this specific scenario, a large coordinate sphere and a resting observer, a small but valuable tool (GOEDELSPHERE) has been developed. This program requires a relatively large and precomputed dataset: We calculate the texture coordinates of the intersection between a primary ray and the coordinate sphere for certain sets of initial directions, Gödel radii r_G and Earth sphere dimensions r_E .

We must precalculate a one-dimensional array of initial directions only where the declination angle is varied from 0 to π . Then, we can exploit the rotational and mirror symmetry of the spacetime and the scene in order to minimize the precomputation effort as well as the dataset size. The discretization is as follows: The radius of the sphere as well as the parameter $a = r_G/2$ can take values between zero and ten in about 500 discrete steps. Also, the angular range mentioned above is discretized in 500 steps. The resulting dataset is about 2 GB in size. We extract the texture coordinates (calculated for the one-dimensional array of initial directions) for

the currently chosen τ_G and τ_E and upload this data to the GPU, which processes the information in an image-based visualization approach.

The graphical user interface is divided into two main parts, as shown in Fig. 7.9. On the left side, we see a quantitative analysis of the egocentric visualization on the right. Additionally, the application provides several sliders and buttons for altering, for example, the Gödel radius, the radius or the texture of the sphere as well as the observer's point of interest. After a change in the scene parameters, the egocentric visualization is shown almost immediately.

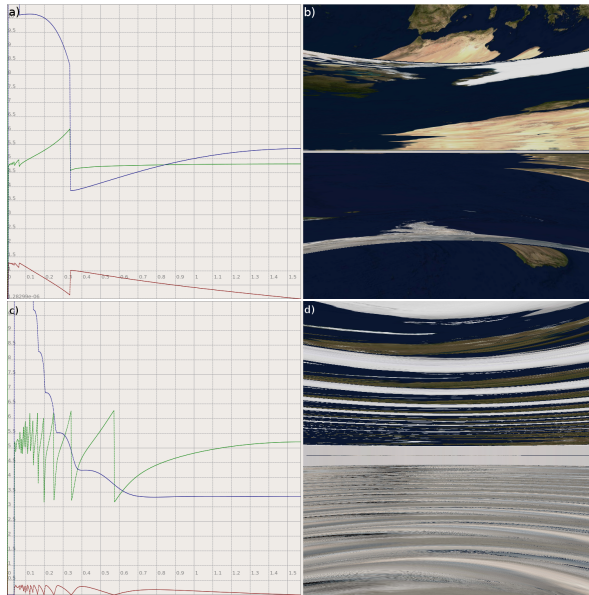


Figure 7.9: Screenshot of the GOEDELSPHERE application ($\tau_E = 5.36$ and $\tau_G = 5.16$ for subfigure a and b; $\tau_E = 3.34$ and $\tau_G = 0.28$ in c and d). The left part of the user interface reveals a quantitative analysis of the egocentric visualization. The abscissa is the declination angle of an initial direction. Three different plots are shown: The latitude (red), the longitude (green) of the surface intersection as well as the light travel time (blue). Again, the Earth texture is used for the coordinate sphere. In this picture, the control elements of the application are omitted for clearness.

Using the quantitative analysis on the left, we can get further insight into the visualization of a coordinate sphere: The abscissa represents the declination angle of the initial directions array.

The red and the green plot depict the latitude and the longitude of the intersection on the sphere for this one-dimensional array of viewing directions, respectively. The blue curve reveals the light travel time. If the Gödel radius is large and the size of the sphere very small, then the observer will see the Earth practically undistorted. Thus, the longitude of the intersection is constant, the latitude reveals a linear behavior and the light travel time can be neglected. If we change the parameters so that the radius of the sphere is slightly less than the Gödel radius, we get a visual appearance as shown in Fig. 7.9. Exactly as in Fig. 7.6, the equatorial region is visually missing and is replaced by higher order images of the polar region (and the temperate zone in Fig. 7.9a and b). As soon as $r_E \ll r_G$, the observer will only see both poles because most of the Earth sphere now lies beyond the horizon, cf. Figs. 7.9c and d.

The coordinate time plot displays several discontinuities, marking the change of the image order n to the next order $n + 1$. The primary rays of the two neighboring viewing directions must then wind n and $n + 1$ times, respectively, before intersecting the sphere. Thus, the height of discontinuity in the blue plot is approximately the coordinate time needed for such a photon to perform one full winding on its path. The red and the green curves, marking the surface intersections, reveal discontinuities at the same angles.

The curve progression between each two neighboring discontinuities is very similar, but for smaller angles the segments appear horizontally compressed – best seen in Figs. 7.9c and d. This effect can be directly identified in the egocentric view as well: Each visible repetition of an Earth part consists of similar surface points (such as the northern part of Africa in Figs. 7.6a and b). However, the closer the image is to the horizontal plane of the observer, the smaller the area filled by this high order image becomes.

The discontinuities are not determined by the application; therefore, the plots are drawn as continuous lines. Also note that, due to the discretization of the dataset on which the quantitative analysis operates, we obtain a somewhat bumpy behavior of the plots regarding the discontinuities when changing the scene parameters. These positions therefore cannot be exactly determined. A remedy to this problem is a higher resolution dataset, which, of course, requires higher standards of the hardware used. The dataset presented in this work is a compromise between accuracy and performance.

7.2.2 Fixed Distances

In this section we want to construct a pseudo-polar grid in the (xy) -plane with equidistant points. The simplest way to accomplish this goal is to use light pulses starting at the observer's position. Along a null geodesic, we can associate the length of a curve with the elapsed coordinate time. For this metric in particular, the elapsed coordinate time is identical to a proper time interval for an observer resting at the origin. Thus, we can define lengths by segmenting null geodesics into pieces of constant proper time intervals.

The main question is: Should light rays be considered that are *emitted* at the observer's position, or does light *absorbed* in his eye represent a better choice? Emitting photons means tracing their path into the future; absorbing them corresponds to a negative time direction. We decide to follow the idea of backtracing the photons in order to create a grid which appears as undistorted as possible: If we place a number of objects on a specific primary ray, then all of these objects could be seen straight ahead from the camera's point of view because this ray defines a single viewing direction.

In Fig. 7.10, an equidistant grid is shown. The Gödel radii are identical to the choice used in Fig. 7.5. In the current scene, the coordinate sphere is removed and the polar grid is replaced by the equidistant grid. The yellow-gray spheres mark equidistant points ($\Delta\tau_{\text{obs}} = 1$) along a geodesic. The observer is positioned at $z = 1/2$ in order to have some overview on the grid. We neglect the error made by this translation.

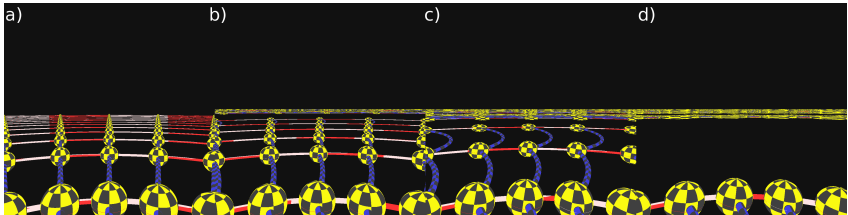


Figure 7.10: An equidistant polar grid with local spheres at the intersection points between the axes and the rings of constant radius (GV). The observer rests, again, slightly above the (xy) -plane ($z = 1/2$) and the viewing direction is the positive x -direction. The Gödel radius decreases from left to right ($r_G \in \{4000, 10, 4.8, 4\}$). Note that the position of the spheres as well as the axes must be calculated anew for every value of the Gödel radius.

For a decreasing Gödel radius, higher order images of the grid become visible as thin, yellow-gray lines. The radial axes (blue-gray) appear bent because these axes are implemented as coordinate objects. As the Gödel radius decreases, the maximum radial extent of the grid decreases as well. Thus, the decreasing Gödel horizon visually approaches the observer. This effect is due to the definition of the grid: We only use the initial outbound part of the lightlike geodesics for the creation of the grid⁴. Otherwise, it cannot be guaranteed that a single spatial point in space is represented by several different grid points, as the defining geodesics intersect.

⁴Equivalently formulated: Only the even segment of zeroth order is used, cf. Fig. 6.5.

7.3 Quasistatic and Illuminated Objects

The last section provided information on the visual appearance of fixed coordinate grids under the influence of a varying Gödel radius r_G . Now, we leave the Gödel horizon unchanged, return to the **scaled** set of coordinates (eq. (4.5)) and discuss how quasistatically moving objects are perceived in the Gödel universe. Since we consider these objects as resting in every rendering, we neglect local velocities, Lorentz transformations in comoving tetrads and the finiteness of the speed of light: Every image is calculated as if all objects were resting.

All egocentric visualizations are rendered using the GÖDEL ENGINE. Also, a local illumination model is applied to discuss how point light sources change the optical appearance of objects. The main goal of this section is to understand which side of an entity can be seen (or is illuminated) depending on the arrangements of objects and their relative distance to the horizon. This discussion will also aid in the understanding of several optical effects resulting from objects moving close to the speed of light (Sec. 7.4). Starting with this section, we will use the scaled set of coordinates, eq. (4.4).

7.3.1 Objects in the (XY) -Plane

The first objects visualized with the GÖDEL ENGINE are entities moving in the (XY) -plane of the coordinate system. The observer is located at the origin.

Scenes without the point light source

When restricting the objects of a scene to the (XY) -plane, there are only two distinct possibilities to formulate quasistatically moving objects. We can push an object radially outwards, starting from the observer's position at the origin and ending somewhere beyond the horizon. Alternatively, the object is moving in a circle around the origin. Any other motion within the horizontal plane of the observer results in optical effects similar to the combination of the two basic motion types. However, due to the cylindrical symmetry of the spacetime, we can omit quasistatic circular motion in the (XY) -plane. Thus, we consider the situation as depicted in Fig. 7.11.

A sphere (indicated using yellow circles in Fig. 7.11) is quasistatically moving from the origin across the horizon, where it becomes invisible to the observer. Also, the interconnecting geodesics are depicted for several positions of the sphere. Since the sphere is moving *quasistatically*, we do not consider the light travel time and thus only two different initial conditions exist for all interconnecting geodesics in each frame: All even images, respectively all odd images, result from one initial condition and can therefore be associated to the same primary ray. Consequently, only the images of zeroth order can be seen. All higher order images are occluded by a zeroth order image if the object itself is not (partially) transparent.

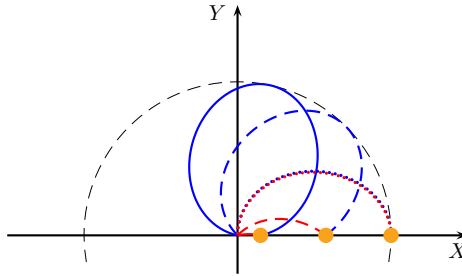


Figure 7.11: A sphere (yellow) moving quasistatically beyond the horizon. For several positions of the sphere ($X \in \{0.15, 0.575, 0.99995\}$), the interconnecting geodesics of zeroth order are depicted. The directions under which the geodesics reach the origin indicate the horizontal visibility angles for the observer. Additionally, the visible side of the sphere can be identified in this plot.

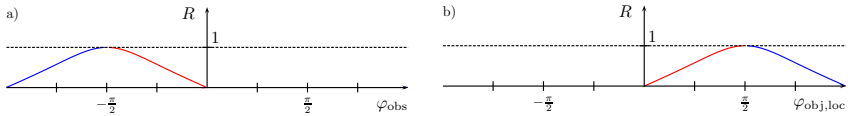


Figure 7.12: Two different angles plotted against the position of the pointlike object. Fig. 7.12a illustrates the observation angle under which the object's central point can be seen. Fig. 7.12b depicts the direction, ultimately the latitude, of the surface intersection between the primary ray and the sphere. All angles are measured in the respective local frame of reference.

The visibility angle, under which the central point of the sphere can be seen, depends on the position of the object. Consider an observer aligning his point of interest with the positive X -axis. He will see the even image right in front of him, as long as the object is located at $0 < X \ll 1$. As the sphere approaches the Gödel horizon, the horizontal visibility angle converges to $-\pi/2$. In the limiting case $X \rightarrow 1$, the observer will see the object to the left of him because the interconnecting geodesic segment at the origin is then tangential to the Y -axis. For the odd image, the visibility angle appears mirrored: If the object is very close to the origin, the observer will absorb the light which is traveling along the blue colored geodesic from behind because the light must travel to the horizon first. If we push the object to the horizon, the odd image will shift to the right and, identically to the even image, the visibility angle converges to $-\pi/2$. Both objects visually disappear under the same angle. Using the analytical solution to the geodesic equations, we can calculate the angles under which a pointlike object is visible. Fig. 7.12a depicts the angle

under which a point on the X -axis is seen. An angle of $\varphi_{\text{obs}} = 0$ is associated to the local $e_{(1)}$ direction and thus to the X -axis. This diagram affirms the qualitative analysis of Fig. 7.11.

Another fundamental difference of the optical appearance of these two images can be identified when inspecting the direction of emission on the object. Clearly, the even image reveals the “front” face of the sphere. This side of the object is spatially the closest to the observer. When pushing the sphere towards the horizon, another part of the object becomes visible. In the definition of the scene, Fig. 7.11, the “upper” region (with positive Y -values) is now focused on the observer. Thus, the even image shows the sphere visually rotating to the right. The odd image, however, displays the back face of the sphere for positions close to the observer. As soon as the sphere approaches the Gödel radius, the visible side of the sphere approaches the visual information of the even image. An analysis is presented in Fig. 7.12b, where we depict the local angle $\varphi_{\text{obj,loc}}$ under which the primary ray impinges the center point of the object. Note that this angle is identical to the latitude of the surface intersection of a sufficiently small sphere.

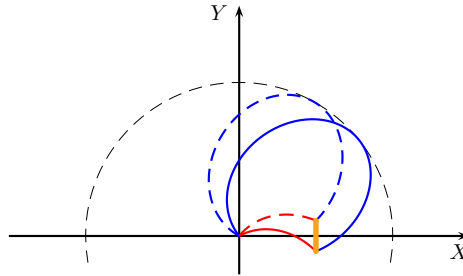


Figure 7.13: A small staff (yellow) parallel to the Y -axis. The even image displays the staff relatively undistorted and can be seen almost in front of the observer. In the odd image (which the observer sees to the left of him), the back side of the object is perceived horizontally mirrored, as the interconnecting geodesics (blue) intersect.

The discussion, so far, suggests that the odd image visually rotates to the left because it reveals the opposite behavior of the even image. However, we must take all effects into account: Fig. 7.13 puts a staff instead of the pointlike sphere into the scene. Thus, we must calculate a multitude of interconnecting geodesics to explain the exact optical appearance. However, for an elementary discussion, the visual rays for both ends of the staff are sufficient. The two primary rays associated to the odd image intersect and, therefore, the image appears mirrored compared to the even image. Due to this additional effect, the odd image will not visually rotate to the left, but to the right as well. The egocentric visualizations, also generated using the GÖDEL ENGINE, are consistent with the analysis presented above. Fig. 7.14 shows the odd and the even image for several initial positions.

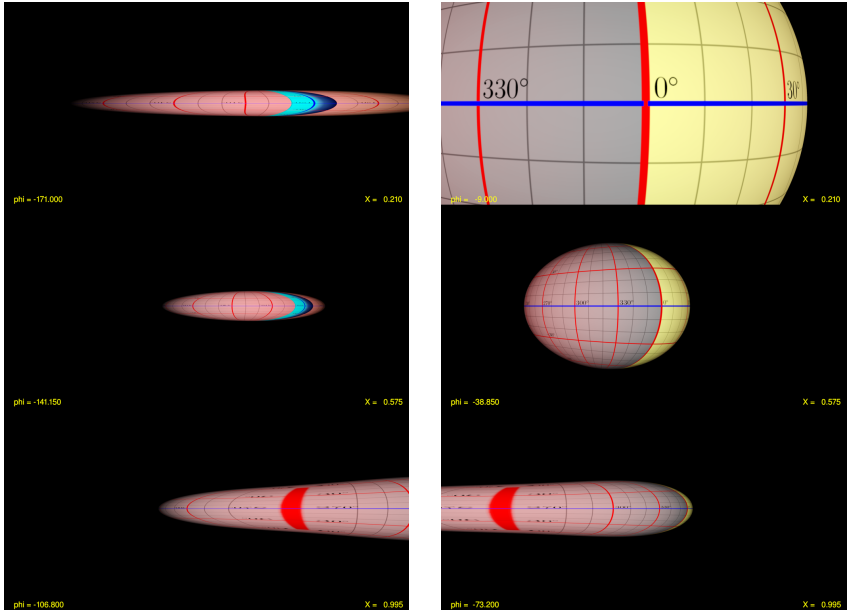


Figure 7.14: Quasistatically pushing a sphere beyond the horizon (GE). The left column shows the odd image, whereas the right column depicts the even image. From top to bottom, different positions (which approximate the values chosen in Fig. 7.11) for the sphere are visualized (`QuasistaticXAmbient.avi`).

The movie sequence `QuasistaticXAmbient.avi` generates an easily interpretable graphic image of the visibility and surface latitude angles. In the bottom right, the current position of the sphere is shown. Additionally, the direction of the point of interest is provided in the lower left. The sequence consists of three parts: First, the observer focuses on the even image and slowly rotates his viewing direction to the left. Second, he aligns his line of vision with the odd image. Finally, the 4π -projection is shown, where the reddish background symbolizes a line of sight, approximately along the positive X -axis.

Fiat lux

Now, we turn on the point light source which is resting at the observer's position. We consider the correct angular dependency between the reflected secondary ray and the direction under which

the primary ray intersects the object. The sphere is pushed across the horizon exactly as in the previous scene. Fig. 7.15 again shows interconnecting geodesics, but illustrates those paths on which the sphere is being illuminated.

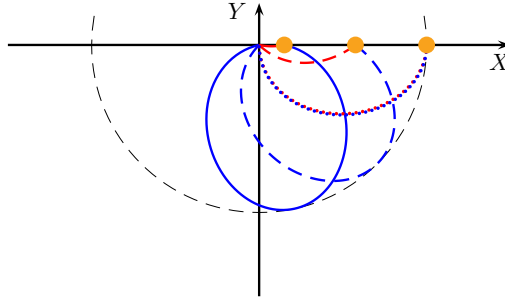


Figure 7.15: Geodesics, comparable to Fig. 7.11, which connect the light source with the object. These future-bound geodesics also start at the origin, but wind counterclockwise.

Similar to the *object images*, these interconnecting geodesics define **light images** – i. e. the images of the object that are “visible” to the point light source. These images are equally arranged into pairs of different order. Of course, the point light source illuminates the object along future-bound geodesics and not past-bound curves, which are used for the observer’s perspective.

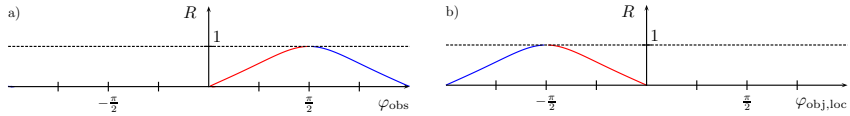


Figure 7.16: How the light source “sees” the object. These two images show under which direction a lightlike geodesic must start in order to hit the object (Fig. 7.16a) and reveals the intersection angle of the light ray with the object (Fig. 7.16b). Again, all angles are measured in the respective local frame.

Contrary to Fig. 7.11, the lightlike geodesics start at the origin but propagate into the future and, consequently, do not evolve clockwise but counterclockwise. As a result, the interconnecting geodesics for the point light source show a comparable but reverted behavior when compared to Fig. 7.11. For object positions close to the origin, the front face of the sphere is illuminated along the even path and the back side is lit due to photons on the odd curve segment. If the sphere is pushed towards the horizon, the two local horizontal angles under which the sphere is illuminated converges to a single value $\varphi_{\text{obj,loc}} = +\pi/2$, cf. Fig. 7.16b.

Similarly, the light source can “see” the right side of the object, as precisely shown in Fig. 7.16a. As the sphere is located closer and closer to the Gödel horizon, the left face can be *seen* but the right side is *illuminated*.

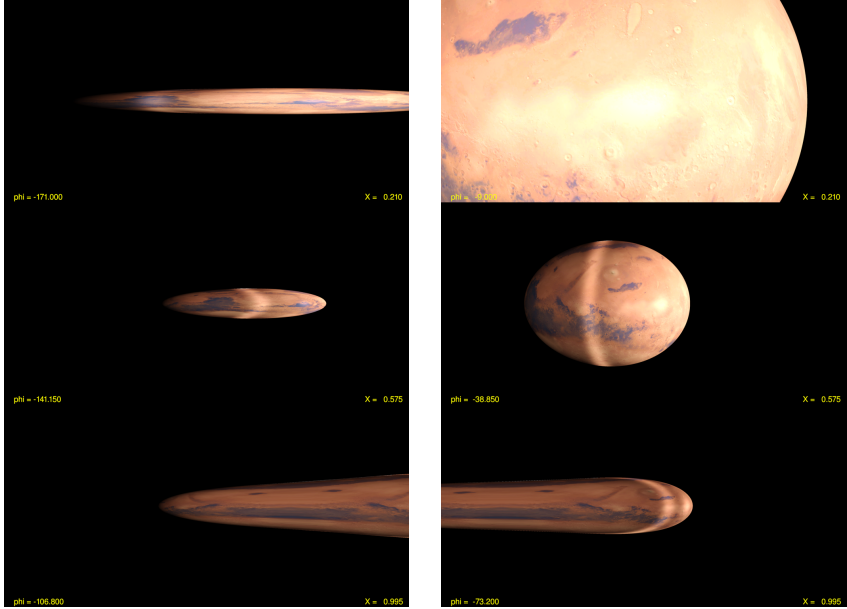


Figure 7.17: Quasistatically pushing a sphere beyond the horizon (GE), now with a Mars texture and the light turned on. Besides these changes, the scene parameters are identical to Fig. 7.14 (QuasistaticXIllumOrigin.avi).

Fig. 7.17 displays the egocentric visualizations utilizing a Mars texture and the light source. The above analysis is confirmed: Close to the origin (upper row), both the front and back face of the sphere are illuminated by light images. Note that non-zero diffuse as well as specular light material coefficients are applied. The latter light component leads to highlights within the illuminated regions of the sphere. The middle and bottom row of Fig. 7.17 show the sphere on positions closer to the horizon. Exactly as the local intersection angle $\varphi_{\text{obj,loc}}$ converges to $+\pi/2$, both highlights approach each other until they merge in a single bright spot, which is as soon as the sphere reaches the horizon. Note that we obtain two highlights for each object image because we consider all relevant interconnecting geodesics.

After this simple case, we move the point light source around the Mars sphere on a circular orbit, as defined in Fig. 7.18. The movie sequence `QuasistaticLightMotionOnCircleXY.avi` shows the result of this simulation.

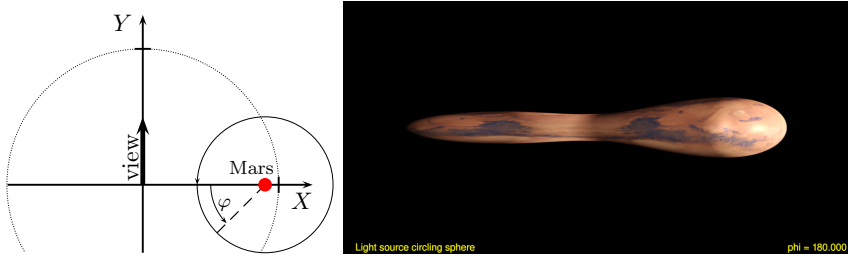


Figure 7.18: Scene definition and egocentric visualization of a light source moving around Mars.

In the rendering on the right, we have the observer, Mars and the light source located along one radial line (GE). The observer is located at the origin, the Mars sphere is at $R = 0.9$ and the point light is located at $R = 1.4$, i. e. beyond the horizon $R = 1$ (`QuasistaticLightMotionOnCircleXY.avi`).

The film clip reveals another interesting property of Gödel's universe. Fig. 7.18 depicts a single frame of the movie at the moment where the light source takes its furthest position from the observer and is located far beyond the horizon. As long as the Mars sphere is located in a common causality region of the light source and the observer (compare Fig. 5.8) photons from this light source are perceivable by the observer at least as indirect light. Thus, it is possible to exchange information across the Gödel horizon. Consider two arbitrarily distant but resting observers and an arrangement of properly aligned mirrors, where each is located within a common causality region of the two adjacent ones. By that means, the two observers are connected by a chain of transfer. Both observers can exchange information using, for instance, Morse code light flashes.

This effect demonstrates the benefits of an interactive approach. It can, of course, be found by investigating the geodesic equations or the diagrams of lightlike paths shown in Sec. 5.1. However, a fast visualization technique allows for a playful approach to scientific insights. Additionally, the prompt visualization feedback even enables the scientific layperson to explore and discover visual or physical effects.

7.3.2 Objects at Arbitrary Positions

After having illustrated the visual impressions for quasistatically moving objects within the equatorial plane, we move on to a more general motion of the object as well as the point light source.

Ambient illumination of a vertically moving sphere

After the restrictive set of scene parameters, we access the Z coordinate for object positions. To develop an idea of what can be expected, we resort to eqns. (6.5). Fig. 7.19 shows a series of plots for these relations. Exactly as in Fig. 6.5, these plots facilitate the identification of the number of visible images as well as the vertical viewing direction for a given set of object positions.

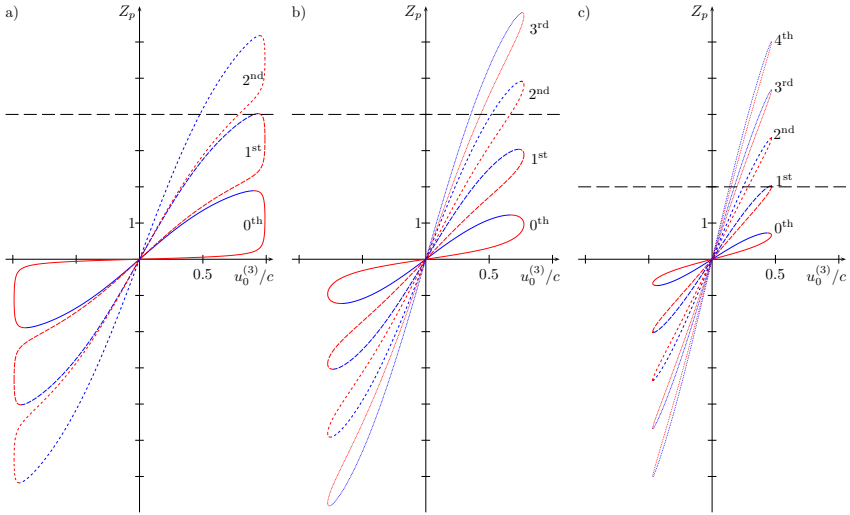


Figure 7.19: Exemplary plots of the left sides of eqns. (6.5), as in Fig. 6.5. The abscissa denotes the cosine of the vertical viewing direction θ (cf. Fig. 6.4). From left to right, the radial coordinate of the destination point is $R_p \in \{0.1, 0.5, 0.8\}$. By setting $Z = Z_p = \text{const.}$, we obtain the vertical angles under which a point at (R_p, Z_p) is visible and which image orders do not appear. For example, Fig. 7.19b reveals that the zeroth and first order images of an object located at $(R_p, Z_p) = (0.5, 4)$ are not visible.

Fig. 7.19a depicts eqns. (6.5) for a rather small radial coordinate ($R_p = 0.1$) of a vertex. After setting $Z_p = \text{const.}$, we can read off the $e_{(3)}$ -component of the primary ray's initial direction. Let, for example, $Z_p = 4$. In this case, the relation does not have a solution for zeroth order. Thus, these two images are visually missing. The first order images are still existent because the relation has two solutions. However, these images have nearly identical vertical viewing directions and it can easily be shown that the respective horizontal visibility angles are similar as well. For an extended object, the stitching algorithm, cf. Sec. 6.3.4, must be executed because several

vertices of the mesh may not be visible for these two first order images. Fig. 7.19b shows a similar situation, where a vertex is located at a radial distance $R_p = 0.5$. In this case, the four images of zeroth and first order are missing; only images starting from second order are observable. Inspecting the whole series of plots, Figs. 7.19a-c, from left to right, we find that the closer a vertex is to the horizon, the smaller the vertical viewing directions become and the fewer image orders there are in sight. Only in the limiting case $Z_p = 0$, all image orders are visible up to the Gödel radius. However, these higher order images are occluded if the object is resting or moving quasistatically (as discussed in the last section).

To simplify matters, we denote lower order images that are not visible due to the above reasons as *being beyond the Gödel horizon*, albeit the *object* itself is still located within the horizon. The entity has crossed the horizon if all (arbitrarily high) order images of every vertex have disappeared. Diagrams as shown in Fig. 7.19 allow for the identification of these events. However, these plots solely consider pointlike objects so that extended objects slightly deviate from the illustrated behavior.

In the movie sequence `QuasistaticZAmbient.avi`, the egocentric visualizations illustrate this train of thought; two frames are shown in Fig. 7.20. The Mars sphere is located at $R_p = 0.8$ and is pushed to positive Z values and, after that, downwards below the (XY) -plane. We observe that the higher order images, which are occluded as long as $Z_p = 0$, fan out and the symmetry of the problem to the (XY) -plane can easily be identified. Note that the small, green sphere resembles a point in the (XY) -plane and solely serves to aid the viewer. Regarding the motion of this green sphere as a reference, we can easily distinguish if the observer is looking slightly up or down.

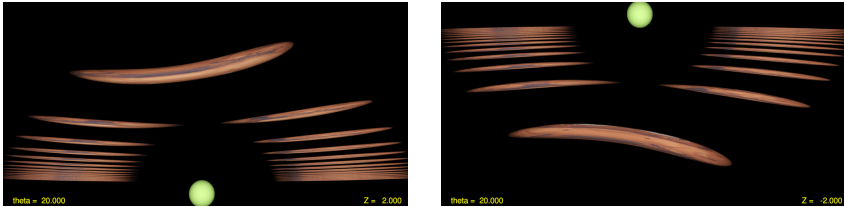


Figure 7.20: Mars located at $R_p = 0.8$ and $Z_p = \pm 2$. The green sphere is located in the (XY) -plane and thereby serves for better visual orientation. The left subimage displays Mars above $Z = 0$, and we have $Z < 0$ for the right subfigure. All images appear arranged on a circle, but the images of zeroth order are missing (cf. Fig. 7.19c and `QuasistaticZAmbient.avi`, (GE)).

Beyond the mere fanning of the object's images, we notice a form of symmetry. The images seem to be, more or less, arranged on a circular path around the green ball. In the last part of

the movie sequence (and in Fig. 7.21), we replace the Mars sphere by a vertically aligned staff. The bar is rendered using a checkerboard texture and visually appears, in deed, as a circle. In the last frames of the movie sequence, the bar is pushed beyond the horizon. It always appears as a circle as long as it is visible. Due to our playful approach, we herein detect an unknown visual effect.

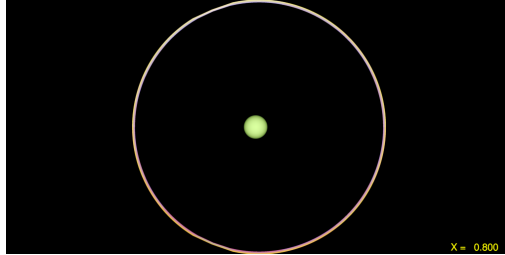


Figure 7.21: A vertical staff located at $R_p = 0.9$ appears as an (almost) perfect circle. (end of `QuasistaticZAmbient.avi`, (GE)).

Using the analytical solution to the geodesic equations, eqns. (5.7), we can compute the two angles under which a point in the equatorial plane of the observer appears. Under the assumption that the visible representation is a circle, we formulate the visual directions constituting this shape. After inserting the initial conditions (5.3) and using the relation between the vertical viewing direction and the Z -coordinate, eqns. (6.5), we find our assumption confirmed. The visual angle α , under which the diameter of the circle is seen, then reads

$$\alpha = 2 \arcsin \left(\sqrt{\frac{1 - R_p^2}{1 + R_p^2}} \right), \quad (7.3)$$

where R_p is the radial coordinate distance of the staff to the origin. We denote this visual effect as **Gödel ring**.

Note that the green orientation sphere is *not* exactly in the middle of the visual circle because it is implemented as an object within the Gödel universe at close proximity to the observer. Thus, the green ball's position is marginally affected by the curved primary rays as well, slightly moving it visually to the left. We also find that the staff does not represent a perfect circle. This effect is, ultimately, a rendering artifact due to numerical issues, cf. Sec. 6.4.2. A raytracing approach, such as `GEOVIS`, generates a fair circular shape.

Resting Mars sphere illuminated by a quasistatically moving point light source

After having moved the Mars sphere in the Z -direction, we now investigate the optical appearance of a sphere, which is resting at $(X, Y, Z) = (0.8, 0, 0.5)$, and a point light source moving upwards tangential to the Gödel horizon of the observer. Several renderings are shown in Fig. 7.22. The left subfigure, Fig. 7.22a, shows the result of the simulation for a point light source where we consider light images up to second order. The corresponding movie sequence, `SphereIllumPushZ_a.avi`, reveals that the light images of zeroth order disappear if the light source is above $Z \approx 2.5$. In this case, the Mars sphere is visually beyond the horizon (as defined on p. 128). For $Z \lesssim 2.5$, we can identify the regions of the Mars sphere that are “visible” or “invisible” to the light source for zeroth order. A clearly recognizable dividing line exists, where the brightness abruptly changes. This line is hinted in Fig. 7.22a using two green arrows. The farther the light source moves upwards, the fewer light images there are visible, until only ambient lighting remains.

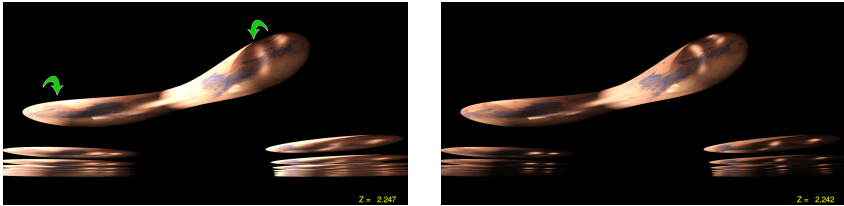


Figure 7.22: Moving the light source vertically. The Mars sphere is located at $(X, Y, Z) = (0.8, 0, 0.5)$, whereas the light source is moving along $(X, Y, Z) = (1, 0, Z)$. In the left subimage, light images up to second order are considered and no distance attenuation is applied. The green arrows identify the borderline where zeroth order light images vanish. The right subimage, illuminated using a linear distance attenuation, shows light images including ninth order. (`SphereIllumPushZ_a.avi`, `SphereIllumPushZ_b.avi`, (GE)).

Fig. 7.22b shows light images up to the order $n = 9$. For this scenario, we enable a linear distance attenuation because the rendering would otherwise be overexposed. Since we consider high order images, the light source can be moved to a large distance from the Mars sphere and still illuminate it. The accompanying sequence, `SphereIllumPushZ_b.avi`, confirms this assumption.

If we move the light source horizontally instead of vertically, we receive a different behavior. While the photons in Gödel’s universe can attain an arbitrary vertical distance to the point of emission, the maximum radial extent is limited by the respective Gödel radius. Thus, moving the light source horizontally would lead to an almost instantaneous disappearance of all light im-

ages. Of course, we must consider the exact definition of the scene, such as the spatial extent of the visualized objects. However, the general behavior is clear: Images of vertically moving light sources disappear order by order, whereas horizontal motion results in a more or less simultaneous vanishing of all light image orders. Since the outcome of such a scene definition is obvious, we omit the renderings within this context.

Pushing one object visually behind another

Consider two objects, one resting at $(X, Y, Z) = (0.8, 0.0, 0.5)$ and the other quasistatically moving along $(X, Y, Z) = (X, -0.4, 0.1)$, i. e. in the X -direction. The spheres are, as usual, formulated with regard to their respective frame and to not permeate each other at any point of the simulation.

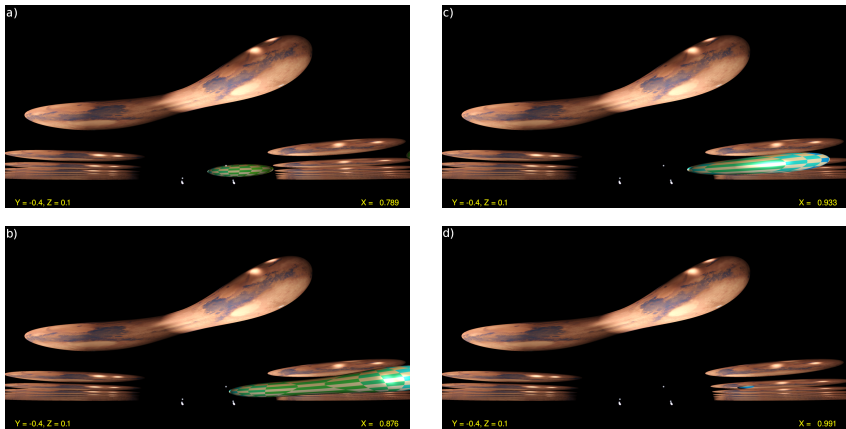


Figure 7.23: Disappearance before occlusion. The Mars sphere (ten image orders shown) rests at $(X, Y, Z) = (0.8, 0.0, 0.5)$. A checkered sphere (only zeroth order images) is moving along $(X, Y, Z) = (X, -0.4, 0.1)$. Along this path, the latter sphere visually disappears behind the horizon *before* being occluded by the higher order images of Mars. The scene is illuminated by a point light source (white dots; see `TwoSpheres.avi`, (GE)).

Fig. 7.23 shows the egocentric renderings and indicates the aim of the scene definition. We try to *visually* push the zeroth order images of the moving (checkered) sphere behind the higher order images of the resting (Mars) sphere. One might expect that the checkered sphere will first be occluded by Mars and, not until then, visually disappear behind the Gödel horizon. However, the

visualizations in the sequence found in Figs. 7.23a-d clearly reveal that the zeroth order images disappear *before* being occluded by the higher order images of the other sphere.

The explanation for this unexpected optical effect is directly found in Fig. 7.19 and constitutes the difference between an object which is entirely beyond the horizon and the *visual* disappearance of object images as defined on p. 128. The essence of Figs. 7.19a-c is that lower order images potentially disappear earlier than higher order images: The two lowest order images, for example, in Fig. 7.19b, are visually beyond the horizon, whereas all other images are still in sight.

Geometrically speaking, consider a vertex that is very close to the actual horizon at a large Z -coordinate. To interconnect this point with the origin a very high number of windings of the helix-like geodesics is required. Lower order images cannot be seen because the corresponding geodesics do not reach radii large enough to hit the point; see Fig. 5.1. Consequently, lower order images disappear, in this sense, earlier than higher order images and thus are not necessarily occluded by the latter.

7.3.3 Shadows

All images so far have been rendered without the consideration of self-shadowing effects. The reasons for this exclusion will be explained below. We have seen that we are confronted with a large amount of visual information after turning on the point light. To prevent a visual overload, the shadowing computations were neglected. After being acquainted with the additional effects resulting from the local illumination model, we incorporate the self-shadowing as described at the end of Sec. 6.3.4. All following images are rendered using a linearly attenuated ambient as well as point light. Thus, higher order images appear less bright.

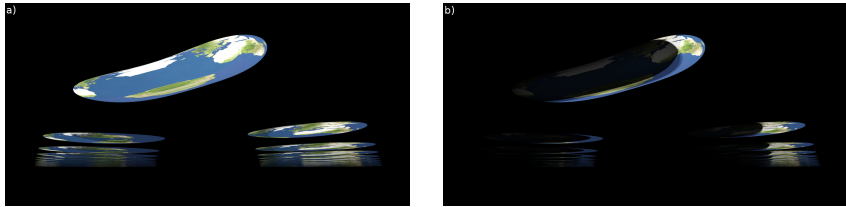


Figure 7.24: Shadow rendering with no angular dependency. Fig. 7.24a shows the Earth sphere without shadowing computations and, moreover, no angular dependency is considered in the illumination calculations. In Fig. 7.24b, the shadowing computations are included (GE).

Consider Fig. 7.24, where we see Earth resting at $(X, Y, Z) = (0, -0.85, 0.6)$. The observer is located at the origin and looks into the positive X -direction (and a bit upwards in order to center

on the visible images of the sphere). We calculate all object images, including 14th order. Due to the distance attenuation of the point light, higher order light images are hardly visible, thus we limit the simulation to fourth order light images. In Fig. 7.24a, the shadowing computations are neglected. Since the light source is located at the origin as well, it “sees” the same vertices as the observer. Thus, each vertex is illuminated and visible. Note that we neglect the angular dependency of the diffuse and specular light components for now. Consequently, the images appear flat. The right subimage in Fig. 7.24b incorporates the self-shadowing and reveals the regions of the Earth sphere which, now, cannot be interconnected to the light source because the light ray would have to traverse the sphere before hitting the surface from the inside.

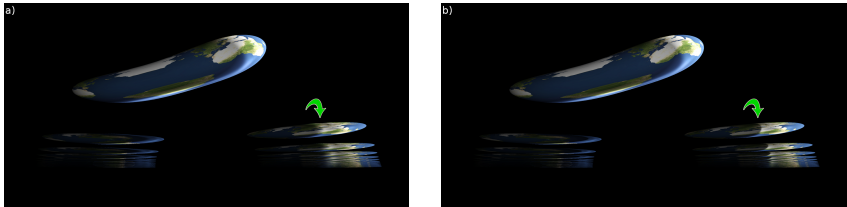


Figure 7.25: Shadow rendering with angular dependency. Fig. 7.24a displays Earth without shadowing computations, but includes the angular dependency of the illumination. Obviously, Fig. 7.24b and Fig. 7.25a have comparable regions that are illuminated. The right subimage, Fig. 7.25b, additionally applies the shadowing calculations which merely partitions dark and lit regions more strictly – as indicated by the green arrows (GE).

If we now apply the angular dependency of the Phong model, we obtain the renderings shown in Fig. 7.25. Obviously, most of the four images in this section are very similar.

The underlying reason for the conformity between Fig. 7.24b, Fig. 7.25a and Fig. 7.25b is given by the Phong illumination model, cf. Sec. 3.1.1. If the scalar product between the involved directions is negative, the corresponding illumination value is set to zero. The computation of the self-shadowing effects is conducted similarly and thus all three renderings are very similar. Note that the self-shadowing procedure is, to be precise, an approximation: Only if the object is convex and the light rays are straight lines, we can compute the precise self-shadowing as detailed in Sec. 6.3.4. For the Gödel universe, the latter condition is not fulfilled.

7.4 Relativistically Moving Objects

In Sec. 6.4.2, we discussed the reason why the GÖDEL ENGINE cannot be used to generate visualizations for fast moving objects. However, even a general raytracing approach exhibits serious

numerical difficulties. In this section, we discuss how these difficulties are overcome and the rendering performance is increased using a simple optimization. We also detail the modifications to the `GeoVis` framework because the worldline of an object must be adapted to the requirements of the raytracing system in order to obtain correct visualizations of time travel.

Now, we discuss the numerical problems arising for fast moving objects, visualized with a raytracing approach. During the calculation of an image, we encounter three linear approximations. First, we formulate the objects with respect to a local frame of reference, which is a linear approximation to the metric at a given point. Second, we must transform a ray segment to the local tetrad of an object during the calculation of an intersection. To formulate this ray segment with respect to a tetrad of the worldline of the object, we use the coordinate difference between a point of the ray segment and the position of the tetrad in order to obtain a vector, which is then expressed with regard to this tetrad. Finally, the worldline of an object is given as a discretized path consisting of four-dimensional, linear segments. A tetrad for an arbitrary position on the worldline is calculated as the weighted sum of the two tetrads at the endpoints of the corresponding segment. We need extraordinary small stepsizes for the light ray as well as for the worldline of the object due to these three linear approximations. Otherwise, we encounter numerical errors resulting from the linear interpolations and manifested in severe rendering artifacts, as shown in Fig. 7.26. These small stepsizes drastically decrease the rendering performance.

To calculate an image with a resolution of 2048×512 pixels, a 128 CPU compute cluster needs approximately 30 minutes. Consequently, a sequence of 1800 images – one minute long at 30 frames per second – needs 1.25 months to render. Fortunately, most of the pixels are black because no object is intersected along the corresponding lightlike geodesic. We can utilize this circumstance to increase the image calculation performance by splitting the rendering process into two consecutive steps. First, we generate a low resolution image of 512×128 pixels which only contains the binary information of an object's visibility. This stencil mask takes 1/16th the time to be generated when compared to the rendering of the full resolution image. In the subsequent step, this mask is exploited for the calculation of the large image. We generate lightlike geodesics solely for the non-empty pixels. Therefore, only these pixels require a non-negligible calculation time. The generation of a stencil mask usually takes approximately 90 seconds and the calculation of the final image an additional 30 seconds, resulting in a total speedup of 15 and therefore finalizing 1800 images in about 2.5 days.

The increased rendering performance is a helpful optimization. However, we must analyze the calculation of a surface intersection again. In the `GeoVis` framework, not every ray segment of each ray is intersected with all segments of an object's worldline. Such an approach would require a tremendous amount of time. Instead, the `GeoVis` framework already retrieves the point of the worldline which is the best match for the currently investigated ray segment.

In technical terms, a binary comparison function returns the local tetrad closest to the ray segment *with respect to the coordinate time*. This binary function necessitates a monotonically

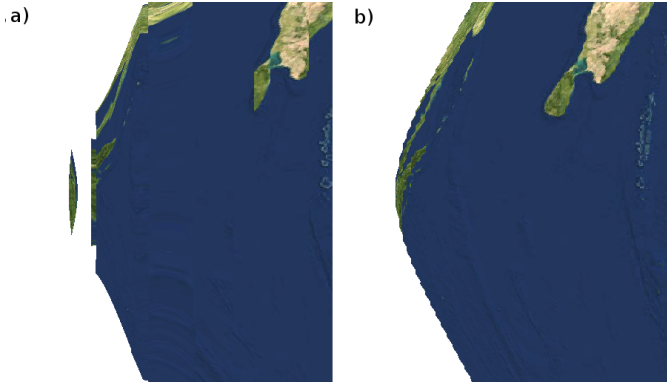


Figure 7.26: Comparison of two renderings obtained using different stepsizes for the lightlike geodesics as well as for the worldline (GV). In these images, the object is traveling on a CTC. In Fig. 7.26a, we use a stepsize of $\Delta\lambda = 10^{-2}$ for the light rays and $\Delta\tau = 5 \times 10^{-5}$. We encounter holes in the visualization alongside other rendering artifacts. Fig. 7.26b is calculated using $\Delta\lambda = 5 \times 10^{-4}$ and $\Delta\tau = 5 \times 10^{-6}$. Slight artifacts are still present, but the image quality is now satisfying. An analysis of the visual appearance of travel on CTCs is given in Sec. 7.4.3.

increasing coordinate time in the array of local tetrads (which represents the worldline). Since time travel is possible in Gödel's universe, the coordinate time can decrease along a worldline and far more than one point of the worldline can be temporally close to the ray segment. Hence, the return value of the binary function is undefined and the calculated images can be false. In a generic approach, the binary comparison function must be replaced by another function, which returns not only one tetrad but an array of tetrads, corresponding to all points of the worldline close to a ray segment with respect to the coordinate time. Fortunately, we can use a simpler approach in Gödel's universe.

Along a worldline, the coordinate time can only decrease (for increasing proper time of the traveling object) outside of the Gödel horizon. Only then the future light cones intersect the planes of constant coordinate time, as shown in Fig. 4.5. The region beyond the Gödel radius is of no interest in an egocentric visualization because objects are only visible along those parts of a worldline that are within the horizon. Consequently, those exterior parts of the worldline can be omitted. In practical terms, we divide a worldline into segments on which the coordinate time is monotonically increasing. This procedure might result in several copies of the same object, residing within the horizon at a certain coordinate time. This is not an inaccuracy, but the goal

of this division into segments because a time traveling object can reappear from beyond the horizon “before” leaving it; see Fig. 5.4 and Fig. 5.9. Thus, this reorganization of the worldline segments is required if the object is moving (partially) beyond the Gödel horizon.

Although the GÖDEL ENGINE cannot be used for the visualization of fast moving objects, we can adopt its functionality for a quantitative analysis of the visualizations shown. Therefore, we utilize the concepts of the CUDA programming model, which facilitates the retrieval of calculated data from the GPU. First, a worldline – representing the central point of an object moving through Gödel’s spacetime – is generated analytically or numerically. It is then uploaded into the GÖDEL ENGINE. For every point x^μ of the worldline, we then calculate the interconnecting geodesic in parallel. In addition to the information stored in the worldline and the analytical solutions to the geodesic equations (eqns. (5.5) and (5.12)), we obtain the time when this point x^μ is visible to the observer and the angle under which it is visible. Another possibility is to determine the proper time of light emission (with respect to the object), plot against the proper time of absorption (with respect to the observer). All diagrams depicting a quantitative analysis, such as Fig. 7.28, are generated using this method.

Note that all images are rendered with a significant vertical zoom because higher order images of an object tend to be very narrow. Panorama projections are rendered with a field of view of 360° horizontally and 12.5° vertically, whereas the aspect ratio of these images is $4 : 1$. Therefore, these images are stretched by a factor $f = 7.2$ in the vertical direction. Spherical projections are rendered using a quadratic image format, where we have $f = 2$.

7.4.1 Geodesical Motion Restricted to the Causal Region

The first scenario that we visualize is geodesical motion starting at the origin. In the limiting case $v \rightarrow c$, we obtain the lightlike motion of photons, which defines the Gödel horizon as shown in Fig. 5.1. For velocities less than the speed of light, the geodesics are of similar shape but smaller in radial extent. Therefore, particles starting at the origin periodically return to $R = 0$ and never reach the horizon because the turning point is at a radial distance

$$R_{\text{turn}} = \sqrt{\frac{v^2}{2c^2 - v^2}} \leq 1. \quad (7.4)$$

The maximum value for the radial turning coordinate R_{turn} is easily obtained using eqns. (5.7b), (5.6) and (5.3a) for timelike geodesics, where $u_0^{(0)} = \gamma c$. In the limit $v \rightarrow c$, we have $R_{\text{turn}} = 1$, which consistently defines the Gödel horizon. In the following visualizations, the observer rests at the origin and aligns his camera to the positive X -direction, as shown in Fig. 7.27. We consider four different initial velocities ($0.2c$, $0.5c$, $0.7c$ and $0.9c$) to get a first impression on the visual appearance of fast objects.

In Fig. 7.28, the quantitative analysis of the visibility is shown. Here, we plot the time of observation against the horizontal viewing direction of the observer. We denote this type of plot as

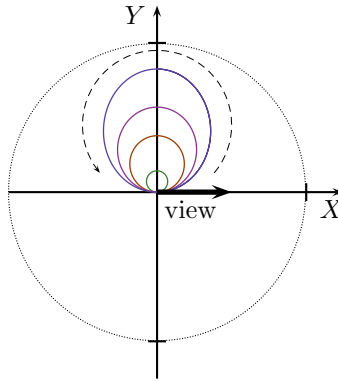


Figure 7.27: Four objects with different initial velocities. The observer is looking along the $+X$ -axis and the objects are starting from the origin in that direction. The different colors of the geodesics denote different initial velocities. The green curve represents an initial velocity of $0.2c$, red depicts $0.5c$, violet characterizes a velocity of $0.7c$ and blue symbolizes $0.9c$. The geodesics evolve counterclockwise, as indicated by the dashed arrow.

a **visibility angle diagram**. This plot can be interpreted as follows: For a fixed observation time τ_{obs} – indicated by the dashed horizontal line in Fig. 7.28a – we obtain the horizontal viewing direction under which the object’s images are visible. For this example, the observer will see the center point under the two angles φ_0 and φ_1 . We can directly identify these angles in the accompanying movie sequences because these visualizations are generated using a panorama camera. An angle of $\varphi = 0$ represents the observer’s point of interest and is located at the center of the egocentric renderings, whereas $\varphi = \pi/2$ marks the negative Y -direction and, therefore, the right vector of the observer’s local frame.

These plots can be used as lookup-tables for the visualizations: For a fixed observer time τ_{obs} , we find the viewing directions as discussed above. Then, we pick the image of the corresponding movie which is the closest to this observer time⁵. Using the curve progression of the plot, we can decide in which direction the object moves without having to consult the entire movie sequence: The quantitative analysis reveals a monotonically decreasing behavior for an ascending viewing direction, consequently the object’s images move to the left for increasing observer time. The plots reveal a remarkable curve linearity; only at high initial velocities (see Fig. 7.28d) we can identify significant deviations from this behavior. Thus, we expect that the Earth sphere will

⁵The observer time for any visualization is located at the bottom right of each movie frame, denoted as tau.

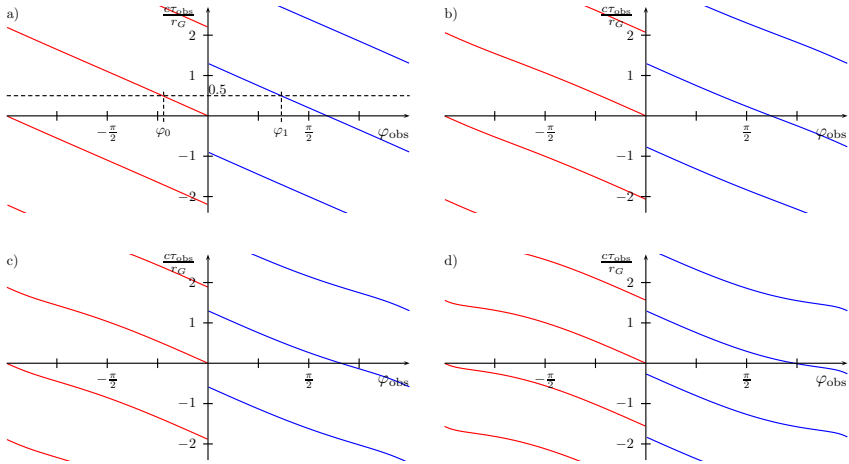


Figure 7.28: Visibility of the center point of the sphere. In these plots, we neglect the spatial extent of the fast traveling sphere and consider the horizontal viewing direction φ_{obs} , depending on the proper time τ_{obs} of the observer. Each subfigure illustrates a specific initial velocity of the moving object ($0.2c$, $0.5c$, $0.7c$ and finally $0.9c$ in Fig. 7.28d). Note that only the even (red) and odd (blue) images of zeroth order are considered to clearly represent the situation without an overload of information. Since the Earth sphere is traveling within the horizontal plane of the observer, we neglect the analysis of the vertical viewing direction.

visually move with almost constant angular velocity to the left. This assumption is confirmed after reviewing the movie sequence *CausalMotionFromOrigin.avi*. Also, the visual motion of the even image (red curve) is restricted to the left half-space, whereas the observer perceives the odd image (blue curve) always to his right. The reason behind this behavior can be understood by investigating Fig. 6.1 in the previous chapter. The yellow circle indicates a point on a timelike geodesic, close to the observer and located in the first quadrant of the coordinate system. The light can reach the observer along two very different paths: The even image resulting from the red curve segment (see Fig. 7.28) is visible to the left and the odd image appears at a position in the observer's right half-space.

The discontinuities in the plots contained in Fig. 7.28 are a result of the chosen angular coordinate: As soon as the object passes the origin, the angular coordinate of its position abruptly changes by π . For instance, the Earth sphere passes the observer at $\tau_{\text{obs}} = \tau_{\text{obj}} = 0$ for all four initial velocities and then moves into the positive X -direction where $\varphi_{\text{obs}} = 0$. The observer

therefore sees the even image of the sphere right in front of him for $\tau_{\text{obs}} \gtrsim 0$ because this image is defined by the shortest interconnecting geodesics for which the light travel time is small. For $\tau_{\text{obs}} \lesssim 0$, the observer will see the image behind him ($\varphi_{\text{obs}} \approx \pm\pi$). Additionally, all plots also show a periodic behavior because the timelike motion of the sphere is not restricted to one loop of the geodesics but is periodical: The Earth sphere passes the observer's position a multitude of times in equal time intervals.

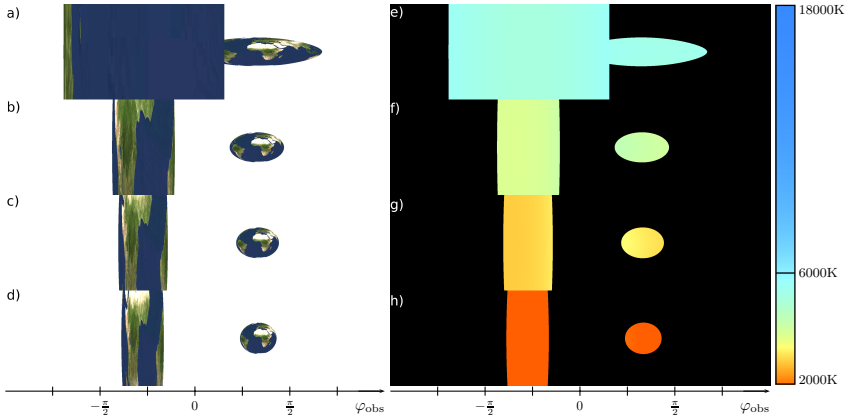


Figure 7.29: Ego-centric visualization (left column) and apparent surface temperature (second column) for an early observation time $\tau_{\text{obs}} = 0.6 r_G/c$, where the sphere has just passed the origin (GV). From top to bottom, the initial velocity increases from $0.2c$ to $0.9c$ (`CausalMotionFromOrigin.avi`, `CausalMotionFromOrigin_redshift.avi`).

Figs. 7.29 and 7.30 reveal the impressions as recorded by the observer's panorama camera. Note that for clarity of the visualization as well as the quantitative analysis, we restrict the backtracing of primary rays such that only the zeroth order images are visible. Higher order images will be discussed in the next section. Thus, we see two images of the sphere at most, where the vertical zoom factor $f = 7.2$ has been applied. The even image shows the Earth sphere along the shortest interconnecting geodesics, and the odd image results from light emitted by the sphere which has propagated to the Gödel horizon first and then reaches the camera. The Doppler shift is also illustrated in these images. Using a surface temperature of 6000 Kelvin – indicated as a small black line in the vertical color bar – we can distinguish the direction in which the object is visually moving. As presumed, the frequency shift for small initial velocities is hardly noticeable. The surface temperature appears to be about 6000 Kelvin for $v = 0.2c$. For an increasing velocity,

the Doppler shift becomes more intense. Foremost at $v = 0.9c$, we can see both images extremely red shifted (Fig. 7.29) at the beginning of the simulation. Thus, these images are moving visually away from the observer. The most interesting example is shown in Fig. 7.30h. The odd image is visually surrounding the observer and its apparent surface temperature covers the entire range of the color bar, allowing for the identification of relative flight directions *within* a specific image. This situation is comparable to the initial frames of the movie `CausalMotionFromOrigin.avi`, where the even image surrounds the observer. There, we see a similar color gradient and can therefore identify the regions moving towards or away from the observer.

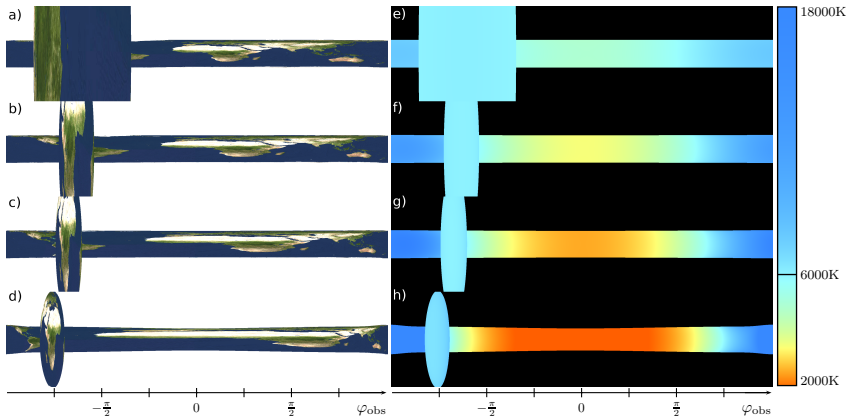


Figure 7.30: Egocentric visualization and apparent surface temperature for a later observation time ($\tau_{\text{obs}} = 1.32 r_G/c$) (GV). The even image visually travels away from the observer and the odd image results from light, which has been emitted when the sphere was at the origin. Due to the rotational symmetry, the odd image is seen across the entire range of the horizontal observation angle (`CausalMotionFromOrigin.avi`, `CausalMotionFromOrigin_redshift.avi`).

To clarify the origin of the light that constitutes the odd images, consider the following situation: Let the central point of the sphere be located near the origin. Additionally, the Earth is not moving, but resting. Then, the observer would see the object surround him because he is located within the sphere. An egocentric visualization would only show the even image of zeroth order because all other images would be occluded by this image of the object. Nevertheless, the odd image of zeroth order (if it could be seen) would show the sphere “surrounding” the observer as well. In contrast to the even image, the odd image would not cover the whole visual range of the observer due to the different light travel paths. Consider, for instance, Earth’s North Pole. For the

even image, the interconnecting geodesic is a straight line aligned with the Z -axis because the observer is located at the center of the sphere. The interconnecting geodesic for the odd image is of a very different shape because light travels on the helix path to the horizon and, not until then, to the observer. Thus, the observer would then perceive the North Pole not above him but somewhere in front of him. Consequently, the odd image would cover a vertical angular range which is considerably less than π . The even images would reveal the object's interior and the odd images – because light travels to the horizon first – would show the exterior of the sphere. The latter image would simply be not visible because it is occluded by the first. Now let the sphere, as discussed in the scenario of this section, be traveling close to the speed of light. Then, the light travel time must be taken into account and we understand that these two images (of the Earth sphere passing the origin) can be seen at very different observation times: The even image is seen at $\tau_{\text{obs}} \approx 0$ and the odd image, due to the light travel time being significantly longer, at the time $\tau_{\text{obs}} \approx 1.32 r_G/c$, as shown in Fig. 7.30. This train of thought is confirmed by Fig. 7.31. The even image of the early observation time (left column) and the odd image for $\tau_{\text{obs}} = 1.32 r_G/c$ (second column) result from very similar object positions but different light travel paths and times.

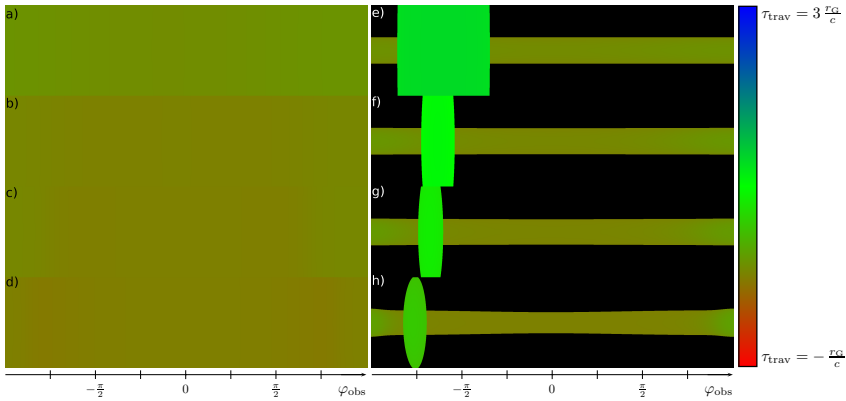


Figure 7.31: Comparing the emission time for objects starting at the origin. The left column shows the times color-coded for several different observation times $\tau_{\text{obs}} \gtrsim 0$ (GV). At these early times, the even image is surrounding the observer and about to leave him. The second column reveals the local time of emission for a later observation time ($\tau_{\text{obs}} = 1.32 r_G/c$). The local time of emission of the even images on the left is very close to the emission time of the following column (pale green with a slight reddish component). Thus, these images emerge from comparable positions of the sphere (`CausalMotionFromOrigin_emissionTime.avi`).

In Sec. 7.3, we discussed that a static object in the horizontal plane of the observer can be seen at most twice, as higher order images are occluded by the even and odd image of zeroth order. If the object is moving close to the speed of light, the occlusion effects of statically or quasistatically moving objects can be removed. For now, we adhere to the visualization of zeroth order images. This section illustrates the basic information, which can be extracted from egocentric visualizations and quantitative analyses: The textured spheres reveal the appearance and orientation of objects in Gödel's universe, the frequency shifted images show relative flight directions and velocities, the color-coded emission times allow for the comparison of light travel times or emission points and images horizontally stretched across the field of view show objects surrounding the observer at some point in time. Thus, we obtain a variety of information just by investigating a single picture (and not an entire movie sequence).

7.4.2 Visualization of Geodesical Time Travel

In Sec. 5.1.2, we analyzed time travel on geodesics. Here, we will visualize the optical appearance of a particle traveling close to the speed of light and starting at $R = 1/2$. For these initial conditions, we approach the maximum (partial) travel through time as described by eq. (5.14). We must apply the terminology defined in Sec. 6.1 very carefully. Until now, we have discussed the appearance of single *objects* and the associated visible *images*. Now, we highlight the optical effects of time travel. Thus, a single *object* may be visible more often. Each of these **instances of a physical entity** generates an arbitrarily high number of visual *images*.

The visualizations presented in this section have been calculated with an initial local velocity $v = 0.995c$; compare Fig. 5.3. The observer rests, again, at the origin. The object is starting radially outwards at $X = 0$ and $Y = -1/2$. The egocentric visualizations cover a time span of $c\tau_{\text{obs}}/r_G = 2.5 \dots 4$. The scene is illustrated in Fig. 7.32.

As in the previous example, the observer aligns his line of sight in the positive X -direction. Therefore, the central point of the egocentric visualization corresponds to the local $e_{(1)}$ -axis and the left and right borders of an image show what can be seen in the opposite direction. The time-like geodesic evolves in an area restricted to the forth quadrant. The observer will, during a large time span, see the object images in front of him due to the peculiar shape of the geodesics in Gödel's spacetime. Due to the time travel, we expect that the object will reappear from beyond the horizon before disappearing. The local time of the reappearing object must be higher (when compared to the disappearing instance) because the proper time along the geodesic monotonically increases despite the fact that the object partially travels into the past of the observer. The proper time always increases along a future-oriented timelike worldline.

These preliminary assumptions are confirmed by the quantitative analysis which is shown in Fig. 7.33. Subfigure 7.33a illustrates how the horizontal visibility angle φ_{obs} depends on the observation time τ_{obs} . In Fig. 7.33b, we see the proper time of the traveler τ_{obs} plot against the

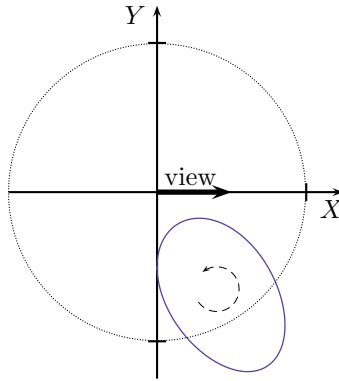


Figure 7.32: The observer is looking along the $+X$ -axis and the time traveling object is moving on the solid line counterclockwise.

proper time τ_{trav} of the observer. To be precise, the time τ_{obs} denotes the time (with respect to his local rest frame), when the observer sees light emitted by the traveler at the time τ_{trav} (measured in the voyager's frame). We refer to this kind of plot as an **emission time diagram**.

In contrast to the previous scenario, the visibility plot in Fig. 7.33a now includes higher order images and reveals that these images – both even and odd – almost coincide with the images of zeroth order. Since the object is traveling almost at the speed of light, the observer will see higher order images from previous loops of the periodical motion of the object: Zeroth order images result from light emitted not long ago, first order images are constituted by light sent out in the previous loop of the object, et cetera.

The even images (red curves) propagate visually to the right, and then reverse the direction of flight and head to the left, where they disappear behind the horizon. The odd images show the opposite behavior. At the horizon, the object reappears before it disappears beyond the visual range of the observer. This effect is hard to notice in these plots because they cover a relatively large span of observation time and the time travel, in contrast, has a very small effect on geodesics. To facilitate the location of this effect, a horizontal bar for a specific observation time is provided in the plot. The object is visible under the angles $\varphi_0, \varphi'_0, \varphi_1,$ and φ'_1 – for the zeroth order. Angles denoted with primes represent the time traveled object and the indices distinguish odd and even images. Thus, we expect not two but four images *per order*.

The latter plot consists of almost vertical line segments, which can be understood in the following way: First, the plot is divided into small segments because the traveler periodically disappears beyond the horizon, where he cannot be seen by the observer. Hence, the observer's

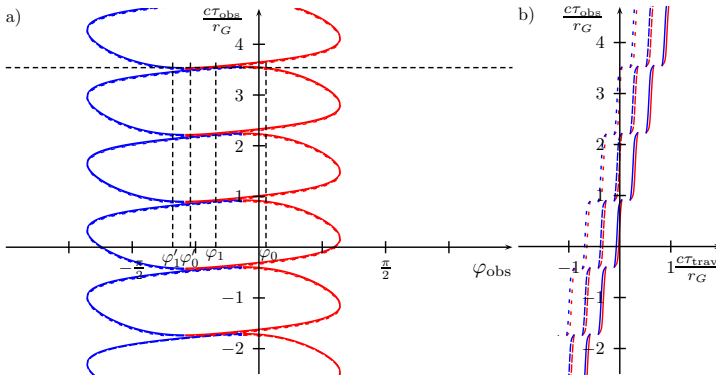


Figure 7.33: Quantitative analysis of geodesical time travel. Fig. 7.33a shows τ_{obs} plot against the viewing angle. In Fig. 7.33b, the proper times of both the observer and the traveling object are compared: For a fixed observer time τ_{obs} , we see the proper time of the object τ_{trav} at the moment of *light emission, not absorption by the observer*. These plots, in contrast to the previous examples, also include higher order images denoted with densely dashed ($n = 0$) and sparsely dashed lines ($n > 0$). Images of higher order almost coincide with the plot of zeroth order in Fig. 7.33a.

measurements regarding the proper time of the traveler must have gaps. Second, the data available to the observer must be represented as almost vertical lines because the voyager is traveling almost at the speed of light. The time dilation is very high and thus the traveler's clock is ticking (from the observer's perspective) very slowly. For an initial speed of $v = 0.9995$, we obtain $\gamma \approx 31.7$.

Furthermore, we can see that the traveler's age increases monotonically as long as he is seen by the observer. If we investigate this plot very thoroughly, we can actually verify that the traveler is indeed time traveling. The reappearing (older) traveler appears before the (younger) traveler disappears. This observer time difference is very small and corresponds to the discussion regarding eq. (5.14) and subfigure 7.33a. Summarizing this analysis, we discover that the observer will see time travel and the traveler will hardly age as long as he is within the horizon of the observer. After reentering the horizon before disappearing, the traveler is (marginally) older and thus has traveled back in time.

An egocentric visualization (as shown in Fig. 7.34) of this scenario accords, in principle, with this analysis. First, we restrict the raytracing procedure so that only zeroth order images are visible. We expect that, at least most of the time, only two images of the traveling Earth sphere

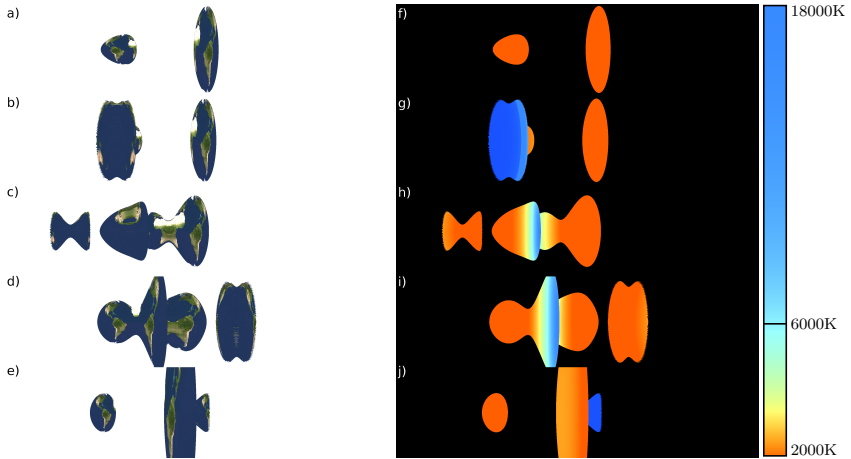


Figure 7.34: Egocentric visualization and apparent surface temperature for several observation times, $c\tau_{\text{obs}}/r_G \in \{3.458, 3.477, 3.530, 3.568, 3.622\}$ (GV). In this small time interval, the Earth sphere time travels and thus reenters the horizon before crossing it (`GeodesicalTimetravel_shortRays.avi`, `GeodesicalTimetravel_shortRays_redShift.avi`).

are visible. Within the short time span, where the sphere already reenters the causal region of Gödel's universe, we expect four images. However, the egocentric visualizations do not entirely reproduce these expectations.

First, the time travel interval appears much longer than analytically presumed. Eq. (5.14) determines that the maximum time travel interval is, in the limiting case $v \rightarrow c$, about $\Delta\tau_{\text{min}}^c \approx -0.038 \frac{r_G}{c}$. However, the accompanying movie sequence reveals that the time travel interval is approximately $\Delta\tau \approx -0.17 \frac{r_G}{c}$. Have we encountered an error in the visualizations? This question is directly solved when we recall that we visualize objects of non-zero size. In this scene and in geometrical units, the radius of the sphere is $r_{\text{loc}} = 0.1$, which is rather large when compared to the Gödel horizon at $R = 1$. This radius was chosen to obtain fairly visible images of the sphere. However, the spatial extent of the Earth yields the following situation: Some regions of the object are closer to the horizon than others. Therefore, these regions commence the time traveling phase earlier than those parts further away from the horizon. As a result, the time span in which the traveling sphere physically exists twice⁶ is much longer than for a pointlike entity. Note that

⁶As pointed out at the beginning of this section, this circumstance is not to be confused with the images of an object.

the sphere does not feel any effects of time travel – for example that some parts are aging at a different rate than others or even get younger – because the object itself is located within its local rest frame and thus within its own respective horizon. Time travel simply does not occur from this local perspective, where the laws of special relativity reign.

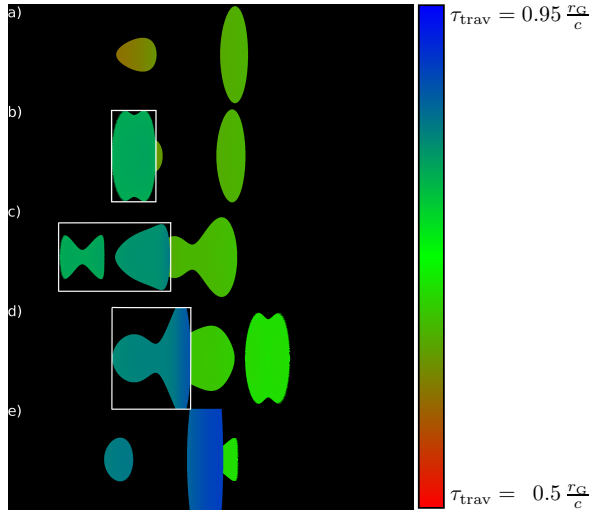


Figure 7.35: Color-coded emission time for the partially time traveling Earth sphere for the observation times $c\tau_{\text{obs}}/r_G \in \{3.458, 3.477, 3.530, 3.568, 3.622\}$ (GV). The first subimage shows the sphere heading towards the horizon. Figs. 7.35b-d show an additional white frame marking the time traveled sphere. In the last subimage, only this sphere is visible twice (`GeodesicalTimetravel_shortRays_emissionTime.avi`).

The second disagreement to the analysis of the pointlike particle is found in the video sequence. It reveals a multitude of complex visual distortions of the object and, of capital importance, sometimes more than four visible images. It can be assumed that these optical properties can be traced back to the non-zero spatial extent of the visualized sphere. Unfortunately, this issue cannot be resolved completely but only qualitatively mitigated: Fig. 7.35 shows the local emission times of the images and permits a visual sorting. The time traveled images are indicated by a white frame in the subimages 7.35b-d. We find that all of those shapes originate – in the respective picture – from a comparable emission time. Thus, we can distinguish the images of the time traveled sphere from the others.

Until now, we restricted the backtracing of visual rays so that only zeroth order images are rendered. Images of higher order can be seen in the movie clips and in Fig. 7.36, where the backtracing of visual rays allows for images up to fourth order: We can see a total of five even and odd images which reveal a very similar behavior but shifted in observation time because they originate from another loop of the periodical motion (as indicated in Fig. 7.36).

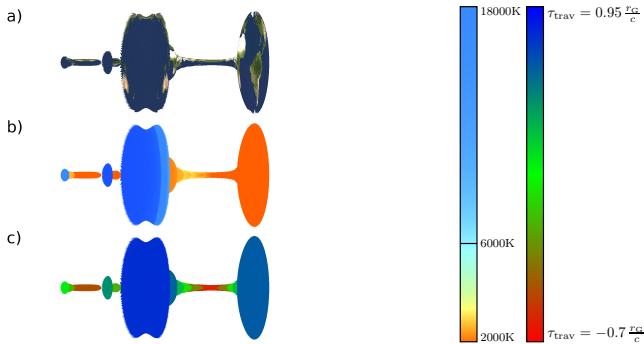


Figure 7.36: Geodesical time travel and higher order images. In these images, the backtraced visual rays allow for higher order images up to fourth order. We see the visual perspective in Fig. 7.36a, the apparent surface temperature in Fig. 7.36b and the local emission times for an observation time $c\tau_{\text{obs}}/r_G = 3.477$ (Fig. 7.36c). This observation time corresponds to Figs. 7.34b and g and Fig. 7.35b. Note that a different tone mapping is used for the emission time visualizations. The color bars are also provided in the movie clips (`GeodesicalTime-travel_longRays.avi`, `GeodesicalTimetravel_longRays_redShift.avi` and `GeodesicalTimetravel_longRays_emissionTime.avi`).

Additionally, the vertical extent of the higher order images is smaller than the images of zeroth order because higher order images are a result of interconnecting geodesics represented by increasingly narrow helix paths and thus smaller vertical viewing directions. The quantitative analysis holds for these visualizations as well, but the optical appearance is, by far, more complex and very challenging to follow. After having discussed geodesical time travel, we move on to the visualization of CTCs. Surprisingly, the interpretation of optical effects is relatively straightforward. On the other hand, the modeling of the scene is more complicated.

7.4.3 Objects Moving on Closed Timelike Curves

The visualization of motion on CTCs critically depends on the exact modeling of the worldline, and there is a multitude of possibilities to do that. The first and straightforward model is to assume that an accelerated spaceship is programmed to forever sustain the needed acceleration for the motion on a CTC. Of course, we must neglect that this spaceship needs an infinite amount of fuel, making the spaceship infinitely large and heavy. We must also disregard that real motion on a CTC is impossible to achieve for solid objects which interact with normal matter: On a CTC, such as depicted in Fig. 5.9, the time traveler arrives back and departs from the origin at the same moment τ_{obs} (with respect to the proper time of an observer located there). If the traveler moves on the CTC forever (with respect to his proper time), he will not only appear twice at that particular moment τ_{obs} . Instead, he will be located there infinitely often because he passes the origin again and again in certain proper time intervals, $\Delta\tau_{\text{trav}} = \tau_0$, cf. eq. (5.36a). All these reoccurring events – traveler reaches the origin – will occur at a single observer time τ_{obs} . This train of thought is valid for every point on the CTC. Consequently, an infinite number of time traveler instances will be situated on a specific point on the CTC for any observation time. Visualizations are impossible to generate for this scenario. If the traveler moves in a luminescent spaceship, this spacecraft will appear with an infinitely high luminosity. In addition to that, the traveler will rotate; see eq. (5.36b). Therefore, it is not possible to determine the color associated to a surface intersection because an infinite number of rotated travelers are located at the same point in space and time.

This discussion offers only one remedy to the problem of defining a reasonable scene. The CTC must be restricted to a certain proper time interval of the traveler. Thus, he will not sustain the motion on the CTC forever. Instead, we define the traveler's motion the following way: He will rest with respect to the cylindrical coordinate set at a certain point in space. Then, he will commence the travel on a CTC with an instantaneous boost, accelerating him to the required three-velocity given by eq. (5.27). He will travel on the CTC, propagating into his own local future, until he returns to his point of departure. With another decelerating boost, he comes to rest and stops his motion on the CTC. To simplify the visualization, the traveler's spaceship turns invisible, as long as it rests. Using this definition of a reduced CTC, the assignment between curve point and traveler age becomes bijective and we eliminate the problem of an infinite number of traveler appearances permeating each other.

Finally, we must decide where the traveler starts. If the starting point on the CTC is beyond the horizon, the traveler moves back in time before he enters the horizon. Within the horizon, the traveler will propagate into the future of the observer because the motion is restricted to the causal region around the origin. After passing the observer, the traveler will cross the horizon again. The last segment of the motion on the CTC includes a travel back in time and beyond the horizon. Obviously, the voyager will not be visible to the observer. Summarizing this scenario, we clearly identify that the observer will not see any time travel at all. To realize time travel on

a reduced CTC, the traveler must start within the horizon. We choose the origin as the starting point of his journey. The observer leaves the origin at his proper time $\tau_{\text{trav}} = 0$ and returns $\Delta\tau_{\text{trav}} = \tau_0$, eq. (5.36a), later. With respect to the observer's proper time, the (older) traveler enters the horizon at $\tau_{\text{obs}} = -\tau_1$ and travels towards the origin. As soon as the (older) traveler reaches the origin, we let him disappear. At the same instance, the (younger) traveler appears and instantaneously commences his travel to the horizon, which is crossed at $\tau_{\text{obs}} = \tau_1$. We obtain τ_1 if we isometrically translate the circular CTC, until it intersects the origin as displayed in Fig. 5.9. After intersecting the transported CTC with the horizon $R = 1$ and calculating the coordinate times of both intersections, a lengthy expression for τ_1 is found. For $R_{\text{ctc}} = 1.5$, we obtain, with respect to the observer's proper frame,

$$\frac{c\tau_1}{r_G} \approx 0.8718984946. \tag{7.5}$$

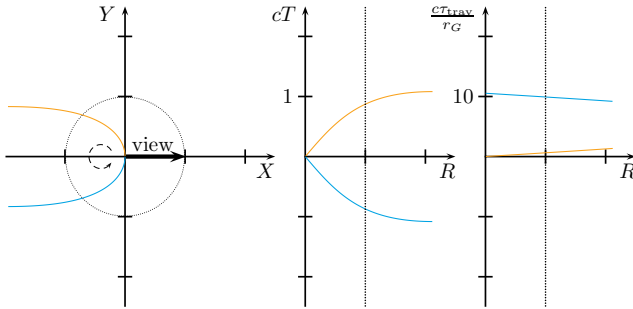


Figure 7.37: Observer resting close to the origin ($X = 0.015$) and a traveler on a CTC, crossing the horizon (dotted circle/line). The traveler starts at the origin and moves on a counterclockwise evolving path. In this diagram, only two segments of the CTC (on which the coordinate time is monotonically increasing) are shown. The light blue segment denotes the (older) returning traveler; the orange part illustrates the (younger) departing explorer. The middle image shows that the observer will see the older and time traveled voyager first.

For mere practical reasons, we use a circular CTC which is shifted into the opposite direction compared to Fig. 5.9. Hence, the resulting CTC is restricted to the left half-plane of the coordinate system. Fig. 7.37 depicts the definition of the scene. The traveler is represented by a very small Earth sphere. If the traveler passes the origin, the observer would be completely surrounded by this object. Thus, we would lose visual information because higher order images of the traveler were occluded. Instead, we position the observer at a point near the origin in order to avoid

this obstacle. As a consequence, the quantitative analysis does not exactly match the egocentric visualizations.

Unlike any other motion in special or general relativity, the travel on such a CTC is not only spatially restricted but also limited to a compact coordinate time interval as well. If the traveler moves on a CTC forever, an infinite number of traveler appearances exists (as discussed above), but only for a limited time. After this time period of $\Delta\tau_{\text{obs}} = 2\tau_1$, the traveler does not exist any more from the observer's point of view: The traveler is “trapped” within a limited coordinate time interval. Only the light emitted from his spaceship may still be visible.

In contrast to the previous section, we start with the analysis of the emission time diagram (Fig. 7.38). The proof that the egocentric visualizations, presented in the course of this section, actually display time travel can be found in this plot. The observer will see a very old traveler ($\tau_{\text{trav}} \approx 10 r_G/c$) for slightly negative observation times ($\tau_{\text{obs}} \lesssim 0$) and, most important, *before* he will perceive the younger version of the voyager, who is leaving the origin at $\tau_{\text{obs}} = 0$. To enunciate the situation: The traveler leaves the origin at $\tau_{\text{obs}} = 0$ and returns there after the motion on the CTC, whereas the observer will actually *perceive* the traveler *returning* before *leaving* the origin. Time travel on CTCs is indeed a visible effect.

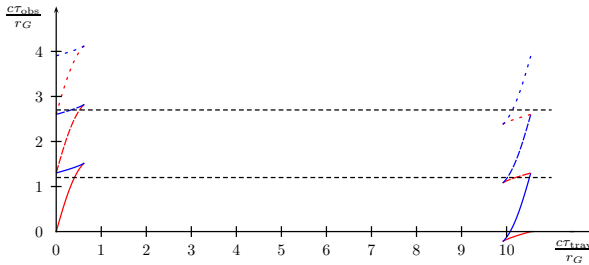


Figure 7.38: Time emission diagram for a voyager traveling once on a CTC and an observer located at the origin. The observer will see the time traveled version of the voyager first, before perceiving the younger version leaving the origin. At most, four images of two instances of the traveler can be seen at once, as indicated by the black and dashed lines. These horizontal lines represent two observation times: $c\tau_{\text{obs}}/r_G \in \{1.2; 2.7\}$. Most of the time, the observer will see an even image of the younger traveler and an odd image of the returning traveler.

Fig. 7.38 also confirms that, although the traveler only exists in a very short proper time interval ($\Delta\tau_{\text{obs}} = 2\tau_1$) of the observer, the voyager will be visible to the observer for an arbitrary long time. The zeroth order images (represented by solid lines) soon cease to exist, but the higher order images (dashed curves) can be seen after that. Each image order is visible for the same

time span and the observer will, at most, perceive the images of the orders n and $n + 1$ at the same time. These images decrease in intensity because the interconnecting geodesics increase in size.

Note that the observer will not be able to communicate with the traveler after the time span of $\Delta\tau_{\text{obs}} = 2\tau_1$ has elapsed, although he will be able to see him. Only within the short proper time interval the observer can, in principle, interact with the traveler and exchange information. After that, the observer can merely receive information from the voyager, if the latter maintains the motion on the CTC his whole span of life. Before this time span, the observer cannot see the traveler at all because the visible traveler is bound to the CTC and light emitted by him propagates to the future.

As stated above, the observer will see the even and the odd image of the returning traveler, starting at slightly negative observation times. More precisely, the even image (red curve) of the returning voyager is visible only for a very short time period because the traveler is rushing towards the origin and the interconnecting geodesics decrease in length. Thus, the observer will collect all incoming photons of the returning voyager in a very short amount of time⁷. The odd image of the returning traveler can be seen over a rather long time period because the observer will collect the light that both has been emitted by the voyager and that has traveled to the horizon once. If, for example, $\tau_{\text{obs}} = 0$, we know from the scene definition that the returning traveler has reached the origin. The interconnecting geodesics of the even image are very short, but those of the odd image reach a maximum length: Light along these geodesics starts at the origin, travels to the horizon and is, not until then, absorbed by the observer's eye.

The behavior is reversed for the images of the younger traveler leaving the origin. Now, the even image is visible for a very long time because the interconnecting geodesics increase in size and, therefore, the light travel time augments as well. The odd image can be seen only for a short time period: Light emitted at the origin returns there only marginally before the light sent out by the traveler close to the horizon.

The entire situation can be qualitatively compared to a thought experiment within classical physics: Consider a car that is traveling close to the speed of sound. Let this car emit n short, but periodical signals. If the car leaves a listener's position, this person will hear the n signals within a certain time span, which is longer compared to a resting car. If, however, the car rushes towards the listener, this person will collect the signals in a very short amount of time. This situation is comparable to the formation of both even images. The odd images can be interpreted similarly, if we extend the thought experiment by a wall – at some distance to the listener – on which the periodic signals are reflected: Considering only these signals, the audible experience is reversed from the listener's position: If the car rushes towards the wall and, therefore, away from the

⁷This is also a reason why a very small sphere is used for the egocentric visualizations. The Earth now has a local radius of 0.01, which is ten times smaller when compared to the scene definition regarding geodesical travel. If we chose $r_E = 0.1$, then the visual information of the object image would entirely clutter up the rendering.

person, the listener will now receive the reflected signals in a very short amount of time and vice versa. This wall, in a way, represents the Gödel horizon on which the photons are “deflected”.

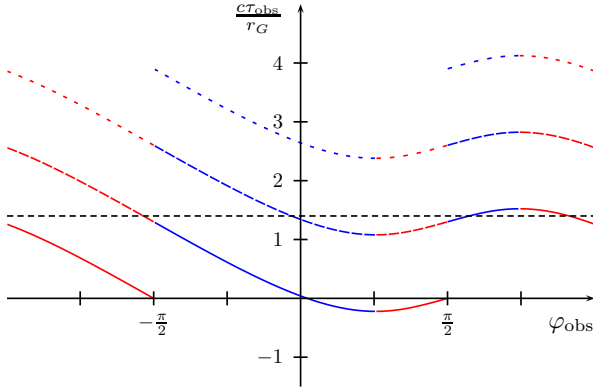


Figure 7.39: Visual appearance of an object traveling on a CTC ($R = 1.5$). This plot reveals under which angles φ_{obs} an observer resting at the origin sees the object. An object traveling on a CTC has four visible images at most for a fixed observer time (as indicated by the horizontal black line for the observation time $c\tau_{\text{obs}} = 1.4$). Sparser lines denote a higher order of the associated image.

The visibility angle diagram, Fig. 7.39, is now, in light of the discussion of the emission time diagram, easier to interpret. Again, we focus on the zeroth order images of the traveler. The traveler appears at a slightly negative observation time; two images are visible. The even image moves visually to the right and the odd image to the left. For $\tau_{\text{obs}} = 0$, the even image visually reaches the origin and thus the horizontal observation angle abruptly changes from $\pi/2$ to $-\pi/2$. Due to the modeling of the scene, where the traveler moves only once on the CTC, the image of the departing voyager shows him before he has time traveled and, consequently, at a younger age. Now, both images move to the left. Approximately at $\tau_{\text{obs}} \approx 1.3 r_G/c$, the visibility angle of the odd image directly changes by $\Delta\varphi_{\text{obs}} = \pi$. At this point, the odd image visually reaches the observer and, therefore, passes through the origin. After that, this image propagates to the right, exactly as the even image does when visually leaving the origin. Thus, we can identify the younger traveler as seen in the odd image leaving the origin. The last stage of the images of zeroth order is their disappearance beyond the horizon: Both images, showing the younger traveler, leave the observer’s visual perception.

The higher order images are integrated seamlessly into the diagram. A short time span before the odd image reaches the origin ($\tau_{\text{obs}} \approx r_G/c$), the images of first order appear and move iden-

tically, but only shifted to later observation times. Note that, again, we only consider the center point of the traveler in these diagrams. This constraint causes the perfect periodical appearance of these plots. We expect minor deviations in the egocentric visualizations. In the following visualizations (Fig. 7.40 and Fig. 7.41), only zeroth order images are shown. Higher order images are incorporated at the end of this section.

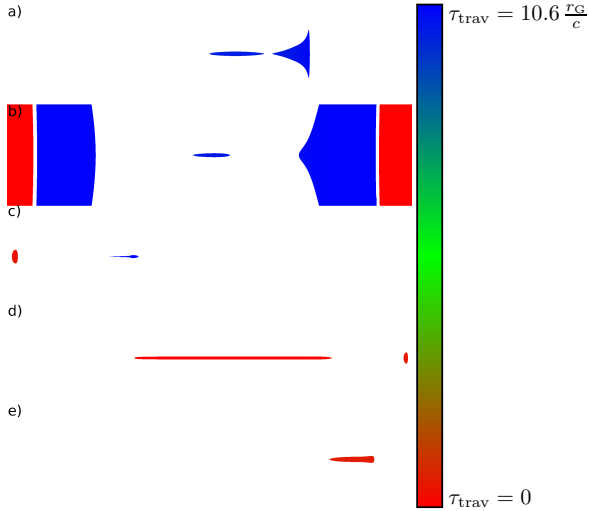


Figure 7.40: Visualization of the local emission time of the Earth sphere moving on a CTC for several observation times ($c\tau_{\text{obs}}/r_G \in \{-0.134, 0.016, 1.163, 1.299, 1.509\}$). The younger and the older version of the traveler, respectively the voyager's visual images, can be clearly distinguished (CTC_shortRays_emissionTime.avi).

In Fig. 7.40, the local emission times are shown from an egocentric perspective of the scene. We can easily identify the age of the traveling sphere and, therefore, distinguish the time traveled Earth from the younger version of it. The older Earth sphere is colored in deep blue, whereas the younger instance (which is leaving from the origin) is shown in bright red.

In contrast to the visualization of geodesical time travel (Fig. 7.35), we do not see a smooth color gradient on an object's image or relatively similar emission times when comparing the different images themselves, but rather a significant difference. Either the image of the object is very old or very young. This is due to the fact that the traveler ages tremendously on his long journey on the CTC when compared to the time span he travels back in time (with respect to the observer).

Fig. 7.40 also enables us to identify the different stages of the simulation as discussed above. For the following visualizations, a white or gray background is used to easily locate the object's images. First, the time traveled and older version of the object appears from beyond the horizon: Both images show a deep blue color. Then, cf. Fig. 7.40b, the even image visually arrives at the origin and, due to the definition of the scene, gets replaced by the younger version. Therefore, the even image shows a discrete change to a red color coding, separated by a vertical white line. In the middle image, we see the younger Earth in the even image, whereas the odd image shows the older Earth because this instance has not yet visually reached the origin. After the odd image has traversed the origin, it also turns red, as shown in Fig. 7.40d. Finally, both images, showing the younger traveler about to cross the horizon the "first" time (with respect to his proper frame), merge and disappear beyond the Gödel radius.

The egocentric visualizations and the apparent surface temperature are displayed in Fig. 7.39. The frequency shift renderings reveal the relative flight directions of an object, although their interpretation is difficult because a multitude of physical effects, such as the rotation of the sphere due to the Fermi-Walker transport of the comoving tetrad, interfere. We discuss, in excerpts, the object's images.

Consider Fig. 7.41g, where the even image at the border of the subfigure clearly shows that the older traveler is rushing towards the origin because the light is extremely shifted to the blue end of the spectrum. On the other hand, the younger traveler appears red shifted because he moves away from the observer's position at a high velocity. Also note that the odd image of Fig. 7.41g might seem peculiar: Although that image should be moving to the origin, it appears red shifted. Of course, we must follow the peculiar shape of the interconnecting geodesics. Although the image indeed corresponds to the physical object rushing towards the observer, the lightlike geodesics increase in length because the light must propagate to the horizon first, before it can be absorbed by the observer. The nearer the object is, the longer the geodesics *for the odd image of zeroth order* become. Therefore, the object visually moves away along these geodesics and the object must appear red shifted. Just before both images disappear behind the horizon, Fig. 7.41j, there is hardly any frequency shift perceivable: Both images are already connected to a single image which reveals a surface temperature of approximately 6000 Kelvin. This effect can be understood after inspecting Fig 7.11. An object very close to the horizon is seen from the lateral face. Therefore, the emission direction of the photon seen by the observer and the flight direction of the sphere are approximately perpendicular and the frequency shift becomes negligible.

Including the higher order images into the visualization of motion on a CTC does not, as expected, yield the tremendous amount of visual information when compared to the situation of geodesical time travel (cf. Fig. 7.36). We can only see the images of two different orders; see also the associated animations. In Fig. 7.42, the visualization parameters are chosen so that all images up to the second order can, in principle, be seen. In these three visualizations, we see the

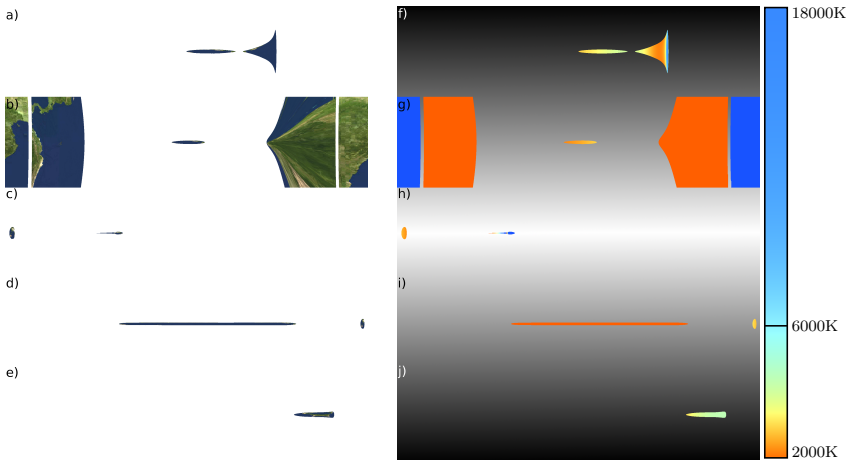


Figure 7.41: Egocentric visualization and apparent surface temperature for the stages shown in Fig. 7.40 (GV). From top to bottom, the (time traveled) voyager appears, reaches the origin, leaves the horizon (as a younger traveler), almost reaches the horizon and disappears behind the Gödel radius (`CTC_shortRays.avi`, `CTC_shortRays_redShift.avi`).

egocentric perspective, the apparent surface temperature and the local emission times for the simulation time $\tau_{\text{obs}} = 1.163 r_G/c$, which corresponds to the middle subfigures in the previous renderings, i. e. Figs. 7.41c and h as well as Fig. 7.40c. The only difference to these images is – as already shown in the visibility angle diagram (Fig. 7.39) – the appearance of the first order images to the right of the observer, before the images of zeroth order disappear.

One might ask how an egocentric visualization of the traveler's perspective appears. We do not anticipate any fundamentally new insights and therefore rely on an analysis of the expected appearance. For our thought experiment, we assume a resting object at the origin of the coordinate system and a traveler that moves on a CTC exactly as the Earth sphere before. The local emission times are encoded as usual. We choose a green color for the time of departure, older objects are colored in blue and younger entities appear red.

Besides the large rotational effect of the comoving tetrad, neglected in this textual analysis, the traveler would see the following: Starting at the origin, he will see the object appearing green because he is close to the object (i. e. the light travel times are short) and also because we set this hue for the time of departure. When traveling towards the Gödel horizon of the object, two coun-

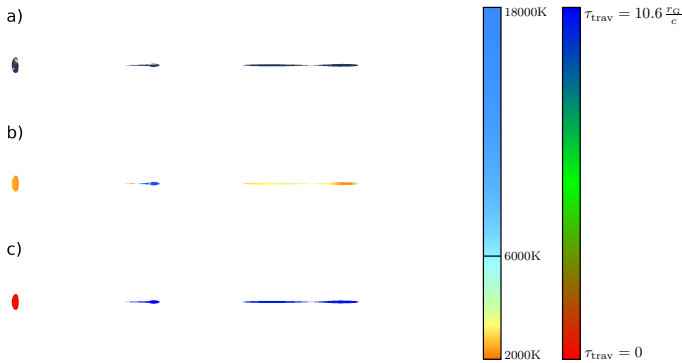


Figure 7.42: The Earth sphere traveling on a CTC. In these images, the backtraced visual rays allow for higher order images. From top to bottom, we see the visual perspective, the apparent surface temperature and the local emission times for an observation time $c\tau_{\text{obs}}/r_G = 1.163$ (CTC_longRays.avi, CTC_longRays_redShift.avi and CTC_longRays_emissionTime.avi).

teracting effects arise: First, the object gets older (more blue) and, second, the light travel time increases. The latter property alone would cause a more red appearance of the object because, exactly as viewing the stars in the sky, the traveler perceives the light emitted longer ago. The traveler will see the object aging slowly because we assume that the first effect dominates over the other. Note that we are discussing the even image of zeroth order, which is generated by the shortest interconnecting geodesics. The odd image as well as all the images of higher order will reveal a behavior as revealed throughout this chapter: Longer interconnecting geodesics result in a longer light travel time and, therefore, images of the younger (more red) object.

As soon as the traveler crosses the horizon of the object, the entity will visually disappear. Since we do not place any other objects into the scene, the traveler will see nothing for the largest part of his journey. We could place several buoys at fixed coordinates for better orientation. However, it can be expected that the additional visual information obfuscates the potential renderings.

Beyond the horizon, the traveler ages normally but moves back in time, as measured from the object's local frame. After this part of the trip, the traveler crosses the horizon again. The object is, then, again in his field of view and will appear a bit younger (more red). The voyager rushes toward the origin and the two effects, which have been counteracting before, now synergize: The object ages and the light travel times decrease. Finalizing his voyage and our thought experiment, the traveler would thus see the object age rather quickly and, upon arrival at the origin, be of the same age (green) when compared to the time of departure.

7.4.4 On the Impossibility of Visualizing Causality Violations

The last section made clear that it is very difficult to formulate a time travel scene for CTCs. The partial time travel on geodesics did not pose a problem because the Earth sphere – in spite of traveling back in time – reentered the horizon at a different angular coordinate. Thus, the timelike curve was not closed. On a CTC, however, we had to assume that only one loop of the cycle was passed through and we were also forced to ascertain that the instances of the sphere did not physically interact. These difficulties, however, merely resemble the starting point of an even more profound dilemma.

Let us recall the basic problem of time travel manifested in causality violations as proposed by the grandfather paradox: A man travels back in time and kills his grandfather before the latter meets his wife. Then, the traveler would never have been born and, therefore, the grandfather could not have been killed. As a result, the traveler would have been conceived and could kill his grandfather. In this type of logical paradox, it is impossible to determine an outcome.

The grandfather paradox is easily transferred to the Gödel universe, in close resemblance to the considerations on closed timelike motion. A traveler leaves the origin, moves on a path very similar to a CTC and returns to a position close to the origin shortly before leaving it. He fires his “quantum torpedoes” and destroys the younger instance of himself. Thus, the younger traveler will not embark on his time traveling journey, will not kill himself and therefore will end up in the same paradox situation.

Now, we ignore the concept of a free will for a while. The above scenario might, as an attempt, be constructed using a programmed spaceship. Even if we drop the free will, the paradox is preserved: If we wish to program such a flight path, we would have to input at least the initial conditions of this orbit. At the very moment the spaceship commences its destructive voyage, the paradox arises. Since it is indeterminable to work out what will happen, we cannot, on no account whatsoever, build such an experiment in a classical or general relativistic universe. Unfortunately, we also reached a dead-end situation for our visualization goals. To generate a rendering sequence of a causality violation we must, exactly as the experimental physicist, build a machine which, in our case, is the scene definition. We are principally unable to formulate the initial conditions of the numerical simulation which is supposed to generate the images.

In Sec. 4.3, we discussed several loopholes to enable such time travel. Noteworthy in this context is the concept of parallel universes (Sec. 4.3.3), which offers a solution. The traveler could, in fact, destroy his younger counterpart *of another universe* without any problems regarding causality. A visualization is possible, but is merely a less-than-ideal solution for our verbalized objectives because it, in a way, circumvents the handling of causality violations.

Another solution is the Novikov self-consistency principle, Sec. 4.3.3, which constitutes that time travel is possible but *must* be causality conserving. In our case, the spaceship is able to travel into the past but, for whatever reason, must be *unable* to fulfill its rogue mission. If causal-

ity is not violated, then the scene is consistent. Recall the precise definition of the traveling sphere in the last section: We neglected the physical interaction between the instances on the CTC and, hereby, automatically formulated a consistent situation. Furthermore, we could even allow interactions between the two instances of the sphere because the direction under which the returning voyager arrives at the origin is precisely the direction under which the younger traveler must start. Thus, the returning sphere could hit the other sphere to initiate the time travel. Albeit being self-consistent, this interpretation of the visualizations of the previous section yielded a predestination paradox. We cannot determine the cause and the effect.

To summarize this important insight: Visualization of causality violations are impossible to generate because we cannot determine the initial conditions of such a simulation.

After the hard work we had in this chapter, we can lean back and enjoy the elegance of Gödel's bewildering model by means of three scenes, where we do not restrict the visualization parameters for didactic reasons but plainly "*visualize*" this elegant universe.

PLAYGROUND

“So, five card stud, nothing wild. And the sky’s the limit.” — JEAN-LUC PICARD

The final main chapter of this work illustrates three advanced scenarios and will be discussed qualitatively. We start with a formulation of the inner solar system within the Gödel universe, which is rendered using `GeoVis` because the four inner planets travel close to the speed of light. The second scenario is based on [MW10] and displays the Hipparcos catalog. The rendering method for the stars as well as the management of the catalog has been extracted from this work and adapted to comply with the requirements of the `Gödel Engine`. Finally, we go on a star trek and visualize a famous spaceship that is flying through the Gödel universe. This last scenario serves a triple purpose. First, it can be regarded as a technology demo of the `Gödel Engine`. Second, the visualizations can be – after the detailed discussions in this chapter – understood albeit the overwhelming amount of visual information. And finally, the corresponding movie sequence provides the opportunity for the acknowledgements of the author.

8.1 Our Solar System

So far, we have discussed the appearance of a single object located in the Gödel universe. After having learned that a single object can appear an infinite number of times, we continue with a composition of spheres. Since Gödel’s model is an alternative universe, we now build a connection to our own world. In this section, the inner solar system – Mercury, Venus, Earth and Mars – is formulated within the Gödel spacetime. The four planets move on geodesical orbits around the origin, where the observer is resting. Inspecting Fig. 5.2, we find a timelike geodesic that is on an almost circular orbit around the origin. Following this insight, we set the radial coordinate velocity in the differential equation (5.4b) to zero and insert the initial conditions (5.3). To enable a circular motion, we set the local velocities to $u_0^{(0)} = \gamma c$, $u_0^{(2)} = \gamma v$ and $u_0^{(3)} = 0$, where v is the

local velocity on the circle. The result of these calculations is a connection between the radius of a circular orbit, R_0 and the local velocity v needed to sustain this motion. We arrive at

$$v = \frac{2\sqrt{2}R_0\sqrt{1+R_0^2}c}{2R_0^2+1} \quad (8.1)$$

and vice versa

$$R_0 = \frac{1}{2}\sqrt{2}\sqrt{\frac{-2c^2+v^2+\sqrt{4c^4-2c^2v^2}}{2c^2-v^2}}. \quad (8.2)$$

Obviously, the maximum radius R_0 is given by the limiting case $v \rightarrow c$ and reads

$$R_{\max} = \frac{1}{2}\sqrt{2}\sqrt{\sqrt{2}-1} \approx 0.4551. \quad (8.3)$$

For the four planets, we chose the initial velocities already used in Sec. 7.4.1. The relative size within the respective local tetrad, r_{loc} , as well as the Z_0 -coordinate of the geodesic result from appropriately scaled radii r_{phys} of the planets themselves. The scene definition, for which we trace the primary rays far into the past, is as follows:

planet	r_{phys} in km	v/c	R_0	Z_0	r_{loc}
Mercury	2,439.7	0.2	0.0712479628	0.24395	0.024395
Venus	6,051.8	0.5	0.1858022705	0.63780	0.060515
Earth	6,371.0	0.7	0.2746549430	-0.06378	0.063780
Mars	3,396.2	0.9	0.3849723672	-0.33960	0.033960

The egocentric visualizations are shown in Fig. 8.1 and Fig. 8.2 using a spherical projection. As stated at the beginning of the previous chapter, this projection visualizes every viewing direction and is, additionally, stretched vertically by a factor of $f = 2$ and thus quadratic. The first subimage, Fig. 8.1a, reveals the observer's visual perceptions. Since all four objects are located within the horizon of the observer, all planets are visible. From this point of view, a multitude of images is visible. On the one hand, the planets themselves are moving on a circle which is located at $Z \neq 0$. Following the discussion in Sec. 7.3.2, more than two images are expected. On the other hand, there is yet another reason for the large number of images. Even if the motion of the planets is restricted to the horizontal plane of the observer, we obtain more than two images because the local velocity is not small when compared to the speed of light. Thus, the light travel time must be taken into account as shown, for instance, in Fig. 7.36. Unlike a resting or quasistatically moving object, such as discussed in Sec. 7.3, higher order images are *not* occluded by their zeroth order counterparts. Generally speaking, the finiteness of the speed of light constitutes the key aspect of the disparity between *measuring* (a property simultaneously at the object) and *seeing* (a visual feature simultaneously at the observer's position). The movie

sequence `InnerSolarSystem.avi` shows the temporal aspects of the scene: All images move at a constant angular velocity visually to the left because the entire scene is symmetric to the Z -axis.

Fig. 8.1b shows the apparent surface temperatures of the planet's images. The apparent mean temperature is approximately the surface temperature of 6000K. The main reason for this effect is, again, the rotational symmetry of the scene. The planets are neither moving towards the observer nor flying away. Thus, no Doppler effect due to relative motion should arise. However, we find a slight horizontal gradient. In several images, we see one side of the object marginally red shifted, while the opposite side appears somewhat blue shifted. The underlying reason for this optical effect is the parallel transport of the comoving local tetrad of any object, which is thereby rotated around the local $e_{(3)}$ -axis. As a consequence, we observe a non-zero velocity on the surface for every image. Those regions visually moving away become slightly red shifted, and parts that rotate towards the observer are blue shifted. If we now recapitulate the movie sequence `InnerSolarSystem.avi`, we clearly see this rotational effect on any image. Despite the visual complexity of the renderings, it is possible to distinguish odd and even images. The latter class of images visually rotates right to left, and the other group rotates in the opposite direction because they appear mirrored, cf. Sec. 7.3.1.

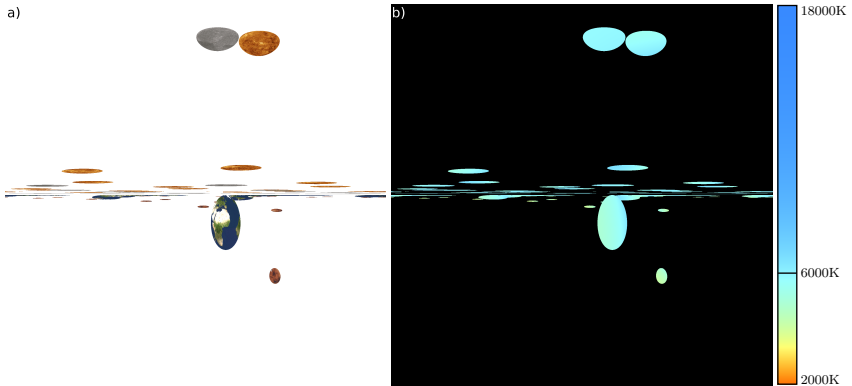


Figure 8.1: Egocentric visualization and Doppler shifts (GV) of the inner solar system within the Gödel universe. A multitude of images is visible and the apparent surface temperature hardly differs from 6000K (`InnerSolarSystem.avi`, `InnerSolarSystem_redShift.avi`).

Finally, we investigate the local emission times of these images, cf. Fig. 8.2. This figure confirms that the light travel time for the interconnecting geodesics is significantly increasing for high

order images. The (large) lower order images all appear in deep blue and therefore represent the planets at a later time, whereas the high order images are visually concentrated to the equatorial plane of the observer. Those images closest to this plane appear in a red tone and show the planets from a more distant time. All images are colored with a single color because the tone mapping covers a very large timespan. Thus, minor deviations of emission times within one images are not detectable.

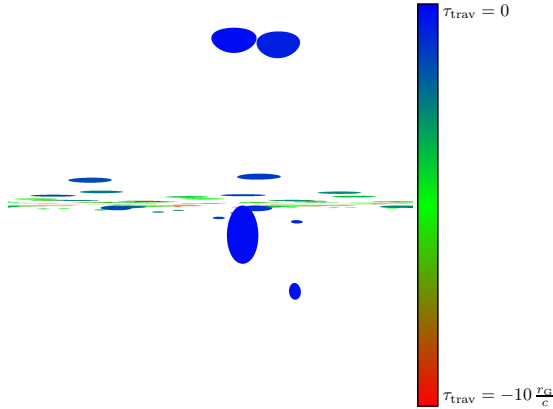


Figure 8.2: Local emission times of all inner solar system planets (GV). Images near the horizontal plane of the observer result from longer interconnecting geodesics and thus appear younger (`InnerSolarSystem_emissionTime.avi`).

8.2 Stars from our Galaxy – The Hipparcos Catalog

The Hipparcos catalog is, using the code fragments provided by Müller and Weiskopf [MW10], implemented into the GÖDEL ENGINE as a further object type. The most distant stars¹ are located on a unit sphere in the Gödel universe. Closer stars are located inside this sphere. The right ascension and the declination angles then determine the positions of the stars, which are directly interpreted as the scaled Cartesian coordinates for the metric. Thus, for a large Gödel radius and, therefore, a relatively flat spacetime, we expect an optical appearance corresponding to our own night sky. This assumption is confirmed when inspecting Fig. 8.3 (and Fig. 8.4, where the colors were inverted), where the catalog is visualized using a 4π -projection. Note that we only

¹Note that the Hipparcos catalog contains stars located at “infinity”. These stars are also placed on the unit sphere, whereas entries with a negative parallax are not used.

visualize the even image of zeroth order and consequently, every star appears exactly once in this image. Consider the Orion constellation in this image, which is indicated by an arrow (pointing to Orion's Belt). This constellation appears almost exactly as seen from our Earth.

Now, we decrease the Gödel radius to $r_G = 5$ and see that, as we expect², the stars move visually to the left. The Orion constellation in Fig. 7.2.1 is marked again using an arrow. We clearly see that the central star of Orion's Belt (Alnilam) is now seen to the left of the other two visible stars of the belt. Thus, this star must be at a larger distance to the observer because the light bending effects are extremal in the vicinity of the horizon. Merely by studying these renderings, we can understand that Alnilam is, in deed, the most distant star in this belt.

The movie sequence reveals that for most of the Gödel radii, the changes in the visualization are not drastic. However, below $r_G \approx 5$, the curvature of the spacetime increases swiftly and thus the stars move quickly to the left before they disappear behind the horizon, which itself is much smaller than the maximum radial extent taken by the catalog.

Unfortunately, the corresponding movie clip reveals the numerical issues of the GÖDEL ENGINE (as discussed in Sec. 6.4.2). During the animation where the Gödel radius is decreased from 35 to almost zero, several stars are slightly shaking and some stars are not visible in certain images. We have rendered these images using the double precision support of a GeForce 280 GTX but, unfortunately, the imprecisions of the underlying computations could not be completely eliminated.

In flat spacetime, the Hipparcos catalog appears as a *single* cluster, if the observer is located at a sufficient distance to the stars. To investigate the corresponding optical appearance for the Gödel universe, we simulate an actual flight through the stars of the catalog. In this context, we visualize higher order images of the stars: All star images, including the second order, are included. In Fig. 8.5, a frame of the movie clip `HipparcosFlyThrough.avi` is presented. The rendering is in close resemblance to sceneries with spheres (as seen, for instance, in Fig. 6.3 and Fig. 7.22 on p. 84 and p. 130, respectively): All representations of the Hipparcos catalog are arranged into image pairs of clustered stars.

By watching the movie clip, the spatial distribution of the stars can be seen and the viewer can get a mental picture of such a flight. This directly leads to the last scenario of this work, which was motivated by this movie clip and the usual appearance of stars as well as their relative motion to a spaceship – as depicted in the Star Trek series.

²See Sec. 7.2.1, where the Gödel radius was altered and we obtained the same effect.

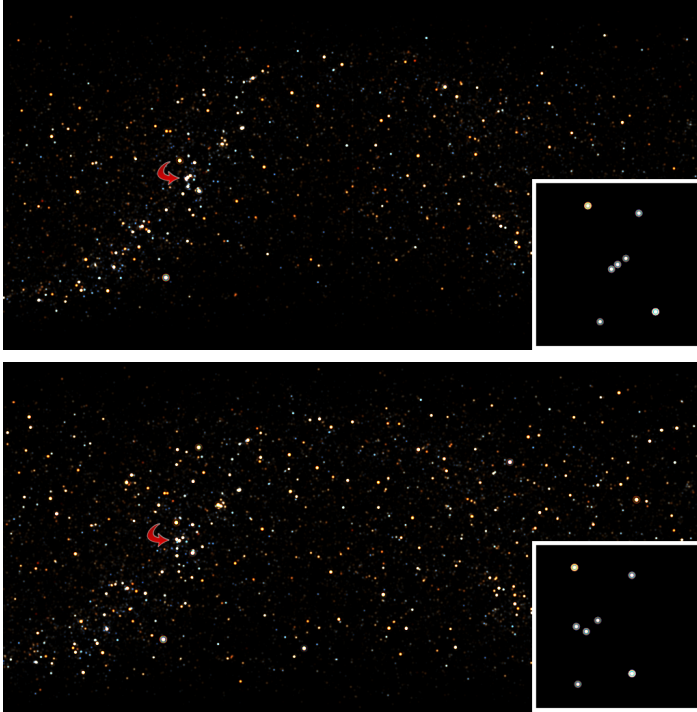


Figure 8.3: The Hipparcos catalog in a 4π -projection for an almost flat spacetime (upper subimage) and as seen in the Gödel universe (lower subimage, $r_G = 5$). A magnification of the Orion constellation is depicted in the lower right corner of the respective subimage (GE) (`HipparcosChangeHorizon.avi`).

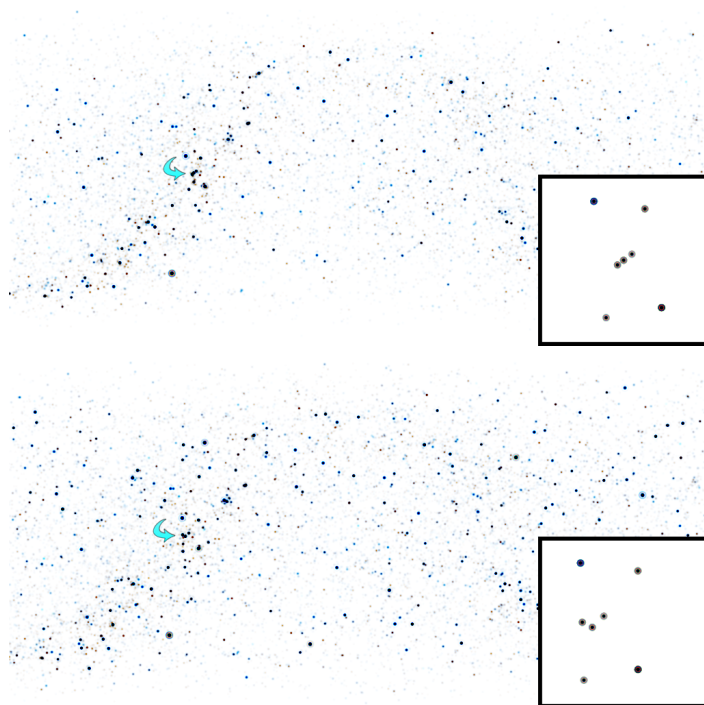


Figure 8.4: For better visibility in the printed version of this document, we depict Fig. 8.3 using inverted colors.

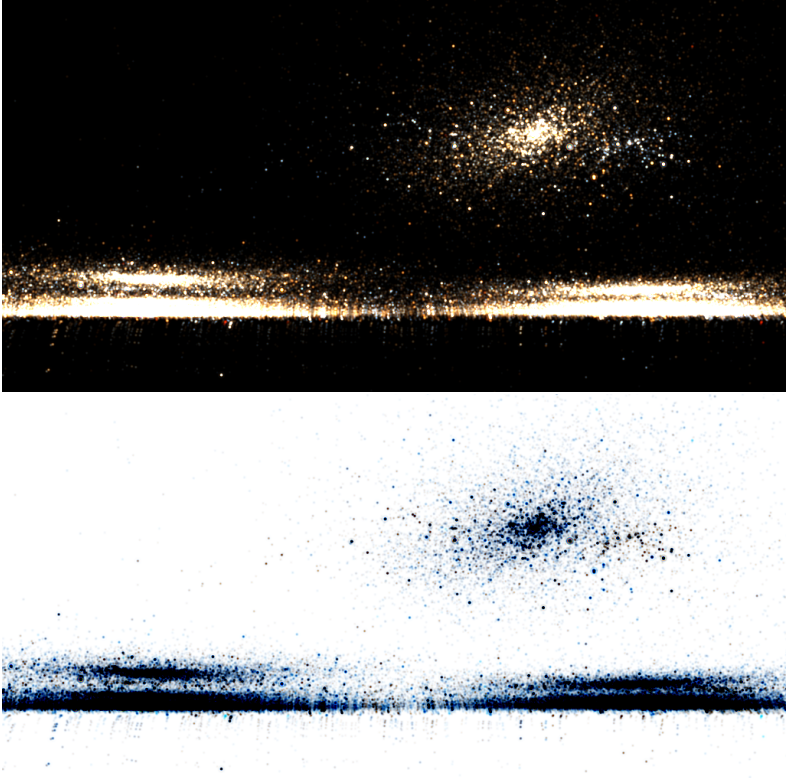


Figure 8.5: Flying through the Hipparcos catalog ($\tau_G = 1$). The movie clip (`HipparcosFly-Through.avi`, (GE)) is generated in a 4π -projection.

8.3 Star Trek

For the reader's delight, we present the opening credits³ of the “Star Trek – The Next Generation” series in a modified version, i. e. as seen in the Gödel universe (TNG_60fps_HQ.avi, TNG_30fps_MQ.avi or TNG_60fps_LQ.avi). As an example, consider Fig. 8.6, where the “Enterprise D” is shown. Note that only one image of the Enterprise D as well as of the Borg sphere can be seen because both objects are located in close proximity to the observer. We will not provide any further qualitative or quantitative discussion on the renderings or the exact scene definition because the movie clip is intended to be a technology demo as well as an entertaining finale of this work.

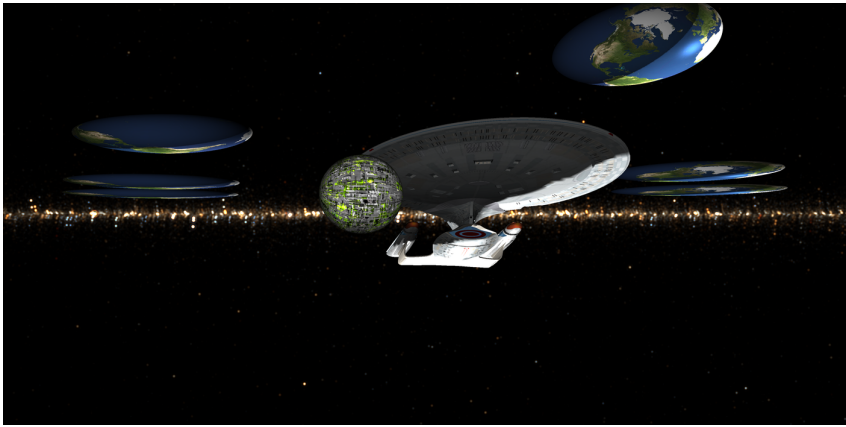


Figure 8.6: The Enterprise D as seen in the Gödel universe (GE). The spaceship appears virtually undistorted because it is very close to the observer.

³Due to copyright issues, the movie sequence does not contain any audio track. The gentle reader may use his/her legal copy of season one in order to obtain the author's intended experience.

CONCLUSION AND OUTLOOK

We are confident that – to revisit the opening question as formulated in the abstract – **a mental image of the Gödel universe was generated**. Now, we conclude this work by summarizing our achievements, investigating the hypotheses (see p. 2) and encouraging future work.

Summary: In Ch. 2 as well as in Ch. 3, we summarized the physical and mathematical prerequisites as well as visualization techniques such as raytracing or interactive approaches. To make this work self-contained, we then reviewed and thoroughly analyzed the physical aspects of the Gödel universe in the last introductory chapter, Ch. 4. The light cone structure especially allegorized the physical effects that allow for closed timelike curves in the Gödel universe. Since the light cones tilt, a traveler can not only travel in his own local future but into the past of another voyager. Furthermore, we recapitulated other time travel universes in general relativity and the logical treatment of causality violations.

In Ch. 5, we derived analytical solutions to the geodesic equations of Gödel's metric for special and general initial conditions. The general solution was used to determine whether or not causality violations arise when traveling on geodesics. A lightlike or massive particle travels back in time if the initial velocity is $v \gtrsim 0.98c$ and the initial radial coordinate is $R_0 \lesssim 1.7$. For a maximum time travel interval, a single particle would exist twice within the Gödel horizon. In all cases, causality is not violated.

The equations of isometric transport for both points and directions were solved for all five Killing vector fields. Special solutions of the geodesic equations and finite isometric transformations were also combined to confirm the general solution of the geodesic equations. After mapping the Gödel horizon, we depicted regions of common causality for different observers.

Then, we described circular CTCs and calculated the Fermi-Walker transport along these circular lines, which lie beyond the horizon. We isometrically transformed these circles to create CTCs, which include the origin. This procedure resulted in time travel starting at the origin. An observer located at the origin can therefore see a time traveler who would otherwise be hidden beyond the optical horizon. Since these CTCs are created using isometric transformations, the results found for circular CTCs remain valid.

The GÖDEL ENGINE was introduced in Ch. 6. We achieved a performance leap of at least four to five orders of magnitudes because the interconnecting geodesics as well as the viewing directions (under which an object is visible) can be calculated directly. In the course of this, we utilized the capabilities of modern, programmable graphics hardware. Using isometric transformations, we were able to apply a local illumination model. We also showed that a simple self-shadowing computation method is possible.

The main chapter of this thesis, Ch. 7, provided egocentric visualizations for a multitude of different scenarios. After the discussion of finite light cone structures, we visualized the transition from flat spacetime to the Gödel universe by constructing a coordinate grid and varying the Gödel radius. Due to the winding behavior of the interconnecting geodesics, the grid as seen from above, rotates counterclockwise for a decreasing Gödel radius. Similarly, objects move visually to the left if the observer aligns his line of sight radially outwards. Resting objects in the observer's equatorial plane are visible twice, whereas objects not located in this plane can be seen infinitely often. If an object is moving to a sufficient distance from the observer, images of the object visually disappear. As soon as the entity is located entirely beyond the horizon, all object images vanish.

In Sec. 7.3, we exploited the full potential of the GÖDEL ENGINE by illuminating several quasistatically moving objects. In a quantitative discussion, we explained under which direction an object is seen by the observer, the visible side of the entity and the face that is illuminated. The interactivity of the application enabled us to discover astounding optical features of Gödel's universe. The accompanying videos clearly reveal these effects: For instance, an object can disappear behind the Gödel horizon before being occluded by a higher order representation of another object. A further example is the quasistatically moving point light source. Although it disappears behind the Gödel horizon, its reflections can still be seen. Furthermore, a vertically aligned staff is seen as a circle ("Gödel ring").

Using GEOVIS, we then visualized objects that are moving close to the speed of light in Sec. 7.4. We investigated motion that was restricted to the causal region of the Gödel universe, non-causality violating geodesical time travel and an object that is moving on a CTC. All quantitative analyses, carried out with the GÖDEL ENGINE, explain and confirm the egocentric visualizations. The computation of apparent surface temperatures facilitated the identification of relative flight directions because only Doppler shifts arise in the Gödel universe. For the visualization of time travel, we relied on a tone mapping, which revealed the local emission times of the objects. Thereby, the relative age of an object in a specific object image was identifiable. We found that time travel is actually a visible property: An observer will, in fact, see a traveler who is moving on a CTC, return before depart. Finally, we provided three advanced scenarios in Ch. 8 in order to compile all previously unveiled effects and, thereby, ended the journey through the Gödel universe.

Conclusion: From a more abstract point of view, the Gödel universe can be interpreted as an example case of time travel universes. In light of our insights, we now return to the hypotheses which we constructed in Ch. 1:

1. Egocentric visualizations enable us to understand time travel intuitively:

This thesis is the first published work concerning egocentric visualizations of time travel within the domain of general relativity. The diagrammatic definition of the scene as well as the quantitative analyses in Sec. 7.4.2 and Sec. 7.4.3 revealed the precise properties of time travel within the Gödel universe. However, the egocentric visualization provided additional information which allowed us to understand time travel on a more intuitive level.

To investigate the substance of the hypothesis, we first must realize that it is formulated very strictly. Do egocentric visualizations *alone* allow us to fully comprehend time travel on an intuitive level? Certainly, the answer is no. Without the fundament of our mathematical investigations and quantitative analyses we would hardly understand the visual information of the accompanying movie sequences. Consider, for example, the visual appearance of the Earth sphere on a CTC, as shown in Sec. 7.4.3 and especially Fig. 7.41a-e on p. 155. Without the preparatory analyses, the film clip `CTC_shortRays.avi` would, most certainly, be understood as “heavily distorted Earth spheres moving towards or away from the observer”. Two enhancements had to be implemented: First, a tone mapping which revealed that the visible images of the sphere had actually traveled through time. Second, analyses such as Fig. 7.38 and Fig. 7.39 that presented the entire simulation in a clear and concise way.

Only the synthesis of mathematical studies of physical phenomena *alongside* egocentric visualizations allow us to gain insight on an intuitive level. For the scientific layperson, the mathematical studies are hard to follow, but the diagrams of the quantitative analyses – for example Fig. 7.39 on p. 152 – can be made accessible. Thus, the combination of these plots *in conjunction with* egocentric visualizations should help a general audience to get acquainted with the advanced properties of general relativity such as time travel.

Consequently, egocentric visualizations do enable us to understand time travel intuitively – but only if additional information is provided.

2. Interactive approaches facilitate the discovery of unknown optical effects:

Certainly, a high rendering speed is desirable because of mere practical reasons: We can quickly obtain results and large computing clusters may become redundant for specific research areas. Additionally, we are able to generate renderings of a hitherto unequalled visual quality using the Phong illumination model. Thus, the analytical results serve as a basis for interactive visualizations.

However, we wish to emphasize the importance of an interactive rendering approach because the interactivity is not an end in itself: As shown in Sec. 7.3.2, we unveiled several

unknown optical effects, which might not have been discovered without a very fast rendering procedure. We found that objects beyond the horizon of the Gödel universe can be seen via indirect light, the visual occlusion of objects is contrary to a straightforward assumption and, above all, vertical staffs are projected onto a visual Gödel ring.

The extension of our ideas to other manifolds – where analytical expressions on curved light rays are available – is possible, and thus, the concept used in the GÖDEL ENGINE can stimulate research in other fields. We expect that unknown optical effects can also be found for those spacetimes. By being able to adjust the scene parameters interactively and in a playful mode of operation, such optical effects can be revealed. Of course, those effects can also be unveiled by thoroughly studying the appropriate equations.

An interactive visualization technique represents an *alternative and complementary* approach.

However, we enunciate the fact that the idea behind the GÖDEL ENGINE will be very hard to transfer to other spacetimes, even if analytical solutions to the geodesic equations are already known. Even for the Gödel universe, the general solution for the geodesic equations is already too complicated, since it is not possible to compute the interconnecting geodesics. The remedy to this issue was the application of finite isometric transformations so that the general solution becomes implicitly utilizable; however, we are restricted to static and quasistatic objects. Such an approach might work for other homogeneous spacetimes because we need at least four independent Killing vector fields to transform the scenery so that an arbitrary point can be mapped onto, for example, the origin of a coordinate system. For mathematically more challenging spacetimes, such as a rotating black hole, an interactive algorithm will be restricted to very special cases. Comparable to the visualization of the Hipparcos catalog around a black hole, cf. [MW10], or our previous work, see [GB08], an application will only be able to interactively visualize a limited set of object types, flight paths or scene parameters because several classes of computations must be precalculated (and then provided as texture or similar data structure). Ultimately, an approach where the GÖDEL ENGINE is used as a black box – insert a scene object and the analytical solutions of an arbitrary spacetime in order to obtain the interconnecting geodesics and viewing directions – seems hardly possible.

Contrariwise, the GeoViS framework can be, in principal, used as an interactive tool because the performance of the computations approximately scales with the number of processors that are used. Thus, we can achieve a very high rendering performance by simply using a cluster that is sufficiently large – about one million CPU cores are required. In the current implementation, we must resort to ambient illumination.

3. It is possible to visualize causality violations:

While the first two hypotheses can be corroborated, this hypothesis must be negated. As shown in Sec. 7.4.4, it is *principally* impossible to visualize a causality violation. This cir-

cumstance cannot be explained by mere common problems such as unavailable analytical results or insufficient computer hardware. We must face a profound impossibility to realize the egocentric visualization of causality violations. This dilemma is, not in the least, restricted to the Gödel universe itself. Even if we neglect general relativity and the concept of a free will within this context, the crux persists: We cannot formulate the initial conditions of an experiment so that a causality violation can be physically described, numerically simulated or visualized in any way:

The inherent logical paradox prevents us from achieving this goal.

We are only able to visualize time travel as long as the scene is (Novikov) self-consistent and *not* causality violating, as depicted and discussed in Sec. 7.4.2 and Sec. 7.4.3.

Outlook: We focused on the egocentric visualization of arbitrary solid objects in the Gödel universe. While we covered a wide range of district scenarios, several topics – beyond the focus of this work – could only be touched upon. Fortunately, new and challenging questions arose as well. Since this work has a strong interdisciplinary character, we encourage future work regarding visualization techniques and physical investigations.

Several concepts – which permit time travel but prevent causality violations – exist, see Sec. 4.3.3. One can easily “write down” several metrics within the domain of general relativity, such as the Gödel spacetime, where closed timelike curves exist, cf. Sec. 4.3.1. However, several researchers, such as Hawking and others, found that the actual construction of such a curve seems to trigger counteracting effects that might prevent the closure of the timelike worldlines. Thus, it is still unclear if time travel is actually possible.

We found that time travel is indeed a visible property in the Gödel universe: We can see the older instance of the traveler returning from the voyage *before* the younger version leaves. This insight should be maintainable for other spacetimes as well. However, we must consider that the actual travel back through time is hidden beyond the Gödel horizon: The *visible* images of the traveler increase in age as the observation time passes – each one *is seeing* the other getting older. During the travel beyond the horizon, the local time of the traveler increases from his own perspective, although he is propagating into the past of the observer. This part of the journey is hidden beyond the horizon and, therefore, we cannot see the process of the voyager *becoming younger*. The observer can only perceive the *result* of the time travel, but not the *process*.

For other spacetimes, the actual travel back through time might be visible. Consider an extremal Kerr black hole, see Sec. 4.3.1 on p. 50, where the two horizons have disappeared and the “naked” ring singularity remains. It is still uninvestigated, if an *optical* horizon exists – comparable to the Gödel horizon. If no such barrier exists, then the *entire* time travel process should be visible, at least from a suitable observation point.

For those spacetimes, the GEOViS framework must be modified. We were able to employ the invisibility of the traveler moving back in time to our advantage: All potential intersections of a

primary ray with an object occur on those segments of the worldline which are monotonically increasing in *coordinate time*. If all segments of the worldline must be considered, then the retrieval of the point which is closest to a ray segment must be entirely re-conceived.

The Gödel universe itself facilitates analytical investigations due to the very large number of symmetries, which are represented by five independent Killing vector fields. Thus, one could also think of calculating the parallel transport for an arbitrary vector, which is transported along a geodesic starting at the origin. Then, one could directly specify the general solution to this problem using finite isometric transformations. Thereby, polarization effects could be investigated as well.

Additionally, we reviewed the basic properties of the stress-energy tensor for Gödel's spacetime, i. e. the distribution of mass and energy, which creates the curvature. While the mathematical representation is concise and clear, the physical interpretation is challenging. Therefore, it is very difficult to intuitively understand the Gödel universe. Especially by investigating extended objects, we found a new approach for the question “what rotates with respect to whom?”. Common infinitesimal considerations confirm that pointlike objects rotate in Gödel's universe. However, being very particular about the homogeneity of the spacetime, we assume that an object of non-zero size *does not rotate*, but that every atomic particle (of which the entity is constituted) *does rotate* exactly as an infinitesimally small object. It is the hope of the author that further investigations shed light on the precise mechanism.

What remains to be visualized egocentrically? The fast moving objects cover the time travel domain and the GÖDEL ENGINE allows us to move arbitrary objects to any desired position. Of course, a multitude of distinct visualization types exist. For example, in Sec. 7.1.1, finite light cones and wave fronts structures are discussed in order to give another perspective on the propagation of light in the Gödel universe. Additionally, one could visualize the motion of massive particles by a similar approach. The propagation of a dust cloud or a solid object under the influence of the geodesic equations – alongside interior forces – can be simulated and then visualized as particle wavefront. Such a simulation directly brings up further questions. We focused on the optical appearance of the Gödel universe, i. e. what objects in this spacetime *look like*. But what does the Gödel universe *feel like*? Could we actually *live* in such a universe? An answer to these issues can be found when considering, for example, geodesical motion and geodesical deviation. Two connected particles with very similar – but not identical – initial conditions experience tidal forces, which can be determined by investigating the relative acceleration.

As detailed in Sec. 6.4.2, it is not possible to illuminate fast moving objects using the GÖDEL ENGINE. However, a combination of this approach with our previous work [GB08] should offer a straightforward remedy: Using GEOVIS, one could precalculate a specific scenario in which fast traveling objects are considered. The resulting dataset provides a lookup-table where each visible pixel is associated with a viewing direction under which the corresponding surface point is seen. This table, in principle, meets the requirements of the GÖDEL ENGINE, which can then

illuminate the scene as a postprocessing step. As a restriction, the light source must be at rest. An open question is how *arbitrarily moving* light sources (alongside a global illumination model) could be realized in general relativity.

Within this work, we restricted shadowing computations to a very simple self-shadowing algorithm: If the light ray intersects a convex object (with a closed surface) from the inside, then it must have traversed the object and the ray can therefore be neglected (see Sec. 6.3.4). By this means, we obtain the correct shadowing of a single object image. However, since the light rays are not represented by straight lines, we cannot compute the precise self-shadowing of distinct images of the *same* object directly. A photon might have already been absorbed along its helix-like path before being able to contribute to the illumination of a higher order image.

To resolve this problem and in order to introduce a precise shadowing computation – where *one object* can cast a shadow on *another* – we must implement another algorithm. While shadow volumes seem inappropriate, shadow mapping is more promising. The generation of the depth map is relatively straightforward because the actual implementation of the local illumination model itself already renders the scene from the point light source's perspective by means of finite isometric transformations. The depth map must be generated using a fairly high resolution, due to the complicated shape of the lightlike geodesics and, moreover, we might need more than one depth map because a shadow on an arbitrary point of an object can be cast along a potentially infinite number of different paths. The subsequent steps (computation of the light space coordinates, depth map test and the actual rendering) should be achievable.

In Sec. 6.3.4, we qualitatively discussed the errors introduced to both the texture coordinates and the illumination values that resulted from the linear interpolation between vertices. One might strive for a remedy to the deficiency which could be achieved using non-linear interpolation kernels for the properties mentioned above. The computation of higher order smoothing curves, implemented as CUDA kernels, could be realized by taking the relative resizing of certain primitives (to which a specific vertex is assigned to) into account. The coefficients of the polynomial smoothing curve, for example, could then be passed to an appropriate shader as vertex attributes. Of course, the “ground truth” is achieved using raytracing.

To enable transparency effects, a straightforward depth peeling is easily implementable into the GÖDEL ENGINE. Alongside photon mapping, one might elevate the quality of the renderings to the next level.

SCHLUSSFOLGERUNGEN UND AUSBLICK

An dieser Stelle werden wir auf die einleitende Frage aus der Kurzbeschreibung zurückkommen und sind zuversichtlich, dass **eine Vorstellung vom Gödel-Universum vermittelt** wurde. Diese Arbeit wird nun mit einer Zusammenfassung der Beiträge als auch einer Untersuchung der Hypothesen (siehe S. 2) abgeschlossen. Zusätzlich soll weitergehende Forschung angeregt werden.

Zusammenfassung: In Kap. 2 und Kap. 3 wurden sowohl die physikalischen und mathematischen Grundlagen der Relativitätstheorie als auch Visualisierungstechniken wie Raytracing und interaktive Methoden behandelt. Um die Arbeit in sich geschlossen zu präsentieren, wurden im letzten Einführungskapitel (Kap. 4) die physikalischen Aspekte des Gödel-Universums ausführlich besprochen und analysiert. Insbesondere mit Hilfe der Lichtkegelstruktur des Gödel-Universums konnten die physikalischen Effekte, welche das Auftreten geschlossener zeitartiger Kurven begründen, anschaulich dargestellt werden. Da die Lichtkegel sehr stark kippen, kann ein Reisender in die Vergangenheit einer anderen Person gelangen, obwohl er stets in seine eigene, lokale Zukunft propagiert. Ebenso wurden im Rahmen der Relativitätstheorie weitere Universen, in denen Zeitreisen prinzipiell möglich sind, zusammengefasst und die logische Behandlung von Kausalitätsverletzungen rekapituliert.

In Kap. 5 haben wir die analytischen Lösungen der Geodätengleichungen für spezielle und allgemeine Anfangsbedingungen hergeleitet. Durch die allgemeine Lösung konnte untersucht werden, ob für geodätische Bewegungen Kausalitätsverletzungen auftreten. Ein lichtartiges oder zeitartiges Teilchen kann in die Vergangenheit reisen, sofern die Anfangsgeschwindigkeit $v \gtrsim 0.98c$ ist und die anfängliche Radialkoordinate $R_0 \lesssim 1.7$ beträgt. Für ein maximales Zeitreiseintervall existiert demzufolge ein einzelnes Teilchen zweimal innerhalb des Gödel-Horizonts, ohne dass eine Kausalitätsverletzung auftritt.

Die Gleichungen des isometrischen Transports (für Punkte als auch Vektoren) wurden für alle fünf Killing-Vektorfelder hergeleitet. Lösungen der Geodätengleichungen für spezielle Anfangsbedingungen konnten unter Verwendung endlicher isometrischer Transformationen auf die allgemeine Lösung der Geodätengleichungen abgebildet werden. Durch dieses Verfahren konnten ebenso die Gödel-Horizonte für verschiedene Beobachter in einem gemeinsamen Diagramm

dargestellt werden, um dadurch deren gemeinsame Kausalitätsregionen zu untersuchen. Danach folgte die Beschreibung kreisförmiger CTCs und des Fermi-Walker-Transports entlang dieser Kurven, welche selbst jenseits des Horizonts liegen. Durch eine isometrische Transformation dieser Kreise wurden CTCs generiert, die den Ursprung beinhalten. Das Resultat dieser Prozedur ist eine Zeitreise, die am Ursprung beginnt. Ein Beobachter, der sich dort befindet, wird daher einen Zeitreisenden sehen, welcher andernfalls hinter dem Horizont verborgen bliebe. Da diese CTCs durch isometrische Transformationen gewonnen wurden, bleiben die aufgefundenen Eigenschaften kreisförmiger CTCs auch für diese Bahnen gültig.

Die GÖDEL ENGINE wurde in Kap. 6 vorgestellt. Wir haben eine drastische Beschleunigung der Berechnung egozentrischer Visualisierungen des Gödel-Universums von mindestens vier bis fünf Größenordnungen erreicht, da die Verbindungsgeodäten und auch die Blickrichtungen (unter denen ein Objekt sichtbar ist) direkt bestimmen werden konnten. Dabei wurden die Möglichkeiten moderner programmierbarer Grafikkhardware verwendet. Mit Hilfe von endlichen isometrischen Transformationen konnte ein lokales Beleuchtungsmodell implementiert werden, und darüber hinaus wurde ein einfaches Modell für Selbstabschattungen realisiert.

In dem Hauptkapitel dieser Dissertation, Kap. 7, wurden egozentrische Visualisierungen für eine Vielzahl verschiedener Szenarien vorgestellt. Im Anschluss an die Ausführungen über endliche Lichtkegelstrukturen wurde der Übergang von der flachen Minkowski-Raumzeit zum Gödel-Universum visualisiert. Dafür wurde ein Koordinatengitter konstruiert und der Gödel-Radius variiert. Da sich Licht im Gödel-Universum auf Schraubenbahnen ausbreitet, dreht sich ein von oben betrachtetes Gitter visuell gegen den Uhrzeigersinn. Ein radial nach außen blickender Beobachter dagegen sieht die Objekte in einer nach links gerichteten Bewegung. Solange ruhende Gegenstände in der Äquatorebene des Beobachters liegen, sind sie zweifach sichtbar. Objekte außerhalb dieser Ebene erscheinen dagegen unendlich oft. Sobald ein Objekt nahe dem optischen Horizont ist, verschwinden einige diese Abbilder. Wenn das Objekt sich außerhalb des Gödel-Horizonts befindet, dann sind auch alle Abbilder nicht mehr sichtbar.

Im Abschnitt 7.3 entfaltete die GÖDEL ENGINE ihr volles Potential. Wir beleuchteten eine Vielzahl sich quasistatisch bewegnender Objekte und konnten (unter Verwendung eines Beleuchtungsmodells nach Phong) Visualisierungen in einer bis dahin unerreichten Qualität erzeugen. Durch eine quantitative Analyse wurde die Blickrichtung, unter der ein Objekt vom Beobachter gesehen wird, die sichtbare Seite eines Objektes als auch die beleuchtete Region der zugehörigen Oberfläche erklärt. Die Interaktivität des Programms ermöglicht es, erstaunliche optische Eigenschaften des Gödel-Universums zu entdecken. Die beigefügten Filmsequenzen zeigen diese Effekte klar auf: Ein Objekt kann visuell hinter dem Gödel-Horizont verschwinden, bevor es von einem Abbild höherer Ordnung eines anderen Gegenstandes verdeckt wird. Ein weiteres Beispiel ist durch eine bewegte Punktlichtquelle gegeben. Obwohl sie zeitweise hinter dem Horizont verschwindet, kann das Streulicht stets wahrgenommen werden. Darüber hinaus wird ein senkrecht ausgerichteter Stab visuell als Kreis („Gödel-Ring“) wahrgenommen.

Unter Verwendung von GEOVIS wurden Objekte visualisiert, die sich fast so schnell wie das Licht bewegen (Abschnitt 7.4). Wir untersuchten kausale Bewegungen, geodätische und nicht kausalitätsverletzende Zeitreisen als auch ein Objekt, das auf einer geschlossenen zeitartigen Kurve fliegt. Alle quantitativen Analysen (durchgeführt mit der GÖDEL ENGINE) erklären und bestätigen die egozentrischen Visualisierungen. Die Berechnung scheinbarer Oberflächentemperaturen ermöglichte dabei die Bestimmung relativer Flugrichtungen, da das Gödel-Universum keine Gravitationsrotverschiebung aufweist. Durch eine geeignete Zuordnung, welche die lokale Emissionszeit auf einem Oberflächenpunkt mit einer bestimmten Farbe verknüpft, konnte eine sinnvolle Darstellung für Zeitreisen gefunden werden. Damit wurde das relative Alter eines Gegenstandes in einem bestimmten Abbild klar erkennbar.

Zeitreisen sind tatsächlich sichtbar: Ein Beobachter wird einen Reisenden auf einer CTC ankommen sehen, bevor dieser zu seiner Reise aufbricht. Allerdings gibt es aufgrund der Gesetze der Logik bei der Visualisierung von Zeitreisen enge Grenzen. Nur solche Zeitreisen sind visualisierbar, welche Novikov-selbstkonsistent sind. Nach dieser wichtigen Erkenntnis wurden alle bis dahin entdeckten visuellen Effekte in Kap. 8 zusammengestellt. Damit endete die Reise durch das Gödel-Universum.

Schlussfolgerungen: Von einem abstrakteren Standpunkt aus soll das Gödel-Universum als Fallbeispiel für ein Zeitreisen-Universum betrachtet werden. Im Lichte der Erkenntnisse dieser Arbeit folgt nun eine Analyse der Hypothesen, die in Kap. 1 aufgestellt wurden:

1. Mit Hilfe von egozentrischen Visualisierungen kann man Zeitreisen intuitiv verstehen:

Diese Dissertation ist die erste veröffentlichte Arbeit über die egozentrische Visualisierung von Zeitreisen im Rahmen der allgemeinen Relativitätstheorie. Die diagrammatische Szenedefinition und ebenso die quantitativen Analysen in den Abschnitten 7.4.2 und 7.4.3 enthüllten die genauen Eigenschaften von Zeitreisen innerhalb des Gödel-Universums. Zusätzlich zu diesen Erkenntnissen konnten die egozentrischen Visualisierungen weitere Informationen liefern, die uns erlaubten, Zeitreisen auf einer intuitiveren Ebene zu verstehen.

Um den Wahrheitsgehalt der Hypothese zu prüfen, muss zunächst festgestellt werden, dass sie sehr strikt formuliert ist: Erlauben egozentrische Visualisierungen *allein*, Zeitreisen vollständig auf intuitiver Ebene zu verstehen? Die Antwort lautet sicherlich nein. Ohne das Fundament der mathematischen Untersuchungen und quantitativen Analysen sind die visuellen Informationen der Filmsequenzen kaum verständlich. Wenn man beispielsweise das Erscheinungsbild der Erdkugel auf einer CTC (Abschnitt 7.4.3 und insbesondere Abb. 7.41a-e) ohne die vorbereitenden Analysen betrachtet, dann würde die Filmsequenz `CTC_shortRays.avi` sicherlich als Visualisierung von „extrem verzerrten Erdkugeln, die entweder auf den Beobachter zu oder von ihm wegfliegen“ interpretiert werden. Zwei Verbesserungen helfen, das egozentrische Erscheinungsbild zu verstehen: Erstens bestätigt

eine Farbzuoordnung, dass die sichtbaren Abbilder der Erde in der Tat durch die Zeit reisen. Zweitens sind Analysen (wie Abb. 7.38 und Abb. 7.39) zwingend erforderlich, um die gesamte Simulation in klarer und präziser Art und Weise darstellen.

Einzig und allein die Synthese von mathematischen Studien physikalischer Phänomene mit egozentrischen Visualisierungen erlaubt es uns, Erkenntnisse auf einer intuitiven Ebene zu gewinnen. Die mathematischen Untersuchungen sind für den wissenschaftlichen Laien sicherlich schwer nachvollziehbar, allerdings kann eine quantitative Analyse – wie beispielsweise Abb. 7.39 auf S. 152 – nahegebracht werden. Daher hilft die Kombination aus diesen Diagrammen *zusammen mit* egozentrischen Visualisierungen auch einem breiteren Publikum, mit den fortgeschrittenen Eigenschaften der allgemeinen Relativitätstheorie vertraut zu werden.

Egozentrische Visualisierungen erlauben es uns, Zeitreisen intuitiv zu verstehen – allerdings nur dann, wenn zusätzliche Informationen bereitgestellt werden.

2. Interaktive Methoden erleichtern die Entdeckung unbekannter optischer Effekte:

Sicherlich ist eine schnelle Bildgenerierung schon allein aufgrund praktischer Beweggründe wünschenswert: Ergebnisse können schnell erzielt werden. Große Rechencluster können dadurch in bestimmten Forschungsbereichen überflüssig werden. Zusätzlich war es in unserem Fall möglich, mit Hilfe des Phong-Beleuchtungsmodells eine bis dato unerreichte Bildqualität zu erreichen. Demzufolge dienen die analytischen Ergebnisse als Fundament für interaktive Visualisierungen.

Die Relevanz interaktiver Bilderzeugungsmethoden muss allerdings deutlich hervorheben werden, da die Interaktivität nicht als Selbstzweck verstanden werden soll: Mehrere unbekannt optische Eigenschaften wurden in Abschnitt 7.3.2 enthüllt, die ohne eine sehr schnelle Bilderzeugungsmethode möglicherweise unentdeckt geblieben wären. Objekte jenseits des Gödel-Horizonts können mittels Streulicht gesehen werden. Außerdem ist die visuelle Verdeckung von Objekten den direkten Annahmen entgegengesetzt. Vor allem fanden wir heraus, dass senkrechte Stäbe auf einen visuellen Gödel-Ring abgebildet werden.

Die Erweiterung unserer Ideen auf andere Mannigfaltigkeiten – für die analytische Ausdrücke für die Lichtausbreitung verfügbar sind – erscheint möglich und daher soll das der GÖDEL ENGINE zugrunde liegende Konzept Forschung in anderen Bereichen anregen. Das Auffinden unbekannter optischer Effekte ist auch für solche Raumzeiten zu erwarten. Sie können gefunden werden, da man die Szeneparameter interaktiv und daher auch in einer spielerischen Art und Weise ändern kann. Natürlich könnten solche Effekte auch durch ausführliche Studien der entsprechenden Gleichungen entdeckt werden.

Eine interaktive Visualisierungstechnik stellt eine *alternative und ergänzende* Herangehensweise dar.

Allerdings müssen auch die zu erwartenden Probleme hervorheben werden. Es wird sehr schwierig sein, die Idee hinter der GÖDEL ENGINE auf andere Raumzeiten zu übertragen, auch wenn es analytische Lösungen der Geodätengleichungen gibt. Selbst für das Gödel-Universum war die allgemeine Form der Geodäten schon zu komplex, so dass es nicht möglich war, die Verbindungsgeodäten zu berechnen. Erst die Anwendung endlicher isometrischer Transformationen brachte eine Abhilfe, denn dadurch wurde die allgemeine Lösung wenigstens implizit handhabbar. Solch eine Herangehensweise wird auch für andere homogene Raumzeiten möglich sein: Mindestens vier voneinander unabhängige Killing-Vektorfelder sind notwendig, um eine Szene so zu transformieren, dass ein beliebiger Punkt beispielsweise auf den Ursprung eines Koordinatensystems abgebildet wird. Für mathematisch herausfordernde Raumzeiten, wie beispielsweise einem rotierenden schwarzen Loch, wird ein interaktiver Algorithmus sicherlich auf Spezialfälle beschränkt sein. Vergleichbar mir der Visualisierung des Hipparcos-Katalogs um ein schwarzes Loch, vgl. [MW10], oder unseren früheren Arbeiten (siehe [GB08]), wird solch eine Applikation nur einen beschränkten Satz an Objekttypen, Flugbahnen oder Szeneparametern interaktiv visualisieren können, da eine bestimmte Menge an Daten stets vorberechnet (und dann als Textur oder ähnliche Struktur bereit gestellt) werden muss. Letztlich ist eine Vorgehensweise, bei denen die GÖDEL ENGINE als Black Box – gebe Szeneobjekt und analytische Lösungen für eine beliebige Raumzeit ein, erhalte die Verbindungsgeodäten und die Blickrichtungen – kaum möglich.

Im Gegensatz dazu ist GEOVIS, wenigstens prinzipiell, als interaktives Werkzeug verwendbar, da die Geschwindigkeit der Bildgenerierung ungefähr mit der Anzahl der Prozessoren skaliert. Eine sehr hohe Berechnungsgeschwindigkeit wird ganz einfach dadurch erzielt, indem eine Cluster ausreichender Größe verwendet wird – etwa eine Million Prozessorkerne sind hierfür notwendig. Allerdings wird in der momentanen Implementierung nur ambiente Beleuchtung verwendet.

3. Kausalitätsverletzende Situationen können visualisiert werden:

Während die ersten beiden Hypothesen bestätigt werden konnten, muss diese Hypothese verworfen werden. Wie in Abschnitt 7.4.4 dargelegt wurde, ist es *prinzipiell* unmöglich Kausalitätsverletzungen zu visualisieren. Dieser Umstand kann nicht durch übliche Probleme wie nichtverfügbare analytische Ergebnisse oder unzureichender Computerhardware begründet werden. Wir müssen einer tiefgreifenden Unmöglichkeit ins Auge sehen: Kausalitätsverletzungen können nicht egozentrisch visualisiert.

Das innewohnende logische Paradoxon macht das Erreichen dieses Zieles unmöglich.

Nur Novikov-selbstkonsistente und daher nicht kausalitätsverletzende Zeitreisen können visualisiert werden – wie jene, die in den Abschnitten 7.4.2 und 7.4.3 behandelt wurden.

Ausblick: In dieser Arbeit konzentrierten wir uns auf die egozentrische Visualisierung beliebiger (aber opaker) Körper im Gödel-Universum. Eine große Bandbreite verschiedener Szenarien wurde behandelt, wohingegen mehrere Aspekte – jenseits des Themenfelds dieser Arbeit – nur gestreift werden konnten. Überdies entsprangen unseren Untersuchungen neue und herausfordernde Fragestellungen. Da diese Arbeit einen stark interdisziplinären Charakter besitzt, sollen zukünftige Arbeiten hinsichtlich bestimmter Visualisierungstechniken als auch in Bezug auf physikalische Untersuchungen angeregt werden.

Es existieren mehrere Konzepte, die Zeitreisen unter Vermeidung von Kausalitätsverletzungen erlauben, vgl. Abschnitt 4.3.3. Außerdem ist es recht einfach, Metriken im Rahmen der Relativitätstheorie „aufzuschreiben“, die geschlossene zeitartige Kurven beinhalten (Abschnitt 4.3.1). Viele Wissenschaftler, unter ihnen Hawking, haben jedoch herausgefunden, dass die tatsächliche Konstruktion einer solchen Kurve offenbar entgegenwirkende Effekte auslöst, die das Schließen einer zeitartigen Weltlinie verhindern. Daher ist immer noch unklar, ob Zeitreisen tatsächlich möglich sind.

Wir haben herausgefunden, dass Zeitreisen tatsächlich eine sichtbare Eigenschaft des Gödel-Universums sind: Die ältere Instanz des Reisenden (welcher von seinem Ausflug jenseits des Horizontes zurückkehrt) ist sichtbar, *bevor* die jüngere Version überhaupt aufbricht. Diese Einsicht sollte auch für andere Raumzeiten haltbar sein. Allerdings muss berücksichtigt werden, dass die eigentliche Reise zurück in der Zeit im hier behandelten Fall durch den Gödel-Horizont verdeckt ist: Die *sichtbaren* Abbilder des Reisenden werden im Verlauf der Beobachtungszeit stets älter – Reisender und Beobachter sehen den anderen jeweils altern. Während der Reise hinter dem Horizont des Beobachters nimmt die Eigenzeit des Reisenden *zu*, obwohl er sich in die Vergangenheit des Beobachters begibt. Dieser Teil des Fluges ist nicht sichtbar und daher kann der Beobachter den Vorgang nicht sehen, in welchem der Reisende *jünger* wird. Der Beobachter kann nur das *Ergebnis* der Zeitreise visuell wahrnehmen, nicht aber den *Prozess* selbst.

Die eigentliche Reise zurück in der Zeit wird allerdings bei anderen Raumzeiten möglicherweise sichtbar sein. Bei einem extremalen Kerr-Loch, vgl. Abschnitt 4.3.1 auf S. 50, sind beide Horizonte verschwunden, nur die „nackte“ Ringsingularität bleibt übrig. Es ist unbekannt, ob ein *optischer* Horizont existiert, der vergleichbar mit dem Gödel-Horizont ist. Falls es keine Barriere dieser Art gibt, dann sollte der *gesamte* Prozess der Zeitreise sichtbar sein (zumindest von einem geeignet gewählten Beobachtungsstandpunkt aus).

Für solche Raumzeiten muss GeoVis modifiziert werden. Bei der Gödel-Raumzeit wurde die Unsichtbarkeit des Reisenden während der Reise zurück in der Zeit zu unserem Vorteil ausgenutzt: Alle potentiellen Schnitte eines Primärstrahls mit einem Objekt sind auf jene Segmente der Weltlinie beschränkt, die monoton steigend bezüglich der *Koordinatenzeit* sind. Sofern die gesamte Weltlinie berücksichtigt werden muss, ist eine vollständig neue Implementierung der Berechnungsmethode des einem Strahlsegments nächstgelegenen Punkts zwingend erforderlich.

Das Gödel-Universum selbst begünstigt analytische Untersuchungen aufgrund seiner hohen Symmetrie, die durch fünf unabhängige Killing-Vektorfelder dargestellt wird. Eine künftige Arbeit könnte den Paralleltransport eines beliebigen Vektors entlang einer aus dem Ursprung startenden Geodäten untersuchen. Dann ist die allgemeine Lösung des Paralleltransports mit Hilfe der von uns bestimmten endlichen isometrischen Transformationen sofort gegeben. Dadurch wird die analytische Untersuchung von Polarisierungseffekten möglich.

Darüber hinaus haben wir die grundlegenden Eigenschaften des Energie-Impuls-Tensors der Gödel-Metrik untersucht, der die Verteilung von Masse und Energie beschreibt und die Raumzeit-Krümmung verursacht. Es ist dabei sehr schwer, das Gödel-Universum intuitiv zu verstehen. Während die mathematische Beschreibung klar und prägnant ist, stellt die physikalische Interpretation eine Herausforderung dar. Insbesondere durch die Untersuchung ausgedehnter Objekte haben wir einen neuen Zugang zu der Frage „was rotiert bezüglich wem?“ gefunden. Übliche infinitesimale Betrachtungen bestätigen, dass punkrtartige Objekte im Gödel-Universum rotieren. Wenn man allerdings die Homogenität der Raumzeit genau nimmt, dann kann man zu folgendem Schluss kommen: Objekte mit einer von Null verschiedenen Ausdehnung drehen sich nicht, aber jeder atomare Baustein, aus welchen der ausgedehnte Gegenstand besteht, rotiert genau wie ein infinitesimales Objekt. Es ist die Hoffnung des Autors, dass weitergehende Untersuchungen Aufschluss über den genauen Mechanismus geben werden.

Welche Szenarien müssen noch egozentrisch visualisiert werden? Mit Hilfe schnell bewegter Objekte wurden Zeitreisen abgedeckt, und die GÖDEL ENGINE erlaubt uns, beliebige Objekte quasistatisch an jeden Ort zu verschieben.

Natürlich gibt es eine Vielzahl verschiedener Visualisierungsmethoden. In Abschnitt 7.1.1 wurden beispielsweise endliche Lichtkegelstrukturen und Wellenfronten untersucht, um eine andere Sichtweise auf die Lichtausbreitung im Gödel-Universum zu ermöglichen. In Anlehnung an dieses Vorgehen könnte man die Bewegung massiver Teilchen darstellen. Die Ausbreitung einer Staubwolke oder eines Festkörpers muss dazu mit den Geodätengleichungen – unter zusätzlicher Berücksichtigung innerer Kräfte – beschrieben werden, um dann als Teilchen-Wellenfront veranschaulicht zu werden. Solch eine Simulation wirft sofort weitere Fragen auf. Wir haben uns auf das optische Erscheinungsbild des Gödel-Universums konzentriert, d. h. wie Objekte in dieser Raumzeit *aussehen*. Wie aber *fühlt* sich das Gödel-Universum *an*? Könnten wir in solch einem Universum überhaupt *leben*? Um eine Antwort auf diese Fragen zu finden, müssen geodätische Bewegungen und geodätische Abweichungen untersucht werden. Zwei miteinander verbundene Teilchen mit sehr ähnlichen – aber nicht identischen – Anfangsbedingungen erfahren Gezeitenkräfte, die mit der zugehörigen Relativbeschleunigung ermittelt werden können.

Wie im Abschnitt 6.4.2 begründet wurde ist es nicht möglich, schnell bewegte Objekte mit der GÖDEL ENGINE zu beleuchten oder überhaupt zu visualisieren. Jedoch erscheint eine Kombination aus der GÖDEL ENGINE mit unserer vorhergehenden Arbeit [GB08] einen leicht realisierbaren Ausweg zu bieten: Mit GEOVIS wird ein bestimmtes Szenario, das schnell bewegte Objekte

beinhaltet, vorberechnet. Der resultierende Datensatz stellt eine Nachschlagetabelle bereit, die jedem sichtbaren Pixel einer Blickrichtung zuordnet, unter welcher der zugehörige Oberflächenpunkt sichtbar ist. Diese Tabelle entspricht prinzipiell den Anforderungen der GÖDEL ENGINE, die dann die Szene in einem Nachbearbeitungsschritt beleuchtet. Jedoch muss die Lichtquelle für solch eine Herangehensweise ruhend sein. Die Verwirklichung *beliebig bewegter* Lichtquellen (in Kombination mit einem globalen Beleuchtungsmodell) ist im Rahmen der allgemeinen Relativitätstheorie ein noch ungelöstes Problem.

In dieser Arbeit wurden die Schattenberechnungen auf einen einfachen Selbstabschattungs-Algorithmus beschränkt: Wenn ein Lichtstrahl ein konvexes Objekt (mit geschlossener Oberfläche) von innen schneidet, dann muss dieser Strahl das Objekt durchquert haben und kann daher vernachlässigt werden (vgl. Abschnitt 6.3.4). Mit Hilfe dieses Verfahrens wird die korrekte Selbstabschattung eines einzelnen Objekt-Abbildes bestimmt. Da die Lichtstrahlen allerdings nicht durch gerade Linien dargestellt werden, kann die GÖDEL ENGINE keine genaue Selbstabschattung verschiedener Abbilder *desselben* Objektes darstellen. Ein Photon könnte entlang der schraubenförmigen Lichtbahn bereits absorbiert worden sein, bevor es zur Beleuchtung eines Abbildes höherer Ordnung überhaupt beiträgt. Um dieses Problem zu lösen und zusätzlich einen exakten Abschattungsmechanismus – wo *ein Objekt* Schatten auf ein *anderen Körper* wirft – zu realisieren, muss ein anderer Weg gegangen werden. Während „Shadow Volumes“ ungeeignet erscheinen, ist das „Shadow Mapping“ vielversprechend. Die Erzeugung der Tiefenkarte ist recht unkompliziert, da die verwendete Implementierung des lokalen Beleuchtungsmodells die Szene bereits aus der Perspektive der Lichtquelle berechnet. Dies ist aufgrund der isometrischen Transformationen möglich, da sie erlauben, einen beliebigen Punkt auf eine beliebige Position abzubilden. Die Tiefenkarte muss, aufgrund der komplizierten Lichtbahnen, eine recht hohe Auflösung besitzen. Darüber hinaus werden möglicherweise mehrere Karten notwendig sein, da ein Schatten auf einem Objekt entlang einer etwaig unendlichen Anzahl verschiedener Wege geworfen wird. Die nachfolgenden Programmschritte (Berechnung der Lichtraumkoordinaten, Test gegen die Tiefenkarte und die eigentliche Bilderzeugung) sollten leicht durchführbar sein.

Im Abschnitt 6.3.4 diskutierten wir Fehler (die aufgrund der linearen Interpolation bei den Texturkoordinaten und den Beleuchtungswerten entstehen) auf qualitativer Ebene. Eine Linderung dieses Problems kann durch nichtlineare Interpolations-Kernels geschaffen werden. Die Berechnung von Glättungskurven hoher Ordnung – als CUDA-Kernel implementiert – wird durch eine Berücksichtigung der relativen Größenänderung der Primitive erreicht. Dazu wären diejenigen Dreiecke zu betrachten, die einem bestimmtem Vertex zugeordnet sind. Die Koeffizienten einer (beispielsweise) polynomialen Glättungskurve müssen dann einem geeigneten Shader als Vertexattribute übermittelt werden. Die „volle Wahrheit“ wird natürlich durch Raytracing erreicht.

Um Transparenzeffekte zu realisieren, ist ein einfaches „Depth Peeling“ leicht in die GÖDEL ENGINE zu implementieren. Unter zusätzlicher Verwendung von „Photon Mapping“ wird dadurch die Qualität der generierten Bilder auf die nächste Stufe angehoben.

DETAILS ON THE GÖDEL METRIC

In this appendix, we provide several general-relativistic quantities calculated for the Gödel space-time. These results can be verified using MAPLE [map] with the GRTENSOR II package [grt] and are also published in [MG09b].

A.1 Cylindrical Coordinates

The Gödel metric in cylindrical coordinates is

$$ds^2 = -c^2 dt^2 + \frac{dr^2}{1+(r/r_G)^2} + r^2 \left[1 - \left(\frac{r}{r_G} \right)^2 \right] d\varphi^2 + dz^2 - 2\sqrt{2}r^2 \frac{c}{r_G} dt d\varphi, \quad (\text{A.1})$$

where r_G is the Gödel radius.

Christoffel symbols:

$$\Gamma_{tr}^t = \frac{2r}{r_G^2} \frac{1}{1+(r/r_G)^2}, \quad \Gamma_{tr}^\varphi = -\frac{\sqrt{2}c}{r_G r} \frac{1}{1+(r/r_G)^2}, \quad (\text{A.2a})$$

$$\Gamma_{t\varphi}^r = \frac{\sqrt{2}cr}{r_G} \left[1 + \left(\frac{r}{r_G} \right)^2 \right], \quad \Gamma_{rr}^r = -\frac{r}{r_G^2} \frac{1}{1+(r/r_G)^2}, \quad (\text{A.2b})$$

$$\Gamma_{r\varphi}^t = \frac{\sqrt{2}r^3}{cr_G^3} \frac{1}{1+(r/r_G)^2}, \quad \Gamma_{r\varphi}^\varphi = \frac{1}{r} \frac{1}{1+(r/r_G)^2}, \quad (\text{A.2c})$$

$$\Gamma_{\varphi\varphi}^r = r \left[1 + \left(\frac{r}{r_G} \right)^2 \right] \left[1 - \frac{1}{2} \left(\frac{2r}{r_G} \right)^2 \right]. \quad (\text{A.2d})$$

Riemann-Tensor:

$$R_{trtr} = \frac{2c^2}{r_G^2} \frac{1}{1+(r/r_G)^2}, \quad R_{trr\varphi} = -\frac{2\sqrt{2}cr^2}{r_G^3} \frac{1}{1+(r/r_G)^2}, \quad (\text{A.3a})$$

$$R_{t\varphi t\varphi} = \frac{2c^2r^2}{r_G^2} \frac{1}{1+(r/r_G)^2}, \quad R_{r\varphi r\varphi} = \frac{2r^2}{r_G^2} \frac{1+3(r/r_G)^2}{1+(r/r_G)^2}. \quad (\text{A.3b})$$

Ricci-Tensor:

$$R_{tt} = \frac{4c^2}{r_G^2}, \quad R_{t\varphi} = \frac{4\sqrt{2}r^2c}{r_G^3}, \quad R_{\varphi\varphi} = \frac{8r^4}{r_G^4}. \quad (\text{A.4})$$

Ricci and Kretschman scalar:

$$\mathcal{R} = -\frac{4}{r_G^2}, \quad \mathcal{K} = \frac{48}{r_G^4}. \quad (\text{A.5})$$

Cosmological constant:

$$\Lambda = \frac{\mathcal{R}}{2} \quad (\text{A.6})$$

Killing vectors:

$$\xi_{\hat{a}}^{\mu} = \begin{pmatrix} 1 \\ 0 \\ 0 \\ 0 \end{pmatrix}, \quad \xi_{\hat{b}}^{\mu} = \frac{1}{\sqrt{1+(r/r_G)^2}} \begin{pmatrix} \frac{r}{\sqrt{2}c} \cos \varphi \\ \frac{r_G}{2} (1+(r/r_G)^2) \sin \varphi \\ \frac{r_G}{2r} (1+2(r/r_G)^2) \cos \varphi \\ 0 \end{pmatrix}, \quad \xi_{\hat{c}}^{\mu} = \begin{pmatrix} 0 \\ 0 \\ 1 \\ 0 \end{pmatrix}, \quad (\text{A.7a})$$

$$\xi_{\hat{d}}^{\mu} = \begin{pmatrix} 0 \\ 0 \\ 0 \\ 1 \end{pmatrix}, \quad \xi_{\hat{e}}^{\mu} = \frac{1}{\sqrt{1+(r/r_G)^2}} \begin{pmatrix} \frac{r}{\sqrt{2}c} \sin \varphi \\ -\frac{r_G}{2} (1+(r/r_G)^2) \cos \varphi \\ \frac{r_G}{2r} (1+2(r/r_G)^2) \sin \varphi \\ 0 \end{pmatrix}. \quad (\text{A.7b})$$

Local tetrad:

For the local tetrad in Gödel's spacetime, an ansatz similar to the local tetrad of a rotating spacetime in spherical coordinates, cf. [MG09b], can be used. After substituting $\theta \rightarrow z$ and swapping base vectors $\mathbf{e}_{(2)}$ and $\mathbf{e}_{(3)}$, an orthonormalized and right-handed local tetrad is obtained.

$$\mathbf{e}_{(t)} = \Gamma (\partial_t + \zeta \partial_\varphi), \quad \mathbf{e}_{(r)} = \sqrt{1+(r/r_G)^2} \partial_r, \quad \mathbf{e}_{(\varphi)} = \Delta \Gamma (A \partial_t + B \partial_\varphi), \quad \mathbf{e}_{(z)} = \partial_z, \quad (\text{A.8a})$$

where

$$A = -\frac{\sqrt{2}r^2c}{r_G} + \zeta r^2 (1-(r/r_G)^2), \quad B = c^2 + \frac{\sqrt{2}\zeta r^2c}{r_G}, \quad (\text{A.9a})$$

$$\Gamma = \frac{1}{\sqrt{c^2 + 2\zeta r^2c/r_G - \zeta^2 r^2 (1-(r/r_G)^2)}}, \quad \Delta = \frac{1}{rc \sqrt{1+(r/r_G)^2}}. \quad (\text{A.9b})$$

Transformation between local direction $y^{(i)}$ and coordinate direction y^μ :

$$y^t = y^{(t)}\Gamma + y^{(\varphi)}\Delta\Gamma A, \quad y^r = y^{(r)}\sqrt{1 + (r/r_G)^2}, \quad y^\varphi = y^{(t)}\Gamma\zeta + y^{(\varphi)}\Delta\Gamma B, \quad y^z = y^{(z)}. \quad (\text{A.10})$$

with the above abbreviations.

A.2 Scaled Cylindrical Coordinates

If we apply the simple transformation

$$T = \frac{t}{r_G}, \quad R = \frac{r}{r_G}, \quad \phi = \varphi, \quad Z = \frac{z}{r_G}, \quad (\text{A.11})$$

we find a formulation for the metric scaling with r_G , which is

$$ds^2 = r_G^2 \left(-c^2 dT^2 + \frac{dR^2}{1+R^2} + R^2(1-R^2)d\phi^2 + dZ^2 - 2\sqrt{2}cR^2 dT d\phi \right). \quad (\text{A.12})$$

Christoffel symbols:

$$\Gamma_{TR}^T = \frac{2R}{1+R^2}, \quad \Gamma_{TR}^\phi = -\frac{\sqrt{2}c}{R(1+R^2)}, \quad (\text{A.13a})$$

$$\Gamma_{T\phi}^R = \sqrt{2}cR(1+R^2), \quad \Gamma_{RR}^R = -\frac{R}{1+R^2}, \quad (\text{A.13b})$$

$$\Gamma_{R\phi}^T = \frac{\sqrt{2}R^3}{c(1+R^2)}, \quad \Gamma_{R\phi}^\phi = \frac{1}{R(1+R^2)}, \quad (\text{A.13c})$$

$$\Gamma_{\phi\phi}^R = R(1+R^2)(2R^2-1). \quad (\text{A.13d})$$

Riemann-Tensor:

$$R_{TRTR} = \frac{2r_G^2 c^2}{1+R^2}, \quad R_{TRR\phi} = -\frac{2\sqrt{2}r_G^2 c R^2}{1+R^2}, \quad (\text{A.14a})$$

$$R_{T\phi T\phi} = 2c^2 r_G^2 R^2(1+R^2), \quad R_{R\phi R\phi} = \frac{2r_G^2 R^2(1+3R^2)}{1+R^2}. \quad (\text{A.14b})$$

Ricci-Tensor:

$$R_{TT} = 4c^2, \quad R_{T\phi} = 4\sqrt{2}cR^2, \quad R_{\phi\phi} = 8R^4. \quad (\text{A.15})$$

Ricci and Kretschman scalar

$$\mathcal{R} = -\frac{4}{r_G^2}, \quad \mathcal{K} = \frac{48}{r_G^4}. \quad (\text{A.16})$$

Cosmological constant:

$$\Lambda = \frac{\mathcal{R}}{2} \quad (\text{A.17})$$

Killing vectors:

$$\xi_a^\mu = \begin{pmatrix} 1 \\ 0 \\ 0 \\ 0 \end{pmatrix}, \quad \xi_b^\mu = \frac{1}{\sqrt{1+R^2}} \begin{pmatrix} \frac{R}{\sqrt{2}c} \cos \varphi \\ \frac{1}{2}(1+R^2) \sin \varphi \\ \frac{1}{2R}(1+2R^2) \cos \varphi \\ 0 \end{pmatrix}, \quad \xi_c^\mu = \begin{pmatrix} 0 \\ 0 \\ 1 \\ 0 \end{pmatrix}, \quad (\text{A.18a})$$

$$\xi_d^\mu = \begin{pmatrix} 0 \\ 0 \\ 0 \\ 1 \end{pmatrix}, \quad \xi_e^\mu = \frac{1}{\sqrt{1+R^2}} \begin{pmatrix} \frac{R}{\sqrt{2}c} \sin \varphi \\ -\frac{1}{2}(1+R^2) \cos \varphi \\ \frac{1}{2R}(1+2R^2) \sin \varphi \\ 0 \end{pmatrix}. \quad (\text{A.18b})$$

Local tetrad:

After the transformation to scaled cylindrical coordinates, the local tetrad reads

$$\mathbf{e}_{(T)} = \frac{\Gamma}{r_G} (\partial_T + \zeta \partial_\varphi), \quad \mathbf{e}_{(R)} = \frac{1}{r_G} \sqrt{1+R^2} \partial_R, \quad \mathbf{e}_{(\phi)} = \frac{\Delta \Gamma}{r_G} (A \partial_T + B \partial_\varphi), \quad \mathbf{e}_{(Z)} = \frac{1}{r_G} \partial_Z, \quad (\text{A.19a})$$

where

$$A = R^2 [-\sqrt{2}c + (1-R^2)\zeta], \quad B = c^2 + \sqrt{2}R^2 c \zeta, \quad (\text{A.20a})$$

$$\Gamma = \frac{1}{\sqrt{c^2 + 2\sqrt{2}R^2 c \zeta - R^2(1-R^2)\zeta^2}}, \quad \Delta = \frac{1}{Rc\sqrt{1+R^2}}. \quad (\text{A.20b})$$

Using the local tetrad for a stationary observer on a circular orbit, eqns. (4.6), the transformation from a local vector $y^{(i)}$ to a coordinate vector y^μ reads

$$y^T = \frac{\Gamma}{r_G} y^{(T)} + \frac{\Delta \Gamma A}{r_G} y^{(\phi)}, \quad y^R = \frac{R}{r_G} \sqrt{1+R^2} y^{(1)}, \quad (\text{A.21a})$$

$$y^\phi = \frac{\Gamma \zeta}{r_G} y^{(T)} + \frac{\Delta \Gamma B}{r_G} y^{(\phi)}, \quad y^Z = \frac{1}{r_G} y^{(Z)}, \quad (\text{A.21b})$$

and the back transformation is given by

$$y^{(T)} = \frac{r_G}{\Gamma} \frac{B y^T - A y^\phi}{B - \zeta A}, \quad y^{(R)} = \frac{r_G}{\sqrt{1+R^2}} y^R, \quad (\text{A.22a})$$

$$y^{(\phi)} = \frac{r_G}{\Delta \Gamma} \frac{y^\phi - \zeta y^T}{B - \zeta A}, \quad y^{(Z)} = r_G y^Z. \quad (\text{A.22b})$$

The transformation rules for the static tetrad, eqns. (4.8), are

$$y^T = \frac{1}{r_G c} \left(y^{(T)} - \frac{\sqrt{2}R}{\sqrt{1+R^2}} y^{(\phi)} \right), \quad y^{(T)} = r_G (c y^T + \sqrt{2}R^2 y^\phi), \quad (\text{A.23a})$$

$$y^R = \frac{1}{r_G} \sqrt{1+R^2} y^{(1)}, \quad y^{(R)} = r_G \frac{R}{\sqrt{1+R^2}} y^R, \quad (\text{A.23b})$$

$$y^\phi = \frac{1}{r_G R} \frac{1}{\sqrt{1+R^2}} y^{(\phi)}, \quad y^{(\phi)} = r_G R \sqrt{1+R^2} y^\phi, \quad (\text{A.23c})$$

$$y^Z = \frac{1}{r_G} y^{(Z)}, \quad y^{(Z)} = r_G y^Z. \quad (\text{A.23d})$$

DETAILS ON THE SOLUTION OF THE GEODESIC EQUATIONS

Considering the equations of motion (5.4), we realize that the radial equation (5.4b) is solely dependent on the radial coordinate and its derivative. The other three equations (5.4a), (5.4c) and (5.4d) require the solution of the radial equation. Hence, we solve the radial equation and use the result to solve the remaining equations. Obviously, these steps can also be used for the geodesic equations for special initial conditions, eq. (5.5).

B.1 Special Initial Conditions

After the separation of variables in the radial equation (5.5b), we obtain

$$\frac{\pm dR}{\sqrt{K_p/K_m - R^2}} = \sqrt{K_m} d\lambda, \quad (\text{B.1})$$

where the two signs on the left-hand side result from extracting the root of eq. (5.5b) and describe a photon leaving or arriving at the origin, respectively. This equation is integrated and arrives at

$$\pm \arcsin \left(R \sqrt{\frac{K_m}{K_p}} \right) - R_0 = \sqrt{K_m} (\lambda - \lambda_{0\pm}) \quad (\text{B.2})$$

with two different integration constants $\lambda_{0\pm}$, which depend on the branch of the solution. Furthermore, we set $R_0 = 0$. The upper equation can then be written as

$$R(\lambda) = \pm \sqrt{\frac{K_p}{K_m}} \sin \left(\sqrt{K_m} (\lambda - \lambda_{0\pm}) \right). \quad (\text{B.3})$$

The different branches of the solution are merged to a continuous function for both incoming and outgoing photons as well as the initial condition R_0 , which directly results in eq. (5.7b). After inserting eq. (5.7b) into (5.5a) we find

$$c \dot{T} = -k_0 \frac{K_m/K_p - \sin^2\left(\sqrt{K_m}\lambda\right)}{K_m/K_p + \sin^2\left(\sqrt{K_m}\lambda\right)}. \quad (\text{B.4})$$

The integral for this equation is given by

$$cT(\lambda) = k_0\lambda + \sqrt{2} \arctan\left(\frac{k_0\sqrt{2}}{\sqrt{K_m}} \tan\left(-\sqrt{K_m}\lambda\right)\right). \quad (\text{B.5})$$

Since $\arctan(\tan(y))$ is a sawtooth function, the floor function $p_q(\lambda)$, as in eq. (5.8a), is introduced. Including the integration constant t_0 , we obtain a continuously differentiable function $t(\lambda)$, as in eq. (5.7a). The angular equation (5.5c) is also solvable after inserting the radial solution (5.7b). The result is

$$\dot{\phi} = \frac{-\sqrt{2}k_0 K_m/K_p}{\left[K_m/K_p + \sin^2\left(\sqrt{K_m}\lambda\right)\right]}. \quad (\text{B.6})$$

The integral reads

$$\phi(\lambda) = \arctan\left(\frac{k_0\sqrt{2}}{\sqrt{K_m}} \tan\left(-\sqrt{K_m}\lambda\right)\right), \quad (\text{B.7})$$

where we again need the floor function $p_q(\lambda)$ to generate a continuously differentiable function. Including the integration constant ϕ_0 , we obtain the solution, eq. (5.7c). Eq. (5.5d) is trivial. For investigating geodesics starting at the origin, we set the integration constant $z_0 = 0$.

B.2 General Initial Conditions

After the separation of variables in eq. (5.4b), we see that

$$\int_{R(0)}^{R(\lambda)} \frac{u \, du}{\sqrt{-K_m u^4 + B_1 u^2 - k_2^2}} = (\pm\lambda - \lambda_0). \quad (\text{B.8})$$

After substituting $u^2 = v$, we can solve this equation using standard integration tables¹, viz.

$$\int \frac{dx}{\sqrt{X}} = \frac{-1}{\sqrt{-a}} \arcsin\left(\frac{2ax + b}{\sqrt{b^2 - 4ac}}\right), \quad (\text{B.9})$$

¹see [BSMM07], integral (241).

where $X = ax^2 + bx + c$. It is necessary, however, that $K_m > 0$ and $B_1^2 - 4K_m k_2^2 > 0$. This is achieved by inserting the initial conditions, eq. (5.3), combined with all the possible choices of local initial directions. The necessary estimate is omitted here because the calculation does not yield any physical insight. We calculate the above integral, solve for $R(\lambda)$ and neglect the negative branch resulting from extracting the root. To decide the algebraic sign in $\pm\lambda$, we discuss the monotonic behavior of the solution. For instance, a geodesic starting radially outwards must be monotonically increasing in R for small λ . We find that radially outgoing geodesics require the negative sign and vice versa. Hence, we substitute $\pm\lambda \rightarrow -\sigma_1\lambda$. We arrive at the radial solution, eq. (5.12b), after determining the integration constant C_1 using $R(0) = R_0$. To solve the angular equation (5.4c), we insert the radial solution, eq. (5.12b). After several simplifications we find, using $\tilde{B} = \sqrt{B_1^2 - 4K_m k_2^2}$,

$$\dot{\phi}(\lambda) = \frac{2K_m k_2}{B_1 - \tilde{B} \sin(v(\lambda)/2)} - \frac{2K_m k_2 + 2\sqrt{2}k_0 K_m}{2K_m + B_1 - \tilde{B} \sin(v(\lambda)/2)}, \quad (\text{B.10})$$

where we used the abbreviations (5.9) and the auxiliary function $v(\lambda)$; see eq. (5.11a). Both terms can be integrated using ²

$$\int \frac{dx}{b + d \sin(ax)} = \frac{2}{a^2 \sqrt{b^2 - d^2}} \arctan \left(\frac{b \tan(ax/2) + d}{\sqrt{b^2 - d^2}} \right), \quad (\text{B.11})$$

where $b^2 > d^2$ is required. Again, this can be shown using eqns. (5.3) and all the possible choices of lightlike and timelike local vectors. Prefactors $2/(a^2 \sqrt{b^2 - d^2})$ are simplified considerably when using $y/\sqrt{y^2} = \text{sgn}(y)$, the integration constant is found when setting $\phi(0) = \phi_0$ and after a lengthy calculation, the solution, eq. (5.12c), is found. The time equation (5.4a) is solved analogously. Again, we use the radial solution (5.12b), the abbreviations B_i , the auxiliary function $v(\lambda)$ and obtain the following equation:

$$c \dot{T} = \frac{k_0(-2K_m + B_1) - 2\sqrt{2}K_m k_2}{2K_m + B_1 - \tilde{B} \sin(v(\lambda)/2)} - \frac{k_0 \tilde{B} \sin(v(\lambda)/2)}{2K_m + B_1 - \tilde{B} \sin(v(\lambda)/2)}. \quad (\text{B.12})$$

The first term is integrated using eq. (B.11); the second term requires the formula ³

$$\int \frac{\sin(ax)dx}{b + d \sin(ax)} = \frac{x}{d} - \frac{b}{d} \int \frac{dx}{b + d \sin(ax)}. \quad (\text{B.13})$$

Again, $b^2 > d^2$ is necessary and fulfilled. After simplifications similar to those used in the angular solution, we must introduce the periodicity function $\tilde{p}(\lambda)$, eq. (5.11d), for continuously differentiable temporal behavior. Requiring $T(0) = T_0$ determines the integration constant C_3 as in our solution, eq. (5.12a).

²see [BSMM07], integral (306a).

³see [BSMM07], integral (307).

DETAILS ON THE SOLUTION OF THE EQUATIONS OF ISOMETRIC TRANSPORT

C.1 Transformation of Points

The equations of isometric transport (2.31) for the Killing vector field ξ_1^μ , eq. (4.19b), read

$$\frac{dT}{d\eta} = \frac{R}{\sqrt{2}c\sqrt{1+R^2}} \cos \phi, \quad (\text{C.1a})$$

$$\frac{dR}{d\eta} = \frac{1}{2} \sqrt{1+R^2} \sin \phi, \quad (\text{C.1b})$$

$$\frac{d\phi}{d\eta} = \frac{1+2R^2}{2R\sqrt{1+R^2}} \cos \phi, \quad (\text{C.1c})$$

$$\frac{dZ}{d\eta} = 0, \quad (\text{C.1d})$$

where both Rr and ϕ are dependent of η . We solve eq. (C.1b) for ϕ , i. e.

$$\phi = \arcsin \left(\frac{2\dot{R}}{\sqrt{1+R^2}} \right). \quad (\text{C.2})$$

All differentiations in this section are given with respect to the isometric parameter η . By inserting this equation into eq. (C.1c), we obtain an uncoupled differential equation. Using $\arcsin'(x) = 1/\sqrt{1-x^2}$ and $\cos(\arcsin(x)) = \sqrt{1-x^2}$, we finally arrive at

$$4R\dot{R} + 4R^3\ddot{R} + 4R^2\dot{R}^2 - 3R^2 + 4\dot{R}^2 - 2R^4 - 2 = 0. \quad (\text{C.3})$$

After substituting $y = R^2$, we find that

$$(1+y)(\ddot{y} - y - 1/2) = 0. \quad (\text{C.4})$$

Since y must be positive, we neglect the first factor and obtain

$$\ddot{y} - y = 1/2, \quad (\text{C.5})$$

which is solved by

$$y(\eta) = D_1 e^{-\eta} + D_2 e^{\eta} - 1/2. \quad (\text{C.6})$$

Eq. (5.16b) is reproduced after the back substitution $R = \sqrt{y}$. The solution $\phi(\eta)$, eq. (5.16c), results from inserting $R(\eta)$ and its derivative $\dot{R}(\eta)$ into eq. (C.2). Both $R(\eta)$ and $\phi(\eta)$ are inserted into eq. (C.1a), which can then be written as

$$\dot{T} = \frac{\sqrt{2}\sqrt{D_1 D_2 - 1/16}}{c(D_1 e^{-\eta} + D_2 e^{\eta} + 1/2)}. \quad (\text{C.7})$$

After the substitutions $e^{\eta} = h$ and $dh/d\eta = e^{\eta}$, we arrive at

$$\frac{dT}{dh} = \frac{\sqrt{2}\sqrt{D_1 D_2 - 1/16}}{c(h^2 D_2 + h/2 + D_1)}, \quad (\text{C.8})$$

which is solved with the appropriate arctan function. After the back substitution, the solution, eq. (5.16a), is found. The integration constants D_1, D_2, D_3 and D_4 , eqns. (5.19), are determined using the initial conditions $x^{\mu}(0) = x_0^{\mu}$. This choice also ensures that the solution is well-behaved, i. e. $D_1 D_2 - 1/16 > 0 \forall x_0^{\mu}$. Note that eq. (C.2) is only valid if ϕ is in the right half-plane. For $\phi \in]\frac{\pi}{2}, \frac{3\pi}{2}[$, we need a different branch of the arcsin function, which results in the parameter σ to distinguish both half-planes; see eq. (5.18). The solution of eq. (4.19c) can be derived from the solution of eq. (4.19b). Considering eq. (4.19), it is obvious [KWSD04] that $\xi_4(\phi) = \xi_1(\phi - \pi/2)$. Hence, the solution of eq. (4.19c) is obtained via shifting the angular coordinate in eq. (5.16) by $+\pi/2$, as stated in eq. (5.17).

C.2 Transformation of Vectors

The equations of isometric transport for vectors (2.32) for the Killing vector field ξ_1^{μ} , eq. (4.19b), are given by eqns. (5.20). To formulate these equations with respect to the local frame of reference, eqns. (A.23), we consider an arbitrary vector $\mathbf{u} = u^{\mu} \partial_{\mu} = u^{(a)} \mathbf{e}_{(a)}$. As both u^{μ} and $u^{(a)}$ depend on the curve parameter η , we find, using $q(R) = \sqrt{1 + R^2}$, that

$$u^T = -\frac{R\sqrt{2}}{cr_G q(R)} u^{(2)} + \frac{1}{cr_G} u^{(0)}, \quad (\text{C.9a})$$

$$u^R = \frac{q(R)}{rg} u^{(1)}, \quad (\text{C.9b})$$

$$u^{\phi} = \frac{1}{r_G R q(R)} u^{(2)}, \quad (\text{C.9c})$$

$$u^Z = \frac{1}{r_G} u^{(3)}, \quad (\text{C.9d})$$

and

$$\dot{u}^T = \frac{\sqrt{2}}{cr_G q(R)} \left(\frac{R^2 \dot{R}}{q^2(R)} u^{(2)} - \dot{R} u^{(2)} - R \dot{u}^{(2)} \right) + \frac{1}{cr_G} \dot{u}^{(0)}, \quad (\text{C.10a})$$

$$\dot{u}^R = \frac{R \dot{R}}{r_G q(R)} u^{(1)} + \frac{q(R)}{r_G} \dot{u}^{(1)}, \quad (\text{C.10b})$$

$$\dot{u}^\phi = \frac{1}{r_G q(R)} \left(\dot{u}^{(2)} - \frac{\dot{R}}{R} u^{(2)} - \frac{\dot{R}}{q^2(R)} u^{(2)} \right), \quad (\text{C.10c})$$

$$\dot{u}^Z = \frac{1}{r_G} \dot{u}^{(3)}, \quad (\text{C.10d})$$

where the derivative is given with respect to η . We insert eqns. (C.9) and (C.10) in eqns. (5.20) and solve for the derivative of the local formulation $\dot{u}^{(a)}$. Note that R and ϕ are evaluated along the solution (5.16), i. e. $R = R_1(\eta)$ and $\phi = \phi_1(\eta)$. Then, the equations of transport (5.20) become

$$\dot{u}^{(1)} = f(\eta) u^{(2)}, \quad (\text{C.11a})$$

$$\dot{u}^{(2)} = -f(\eta) u^{(1)}, \quad (\text{C.11b})$$

with

$$f(\eta) = \frac{\cos \phi_1(\eta)}{2R_1(\eta)q(R_1(\eta))} = \frac{\sqrt{D_1 D_2 - 1/16}}{R_1^2(\eta)[1 + R_1^2(\eta)]}. \quad (\text{C.12})$$

Additionally, we have $\dot{u}^{(0)} = \dot{u}^{(3)} = 0$. Hence, both components, $u^{(0)}$ and $u^{(3)}$, remain unchanged during transport, while $u^{(1)}$ and $u^{(2)}$ are rotated around the local $e_{(3)}$ axis. Analytical solutions to these equations can be found when using an ansatz specific to the rotational symmetry and then applying the variation of constants method. The extension reads

$$u^{(1)}(\eta) = D_6 \cos(F(\eta)) - D_7 \sin(F(\eta)), \quad (\text{C.13a})$$

$$u^{(2)}(\eta) = D_6 \sin(F(\eta)) + D_7 \cos(F(\eta)), \quad (\text{C.13b})$$

where

$$F(\eta) = \int f(\eta') d\eta' + D_5. \quad (\text{C.14})$$

The integration of $f(\eta)$ and the determination of D_5 using $F(0) = 0$ reproduce the solution as shown in eq. (5.22). Note that the parameter σ , eq. (5.18), ensures the correct behavior for both half-planes. The integration constants, D_6 and D_7 , correspond to the components $u_0^{(1)}$ and $u_0^{(2)}$ of the initial vector with respect to the local frame of reference, respectively. Again, we can derive the solution for the Killing vector field ξ_4^μ (eq. (4.19c)) using this solution for the Killing vector field ξ_1^μ . Since the finite transport for points only yields a constant angular shift of $\Delta\phi = +\pi/2$, which, in particular, is independent of the curve parameter η , the solution using ξ_4^μ is identical to this solution for ξ_1^μ .

List of Figures

2.1	Definition of a manifold	8
2.2	Definition of a curve on a manifold	9
2.3	2D manifold, tangent space and local tetrad	11
2.4	Initial direction with respect to the local tetrad	15
3.1	3D raytracing	20
3.2	4D raytracing	22
3.3	Connecting points for interactive visualizations	24
3.4	Comparison of CPU and GPU	26
3.5	Rendering pipeline	27
3.6	Arrangement of threads in blocks on a grid	29
3.7	Symbolic program flow of a CUDA application	30
4.1	Gödel's original publication	37
4.2	Lightlike geodesics in (XY) -subspace using pseudo-Cartesian coordinates	39
4.3	Homogeneity and rotating matter	42
4.4	Light cone structure in special relativity	46
4.5	Light cones and time travel in the Gödel universe	47
5.1	Lightlike geodesics starting at the origin	61
5.2	Planar lightlike geodesics not starting at the origin	63
5.3	Time travel on geodesics	65
5.4	Testing if causality can be violated on geodesics	66
5.5	Isometrical transport of A to the spatial origin	67
5.6	Projection of Killing vector field ξ_1^μ onto the (XY) -plane	70
5.7	Isometrically transporting points on the X -axis along the Killing vector field ξ_1^μ	71
5.8	Three horizons of three different observers	73
5.9	Isometrically transporting a circular CTC	77
5.10	Three-dimensional presentation of Fig. 5.9a	78
6.1	Geodesics in the (XY) -plane	82

6.2	Light paths from a small sphere to an observer located at the origin	83
6.3	Optical appearance of an infinitely often visible sphere	84
6.4	Starting direction of the geodesic using local angular coordinates	84
6.5	Exemplary plot of the left sides of eqns. (6.5)	86
6.6	Concatenation of isometric transformations	88
6.7	Internal structure of the GÖDEL ENGINE	90
6.8	Illustration of geometry images	91
6.9	Screenshot of the GÖDEL ENGINE server application	92
6.10	Stitching of an image pair to a continuous surface	97
6.11	High quality image of multiple appearing object images	100
7.1	Finite light cones in Gödel's universe	108
7.2	Spatial projection of a wavefront in the Gödel universe	109
7.3	Mapping the temperature of a black body to a color	111
7.4	Mapping a local emission time of an object to a color	112
7.5	An equidistant polar grid as seen from an observer at $z = 10$ looking down	113
7.6	An equidistant polar grid and a coordinate sphere ($r = 5$)	114
7.7	Illustrating the visually missing parts of the Earth sphere	115
7.8	A coordinate sphere and a polar grid in the Gödel universe	116
7.9	Screenshot of the GOEDELSPHERE application	117
7.10	Equidistant polar grid	119
7.11	Sphere moving quasistatically beyond the horizon	121
7.12	Two different angles plotted against the position of the pointlike object	121
7.13	A small staff parallel to the Y -axis	122
7.14	Quasistatically pushing a sphere beyond the horizon	123
7.15	Geodesics which connect the light source with the object	124
7.16	How the light source "sees" the object	124
7.17	Quasistatically pushing a sphere beyond the horizon	125
7.18	Scene definition and visualization of light source moving around Mars	126
7.19	Exemplary plots of the left sides of eqns. (6.5), as in Fig. 6.5	127
7.20	Mars located at $R_p = 0.8$ and $Z_p = \pm 2$	128
7.21	A vertical staff located at $R_p = 0.8$	129
7.22	Moving the light source vertically	130
7.23	Disappearance before occlusion	131
7.24	Shadow rendering with no angular dependency	132
7.25	Shadow rendering with angular dependency	133
7.26	Comparison of two renderings obtained using different stepsizes	135
7.27	Four objects with different initial velocities	137
7.28	Visibility of the sphere's center point	138

7.29	Visualization and surface temperature for an early time	139
7.30	Visualization and surface temperature for a later time	140
7.31	Comparing the emission time for objects starting at the origin	141
7.32	Observer looking along the $+X$ -axis and a time traveling object	143
7.33	Quantitative analysis of geodesical time travel	144
7.34	Visualization and surface temperature for geodesical time travel	145
7.35	Color-coded emission time for the partially time traveling Earth sphere	146
7.36	Geodesical time travel and higher order images	147
7.37	Observer resting close to the origin and a traveler on a CTC	149
7.38	Time emission diagram for a voyager traveling on a CTC	150
7.39	Visual appearance of an object traveling on a CTC	152
7.40	Visualization of the local emission time of the Earth sphere moving on a CTC	153
7.41	Visualization and surface temperature of Earth on a CTC	155
7.42	The Earth sphere traveling on a CTC	156
8.1	Egocentric visualization and Doppler shifts for the inner solar system (GV)	161
8.2	Local emission times of all inner solar system planets (GV)	162
8.3	Hipparcos catalog in a 4π -projection in nearly flat spacetime and in the	164
8.4	Hipparcos catalog in a 4π -projection (inverted colors)	165
8.5	Flying through the Hipparcos catalog	166
8.6	The Enterprise D in the Gödel universe	167

Index

- API, 29
- CUDA, 29
- DIRECTX, 25
- GLSL, 26
- GÖDEL ENGINE, 81
- GEOVIS, 22
- OPENCL, 29
- OPENGL, 25
- QT, 89
- RAYVIS, 22
- STREAM SDK, 29

- affine connection, 12
- affine parameter, 14
- ALU, 25
- ambient, 21
- anti de Sitter spacetime, 14
- atlas, 8

- base, 9
- blue shift, 110
- borderlines, 96

- cache, 25
- chart, 8
- Christoffel symbols, 12
- chromaticity coordinates, 110
- chronology protection conjecture, 55
- CIE color matching functions, 110
- CNC, 47

- constants of motion, 15
- control unit, 25
- coordinate base, 9
- cosmological constant, 13
- covariant derivative, 12
- CPU, 25
- CTC, 37, 47
- curve, 8
 - closed lightlike, 47
 - closed timelike, 37, 47, 52
 - past traveling, 47

- data
 - display, 91
 - reference, 89
- data-parallel processing, 27
- de Sitter spacetime, 14
- deferred shading, 28
- depth buffer, 27
- depth peeling, 99
- device, 29
- diagram
 - emission time, 143
 - visibility angle, 137
- diffuse, 21
- Doppler effect, 110
- DRAM, 25

- Einstein tensor, 13
- equations of isometric transport

- for points, 17
 - for vectors, 17
- event, 10
- Fermi-Walker derivative, 16
- Fermi-Walker transport, 16
- finite isometric displacements, 17
- finite light cones, 107
- fragments, 26
- frame buffer, 27
- frame dragging, 46
- framebuffer object, 97
- frequency shift, 110
- function, 8
- Gödel horizon, 40
- Gödel radius, 38
- Gödel ring, 129
- geodesic equations, 14
- geodesics
 - interconnecting, 84
- geometry
 - Lorentzian, 10
 - pseudo-Riemannian, 10
 - Riemannian, 10
- geometry images, 81, 90
- Gnu Scientific Library, 15
- GPU, 25
- gravitational constant, 13
- gravitational frequency shift, 110
- grid, 29
- GUI, 89
- high arithmetic intensity, 27
- host, 29
- image, *xiv*
 - object, *xiv*
- image-based approaches, 27
- images, 83
 - even, 83
 - light, 83, 124
 - object, 83
 - odd, 83
- index
 - contravariant, 10
 - coordinate, 11
 - covariant, 10
 - tetrad, 11
- instance, *xiv*
- instances, 142
- interconnecting geodesic, 83
- isometric transformation, 17
- isometries, 17
- kernel, 26
- Killing equation, 17
- Killing vector field, 17
- Kronecker-delta, 9
- Lagrangian formalism, 15
- line element, 10
- local light cone structure, 45
- local Minkowski system, 10
- loop quantum gravity, 53
- manifold, 8
- many-world interpretation, 53
- metric, 10
 - Gödel, 37
 - Gödel cylindrical, 38
 - Gödel scaled cylindrical, 38
- norm, 9
- Novikov self-consistency principle, 54
- Numerical Recipes, 15
- object, *xiv*, 83
 - coordinate, 22
 - defined by light flashes, 22

- local, 22
- object-space algorithms, 27
- ontological paradox, 54
- order, 83

- parallel transport, 16
- parameterization, 8
- Phong illumination model, 21
- predestination paradox, 54
- primary ray, 20
- proper time, 14
- PTC, 47

- rasterization, 26
- raytracing
 - 3D, 20
 - 4D, 22
- red shift, 110
- rendering, 26
- rendering pipeline, 26
- Ricci scalar, 13
- Ricci tensor, 12
- Riemann tensor, 12, 16
- rotation scalar, 38

- scalar product, 9
- scene description, 26
- secondary rays, 21
- shader
 - fragment, 27
 - vertex, 26
- shading language, 26
- shadow mapping, 96
- shadow volumes, 95
- signal, 92
- signature, 10
- slot, 92
- spatial wavefronts, 107
- specular, 21

- spin-curvature coupling, 45

- tangential vector, 9
- tensor, 10
 - Einstein, 13
 - Ricci, 12
 - Riemann, 12, 16
- tessellation, 98
- tetrad
 - dual, 11
 - for the Gödel universe, 40
 - local, 10
 - natural local, 12
- texture space lighting, 95
- thread, 29
- thread block, 29

- vector, 8
 - lightlike, 10
 - spacelike, 10
 - timelike, 10
- vector space
 - cotangent vector space, 9
 - dual vector space, 9
 - tangent vector space, 9
- vertex buffer objects, 90
- vertices, 26

Bibliography

- [Alc94] ALCUBIERRE M.: The warp drive: hyper-fast travel within general relativity. *Class. Quan. Grav.* 11 (1994), L73–L77.
- [Asi75] ASIMOV I.: *The end of eternity*. Fawcett Books, 1975.
- [Bar] BARIJAVEL R.: *Le Voyageur imprudent (The imprudent traveler)*.
- [BJ00] BINI D., JANTZEN R. T.: Circular orbits in Kerr spacetime: equatorial plane embedding diagrams. *Class. Quan. Grav.* 17 (2000), 1637–1647.
- [BJS85] BARROW J. D., JUSZKIEWICZ, SONODA D. H.: Universal rotation: how large can it be? *Mon. Not. R. Astron. Soc.* 213 (1985), 917–943.
- [BL03] BORSHUKOV G., LEWIS J. P.: Realistic human face rendering for "The Matrix Reloaded". In *SIGGRAPH '03: ACM SIGGRAPH 2003 Sketches & Applications* (New York, NY, USA, 2003), ACM, pp. 1–1.
- [BMC*08] BRIDGES M., MCEWEN J. D., CRUZ M., HOBSON M. P., LASENBY A. N., VIELVA P., MARTÍNEZ-GONZÁLEZ E.: Bianchi VII_h models and the cold spot texture. *Mon. Not. R. Astron. Soc.* 390, 4 (Nov. 2008), 1372–1376.
- [BMLH07] BRIDGES M., MCEWEN J. D., LASENBY A. N., HOBSON M. P.: Markov chain Monte Carlo analysis of Bianchi VII_h models. *Mon. Not. R. Astron. Soc.* 377, 4 (Jun. 2007), 1473–1480.
- [Bor05] BORCHERS M.: *Interaktive und stereoskopische Visualisierung in der speziellen Relativitätstheorie*. PhD thesis, Eberhard-Karls-Universität Tübingen, 2005.
- [BSMM07] BRONSTEIN I., SEMENDJAJEW K., MUSIOL G., MÜHLIG H.: *Handbook of Mathematics*. Springer, 2007.
- [Car68] CARTER B.: Global Structure of the Kerr Family of Gravitational Fields. *Phys. Rev.* 174, 5 (Oct. 1968), 1559–1571.
- [Car00] CARNEIRO S.: A Gödel-Friedmann cosmology? *Phys. Rev. D* 61, 8 (2000), 83506.
- [Car01] CARROLL S. M.: The Cosmological Constant. *Living Rev. Relativity* 4 (2001). <http://relativity.livingreviews.org/Articles/lrr-2001-1/>.
- [Cro77] CROW F. C.: Shadow algorithms for computer graphics. *ACM SIGGRAPH Computer Graphics* 11, 2 (1977), 242–248.

- [Cut92] CUTLER C.: Global structure of Gott's two-string spacetime. *Phys. Rev. D* 45, 2 (Jan. 1992), 487–494.
- [CW61] CHANDRASEKHAR S., WRIGHT J. P.: The Geodesics in Gödel's Universe. *Proc. Natl. Acad. Sci. U.S.A* 47 (1961), 341–347.
- [DG73] DEWITT B. S., GRAHAM N. (Eds.): *The Many-Worlds Interpretation of Quantum Mechanics*. Princeton Series in Physics. Princeton University Press, 1973.
- [DSS02] DELGADO A., SCHLEICH W. P., SÜSSMANN G.: Quantum gyroscopes and Gödel's universe: entanglement opens a new testing ground for cosmology. *NJP* 4 (2002), 37.
- [DWS*88] DEERING M., WINNER S., SCHEDIWIY B., DUFFY C., HUNT N.: The triangle processor and normal vector shader: a VLSI system for high performance graphics. *SIGGRAPH Comput. Graph.* 22, 4 (1988), 21–30.
- [Ein05] EINSTEIN A.: Zur Elektrodynamik bewegter Körper. *Annalen der Physik* 17, 10 (Aug. 1905), 891–921.
- [Ein15] EINSTEIN A.: Zur Allgemeinen Relativitätstheorie. *Sitzber. Preuss. Akad. Wiss. Berlin, Kl. Math.-Phys. Tech.* (1915), 778–786.
- [Eis07] EISELE M.-T.: *Baryogenesis, Neutrino Masses, and Dynamical Dark Energy*. PhD thesis, Technische Universität München, München, 2007.
- [EKT91] ECHEVERRIA F., KLINKHAMMER G., THORNE K. S.: Billiard balls in wormhole spacetimes with closed timelike curves: Classical theory. *Phys. Rev. D* 44, 4 (Aug. 1991), 1077–1099.
- [Euc45] EUCLID: *The optics of Euclid*. Journal of the Optical Society of America, 1945.
- [Eve57] EVERETT H.: Relative State Formulation of Quantum Mechanics. *Rev. Mod. Phys.* 29 (1957), 454–462.
- [Fec03] FECHTIG O.: *Physikalische Aspekte und Visualisierung von stationären Wurmlöchern*. Master's thesis, Universität Stuttgart, 2003.
- [FMN*90] FRIEDMAN J., MORRIS M. S., NOVIKOV I. D., ECHEVERRIA F., KLINKHAMMER G., THORNE K. S., YURTSEVER U.: Cauchy problem in spacetimes with closed timelike curves. *Phys. Rev. D* 42, 6 (Sep. 1990), 1915–1930.
- [FN90] FROLOV V. P., NOVIKOV I. D.: Physical effects in wormholes and time machines. *Phys. Rev. D* 42, 4 (Aug. 1990), 1057–1065.
- [FVDFH95] FOLEY J. D., VAN DAM A., FEINER S. K., HUGHES J. F.: *Computer graphics: Principles and Practice in C*. Addison-Wesley Systems Programming Series. Addison-Wesley Professional, 1995.
- [Gam39] GAMOW G. A.: *Mr. Tompkins in Wonderland*. Cambridge University Press, 1939.

- [GB08] GRAVE F, BUSER M.: Visiting the Gödel Universe. *IEEE Transactions on Visualization and Computer Graphics* 14, 6 (Nov.-Dec. 2008), 1563–1570.
- [GBM*09] GRAVE F, BUSER M., MÜLLER T., WUNNER G., SCHLEICH W. P.: The Gödel universe: Exact geometrical optics and analytical investigations on motion. *Phys. Rev. D* 80, 103002 (2009).
- [GFAMA08] GRAVE F, FRUTOS-ALFARO F, MÜLLER T., ADIS D.: Wave Fronts in General Relativity Theory. In *Proceedings of the Eleventh Marcel Grossmann Meeting on General Relativity* (Sep. 2008), World Scientific, pp. 1737–1739.
- [GGH02] GU X., GORTLER S., HOPPE H.: Geometry images. vol. 21, pp. 355–361.
- [GMDW09] GRAVE F, MÜLLER T., DACHSBACHER C., WUNNER G.: The Gödel Engine - An interactive approach to visualization in general relativity. In *Computer Graphics Forum (Proc. Eurovis 09)* (2009), Hege H.-C., Hotz I., Munzner T., (Eds.), vol. 28 of *The International Journal of the Eurographics Association*, Blackwell Publishing, pp. 807–814.
- [GMW*07] GRAVE F, MÜLLER T., WUNNER G., ERTL T., BUSER M., SCHLEICH W.: Visualization of the Gödel Spacetime. In *Proceedings of the 4th High-End Visualization Workshop* (2007), Bengler W., Heinzl R., Kapferer W., Schoor W., Tyagi M., Venkataraman S., Weber G. H., (Eds.), Lehmanns Media, pp. 62–75.
- [GNU] GNU: GSL – GNU Scientific Library. <http://www.gnu.org/software/gsl/>.
- [Got91] GOTT J. R.: Closed timelike curves produced by pairs of moving cosmic strings: Exact solutions. *Phys. Rev. Lett.* 66, 9 (Mar. 1991), 1126–1129.
- [Got02] GOTT J. R.: *Time travel in Einstein's universe: the physical possibilities of travel through time*. Mariner Books, 2002.
- [Gra04] GRAVE F.: *Visualisierung zum Gravitationskollaps und Wellenfronten in der Allgemeinen Relativitätstheorie*. Master's thesis, Universität Stuttgart, 2004.
- [Gro96] GROENE A.: *Entwurf eines objektorientierten Visualisierungssystems auf der Basis von Raytracing*. PhD thesis, Eberhard-Karls-Universität Tübingen, 1996.
- [grt] <http://grtensor.phy.queensu.ca/>.
- [GSR03] GIBBONS G. W., SHELLARD E. P. S., RANKIN S. J. (Eds.): *The Future of Theoretical Physics and Cosmology: Celebrating Stephen Hawking's Contributions to Physics*, 1 ed. Cambridge University Press, 2003.
- [Gö49] GÖDEL K.: An Example of a New Type of Cosmological Solutions of Einstein's Field Equations of Gravitation. *Rev. Mod. Phys.* 21, 3 (Jul. 1949), 447–450. Gödel's original paper on the Gödel universe.
- [Gö90] GÖDEL K.: *Kurt Gödel: Collected Works, Vol. II, Publications 1938–1974*. Oxford University Press, 1990.

- [Gö95] GÖDEL K.: *Kurt Gödel: Collected Works, Vol. III, Unpublished essays and lectures*. Oxford University Press, 1995.
- [Haw92] HAWKING S. W.: Chronology protection conjecture. *Phys. Rev. D* 46, 2 (Jul. 1992), 603–611.
- [Haw01] HAWKING S. W.: *The Universe in a Nutshell*. Bantam Dell Pub Group, 2001.
- [Her03] HERDEIRO C. A. R.: The Kerr–Newman–Gödel black hole. *Class. Quan. Grav.* 20 (2003), 4891–4900.
- [Hua99] HUANG W. H.: Chronology protection in generalized Gödel spacetime. *Phys. Rev. D* 60, 6 (1999), 67505.
- [Int] INTERNATIONAL ORGANISATION FOR STANDARDIZATION: *ISO 31: Quantities and units*. <http://www.iso.org/>.
- [JBE*05] JAFFE T. R., BANDAY A. J., ERIKSEN H. K., GÓRSKI K. M., HANSEN E. K.: Evidence of Vorticity and Shear at Large Angular Scales in the WMAP Data: A Violation of Cosmological Isotropy? *ApJ* 629 (Aug. 2005), L1–L4.
- [KDN*09] KOMATSU E., DUNKLEY J., NOLTA M. R., BENNETT C. L., GOLD B., HINSHAW G., JAROSIK N., LARSON D., LIMON M. AND PAGE L., ET AL.: Five-Year Wilkinson Microwave Anisotropy Probe Observations: Cosmological Interpretation. *ApJ* 180, 2 (2009), 330–376.
- [Kea03] KNOP R. A., ET AL.: New Constraints on Ω_M , Ω_A , and w from an Independent Set of Eleven High-Redshift Supernovae Observed with HST. *ApJ* 598, 102 (2003).
- [Ker63] KERR R. P.: Gravitational Field of a Spinning Mass as an Example of Algebraically Special Metrics. *Phys. Rev. Lett.* 11, 5 (Sep. 1963), 237–238.
- [Kun56] KUNDT W.: Trägheitsbahnen in einem von Gödel angegebenen kosmologischen Modell. *Z. Phys.* 145 (1956), 611–620.
- [KWSD04] KAJARI E., WALSER R., SCHLEICH W. P., DELGADO A.: Sagnac Effect of Gödel's Universe. *Gen. Rel. Grav.* 36, 10 (Oct. 2004), 2289–2316.
- [KZ] KRAUS U., ZAHN C.: Relativity visualized – Space Time Travel. <http://www.spacetimetravel.org/>.
- [Lan24] LANCZOS C.: Über eine stationäre Kosmologie im Sinne der Einsteinischen Gravitationstheorie. *Z. Phys.* 21, 1 (1924), 73–110.
- [LC02] LOBO E., CRAWFORD P.: Time, closed timelike curves and causality. *Arxiv preprint gr-qc/0206078* (2002).
- [map] <http://www.maplesoft.com/products/maple/>.

- [MG09a] MÜLLER T., GRAVE F.: Motion4D - A library for lightrays and timelike worldlines in the theory of relativity. *CPC 180* (2009), 2355–2360.
- [MG09b] MÜLLER T., GRAVE F.: Catalogue of Spacetimes. *Arxiv* (2009).
- [MG10] MÜLLER T., GRAVE F.: GeodesicViewer - A tool for exploring geodesics in the theory of relativity. *CPC 181* (2010), 413–419.
- [MT88] MORRIS M. S., THORNE K. S.: Wormholes in spacetime and their use for interstellar travel: A tool for teaching general relativity. *AJP 56*, 5 (May. 1988), 395–412.
- [MTW73] MISNER C. W., THORNE K. S., WHEELER J. A.: *Gravitation*. W. H. Freeman, 1973.
- [MVM09] MILLER F. P., VANDOME A. F., MCBREWSTER J. (Eds.): *Ontological paradox: Newcomb's paradox, Kavka's toxin puzzle, Time travel in fiction, Time viewer, Grandfather paradox, Predestination paradox, Predestination paradoxes in popular culture*. Alphascript Publishing, 2009.
- [MW10] MÜLLER T., WEISKOPF D.: Distortion of the stellar sky by a Schwarzschild black hole. *AJP 78*, 204–214 (2010).
- [Mü06] MÜLLER T.: *Visualisierung in der Allgemeinen Relativitätstheorie*. PhD thesis, Eberhard-Karls-Universität Tübingen, 2006.
- [Mü08] MÜLLER T.: Exact geometric optics in a Morris-Thorne wormhole spacetime. *Phys. Rev. D 77*, 4 (2008).
- [Nak90] NAKAHARA M.: *Geometry, Topology and Physics*. Inst. Phys. Pub., 1990.
- [Nav70] NAVEZ J.: Le Groupe de mouvements des espaces de Gödel. *Bulletin de la Société Royale des Sciences de Liège 39* (1970), 470–473.
- [Ngu07] NGUYEN H.: *GPU Gems 3*. Addison-Wesley Professional, 2007.
- [NMAA08] NÉMETI I., MADARÁSZ J. X., ANDRÉKA H., ANDAI A.: Visualizing some ideas about Gödel-type rotating universes. *Arxiv preprint arXiv:0811.2910* (2008).
- [Nov92] NOVIKOV I. D.: Time machine and self-consistent evolution in problems with self-interaction. *Phys. Rev. D 45*, 6 (Mar. 1992), 1989–1994.
- [NST83] NOVELLO M., SOARES I. D. A., TIOMNO J.: Geodesic motion and confinement in Gödel's universe. *Phys. Rev. D 27*, 4 (Feb. 1983), 779–788.
- [NVI] NVIDIA: NVIDIA CUDA™ Programming Guide. <http://www.nvidia.com/cuda>.
- [OS03] OZSVÁTH I., SCHÜCKING E.: *AJP 71* (2003), 801.
- [Pfa81] PFARR J.: Time Travel in Gödel's Space. *Gen. Rel. Grav. 13*, 11 (1981), 1073–1091.
- [Pho75] PHONG B. T.: Illumination for computer generated pictures. *Communications of the ACM 18*, 6 (1975), 317.

- [PTVF07] PRESS W. H., TEUKOLSKY S. A., VETTERLING W. T., FLANNERY B. P.: *Numerical Recipes: The Art of Scientific Computing, 3rd edition*. Cambridge University Press, 2007.
- [PW09] PENG J. J., WU S. Q.: Extremal Kerr black hole/CFT correspondence in the five-dimensional Gödel universe. *Phys. Rev. B* 673, 3 (2009), 216–219.
- [Rin06] RINDLER W.: *Relativity: Special, General, and Cosmological, 2nd edition*. Oxford University Press, 2006.
- [Rin09] RINDLER W.: Gödel, Einstein, Mach, Gamow, and Lanczos: Gödel's remarkable excursion into cosmology. *AJP* 77, 6 (Jun. 2009), 498–510.
- [RL07] ROSA V. M., LETELIER P. S.: Stability of closed timelike curves in the Gödel universe. *Gen. Rel. Grav.* 39, 9 (2007), 1419–1435.
- [Ros05] ROST R. J.: *OpenGL (R) Shading Language*. Addison-Wesley Professional, 2005.
- [Rov08] ROVELLI C.: Loop Quantum Gravity. *Living Rev. Relativity* 11 (2008). <http://www.livingreviews.org/lrr-2008-5>.
- [RT80] RAYCHAUDHURI A. K., THAKURTA S. N. G.: Homogeneous space-times of the Gödel type. *Phys. Rev. D* 22, 4 (Aug. 1980), 802–806.
- [RT83] REBOUÇAS M. J., TIOMNO J.: Homogeneity of Riemannian space-times of Gödel type. *Phys. Rev. D* 28, 6 (Sep. 1983), 1251–1264.
- [SBD*07] SPERGEL D. N., BEAN R., DORE O., NOLTA M. R., BENNETT C. L., DUNKLEY J., HINSHAW G., JAROSIK N., KOMATSU E., PAGE L., ET AL.: Wilkinson Microwave Anisotropy Probe (WMAP) three year results: Implications for cosmology. *ApJS* 170 (2007), 377–408.
- [SSM07] SAVAGE C. M., SEARLE A., MCCALMAN L.: Real Time Relativity: Exploratory learning of special relativity. *AJP* 75, 9 (Sept. 2007).
- [Ste70] STEIN H.: *Philos. Sci.* 37 (1970), 589.
- [Ste90] STEPHANI H.: *General Relativity: An introduction to the theory of the gravitational field*. Cambridge University Press, New York, 1990.
- [Ste98] STEADMAN B. R.: Confinement of null geodesics in the van Stockum exterior. *Class. Quan. Grav.* 15 (1998), 1357–1365.
- [Sto37] STOCKUM W. J.: The gravitational field of a distribution of particles rotating around an axis of symmetry. *Proc. Roy. Soc. Edinburgh* 57 (1937), 135.
- [Str04] STRAUMANN N.: *General Relativity With Applications to Astrophysics*. Springer, 2004.
- [SVP*03] SPERGEL D. N., VERDE L., PEIRIS H. V., KOMATSU E., NOLTA M. R., BENNETT C. L., HALPERN M., HINSHAW G., JAROSIK N., KOGUT A., ET AL.: First-Year Wilkinson Microwave Anisotropy Probe (WMAP) 1 Observations: Determination of Cosmological Parameters. *ApJS* 148, 1 (2003), 175–194.

- [SWND05] SHREINER D., WOO M., NEIDER J., DAVIS T.: *OpenGL (R) Programming Guide: The Official Guide to Learning OpenGL (R), Version 2 (OpenGL)*. Addison-Wesley Professional, 2005.
- [Ter59] TERRELL J.: Invisibility of the Lorentz contraction. *Phys. Rev.* 116, 4 (Nov. 1959), 1041–1045.
- [Tho92] THORNE K. S.: Closed Timelike Curves. In *General Relativity and Gravitation* (1992), Gleiser R., Kozameh C., Moreschi O., (Eds.), Proceedings of the 13th International Conference on General Relativity and Gravitation, Inst. Phys. Pub., pp. 295–315.
- [Tho95] THORNE K. S. (Ed.): *Black Holes and Time Warps: Einstein's Outrageous Legacy*. W. W. Norton & Company, 1995.
- [Tip73] TIPLER F. J.: Rotating cylinders and the possibility of global causality violation. *Phys. Rev. D* 9, 8 (1973).
- [Vis96] VISSER M.: *Lorentzian Wormholes - From Einstein to Hawking*. Springer-Verlag New York, Inc., 1996.
- [WA99] WEISKOPF D., ANSORG M.: Visualization of the general relativistic rigidly rotating disk of dust. *Annalen der Physik* 9, Spec. Issue (1999), 179–185.
- [Wal] WALKER J.: Colour Rendering of Spectra. <http://www.fourmilab.ch/documents/specrend>.
- [Wal84] WALD R. M.: *General Relativity*. The University of Chicago Press, 1984.
- [Wei01] WEISKOPF D.: *Visualization of Four-Dimensional Spacetimes*. PhD thesis, Eberhard-Karls-Universität Tübingen, 2001.
- [Wel92] WELLS H. G.: *The time machine*. Tor Classics, 1992.
- [WFR00] WHEELER J. A., FORD K., RIGDEN J. S.: Geons, Black Holes and Quantum Foam: A Life in Physics. *AJP* 68 (2000), 584.
- [Whi80] WHITTED T.: An improved illumination model for shaded display. *Communications of the ACM* 23, 6 (1980), 343–349.
- [Wil78] WILLIAMS L.: Casting curved shadows on curved surfaces. *ACM SIGGRAPH Computer Graphics* 12, 3 (1978), 270–274.
- [WL04] WRIGHT R. S., LIPCHAK B.: *OpenGL superbible*. Sams Indianapolis, 2004.
- [Zat05] ZATLOUKAL M.: *Visualisierung in der Kerr-Raumzeit*. Master's thesis, Eberhard-Karls-Universität Tübingen, 2005.

Danksagung

Ich danke Günter Wunner für die freundliche Aufnahme an seinem Institut und für seine große Hilfsbereitschaft bei physikalischen Fragen und organisatorischen Problemen, Daniel Weiskopf für die Erstellung des Zweitgutachtens und die gute Betreuung, Carsten Dachsbacher für die vielen hilfreichen und punktgenauen Analysen („schau mal da nach, das ist genau was du brauchst“) und Thomas Ertl für die Möglichkeit, an seinem Institut einen tollen Arbeitsplatz zu erhalten. Ich konnte durch die Zusammenarbeit mit allen Beteiligten ein sehr interessantes Forschungsgebiet bearbeiten und erhielt durch die Finanzierung der DFG (Proj. Nr. 99015432) die Möglichkeit, lehrreiche Konferenzen an vielen schönen Orten zu besuchen. Außerdem danke ich Endre Kajari, Michael Buser und Wolfgang Schleich vom Institut für Quantenphysik der Universität Ulm.

Weiterhin bin ich Thomas Müller zu großem Dank verpflichtet, dessen außergewöhnlich gute Betreuung – welche oftmals über die eigentlichen physikalischen Fragestellungen hinausging – meine Arbeit in dieser Form erst ermöglicht hat.

Außerdem bin ich meinen Kollegen am VIS/US tief verbunden, insbesondere Katrin Bidmon für das Korrekturlesen meiner Arbeit und für die vielen interessanten Gespräche, Sebastian Grottel für die Hilfe bei Grundlagenfragen („Klar, so etwas gibt es schon, das heißt . . .“) und seine erheiternden Vorträge, Christoph Müller als mein CUDA-Berater („Klar kann das so nicht gehen“) und für die grandiosen Kuchen und Filip Sadlo für die off-topic Gespräche.

Auf der privaten Seite schätze ich mich sehr glücklich wegen meiner tollen Freunde und meiner beiden Familien, welche mich in den letzten Jahren treu und zuverlässig begleitet haben. Es ist beinahe unmöglich, allen den gebührenden Dank zukommen zu lassen. Deswegen werde ich mich nur bei einigen wenigen Menschen explizit bedanken. Ich hoffe, Ihr wisst *alle* wie wichtig Ihr für mich seid und wie dankbar ich Euch bin. Ausdrücklich danken möchte ich Oliver Fechtig („purpurrot find ich prima“) für die tiefe Freundschaft, die gemeinsame Zeit in Tübingen und die vielen irrsinnig witzigen Gespräche, welche unsere Umgebung mehr als einmal in komplette Ratlosigkeit versetzt hat. Erik Puscher („langsam in die Kurve gehen“) danke ich für seine Bemühungen, den Cannstatter Trupp auch in Zukunft zusammenzuhalten, Dirk Strohm („was mach'sch denn für einen . . .“) für die vielen erheiternden Skatabende und Toni Heyler für das Korrekturlesen.

An letzter Stelle auf dieser Seite und an erster Stelle in meinem Leben danke ich Andrea Halbig, denn ohne sie wäre nicht nur diese Arbeit nicht möglich gewesen. Ich danke ihr für die Motivation, ihr offenes Ohr in allen Lebensfragen und alles andere was den Rahmen dieser Danksagung eindeutig sprengen würde. Sie weiß, was ich meine.

Ehrenwörtliche Erklärung

Ich erkläre, dass ich diese Dissertation, abgesehen von den ausdrücklich bezeichneten Hilfsmitteln und den Ratschlägen von den jeweils namentlich aufgeführten Personen, selbständig verfasst habe.

Stuttgart, den 31. März 2010

der Autor

Vita

Persönliche Daten

Name **Frank Grave**
Geburtsdatum **18.01.1978**
Geburtsort **Ludwigsburg**

Schulbildung

08/1984 – 07/1988 **Grundschule**, *Tamm*
08/1988 – 07/1997 **Gymnasium**, *Friedrich-List-Gymnasium Asperg*
06/1997 **Abitur**

Studium

10/1998 – 09/2004 **Studium im Fach Physik**, *Universität Stuttgart*
10/2000 **Vordiplom**, *Universität Stuttgart*
10/2004 **Diplom**, *Universität Stuttgart*
„Visualisierung zum Gravitationskollaps und Wellenfronten in der Allgemeinen Relativitätstheorie“

Promotion

01/2007 – 05/2010 **Dissertation**, *Universität Stuttgart*.
„The Gödel Universe – Physical Aspects and Egocentric Visualizations“.

Akademische Lehrer

Carsten Dachsbacher, Thomas Ertl, Thomas Müller, Hanns Ruder, Daniel Weiskopf, Günter Wunner

